



**University of Crete**

**Chemistry  
Department | PhD Thesis**

***Development of responsive  
biomimetic polymer surfaces***

**Melani A. Frysali  
Chemical Engineer ATh, MSc.**

**Advisor: Prof. Spiros H. Anastasiadis**

*Heraklion, March 2017*



**University of Crete**

**Chemistry  
Department | PhD Thesis**

# *Development of responsive biomimetic polymer surfaces*

**Melani Frysalı**

**Chemical Engineer ATh, MSc.**

## **Dissertation committee:**

Prof.	Spiros H. Anastasiadis	Advisor, Chemistry Department, UOC
Ass. Prof.	Maria Vamvakaki	Department of Materials, UOC
Prof.	Demetrios Ghanotakis	Chemistry Department, UOC
Prof.	Demetrios Anglos	Chemistry Department, UOC
Dr.	Emmanuel Stratakis	IESL-FORTH
Dr.	George Kenanakis	IESL-FORTH
Dr.	Loppinet Benoit	IESL-FORTH

*Heraklion, March 2017*

*“Chance favors only the prepared mind”*

*Louis Pasteur*

## *Acknowledgments*

First of all, I would like to express my deepest appreciation to my supervisor, *Prof. Spiros Anastasiadis*, who gave me the opportunity to work in the laboratories of the Institute of Electronic Structure and Laser of the Foundation for Research and Technology – Hellas and accomplish this Ph.D Thesis. He has always been there for guidance, support, encouraging independent thinking and given me the freedom to work on the projects which I thought were interesting.

I owe my deepest gratitude to *Lampros Papoutsakis* for initiating me in the surface science. Without his guidance, his helpful advice and his valuable insights, nothing would be realized.

I am greatly indebted to *Prof. Maria Vamvakaki*, who closely supervised a part of this work. Her helpful suggestions, time and advice, were of vital importance for the successful completion of my research.

My special thanks to *Dr. Emmanuel Stratakis* for his helpful advice, for the invaluable assistance, guidance and support. I am also thankful to all the members of his group for the excellent collaboration we had.

I would also like to express my special thanks and gratitude to *Dr. George Kenanakis* for the new techniques he taught me, the interest discussions we had, for his advices, and for contributing in countless ways during the entire time of this work.

---

I am grateful to *Dr. Georgia Kaklamani*, for both friendship and collaboration and for her expertise regarding the biological section. But most of all, I thank her for being a source of motivation and encouragement.

I would also thank my dissertation committee members *Prof. Dimitris Ghanotakis*, *Prof. Dimitris Anglos* and *Dr. Loppinet Benoit* for their contribution to the success of this work.

Many thanks go to *Dr. George Konstantinidis* and Micro/Nano Electronics Group for the collaboration on a part of this work, *Aleka Manousaki* and *Dr. Vassilios Dracopoulos* (ICE-HT) for recording the SEMs of the samples and *Prof. Taubert* for hosting me in Potsdam University and giving me the opportunity to work in his lab.

I am thankful to all past and current members of the Hybrid Nanostructures Group. Their continuous support has been invaluable to me.

Many warm thanks go to my mom, dad, and sister. My hard-working parents have sacrificed their lives for my sister and myself and provided unconditional support, love and care.

Last but not least, I would like to thank my husband and love of my life, *Niko*, for his constant love, continuous patience and for giving me the energy to do all that I do.

***Thank You all - March 2017***

***Melina Frysalis***

# Contents

Acknowledgments.....	3
Contents.....	5
List of Figures.....	10
List of Tables.....	20
<b>Chapter 1</b>	
1. Introduction and overview.....	21
1.1. Introduction .....	21
1.2. Contents of this thesis.....	26
1.3. References .....	29
<b>Chapter 2</b>	
2. Functional ZnO surfaces with photocatalytic behavior and reversible wettability ....	37
2.1. Introduction .....	37
2.1.1. Basic properties and applications of ZnO .....	41
2.1.2. ZnO mediated heterogeneous photocatalysis .....	44
2.1.3. The mechanism of ZnO reversible wettability .....	48
2.1.4. ZnO nanowires: growth and applications .....	49
2.1.5. Properties of Poly(methyl methacrylate), PMMA.....	50
2.1.6. Properties of Poly(2-vinylpyridine), P2VP .....	52
A) Development of Si spikes covered with ZnO coating, exhibiting both photocatalytic behavior and reversible wettability.....	53
2.1. Introduction .....	53
2.2. Experimental Part .....	54
2.2.1. Surface manufacturing with fs laser .....	54
2.2.2. Deposition of ZnO films on Si spikes .....	55
2.2.3. Photocatalytic behavior of the developed surfaces .....	57
2.3. Wettability of the prepared samples .....	58

2.4.	Results and Discussion.....	58
2.4.1.	Surface characterization .....	58
2.4.2.	Photocatalytic activity .....	62
2.4.3.	Wettability .....	65
2.4.4.	Stability test .....	66
2.5.	Conclusions .....	68
B)	Development of polymer brush ZnO nanowires exhibiting high photocatalytic behavior.....	69
2.6.	Introduction .....	69
2.7.	Experimental Part .....	69
2.7.1.	Deposition of ZnO seed layers and nanowires .....	69
2.7.2.	Deposition of polymer films on ZnO nanorods .....	70
2.7.3.	Silane-modified ZnO nanorods.....	71
2.7.4.	Photocatalytic behavior of the developed surfaces.....	72
2.7.5.	Wettability of the prepared samples .....	73
2.8.	Results and Discussion .....	73
2.8.1.	Surface characterization.....	73
2.8.2.	Photocatalytic activity .....	83
2.8.3.	Wettability of the developed surfaces.....	86
2.9.	Conclusions.....	91
2.10.	References.....	93
<b>Chapter 3</b>		
3.	Dual pH- thermo responsive surfaces.....	102
3.1.	Introduction.....	102
3.1.1.	Applications of smart polymers with reversible wettability .....	105
3.1.2.	Covalent bonding of polymers on surfaces.....	106
3.1.3.	Properties of poly(N-isopropylacrylamide), PNIPAM .....	107
3.1.4.	Effect of surface characteristics on cell attachment and proliferation.....	109
3.2.	Experimental Part... ..	111

3.2.1.	Surface Modification with fs Laser.....	111
3.2.2.	Silanization and thermal oxide growth process on Silicon.....	112
3.2.3.	End-Grafted PNIPAm and P2VP Thin Films .....	112
3.2.4.	Surface characterization.....	113
3.2.5.	Wettability of the prepared samples.....	114
3.2.6.	Cell culture experiments .....	114
3.3.	Results and Discussion.....	115
3.3.1.	Surface characterization of polymer coated surfaces.....	115
3.3.2.	Wettability of polymer coated surfaces .....	118
3.3.3.	Cell adhesion to polymer surfaces.....	131
3.4.	Conclusions.....	141
3.5.	References.....	142
<b>Chapter 4</b>		
4.	Anisotropic directionality on patterned surfaces .....	150
4.1.	Introduction.....	150
4.1.1.	Contact angle hysteresis.....	153
4.1.2.	Anisotropic wetting.....	154
4.1.3.	Anisotropic wetting phenomena in nature with low hysteresis .....	155
4.1.4.	High adhesive surfaces in nature .....	159
A)	Superhydrophobic non-adhesive surfaces with unidirectional droplet roll-off behavior.....	162
4.2.	Introduction.....	162
4.3.	Experimental Part.....	163
4.3.1.	Surface manufacturing with fs laser.....	163
4.3.2.	Making Si spikes superhydrophobic .....	164
4.3.3.	Wettability of the prepared samples.....	165
4.4.	Results and Discussion.....	166
4.4.1.	Surface characterization.....	166
4.4.2.	Wettability.....	178

4.5.	Conclusions .....	187
B)	Unidirectional wetting of surfaces with macro-, micro- and nano- structuring.....	188
4.6.	Introduction .....	188
4.7.	Experimental Part.....	189
4.7.1.	Surface manufacturing with photolithography .....	189
4.7.2.	Surface manufacturing with fs laser.....	189
4.7.3.	Silanization process of the surfaces .....	190
4.7.4.	Thermal Oxide growth process on Silicon.....	190
4.7.5.	Wettability of the prepared samples.....	190
4.8.	Results and Discussion.....	191
4.8.1.	Surface characterization.....	191
4.8.2.	Wettability of surfaces after thermal oxidation.....	193
4.8.3.	Wettability of surfaces after silanization .....	194
4.9.	Conclusions .....	200
C)	Anisotropic surfaces with high adhesion and unidirectional properties.....	200
4.10.	Introduction .....	200
4.11.	Experimental part .....	201
4.11.1.	Surface manufacturing with fs laser.....	201
4.11.2.	Surface silanization.....	201
4.11.3.	Surface wettability .....	202
4.12.	Results and Discussion.....	202
4.12.1.	Surface characterization.....	202
4.12.2.	Wettability of surfaces .....	208
4.13.	Conclusions .....	217
4.14.	References .....	218
<b>Chapter 5</b>		
5.	Covalent immobilization of metal nanoparticle containing microgels onto solid substrates.....	225
5.1.	Introduction .....	225

5.1.1.	Polymeric microgels .....	227
5.1.2.	Synthesis of the microgels .....	228
5.1.3.	Syntheis of metal containing microgels .....	229
5.1.4.	Immobilization of microgels onto surfaces: Deposition techniques .....	229
5.2.	Experimental Part .....	230
5.2.1.	Synthesis of metal containing microgels .....	230
5.2.2.	Characterization of the metal containing microgels .....	231
5.2.3.	Immobilization of microgels onto solid surfaces .....	232
5.2.4.	Stability tests .....	237
5.2.5.	Surface analysis with Image J and Matlab code .....	238
5.2.6.	Hydrogenation reaction with metal containing microgels as catalysts .....	241
5.3.	Results and Discussion.....	242
5.3.1.	Characterization of metal containing microgels .....	242
5.3.2.	Immobilization of microgels onto solid surfaces .....	245
5.3.3.	Determination of microgels density, before and after the stability tests with Image J and Matlab code.....	262
5.3.4.	Catalytic activity of metal containing microgels on a model hydrogenation reaction .....	270
5.4.	Conclusions .....	277
5.5.	References .....	278
<b>Chapter 6</b>		
6.1	Concluding remarks.....	283
6.2	Future work.....	287

## *List of Figures*

Figure 2.1. Hexagonal wurtzite crystal structure of ZnO. ....	42
Figure 2.2. Schematic mechanism of ZnO, acting as photocatalyst. ....	45
Figure 2.3. Chemical structure of stearic acid. ....	45
Figure 2.4. Structural formula of methylene blue. ....	47
Figure 2.5. Chemical structure of carboxy terminated Poly(methyl methacrylate). ....	51
Figure 2.6. Chemical structure of carboxy terminated Poly(2- vinyl pyridine). ....	52
Figure 2.7. Experimental set up of fs laser. ....	55
Figure 2.8. Schematic presentation of ZnO deposition on Si spikes. ....	56
Figure 2.9. Custom made set up for the UV illumination of the studied samples. ....	57
Figure 2.10. AFM image (scan size $1\mu\text{m}\times 1\mu\text{m}$ ; z-range $\sim 62\text{nm}$ ), (a), and X-ray diffractogram, (b), of a $\sim 80\text{nm}$ thick ZnO film on a flat Silicon substrate. ....	59
Figure 2.11. FE-SEM micrographs of bare Si spikes prepared by fs laser irradiation on Silicon (a) and coated with ZnO by the sol-gel/spin-coating process (b). ....	60
Figure 2.12. SEM micrographs of the laser irradiated Si substrates after ZnO coating. ....	61
Figure 2.13. UV-Vis absorption spectra of aqueous solution of methylene blue in contact with a surface with a ZnO coating on top of silicon spikes following UV irradiation for various times. ....	62
Figure 2.14. Normalized absorption of aqueous solutions of methylene blue at $\lambda_{\text{max}}=665\text{nm}$ under UV light irradiation, for Samples A, B, C and D. ....	63
Figure 2.15. Normalized absorption of aqueous solutions of methylene blue at $\lambda_{\text{max}}=665\text{nm}$ under UV light irradiation for flat Si substrate (triangles), Si spikes (circles), $4\times\text{ZnO}$ coating on flat silicon (squares) and $4\times\text{ZnO}$ coating on silicon spikes (left) and plot of $-\ln(C/C_0)$ vs irradiation time for photodegradation for Sample C (right). ....	64
Figure 2.16. Photographs of representative water drops and the respective equilibrium contact angles on specimens with (a) ZnO coating onto a flat Si substrate and (b) ZnO coating onto a surface with silicon spikes. Drops are shown for the specimens following UV irradiation (on the right) and after thermal treatment at $200^\circ\text{C}$ (on the left). ....	65
Figure 2.17. Dependence of the water contact angle on a surface with a ZnO coating on top of the silicon spikes following (a) UV irradiation and (b) heating at $200^\circ\text{C}$ for various times. ....	66
Figure 2.18. Average contact angle values of water droplets situated on specimens with ZnO coating onto a flat Si substrate (squares) and ZnO coating onto a surface with silicon spikes	

(diamonds) for five irradiation cycles of UV irradiation (UV lamp centered at 365 nm with a light intensity of  $\sim 10 \text{ mW} / \text{cm}^2$ ) for 50 min and 3h thermal heating at  $200^\circ\text{C}$ .....67

Figure 2.19. FE-SEM micrographs of ZnO nanowires grown on Corning glasses, top view (left) and side view (right). .....74

Figure 2.20. FE-SEM micrographs of ZnO nanowires coated with PMMA film. ....77

Figure 2.21. FE-SEM micrographs of ZnO nanowires coated with P2VP film. ....81

Figure 2.22. FE-SEM images of ZnO nanowires grafted with P2VP (sample G) and covered with stearic acid. ....82

Figure 2.23. FE-SEM micrograph of silanized ZnO nanowires. ....83

Figure 2.24. FT-IR transmittance versus wavenumber spectra demonstrating the degradation of stearic acid vs. irradiation time: (left) on the ZnO nanowires covered with PMMA (0.1 wt % in toluene) and (right) on the ZnO nanowires covered with PMMA (0.01 wt % in toluene). .....84

Figure 2.25. Normalized absorption of chloroform solutions of stearic acid under UV light irradiation for PMMA coated ZnO nanowires in concentrations 0.01(circles) and 0.1 wt % (squares). .....84

Figure 2.26. Normalized absorption of chloroform solutions of stearic acid under UV light irradiation for P2VP coated, 0.001 wt % (diamonds), 0.01 (circles) wt % and 0.1 wt % (squares), ZnO nanowires. ....85

Figure 2.27. Photographs of representative water drops and the respective equilibrium contact angles on glass substrates with ZnO nanorods covered with P2VP (0.01 wt % in toluene) after immersion in pH 2 (left) and pH 12 (right). .....89

Figure 2.28. Average contact angle values of water droplets onto ZnO nanorods coated with P2VP brushes, for 6 cycles of pH environment changes. ....90

Figure 2.29. Photographs of the representative water drops and the respective equilibrium contact angles on glass substrates with ZnO nanowires, before (left) and after the silanization process (right). ....91

Figure 3.1. Schematic presentation of methods for polymer chains immobilization. ....107

Figure 3.2. Chemical structure of carboxy terminated PNIPAm. ....107

Figure 3.3. Micro/nano-structured Si substrate by fs-laser irradiation (at  $1.4 \text{ J}\cdot\text{cm}^{-2}$  fluence) under reactive  $\text{SF}_6$  atmosphere before (left) and after (right) coating with P2VP brushes....116

Figure 3.4. Microstructured Si surface by fs-laser irradiation under reactive  $\text{SF}_6$  atmosphere irradiated at 0.5 (left) and  $2.1 \text{ J}\cdot\text{cm}^{-2}$  (right) after coating with P2VP brushes. ....116

Figure 3.5. ATR-FTIR spectra of the P2VP brush, the PNIPAm brush and the 50/50 mixed P2VP/PNIPAm brush. ....117

Figure 3.6. Photographs of representative water drops and the respective contact angles on (a) flat Si and (b) laser micro/nano-structured Si substrates (  $1.4 \text{ J}\cdot\text{cm}^{-2}$  ) coated with P2VP

brushes ( $M_n = 53,000 \text{ g}\cdot\text{mol}^{-1}$ ) following immersion in high and low pH solutions (pH 9 and pH 2, respectively).....	118
Figure 3.7. Photograph of representative water drop Si Laser irradiated substrate coated with dichlorodimethylsilane.....	119
Figure 3.8. Average contact angle values of water droplets onto flat Si substrate and Si spikes (irradiated at $1.4 \text{ J}\cdot\text{cm}^{-2}$ ) coated with P2VP brushes ( $M_n = 53,000 \text{ g}\cdot\text{mol}^{-1}$ ), for 5 cycles of pH environment changes.....	120
Figure 3.9. Average contact angle values of water droplets onto Si spikes coated with P2VP brushes ( $M_n = 53,000 \text{ g}\cdot\text{mol}^{-1}$ ), irradiated at $0.5$ (circles) and $2.1 \text{ J}\cdot\text{cm}^{-2}$ (squares), for 3 cycles of pH environment changes. Insets are SEM images of the micro-structured Si surfaces coated with P2VP brushes, irradiated at $0.5$ and $2.1 \text{ J}\cdot\text{cm}^{-2}$ respectively. ....	121
Figure 3.10. Average contact angle values of water droplets onto flat Si substrate (squares) and Si spikes (circles) coated with hydroxyl terminated P2VP brushes ( $M_n = 80,500 \text{ g}\cdot\text{mol}^{-1}$ ), for 5 cycles of pH environment changes.....	122
Figure 3.11. Representative water droplets onto flat Si substrate and Si spikes coated with hydroxyl terminated P2VP brushes ( $M_n = 172,000 \text{ g}\cdot\text{mol}^{-1}$ ), after immersion in high and low pH solutions. ....	122
Figure 3.12. Photographs of representative water drops and the respective contact angles on (a) flat silicon and (b) laser micro/nano-structured silicon substrates (at $1.4 \text{ J}\cdot\text{cm}^{-2}$ fluence) coated with PNIPAm brushes ( $M_n = 43,000 \text{ g}\cdot\text{mol}^{-1}$ ) following temperature treatments at $25^\circ\text{C}$ and $40^\circ\text{C}$ .....	124
Figure 3.13. Average contact angle values of water droplets onto flat Si substrates (circles) and Si spikes (squares), irradiated at $1.4 \text{ J}\cdot\text{cm}^{-2}$ and coated with PNIPAm brushes ( $M_n = 43,000 \text{ g}\cdot\text{mol}^{-1}$ ), for 5 cycles of temperature changes.....	125
Figure 3.14. Average contact angle values of water droplets onto flat Si substrate (squares) and Si spikes (circles) coated with PNIPAm brushes ( $M_n = 80,000 \text{ g}\cdot\text{mol}^{-1}$ ), for 5 cycles of temperature change. ....	126
Figure 3.15. Representative water droplets onto flat Si substrate and Si spikes coated with hydroxyl terminated PNIPAm brushes ( $M_n = 130,000 \text{ g}\cdot\text{mol}^{-1}$ ), before and after heating. ....	126
Figure 3.16. Photographs of representative water drops and the respective contact angle values for a hierarchically roughened silicon substrate coated with a mixed 50/50 P2VP/PNIPAm brush exposed to immersion to solutions of different pH and exposure to different temperatures. ....	129
Figure 3.17. Average contact angle values of water droplets onto Si spikes (irradiated at $1.4 \text{ J}\cdot\text{cm}^{-2}$ ) coated with a mixed 50/50 P2VP/PNIPAm brush, for 5 cycles of pH / temperature variation. ....	130
Figure 3.18. A, B, C) Different magnifications of the micro-structured Si surface irradiated with $1.4\text{ J cm}^{-2}$ after thermal oxidation and seeded with fibroblasts for 7 days. D) Border between the surface with spikes and the surface without spikes, after thermal oxidation and seeded with fibroblasts for 7 days.....	132

Figure 3.19. A, B, C) Different magnifications of the micro-structured Si surface irradiated with  $1.4 \cdot J \text{ cm}^{-2}$ , without treatment, seeded with fibroblasts for 7 days. D) Bare silicon substrate without spikes seeded with fibroblasts for 7 days. .... 133

Figure 3.20. A, B, C) Different magnifications of the micro-structured Si surface irradiated with  $1.4 \cdot J \text{ cm}^{-2}$ , treated with dichlorodimethylsilane and seeded with fibroblasts for 7 days. D) Border between the surface with spikes and the surface without spikes, after treatment with dichlorodimethylsilane and seeded with fibroblasts for 7 days. .... 134

Figure 3.9. A-F) Different magnifications of the micro-structured Si surface irradiated with  $1.4 \cdot J \text{ cm}^{-2}$  after coating with P2VP and seeded with fibroblasts for one day. G-H) Border between the P2VP coated surface with spikes and the surface without spikes and seeded with fibroblasts for one day. .... 137

Figure 3.10. A-F) Different magnifications of the micro-structured Si surface irradiated with  $1.4 \cdot J \text{ cm}^{-2}$  after coating with P2VP and seeded with fibroblasts for 7 days. G-H) Border between the P2VP coated surface with spikes and the surface without spikes and seeded with fibroblasts for 7 days. .... 138

Figure 3.11. A) Border between the PNIPAm coated surface with spikes and the surface without spikes and seeded with fibroblasts for one day. B-D) Different magnifications of the micro-structured Si surface irradiated with  $1.4 \cdot J \text{ cm}^{-2}$  after coating with PNIPAm and seeded with fibroblasts for one day. .... 139

Figure 3.12. A-C) Different magnifications of the micro-structured Si surface irradiated with  $1.4 \cdot J \text{ cm}^{-2}$  after coating with PNIPAm and seeded with fibroblasts for 7 days. D) Border between the PNIPAm coated surface with spikes and the surface without spikes and seeded with fibroblasts for 7 days. .... 140

Figure 4.1. Digital photo and scanning electron microscope (SEM) images of butterfly wings. .... 156

Figure 4.2. Digital photo and scanning electron microscope (SEM) images of rice leaf. .... 156

Figure 4.3. Photographs of the *Strelitzia reginae* plant and flower. .... 157

Figure 4.4. Digital photo and scanning electron microscope (SEM) images of shark skin. .... 158

Figure 4.5. Digital photo and scanning electron microscope (SEM) images of fish scale. ... 158

Figure 4.6. Rose petal with high adhesion. .... 159

Figure 4.7. (a) Chinese Kafir and (b) sunflower petal. .... 160

Figure 4.8. Peanut leave (left) and surface wettability and structural hierarchy of peanut leaves (right). .... 160

Figure 4.9. Skunk cabbage leaf (left) and surface wettability and structural hierarchy of the same leaf (right). .... 161

Figure 4.10. Hierarchical adhesive structures of Gecko. (a) A toe of gecko contains hundreds of thousands of setae and each seta contains hundreds of spatula, (b): scanning electron micrographs of rows of setae at different magnifications and (c): spatulae, the finest terminal branches of seta. .... 162

Figure 4.11. Schematic diagram of a femtosecond laser micromachining system for fabrication of tilted microstructures. ....	164
Figure 4.12. Top-view (left) and 45-degree view (right) scanning electron micrographs of a silicon surface after irradiation with laser pulses of fluence (a) 0.5 J/cm <sup>2</sup> , (b) 1 J/cm <sup>2</sup> , (c) 1.5 J/cm <sup>2</sup> . Insets are higher magnification images from the same samples. ....	167
Figure 4.13. Top-view (left) and 45-degree view (right) scanning electron micrographs of a silicon surface after irradiation at a 10° tilt angle, with laser pulses with fluence: (a) 0.5 J/cm <sup>2</sup> , (b) 0.7 J/cm <sup>2</sup> , (c) 1 J/cm <sup>2</sup> , d) 1.5 J/cm <sup>2</sup> e) 2 J/cm <sup>2</sup> and f) 2.8 J/cm <sup>2</sup> . Insets are higher magnification images from the same samples. ....	169
Figure 4.14. Top-view (left) and 45-degree view (right) scanning electron micrographs of a silicon surface after irradiation at a 20° tilt angle, with laser pulses with fluence: (a) 0.5 J/cm <sup>2</sup> , (b) 0.7 J/cm <sup>2</sup> , (c) 1 J/cm <sup>2</sup> , d) 1.5 J/cm <sup>2</sup> e) 2 J/cm <sup>2</sup> and f) 2.8 J/cm <sup>2</sup> . Insets are higher magnification images from the same samples. ....	171
Figure 4.15. Top-view (left) and 45-degree view (right) scanning electron micrographs of a silicon surface after irradiation at a 30° tilt angle, with laser pulses with fluence: (a) 0.5 J/cm <sup>2</sup> , (b) 0.7 J/cm <sup>2</sup> , (c) 1 J/cm <sup>2</sup> and d) 1.5 J/cm <sup>2</sup> . Insets are higher magnification images from the same samples. ....	172
Figure 4.16. Top-view (left) and 45-degree view (right) scanning electron micrographs of a silicon surface after irradiation at 45° tilt angle, with laser pulses with fluence: (a) 0.5 J/cm <sup>2</sup> , (b) 0.7 J/cm <sup>2</sup> , (c) 1 J/cm <sup>2</sup> and d) 1.5 J/cm <sup>2</sup> . Insets are higher magnification images from the same samples. ....	174
Figure 4.17. Top-view (left) and 45-degree view (right) scanning electron micrographs of a silicon surface after irradiation on a 10° tilt angle, with laser pulses with y step: (a) 8 μm, (b) 16 μm and (c) 30 μm. Insets are higher magnification images from the same samples. ....	175
Figure 4.18. Top-view (left) and 45-degree view (right) scanning electron micrographs of a silicon surface after irradiation at a 20° tilt angle, with laser pulses with y step: (a) 8 μm, (b) 16 μm and (c) 30 μm. Insets are higher magnification images from the same samples. ....	176
Figure 4.19. Top-view (left) and 45-degree view (right) scanning electron micrographs of a silicon surface after irradiation at a 30° tilt angle, with laser pulses with y step: (a) 8 μm, (b) 16 μm and (c) 30 μm. Insets are higher magnification images from the same samples. ....	177
Figure 4.20. Representative water drop contact angle for 10° tilted spikes. ....	179
Figure 4.21. Selected snapshots of the impact and rebound of water drops on artificial surfaces of Si tilted spikes with an angle of irradiation of 10°. ....	180
Figure 4.22. Selected snapshots of the impact and rebound of water drops on artificial surfaces of Si tilted spikes with an angle of irradiation of 10°. ....	180
Figure 4.23. Representative water drop contact angle for 20° tilted spikes. ....	181
Figure 4.24. Selected snapshots of the impact and rebound of water drops on artificial surfaces of Si tilted spikes with an angle of irradiation of 20°. ....	183

Figure 4.25. Selected snapshots of the impact and rebound of water drops on artificial surfaces of Si tilted spikes with an angle of irradiation of 20°. ..... 183

Figure 4.26. Representative water drop contact angle for 30° tilted spikes. .... 184

Figure 4.27. Selected snapshots of the impact and rebound of water drops on artificial surfaces of Si tilted spikes with an angle of irradiation of 30°. ..... 185

Figure 4.28. Selected snapshots of the impact and rebound of water drops on artificial surfaces of Si tilted spikes with an angle of irradiation of 30°. ..... 186

Figure 4.29. Representative water drop contact angle for 45° tilted spikes. .... 186

Figure 4.30. SEM image of Si substrate, patterned with “Grooves A”. ..... 191

Figure 4.31. SEM image of Si substrate, patterned with “Grooves B”. ..... 192

Figure 4.32. SEM image of Si substrate, patterned with “Grooves C”. ..... 192

Figure 4.33. Top-view (left) and 45-degree-view (right) SEM characterization of Grooves A patterned with 30° tilted spikes. .... 192

Figure 4.34. Selected snapshots of a 3 μL droplet, rolling on the surface with 30° tilted spikes, in the direction of the pattern. .... 193

Figure 4.35. Representative contact angle measurement of Grooves A patterned with 30° tilted spikes after silanization. .... 194

Figure 4.36. Selected snapshots from the sliding angle measurement, with the droplet motion parallel to the channel of the Grooves A patterned with 30° tilted spikes. .... 195

Figure 4.37. Selected snapshots from the sliding angle measurement, with the droplet motion perpendicular to the channel of the Grooves A patterned with 30° tilted spikes. .... 195

Figure 4.38. Representative contact angle measurement of Grooves B patterned with 30° tilted spikes after silanization. .... 196

Figure 4.39. Selected snapshots of the impact and rebound of water drops on Grooves B patterned with 30° tilted spikes. .... 197

Figure 4.40. Representative contact angle measurement of Grooves C patterned with 30° tilted spikes after silanization. .... 198

Figure 4.41. Selected snapshots of the impact and rebound of water drops on Grooves C patterned with 30° tilted spikes. .... 199

Figure 4.42. Top-view scanning electron micrographs comparing surface morphology for different fluencies: a) 0.54 J · cm<sup>-2</sup>, b) 1.2 J · cm<sup>-2</sup>, c) 1.6 J · cm<sup>-2</sup>, d) 2.1 J · cm<sup>-2</sup> and e) 2.4 J · cm<sup>-2</sup>. The insets show a greater magnification of the same areas. .... 204

Figure 4.43. Top-view (left) and tilted-view (right) scanning electron micrographs, of samples irradiated at a tilted angle 30°, comparing the surface morphology by increasing the step distance in the y-direction: a) 10 μm, b) 15 μm, c) 20 μm and d) 25 μm. .... 205

Figure 4.44. Top-view(left) and tilt-view (right) scanning electron micrographs, of samples irradiated at a tilted angle 45°, comparing the surface morphology by increasing the step distance in the y-direction: a) 10 μm, b) 15 μm, c) 20 μm d) 25 μm and e) 30 μm ..... 207

Figure 4.45. Top-view(left) scanning electron micrographs of samples irradiated at a tilt angle 30°, comparing the surface morphology after immersion of samples at HF 10 % v/v solution for: a) 0.5 h, b) 2 h and c) 4 h..... 207

Figure 4.46. Selected snapshots of a 10 μL droplet, spreading on the surface with 30° tilted spikes, opposite to the direction of the pattern. .... 208

Figure 4.47. Selected snapshots of a 10 μL droplet, spreading on the surface with 30° tilted spikes, in the direction of the pattern. .... 209

Figure 4.48. Representative contact angle of Si substrate irradiated at a tilted angle 30°..... 210

Figure 4.49. Representative water drops on the 30° tilted spikes, for the 30°, 45° and 60° angle of inclination of the sample plate. .... 211

Figure 4.50. Representative water drops of the 30° tilted spikes, for the 90° inclined plate. 212

Figure 4.51. Representative water drops of the 30° tilted spikes, for the 180° inclined plate.... .  
.....213

Figure 4.52. Representative water drops of the 45° tilted spikes, for the 30°, 45° and 60° angle of inclination of the same plate. .... 214

Figure 4.53. Representative water drops of the 45° tilted spikes, for the 90° inclined plate. 215

Figure 4.54. Representative water drops of the 45° tilted spikes, for the 180° inclined plate..... 216

Figure 4.55. Advancing (left) and receding (right) contact angle measurement for the 30° tilted spikes. .... 216

Figure 4.56. Advancing (left) and receding (right) contact angle measurement for 45° tilted spikes..... 217

Figure 5.1. Schematic presentation of emulsion polymerization system .....228

Figure 5.2. Schematic presentation of dip coating process.....233

Figure 5.3. Pickering Emulsion method followed for “trapping” the microgel particles at an interface.....234

Figure 5.4. Vortical surface method followed for “trapping” the microgel particles at an interface.....235

Figure 5.5. Schematic presentation of the immobilization procedure. ....237

Figure 5.6. Schematic presentation of the water flow stability test. ....238

Figure 5.7. Model hydrogenation reaction.....242

Figure 5.8. (a) TEM image of a PDEAEMA microgel containing Pd nanoparticles. The scale bar denotes 50nm. (b) XRD patterns of PAA microgels containing Ru nanoparticles and the precursor PAA microgels.....	244
Figure 5.9. TEM image of the PMAA microgels containing Pd nanoparticles. The scale bar denotes 50 nm. ....	244
Figure 5.10. FE-SEM images of PMAA microgels (0.01%wt) on glass substrate using drop casting method. ....	245
Figure 5.11. PMAA microgels (0.001% wt) on glass substrate using drop casting method. .	246
Figure 5.12. PMAA microgels anchored on glass substrate with drop casting method, prepared from suspensions with pH higher than the $pK_a$ of PMAA at $c=0.001\%$ wt. ....	247
Figure 5.13. PMAA microgels (0.001% wt) on glass substrates before (left) and after (right) extra immersion in pure water for a period of two hours. ....	247
Figure 5.14. PMAA microgels (0.01%wt) on glass substrate using dip coating method. ....	248
Figure 5.15. PMAA microgels (0.01% wt) on glass substrates before (left) and after (right) extra immersion in pure water for a period of two hours. ....	249
Figure 5.16. PAA microgels deposited onto glass substrates utilizing the Pickering emulsion method. The suspension concentrations were (a) 0.35% wt. and (b) 0.035% wt. ....	250
Figure 5.17. PAA deposited onto glass substrates utilizing the Pickering emulsion method with the addition of 5% wt. (left) and 50% wt. (right) of ethanol. ....	250
Figure 5.18. PAA deposited onto glass substrates utilizing the Pickering emulsion method and (a) vertical and (b) horizontal dipping.....	251
Figure 5.19. Silica particles deposited onto glass substrate from an aqueous suspension at 0.35% wt. using the Pickering emulsion method.....	252
Figure 5.20. FE-SEM image of Pd-containing PDEAEMA microgels on a glass substrate. ....	252
Figure 5.21. Pd-containing PDEAEMA microgels on a glass substrate following rinsing with water (a) and after immersion in water for 24h (b).....	253
Figure 5.22. PAA-Ru microgels dispersed on glass (left) using the Pickering emulsion method.....	254
Figure 5.23. PAA-Ru microgel polymeric particles immersed in water for various time intervals; As prepared (upper left), 1 hr (upper right), and 24 hrs (lower). ....	255
Figure 5.24. PAA microgel particles on a glass surface ( $c=0.35\%$ wt) using the vortical surface method. ....	256
Figure 5.25. PAA-Ru microgels dispersed on glass substrate, using the vortical surface method.....	257

Figure 5.26. FE-SEM images of PMAA microgels (left column) and Pd containing PMAA microgels (right column) covalently bound onto glass substrates at three different magnifications (3.33 KX, 10.00 KX and 20.00 KX). .....	258
Figure 5.27. FE-SEM images of the Pd nanoparticle containing PMAA sample rinsed with 2 L of water (left) and 10 L of water (right). The insets are higher magnification images. ....	259
Figure 5.28. FE-SEM images of Pd nanoparticle containing PMAA microgels anchored on glass substrates after heating at 40°C for 4 h (left) and heating at 40°C for 4 h and rinsing with 2 L of de-ionized water (right). .....	260
Figure 5.29. FE-SEM images of Pd nanoparticle containing PMAA microgels anchored on glass substrates after heating at 40°C for 24 h (left) and heating at 40°C for 24 h and rinsing with 2 L of de-ionized water (right). .....	260
Figure 5.30. FE-SEM images of Pd nanoparticle containing PMAA microgels anchored on glass substrates after heating at 80°C for 24 h and heating at 80°C for 24 h and rinsing with 2 L of de-ionized water. ....	261
Figure 5.31. FE-SEM images of Pd nanoparticle containing PMAA microgels anchored on glass substrates after immersion in high pH water for 24 h. The insets show FE-SEM images from the same samples at higher magnification. ....	261
Figure 5.32. FE-SEM image of a sample after immersion in pH, heated at 80°C and rinsing with water flow. Inset is the sample at higher magnification. ....	262
Figure 5.33. FE-SEM images of the Pd containing PMAA microgels anchored on a glass substrate: (left) original FE-SEM image, (center) after transformation to the binary image with ImageJ and (right) after transformation using a Matlab code. ....	263
Figure 5.34. FE-SEM images of the Pd containing PMAA microgels anchored on a glass substrate after rinsing with 2 L of water: (left) original FE-SEM image, (center) after transformation to the binary image with ImageJ and (right) after transformation using a Matlab code. ....	263
Figure 5.35. FE-SEM images of the Pd containing PMAA microgels anchored on a glass substrate after rinsing with 10 L of water at 20.00K X magnification: (left) original image, (center) after transformation to the binary image with ImageJ, (right) after transformation using a Matlab code. ....	263
Figure 5.36. Histogram of the area occupied by the microgels: for the a) as prepared sample, (b) after rinsing with 2 L of water and (c) after rinsing with 10 L of water. The images were analyzed with ImageJ and a Matlab code. ....	264
Figure 5.37. FE-SEM images of the Pd containing PMAA microgels anchored on a glass substrate after heating at 40°C for 24 h at 20.00K X magnification: (left) original image, (center) after transformation to the binary image with ImageJ, (right) after transformation using a Matlab code. ....	265
Figure 5.38. FE-SEM images of the Pd containing PMAA microgels anchored on a glass substrate after heating at 40°C for 24 h and rinsing with 2 L of water at 20.00K X magnification: (left) original image, (center) after transformation to the binary image with ImageJ, (right) after transformation using a Matlab code. ....	265

- Figure 5.39. Histogram of the area occupied by the Pd nanoparticle containing microgels for a) the as prepared sample, b) after heating to 40°C for 4 h, c) after heating to 40°C for 4 h and rinsing, d) after heating to 40°C for 24 h and e) after heating to 40°C for 24 h and rinsing..266
- Figure 5.40. FE-SEM images of the Pd containing PMAA microgels anchored on a glass substrate after heating at 80°C for 4 h at 20.00K X magnification: (left) original image, (center) after transformation to the binary image with ImageJ, (right) after transformation using a Matlab code. ....266
- Figure 5.41. FE-SEM images of the Pd containing PMAA microgels anchored on a glass substrate after heating at 80°C for 4 h and rinsing with 2 L of water at 20.00K X magnification: (left) original image, (center) after transformation to the binary image with ImageJ, (right) after transformation using a Matlab code.....267
- Figure 5.42. FE-SEM images of the Pd containing PMAA microgels anchored on a glass substrate after heating at 80°C for 24 h at 20.00K X magnification: (left) original image, (center) after transformation to the binary image with ImageJ, (right) after transformation using a Matlab code. ....267
- Figure 5.43. FE-SEM images of the Pd containing PMAA microgels anchored on a glass substrate after heating at 80°C for 24 h and rinsing with 2 L of water at 20.00K X magnification: (left) original image, (center) after transformation to the binary image with ImageJ, (right) after transformation using a Matlab code.....267
- Figure 5.44. Histogram of the area occupied by the Pd nanoparticle containing microgels for a) the as prepared sample, b) after heating to 80°C for 4 h, c) after heating to 80°C for 4 h and rinsing, d) after heating to 80°C for 24 h and e) after heating to 80°C for 24 h and rinsing..268
- Figure 5.45. Histogram of the area occupied by the Pd nanoparticle containing microgels after a) immersion at low pH for 24 h, b) immersion at low pH for 24 h and rinsing, c) immersion at high pH for 24 h, and d) immersion at high pH for 24 h and rinsing. ....269
- Figure 5.46. Histogram of the area occupied by the microgels for a) the as prepared sample b) after immersion in pH 8 and heating at 80°C, c) after immersion in pH 8 and rinsing with 2 L water, d) after heating at and rinsing with water and e) after immersion in pH 8, heating at 80°C and rinsing with 2 L water. ....270
- Figure 5.47. UV-Vis absorption spectrum for 4-NP in the absence of NaBH<sub>4</sub> (left) and for 4-AP (right). ....271
- Figure 5.48. Calibration curve of a standard aqueous solution of 4-NP+NaBH<sub>4</sub>.....272
- Figure 5.49. spectrum of hydrogenation reaction of PDEAEMA-Au in low pH after 10 min reaction.....272
- Figure 5.50. Hydrogenation reaction of PDEA-Au nanocatalysts after the ion-exchange reaction.....273
- Figure 5.51. Hydrogenation reaction using PMAA-Pd nanocatalysts under basic conditions. ....274
- Figure 5.52. Hydrogenation reaction using 120 mg of PDEAEMA/Au nanocatalysts (75% quaternized, 1.5 % in Au). ....275

Figure 5.53. Hydrogenation reaction using 90 mg of PDEAEMA/Au nanocatalysts (75% quaternized, 1.5 % in Au). .....275

Figure 5.54. Hydrogenation reaction using 60 mg of PDEAEMA/Au nanocatalysts (75% quaternized, 1.5 % in Au). .....276

## *List of Tables*

Table 2.1. Key properties of ZnO. ....	43
Table 2.2. Band positions ( $\lambda$ ) and extinction coefficients ( $\epsilon$ ) of methylene blue. ....	48
Table 2.3. Physical and mechanical properties of PMMA. ....	52
Table 2.4. Parameters of the fs Laser used for the fabrication of ZnO coated Si spikes. ....	60
Table 2.5. Repeatability of the specimen performance. ....	68
Table 2.6. Parameters of the PMMA film coating on ZnO nanowires. ....	75
Table 2.7. Parameters of the P2VP film coating on ZnO nanowires. ....	79
Table 2.8. Average contact angle values of P2VP (0.01 wt % in toluene) coated nanorods on glass surfaces. ....	87
Table 2.9. Average contact angle values of P2VP (1 wt % in toluene) coated ZnO nanorods on glass surfaces. ....	88
Table 3.1. Average contact angle values of water droplets onto micro/nano-structured silicon substrates coated with mixed P2VP/PNIPAm brushes of three different P2VP/PNIPAm ratios: 30/70, 50/50 and 70/30. ....	128
Table 4.1. Dimensions of the Si grooves-patterned surfaces. ....	191
Table 5.1. Matlab code for the analysis of the FE-SEM images. ....	239
Table 5.2. Characterization data for the synthesized pH-responsive microgels. ....	243

# Chapter 1

## 1. Introduction and overview

### 1.1. Introduction

Novel multifunctional surfaces, which would be able to alter their wetting behavior all the way from superhydrophilic to superhydrophobic and water repellent in response to changes in single or multiple external stimuli, have gained the focus of considerable research, due to their emerging applications.<sup>1</sup> Although biomimetics has emerged in the 1960s,<sup>2</sup> numerous micro/mechanical applications require novel surfaces with new properties.

#### Wettability on rough surfaces

The wettability of a solid material, first introduced in 1805,<sup>3</sup> is controlled by its surface energy: when a liquid is in contact with an ideal, homogeneous solid surface in static equilibrium with its vapor, the liquid may form a contact angle  $\theta$  with the surface (partial wetting) when the various surface tensions obey Young's equation:<sup>4</sup>

$$\gamma_{LV} \cos \theta = \gamma_{SV} - \gamma_{SL}$$

where  $\gamma_{SV}$  is the surface tension of the solid,  $\gamma_{LV}$  that of the liquid, and  $\gamma_{SL}$  the solid-liquid interfacial tension. The surface energy is defined as:

$$dE = (\gamma_{SL} - \gamma_{SV}) dx + \gamma_{LV} dx \cos \theta$$

However, surfaces are not ideal and chemically heterogeneous. This modifies the Young's model, as it affects the value of the apparent contact angle, (first reported from Wenzel<sup>5,6</sup> and Cassie<sup>7,8</sup>).<sup>3</sup> According to the Wenzel model, the surface area of a material increases in the case of a roughened surface. As a result, the liquid has the tendency to spread more on a rough hydrophilic surface, in order to enhance the solid-liquid contact. Conversely, on a rough hydrophobic material, the contact is unfavorable. Thus, the roughness factor was introduced, as the ratio of the actual surface area (taking into account the asperities of the solid) over its apparent one.<sup>3</sup> The surface energy is calculated from the following equation:

$$dE = r (\gamma_{SL} - \gamma_{SV}) dx + \gamma_{LV} dx \cos\theta^*$$

where  $r$  is the roughness factor and  $\theta^*$  is the apparent contact angle. For  $r = 1$  (flat solid) the equation is the same with Young's model.

For  $r > 1$ , the Wenzel's equation is:  $\cos\theta^* = r \cos\theta$ .

So, according to the Wenzel model, the rougher the hydrophobic material, the higher the contact angle. However, this is not true: Contact angles generally spread in quite a large interval, which often referred as contact angle hysteresis. This phenomenon is responsible for the sticking of drops, an effect in contradiction with water repellency. Furthermore, for very rough hydrophobic materials, the energy stored for following the solid surface is much larger than the energy associated with the air pockets, which makes it impossible to reach high values of  $\theta^*$ .<sup>9</sup>

According to the Cassie-Baxter model,<sup>3,10</sup> the liquid may not penetrate fully into the surface texture, but rather 'bead-up' to form a composite (solid-liquid-air) interface. In this scenario, air remains trapped inside the asperities, so that the drop can sit on the top of them on a fraction  $\phi_s$ . This phenomenon is also known as fakir droplet.<sup>3</sup> The smaller the  $\phi_s$ , the higher

the hydrophobicity. So, the contact angle  $\theta^*$  and the surface energy are calculated by the following equations:<sup>3,9</sup>

$$\cos\theta^* = -1 + \phi_s (\cos\theta + 1)$$

$$dE = \phi_s (\gamma_{SL} - \gamma_{SV}) dx + (1 - \phi_s) \gamma_{LV} dx + \gamma_{LV} dx \cos\theta^*$$

However, there are cases that the two models, Wenzel and Cassie-Baxter, can coexist. This can be observed in the case that the density of the defects is large enough to sustain the fakir drop, which means that each defect leads to a capillary force that opposes penetration of the asperities. The metastable fakir state was first introduced from Lafuma and Quere.<sup>3,11</sup>

### Superhydrophobic surfaces

Super-hydrophobic materials are widely used in outdoor weather-proof paints, easy-clean textiles, microfluidics, lab-on-chip devices, low friction coatings (e.g. for ships) and solar panels.<sup>9,12-15</sup> The inspiration for designing and developing self-cleaning materials comes from nature;<sup>1</sup> the *Lotus* effect, which results in super-hydrophobicity and very high water repellence, as exhibited by the leaves of sacred Lotus (*Nelumbo nucifera*), was first reported by Barthlott and Neinhuis.<sup>16,17</sup> The water repellency and the self-cleaning properties of these biological species has been attributed to both chemical composition and surface geometry.<sup>1</sup> The research efforts have been focused on the fabrication of surfaces to replicate the Lotus leaf.<sup>1,18-20</sup> The most common way to generate effective super-hydrophobic surfaces is to build multiscale hierarchical roughness. One way this can be achieved is by micro/nano-structuring a surface utilizing ultrafast lasers, which creates dual scale roughness in an one-step process.<sup>13,21</sup> The first conical microstructures with multiscale roughness were reported by Her and Mazur<sup>22</sup> in 1998. Since then, femtosecond laser has proved to be a promising method for fabricating hierarchical structures with multiscale roughness.<sup>23</sup> So far, a vast number of

superhydrophobic and water-repellent surfaces have been fabricated, owing to their great applications in self-cleaning, anti-icing, inkjet printing, agriculture and spray cooling.<sup>1,13,18,24–</sup>

31

However the study of the plants surface wettability revealed another interesting phenomenon, the rose petal effect.<sup>20</sup> Unlike Lotus leaf, rose petals, scallions and garlic, exhibit superhydrophobic behavior with high adhesion.<sup>32,33</sup> Besides the “sticky” superhydrophobic species, another remarkable category of plants are the so-called “parahydrophobic” plants, which exhibit high contact angles, but not above 150°, with high adhesion. An important family among this kind of species are most of the thermogenic plants, which can raise their temperature above the ambient.<sup>32</sup> Other plants that belong to this category are the banana leaf, the red-veined prayer plant<sup>34</sup>, the oak leaves<sup>35</sup>, the ceratonia siliqua<sup>36</sup>, the majority of hairy leaves<sup>37</sup> and many others.<sup>38–40</sup> Adhesive hydrophobic materials can find applications as barrier materials, micromanipulators and oil-water separators.<sup>41</sup>

### **Responsive surfaces**

Multifunctionality, however, has been identified as another main research task in the field of surface technology. This can be achieved by using “smart” coatings, which can respond to external stimuli, such as light,<sup>26,42–45</sup> temperature,<sup>42,46–48</sup> electric field,<sup>42,48–50</sup> pH<sup>42,51,52</sup> or solvent selectivity.<sup>42,53</sup> The uniqueness of these materials lies not only on the fast changes occurring, but also on the fact that these transitions are reversible. Until now several smart materials have been reported which can switch between superhydrophobicity and superhydrophilicity, with promising applications in switchable valves<sup>54</sup>, biosensors<sup>55</sup>, selective separation<sup>56</sup>, tunable microlenses<sup>57</sup> and “lab-on chip” devices<sup>52</sup>. Among the “smart” coatings found in the literature, the wetting properties of ZnO have been widely studied, since it can reversibly switch from super-hydrophilic to super-hydrophobic in response to UV

irradiation and heating or dark storage, respectively.<sup>58–61</sup> ZnO, with probably the largest variety of different nanostructures, has attracted much attention within the scientific community as a "future material."

Apart from ZnO, the wetting properties of smart polymers have been widely studied.<sup>19</sup> Stimuli-sensitive polymers can be sensitive to a number of factors, such as pH, humidity, temperature, light, magnetic field or electric field.<sup>1,52,61</sup> Depending on the type of stimulus, smart polymer surfaces can be applied in drug delivery, tissue-engineering, sensors, bio-separations, protein purification, gene therapy and in microfluidics.<sup>1,62–66</sup>

Among, the smart polymers, microgels have been widely utilized. Their small size, extended circulating time, biocompatibility as well as their ability to incorporate drug molecules within the polymer network make them attractive for use in drug delivery.<sup>67–71</sup> Furthermore, microgels can find numerous applications in energy, medicine, nanobiotechnology, light emitting devices, photovoltaics, detectors and biolabels,<sup>67,72</sup> in the fabrication of microlenses, in biosensors, in cosmetics<sup>73</sup> as well as in cell immobilization.<sup>67,70,74–80</sup> Moreover, pH-responsive microgels have gained attention in the field of catalysis, as they can be utilized as microreactors.<sup>80–88</sup>

### **Anisotropic surfaces**

Besides the isotropic textures in nature, there are also directional structures, exhibiting both superhydrophobicity and anisotropic wetting.<sup>66,89</sup> Such examples are the butterfly wings,<sup>66,89–92</sup> the water striders,<sup>66,89</sup> the rice leaf,<sup>66,91</sup> the cicada wings<sup>26</sup> and the fish scale.<sup>66</sup> In each case, such surfaces comprise directional dependent geometrical structures, that produce anisotropic wetting.<sup>90</sup> Another interesting phenomenon, revealed from the study of nature, is the gecko's feet. The special wetting properties of gecko's feet, arise from the keratinous hairs, called

setae, in its structure.<sup>93</sup> Such surfaces, have many applications, such as in liquid transportation without loss and in the analysis of very small volumes of liquid samples.<sup>66,93–95</sup>

## 1.2. Contents of this thesis

This thesis is organized as follows:

In the present **Chapter 1**, the general introduction and the overview of the contents of the thesis are presented.

**Chapter 2**, reviews the work on the functional ZnO surfaces with photocatalytic behavior and reversible wettability. The development of ZnO coatings exhibiting reversible wettability and photocatalytic activity was reported, following an environmentally friendly approach. The as-grown samples are prepared following a two-step fabrication process. First, silicon (Si) wafers were irradiated with femtosecond (fs) laser pulses in order to produce Si surfaces with dual scale roughness (Si spikes).<sup>13,27,96</sup> Then, the rough Si samples were coated with a ZnO film prepared by a simple sol-gel process.<sup>97–99</sup> The artificial surfaces exhibit reversible wettability from super-hydrophilic (upon UV irradiation) to super-hydrophobic (upon heating), while the as-grown samples revealed high photocatalytic activity investigated by means of the decolorization of methylene blue as a model system.<sup>100–102</sup> Moreover, the reproducibility and sustainability of the system were thoroughly studied.

In parallel, ZnO nanowires were developed with enhanced stability and high photocatalytic behavior, using polymeric stabilizers. First, ZnO nanowires were grown on ZnO pre-coated glass substrates via aqueous solution growth.<sup>97</sup> Afterwards, the samples were coated with polymers with the spin casting method. Poly(methylmethacrylate), PMMA, and Poly(2-vinyl pyridine), P2VP were utilized for this purpose. Samples were characterized with Scanning Electron Microscopy (SEM) and were tested for their photocatalytic behavior using Fourier

Transform Infrared Spectroscopy (FTIR). Stearic acid was utilized as a test organic pollutant. Samples were also tested for their wettability. ZnO nanowires were also coated with dichlorodimethylsilane for comparison reasons.

In **Chapter 3**, the development of responsive surfaces with “parahydrophobic” behavior is presented. “Parahydrophobic” behavior was achieved with high contact angles in the hydrophobic state ( $\sim 120^\circ$ ), however, with high adhesion ( $\sim 30^\circ$  contact angle hysteresis). Initially silicon wafers were treated with femtosecond (fs) laser pulses in order to produce the dual scale roughness, Si spikes.<sup>13,52,58</sup> Afterwards, organic coatings, Poly(2-vinyl pyridine), P2VP or PNIPAm, were introduced by anchoring end-functionalized polymer chains utilizing the "grafting-to" method. The responsiveness of the mixed end-anchored polymers, P2VP and Poly(N-isopropylacrylamide), PNIPAm onto one surface was also investigated.

Finally, the Si surfaces produced using fs laser (Si spikes) with different wetting properties, and the Si spikes coated with P2VP and PNIPAm were seeded with 3T3 fibroblasts in order to examine the cell response on these substrates. Thus, cell attachment and proliferation were examined for different surface wetting properties, roughness and chemistry for 7 days of cell culture.

In **Chapter 4**, three types of anisotropic surfaces were developed. Initially, superhydrophobic non-adhesive surfaces with unidirectional droplet roll-off behavior were successfully fabricated. For this reason, Si wafers were treated with femto-second laser, not in a conventional way, but in a tilt angle. The substrate was tilted and as a result, the laser beam was not pointed perpendicular to the surface. This procedure led to the formation of tilted periodic spikes. Such surfaces after a silanization process exhibit anisotropic wettability, with a droplet motion on the direction of the spikes. It was observed that the velocity of the droplet

motion was different, depending on the chosen tilt angle. To the best of our knowledge, this is the first work, referring to tilted spikes, treated with fs-laser.

Afterwards, a third level of macro-structuring was introduced by patterning the inorganic surfaces using photolithography in order to enhance the anisotropic wetting behavior. Si substrates, patterned with grooves, were irradiated with fs Laser at a tilt angle. The effect of the depth and the diameter of the grooves on the final contact angle were investigated. These surfaces exhibit a superhydrophilic directionality, after thermal oxidation, or superhydrophobic directionality after silanization.

Finally, superhydrophobic surfaces with high unidirectional hysteresis were developed. For this purpose, the irradiation of Si wafers was performed at a tilt angle. In order to achieve the high hysteresis, central wavelength of 800 nm was utilized and the different parameters of laser irradiation were investigated. This procedure led to the formation of tilted periodic spikes. Such surfaces after a silanization process exhibit anisotropic wettability, with a droplet motion on the direction of the spikes and a superhydrophilic directionality after thermal oxidation.

In **Chapter 5**, the covalent immobilization of metal nanoparticle containing microgels onto solid substrates is illustrated. The immobilization of the microgels was initially performed by conventional dip or drop casting as well as with the Pickering emulsion and Vortical surface method.<sup>83</sup> However, these methods led to low homogeneity and multi-layer structures. For this purpose, microgels were immobilized onto glass substrates using the amine coupling chemistry.<sup>75</sup> The immobilized microgels were subjected to environmental changes (heating temperature, heating time, flow rate and pH) in order to examine their stability under microfluidic flow conditions for their efficient implementation in mild industrial catalytic processes. The surfaces after the immobilization of the microgel nanoparticles were studied

by Scanning Electron Microscopy (SEM). Afterwards, the catalytic behavior of the synthesized metal containing microgels was studied through a model hydrogenation reaction.

**Chapter 6** summarizes the conclusions and lists the future outlook experiments, which can be done for the projects described in the previous chapters.

### 1.3. References

- (1) Anastasiadis, S. H. Development of Functional Polymer Surfaces with Controlled Wettability. *Langmuir* **2013**, *29* (30), 9277–9290.
- (2) Stratakis, E.; Ranella, A.; Fotakis, C. Biomimetic Micro/nanostructured Functional Surfaces for Microfluidic and Tissue Engineering Applications. *Biomicrofluidics* **2011**, *5* (1).
- (3) Quéré, D. Non-Sticking Drops. *Reports Prog. Phys.* **2005**, *68* (11), 2495–2532.
- (4) Anastasiadis, S. H.; Retsos, H.; Pispas, S.; Hadjichristidis, N.; Neophytides, S. Smart Polymer Surfaces. *Macromolecules* **2003**, *36* (6), 1994–1999.
- (5) Wenzel, R. N. Resistance of Solid Surfaces to Wetting by Water. *J. Ind. Eng. Chem. (Washington, D. C.)* **1936**, *28*, 988–994.
- (6) Wenzel, R. N. Surface Roughness and Contact Angle. *J. Psychosom. Res.* **1949**, *53* (9), 1466–1467.
- (7) Cassie, A. B. D.; Baxter, S. Wettability of Porous Surfaces. *Trans. Faraday Soc.* **1944**, *40* (5), 546–551.
- (8) Cassie, A. B. D. Contact Angles. *Discuss. Faraday Soc.* **1948**, *3*, 11–15.
- (9) Callies, M.; Quéré, D. On Water Repellency. *Soft Matter* **2005**, *1* (1), 55.
- (10) Choi, W.; Tuteja, A.; Mabry, J. M.; Cohen, R. E.; McKinley, G. H. A Modified Cassie-Baxter Relationship to Explain Contact Angle Hysteresis and Anisotropy on Non-Wetting Textured Surfaces. *J. Colloid Interface Sci.* **2009**, *339* (1), 208–216.
- (11) Lafuma, A.; Quéré, D. Superhydrophobic States. *Nat. Mater.* **2003**, *2* (7), 457–460.
- (12) Bhushan, B.; Jung, Y. C.; Koch, K. Micro-, Nano- and Hierarchical Structures for Superhydrophobicity, Self-Cleaning and Low Adhesion. *Philos. Trans. A. Math. Phys. Eng. Sci.* **2009**, *367* (1894), 1631–1672.
- (13) Zorba, V.; Stratakis, E.; Barberoglou, M.; Spanakis, E.; Tzanetakis, P.; Anastasiadis, S. H.; Fotakis, C. Biomimetic Artificial Surfaces Quantitatively Reproduce the Water Repellency of a Lotus Leaf. *Adv. Mater.* **2008**, *20* (21), 4049–4054.
- (14) Blossey, R. Self-Cleaning Surfaces--Virtual Realities. *Nat. Mater.* **2003**, *2* (5), 301–306.

- (15) Nakajima, A.; Fujishima, A.; Hashimoto, K.; Watanabe, T. Preparation of Transparent Superhydrophobic Boehmite and Silica Films by Sublimation of Aluminum Acetylacetonate. *Adv. Mater.* **1999**, *11* (16), 1365–1368.
- (16) Barthlott, W.; Neinhuis, C. Purity of the Sacred Lotus, or Escape from Contamination in Biological Surfaces. *Planta* **1997**, *202* (1), 1–8.
- (17) Füstner, R.; Barthlott, W.; Neinhuis, C.; Walzel, P. Wetting and Self-Cleaning Properties of Artificial Superhydrophobic Surfaces. *Langmuir* **2005**, *21*, 956–961.
- (18) Genzer, J.; Efimenko, K. Recent Developments in Superhydrophobic Surfaces and Their Relevance to Marine Fouling: A Review. *Biofouling* **2006**, *22* (5–6), 339–360.
- (19) Chen, J. K.; Chang, C. J. Fabrications and Applications of Stimulus-Responsive Polymer Films and Patterns on Surfaces: A Review. *Materials (Basel)*. **2014**, *7* (2), 805–875.
- (20) Bhushan, B. Biomimetics. **2016**, 23–34.
- (21) Hsu, S.-T.; Wang, H.; Satoh, G.; Yao, Y. L. Applications of Surface Structuring with Lasers. *ICALEO* **2011**, 1095–1104.
- (22) Her, T.-H.; Finlay, R. J.; Wu, C.; Deliwala, S.; Mazur, E. Microstructuring of Silicon with Femtosecond Laser Pulses. *Appl. Phys. Lett.* **1998**, *73* (12), 1673.
- (23) Zhang, D.; Chen, F.; Yang, Q.; Yong, J.; Bian, H.; Ou, Y.; Si, J.; Meng, X.; Hou, X. A Simple Way to Achieve Pattern-Dependent Tunable Adhesion in Superhydrophobic Surfaces by a Femtosecond Laser. *ACS Appl. Mater. Interfaces* **2012**, *4* (9), 4905–4912.
- (24) Yong, J.; Chen, F.; Yang, Q.; Fang, Y.; Huo, J.; Hou, X. Femtosecond Laser Induced Hierarchical ZnO Superhydrophobic Surfaces with Switchable Wettability. *Chem. Commun.* **2015**, *51*, 9813–9816.
- (25) George, J. E. Fabrication of Superhydrophobic Surfaces from Femtosecond Laser Patterned Surfaces. *Proc. Indian Natl. Sci. Acad.* **2015**, *81* (2), 533–536.
- (26) Feng, X.; Jiang, L. Design and Creation of Superwetting/antiwetting Surfaces. *Adv. Mater.* **2006**, *18* (23), 3063–3078.
- (27) Barberoglou, M.; Zorba, V.; Stratakis, E.; Spanakis, E.; Tzanetakis, P.; Anastasiadis, S. H.; Fotakis, C. Bio-Inspired Water Repellent Surfaces Produced by Ultrafast Laser Structuring of Silicon. *Appl. Surf. Sci.* **2009**, *255* (10), 5425–5429.
- (28) Neinhuis, C. Characterization and Distribution of Water-Repellent, Self-Cleaning Plant Surfaces. *Ann. Bot.* **1997**, *79* (6), 667–677.
- (29) Balu, B.; Breedveld, V.; Hess, D. W. Fabrication Of “roll-Off” and “sticky” superhydrophobic Cellulose Surfaces-via Plasma Processing. *Langmuir* **2008**, *24* (9), 4785–4790.
- (30) Wang, B.-B.; Feng, J.-T.; Zhao, Y.-P.; Yu, T. X. Fabrication of Novel Superhydrophobic Surfaces and Water Droplet Bouncing Behavior — Part 1: Stable ZnO–PDMS Superhydrophobic Surface with Low Hysteresis Constructed Using ZnO

- Nanoparticles. *J. Adhes. Sci. Technol.* **2010**, *24* (15–16), 2693–2705.
- (31) Hao, C.; Li, J.; Liu, Y.; Zhou, X.; Liu, Y.; Liu, R.; Che, L.; Zhou, W.; Sun, D.; Li, L.; et al. Superhydrophobic-like Tunable Droplet Bouncing on Slippery Liquid Interfaces. *Nat. Commun.* **2015**, *6*, 7986.
- (32) Ramachandran, R.; Nosonovsky, M. Surface Micro/nanotopography, Wetting Properties and the Potential for Biomimetic Icephobicity of Skunk Cabbage *Symplocarpus Foetidus*. *Soft Matter* **2014**, *10* (39), 7797–7803.
- (33) Chang, F. M.; Hong, S. J.; Sheng, Y. J.; Tsao, H. K. High Contact Angle Hysteresis of Superhydrophobic Surfaces: Hydrophobic Defects. *Appl. Phys. Lett.* **2009**, *95* (6), 2012–2015.
- (34) Gilet, T.; Bourouiba, L. Rain-Induced Ejection of Pathogens from Leaves: Revisiting the Hypothesis of Splash-on-Film Using High-Speed Visualization. *Integr. Comp. Biol.* **2014**, *54* (6), 974–984.
- (35) Fernández, V.; Sancho-Knapik, D.; Guzmán, P.; Peguero-Pina, J. J.; Gil, L.; Karabourniotis, G.; Khayet, M.; Fasseas, C.; Heredia-Guerrero, J. A.; Heredia, A.; et al. Wettability, Polarity and Water Absorption of *Quercus Ilex* Leaves: Effect of Leaf Side and Age. *Plant Physiol.* **2014**, *166* (September), 168–180.
- (36) Kolyva, F.; Stratakis, E.; Rhizopoulou, S.; Chimona, C.; Fotakis, C. Leaf Surface Characteristics and Wetting in *Ceratonia Siliqua* L. *Flora Morphol. Distrib. Funct. Ecol. Plants* **2012**, *207* (8), 551–556.
- (37) Kortekamp, A.; Wind, R.; Zyprian, E. The Role of Hairs on the Wettability of Grapevine (*Vitis* Spp.) Leaves. *Vitis* **1999**, *38* (3), 101–105.
- (38) Haines, B. L.; Jernstedt, J. A.; Neufeld, H. S. Direct Foliar Effects of Simulated Acid-Rain .2. Leaf Surface Characteristics. *New Phytol.* **1985**, *99* (3), 407–416.
- (39) Hall, D. M.; Burke, W. Wettability of Leaves of a Selection of New Zealand Plants. *New Zeal. J. Bot.* **1974**, *12* (3), 283–298.
- (40) Guo, H. Bio-Inspired Surface Engineering for Hydrophobicity. *Thesis* **2014**.
- (41) Guo, Z. G.; Liu, W. M. Sticky Superhydrophobic Surface. *Appl. Phys. Lett.* **2007**, *90* (22).
- (42) Wang, S.; Song, Y.; Jiang, L. Photoresponsive Surfaces with Controllable Wettability. *J. Photochem. Photobiol. C Photochem. Rev.* **2007**, *8* (1), 18–29.
- (43) Rosario, R.; Gust, D.; Hayes, M.; Jahnke, F.; Springer, J.; Garcia, A. a. Photon-Modulated Wettability Changes on Spiropyran-Coated Surfaces. *Langmuir* **2002**, *18* (21), 8062–8069.
- (44) Liu, H.; Feng, L.; Zhai, J.; Jiang, L.; Zhu, D. Reversible Wettability of a Chemical Vapor Deposition Prepared ZnO Film between Superhydrophobicity and Superhydrophilicity. *Langmuir* **2004**, *20* (14), 5659–5661.
- (45) Irie, H.; Ping, T. S.; Shibata, T.; Hashimoto, K. Reversible Control of Wettability of a TiO<sub>2</sub> Surface by Introducing Surface Roughness. *Electrochem. Solid-State Lett.*

- 2005, 8 (9), D23.
- (46) Crevoisier, G. D. Switchable Tackiness and Wettability of a Liquid Crystalline Polymer. *Science* (80-. ). **1999**, 285 (5431), 1246–1249.
- (47) Fu, Q.; Rao, G. V. R.; Basame, S. B.; Keller, D. J.; Artyushkova, K.; Fulghum, J. E.; Lopez, G. P. Reversible Control of Free Energy and Topography of Nanostructured Surfaces. *J. Am. Chem. Soc.* **2004**, 126 (29), 8904–8905.
- (48) Sun, T.; Wang, G.; Feng, L.; Liu, B.; Ma, Y.; Jiang, L.; Zhu, D. Reversible Switching between Superhydrophilicity and Superhydrophobicity. *Angew. Chemie - Int. Ed.* **2004**, 43 (3), 357–360.
- (49) Lahann, J.; Mitragotri, S.; Tran, T.-N.; Kaido, H.; Sundaram, J.; Choi, I. S.; Hoffer, S.; Somorjai, G. a; Langer, R. A Reversibly Switching Surface. *Science* **2003**, 299 (5605), 371–374.
- (50) Krupenkin, T. N.; Taylor, J. A.; Schneider, T. M.; Yang, S. From Rolling Ball to Complete Wetting: The Dynamic Tuning of Liquids on Nanostructured Surfaces. *Langmuir* **2004**, 20 (10), 3824–3827.
- (51) Yu, X.; Wang, Z.; Jiang, Y.; Shi, F.; Zhang, X. Reversible pH-Responsive Surface: From Superhydrophobicity to Superhydrophilicity. *Adv. Mater.* **2005**, 17 (10), 1289–1293.
- (52) Stratakis, E.; Mateescu, A.; Barberoglou, M.; Vamvakaki, M.; Fotakis, C.; Anastasiadis, S. H. From Superhydrophobicity and Water Repellency to Superhydrophilicity: Smart Polymer-Functionalized Surfaces. *Chem. Commun.* **2010**, 46 (23), 4136.
- (53) Minko, S.; Müller, M.; Motornov, M.; Nitschke, M.; Grundke, K.; Stamm, M. Two-Level Structured Self-Adaptive Surfaces with Reversibly Tunable Properties. *J. Am. Chem. Soc.* **2003**, 125 (13), 3896–3900.
- (54) Chunder, A.; Etcheverry, K.; Londe, G.; Cho, H. J.; Zhai, L. Conformal Switchable Superhydrophobic/hydrophilic Surfaces for Microscale Flow Control. *Colloids Surfaces A Physicochem. Eng. Asp.* **2009**, 333 (1–3), 187–193.
- (55) Caputo, G.; Nobile, C.; Kipp, T.; Blasi, L.; Grillo, V.; Carlino, E.; Manna, L.; Cingolani, R.; Cozzoli, P. D.; Athanassiou, A. Reversible Wettability Changes in Colloidal TiO Nanorod Thin-Film Coatings under Selective UV Laser Irradiation Reversible Wettability Changes in Colloidal TiO<sub>2</sub> Nanorod Thin-Film Coatings under Selective UV Laser Irradiation. **2008**, 701–714.
- (56) Guo, Y.; Xia, F.; Xu, L.; Li, J.; Yang, W.; Jiang, L. Switchable Wettability on Cooperative Dual-Responsive Poly-L-Lysine Surface. *Langmuir* **2010**, 26 (2), 1024–1028.
- (57) Fujii, S.; Kameyama, S.; Armes, S. P.; Dupin, D.; Suzaki, M.; Nakamura, Y. pH-Responsive Liquid Marbles Stabilized with poly(2-Vinylpyridine) Particles. *Soft Matter* **2010**, 6 (3), 635.
- (58) Papadopoulou, E. L.; Barberoglou, M.; Zorba, V.; Manousaki, A.; Pagkozidis, A.; Stratakis, E.; Fotakis, C. Reversible Photoinduced Wettability Transition of

- Hierarchical ZnO Structures. *J. Phys. Chem. C* **2009**, *113* (7), 2891–2895.
- (59) Papadopoulou, E. L.; Zorba, V.; Pagkozidis, a.; Barberoglou, M.; Stratakis, E.; Fotakis, C. Reversible Wettability of ZnO Nanostructured Thin Films Prepared by Pulsed Laser Deposition. *Thin Solid Films* **2009**, *518* (4), 1267–1270.
- (60) Kenanakis, G.; Stratakis, E.; Vlachou, K.; Vernardou, D.; Koudoumas, E.; Katsarakis, N. Light-Induced Reversible Hydrophilicity of ZnO Structures Grown by Aqueous Chemical Growth. *Appl. Surf. Sci.* **2008**, *254* (18), 5695–5699.
- (61) Frysali, M. A.; Papoutsakis, L.; Kenanakis, G.; Anastasiadis, S. H. Functional Surfaces with Photocatalytic Behavior and Reversible Wettability: ZnO Coating on Silicon Spikes. *J. Phys. Chem. C* **2015**, *119* (45), 25401–25407.
- (62) Meyer, D. E.; Shin, B. C.; Kong, G. A.; Dewhurst, M. W.; Chilkoti, A. Drug Targeting Using Thermally Responsive Polymers and Local Hyperthermia. *J. Control. Release* **2001**, *74* (1), 213–224.
- (63) Ahn, S.; Kasi, R. M.; Kim, S.-C.; Sharma, N.; Zhou, Y. Stimuli-Responsive Polymer Gels. *Soft Matter* **2008**, *4* (6), 1151.
- (64) Lee, J. H.; Jung, H. W.; Kang, I.-K.; Lee, H. B. Cell Behaviour on Polymer Surfaces with Different Functional Groups. *Biomaterials* **1994**, *15* (9), 705–711.
- (65) Motornov, M.; Minko, S.; Eichhorn, K. J.; Nitschke, M.; Simon, F.; Stamm, M. Reversible Tuning of Wetting Behavior of Polymer Surface with Responsive Polymer Brushes. *Langmuir* **2003**, *19* (19), 8077–8085.
- (66) Wang, S.; Liu, K.; Yao, X.; Jiang, L. Bioinspired Surfaces with Superwettability: New Insight on Theory, Design, and Applications. *Chem. Rev.* **2015**, *115* (16), 8230–8293.
- (67) Das, M. Stimulus-Responsive Microgels : Design , Properties and Applications Stimulus-Responsive Microgels : Design , Properties and Applications Mallika Das Department of Chemistry. **2008**.
- (68) De Geest, B. G.; Urbanski, J. P.; Thorsen, T.; Demeester, J.; De Smedt, S. C. Synthesis of Monodisperse Biodegradable Microgels in Microfluidic Devices. *Langmuir* **2005**, *21* (23), 10275–10279.
- (69) Haider, I.; Siddiq, M.; Shah, S. M.; ur Rehman, S. Synthesis and Characterization of Multi-Responsive Poly (NIPAm-Co-AAc) Microgels. *IOP Conf. Ser. Mater. Sci. Eng.* **2014**, *60*, 12046.
- (70) Hashmi, S. M.; Dufresne, E. R. Mechanical Properties of Individual Microgel Particles through the Deswelling Transition. *Soft Matter* **2009**, *5* (19), 3682.
- (71) Li, Y. Smart Microgels for Controlled Uptake and Release, Wageningen University, 2011.
- (72) Baig, M. W.; Siddiq, M. Quantum Mechanics of In Situ Synthesis of Metal Nanoparticles within Anionic Microgels. *J. Theor. Chem.* **2013**, 1–5.
- (73) Hou, L.; Wu, P. Microgels with Linear Thermosensitivity in a Wide Temperature Range. *Macromolecules* **2016**, *49* (16), 6095–6100.

- (74) Cai, J.; Guo, J.; Ji, M.; Yang, W.; Wang, C.; Fu, S. Preparation and Characterization of Multiresponsive Polymer Composite Microspheres with Core-Shell Structure. *Colloid Polym. Sci.* **2007**, 285 (14), 1607–1615.
- (75) Argentiere, S.; Blasi, L.; Ciccarella, G.; Cazzato, A.; Barbarella, G.; Cingolani, R.; Gigli, G. Smart Surfaces for pH Controlled Cell Staining. *Soft Matter* **2009**, 5 (21), 4101.
- (76) Nayak, S.; Andrew Lyon, L. Soft Nanotechnology with Soft Nanoparticles. *Angew. Chemie - Int. Ed.* **2005**, 44 (47), 7686–7708.
- (77) Hendrickson, G. R. Harnessing Microgel Softness for Biointerfacing, Georgia Institute of Technology, 2013.
- (78) Klinger, D.; Landfester, K. Stimuli-Responsive Microgels for the Loading and Release of Functional Compounds: Fundamental Concepts and Applications. *Polym. (United Kingdom)* **2012**, 53 (23), 5209–5231.
- (79) Kobayashi, H.; Winkler, R. G. Structure of Microgels with Debye-Hückel Interactions. *Polymers (Basel)*. **2014**, 6 (5), 1602–1617.
- (80) Nayak, S. Design, Synthesis and Characterization of Multiresponsive Microgels, Georgia Institute of Technology, 2005.
- (81) Farooqi, Z. H.; Khan, S. R.; Begum, R.; Kanwal, F.; Sharif, A.; Ahmed, E.; Majeed, S.; Ijaz, K.; Ijaz, A. Effect of Acrylic Acid Feed Contents of Microgels on Catalytic Activity of Silver Nanoparticles Fabricated Hybrid Microgels. *Turkish J. Chem.* **2015**, 39, 96–107.
- (82) Christodoulakis, K. E.; Vamvakaki, M. pH-Responsive Microgel Particles Comprising Solely Basic or Acidic Residues. *Macromol. Symp.* **2010**, 291–292 (1), 106–114.
- (83) Kaliva, M.; Frysali, M. A.; Flouraki, C.; Papoutsakis, L.; Vamvakaki, M.; Anastasiadis, S. H. Metallic Nanocatalysts Embedded within pH-Responsive Polymeric Microgels and Deposition onto Solid Substrates. *Macromol. Symp.* **2013**, 331–332 (1), 17–25.
- (84) Lu, Y.; Proch, S.; Schrinner, M.; Drechsler, M.; Kempe, R.; Ballauff, M. Thermosensitive Core-Shell Microgel as a “nanoreactor” for Catalytic Active Metal Nanoparticles. *J. Mater. Chem.* **2009**, 19 (23), 3955.
- (85) Lu, Y.; Mei, Y.; Drechsler, M.; Ballauff, M. Thermosensitive Core-Shell Particles as Carriers for Ag Nanoparticles: Modulating the Catalytic Activity by a Phase Transition in Networks. *Angew. Chemie - Int. Ed.* **2006**, 45 (5), 813–816.
- (86) Vinogradov, S. V. Colloidal Microgels in Drug Delivery Applications. *Curr Pharm Des.* **2006**, 12 (36), 4703–4712.
- (87) Mei, Y.; Lu, Y.; Polzer, F.; Ballauff, M.; Drechsler, M. Catalytic Activity of Palladium Nanoparticles Encapsulated in Spherical Poly Electrolyte Brushes and Core-Shell Microgels. *Chem. Mater.* **2007**, 19 (5), 1062–1069.
- (88) Zhang, J. T.; Wei, G.; Keller, T. F.; Gallagher, H.; Stötzl, C.; Müller, F. a.; Gottschaldt, M.; Schubert, U. S.; Jandt, K. D. Responsive Hybrid Polymeric/metallic

- Nanoparticles for Catalytic Applications. *Macromol. Mater. Eng.* **2010**, 295 (11), 1049–1057.
- (89) Quéré, D. Wetting and Roughness. *Annu. Rev. Mater. Res.* **2008**, 38 (1), 71–99.
- (90) Malvadkar, N. a; Hancock, M. J.; Sekeroglu, K.; Dressick, W. J.; Demirel, M. C. An Engineered Anisotropic Nanofilm with Unidirectional Wetting Properties. *Nat. Mater.* **2010**, 9 (12), 1023–1028.
- (91) Liu, M.; Zheng, Y.; Zhai, J. I. N.; Jiang, L. E. I. Bioinspired Super-Antiwetting Interfaces with Special Liquid - Solid Adhesion. **2010**, 43 (3).
- (92) Zheng, Y.; Gao, X.; Jiang, L. Directional Adhesion of Superhydrophobic Butterfly Wings. *Soft Matter* **2007**, 3 (2), 178.
- (93) Cho, W. K.; Choi, I. S. Fabrication of Hairy Polymeric Films Inspired by Geckos: Wetting and High Adhesion Properties. *Adv. Funct. Mater.* **2008**, 18 (7), 1089–1096.
- (94) Jin, M.; Feng, X.; Feng, L.; Sun, T.; Zhai, J.; Li, T.; Jiang, L. Superhydrophobic Aligned Polystyrene Nanotube Films with High Adhesive Force. *Adv. Mater.* **2005**, 17 (16), 1977–1981.
- (95) Hong, X.; Gao, X.; Jiang, L. Application of Superhydrophobic Surface with High Adhesive Force in No Lost Transport of Superparamagnetic Microdroplet. *J. Am. Chem. Soc.* **2007**, 129 (6), 1478–1479.
- (96) Zorba, V.; Persano, L.; Pisignano, D.; Athanassiou, a; Stratakis, E.; Cingolani, R.; Tzanetakis, P.; Fotakis, C. Making Silicon Hydrophobic: Wettability Control by Two-Lengthscale Simultaneous Patterning with Femtosecond Laser Irradiation. *Nanotechnology* **2006**, 17 (13), 3234–3238.
- (97) Kenanakis, G.; Vernardou, D.; Katsarakis, N. Light-Induced Self-Cleaning Properties of ZnO Nanowires Grown at Low Temperatures. *Applied Catalysis A: General.* 2012, pp 7–14.
- (98) Kenanakis, G.; Katsarakis, N. ZnO Nanowires on Glass via Chemical Routes: A Prospective Photocatalyst for Indoors Applications. *J. Environ. Chem. Eng.* **2014**, 2 (3), 1416–1422.
- (99) Kenanakis, G.; Pervolaraki, M.; Giapintzakis, J.; Katsarakis, N. The Use of Pulsed Laser Deposited Seed Layers for the Aqueous Solution Growth of Highly Oriented ZnO Nanowires on Sapphire Substrates at 95°C: Study of Their Photocatalytic Activity in Terms of Octadecanoic (Stearic) Acid Degradation. *Appl. Catal. A Gen.* **2013**, 467, 559–567.
- (100) Garg, V. K.; Amita, M.; Kumar, R.; Gupta, R. Basic Dye (Methylene Blue) Removal from Simulated Wastewater by Adsorption Using Indian Rosewood Sawdust: A Timber Industry Waste. *Dye. Pigment.* **2004**, 63 (3), 243–250.
- (101) Salem, I. A.; El-Maazawi, M. S. Kinetics and Mechanism of Color Removal of Methylene Blue with Hydrogen Peroxide Catalyzed by Some Supported Alumina Surfaces. *Chemosphere* **2000**, 41 (8), 1173–1180.
- (102) Rahimi, R.; Shokrayian, J.; Rabbani, M. Photocatalytic Removing of Methylene Blue

by Using of Cu-Doped ZnO, Ag-Doped ZnO and Cu,Ag-Codoped ZnO Nanostructures. *Proc. 17th Int. Electron. Conf. Synth. Org. Chem.* **2013**, b019.

## Chapter 2

# 2. Functional ZnO surfaces with photocatalytic behavior and reversible wettability

### 2.1. Introduction

Self-cleaning surfaces have gained the focus of considerable research due to their strong potential for exploitation in a number of industrial applications.<sup>1</sup> Super-hydrophobic materials are widely used in outdoor weather-proof paints, easy-clean textiles, microfluidics, lab-on-chip devices, low friction coatings (e.g. for ships) and solar panels.<sup>2-6</sup> On the other hand, super-hydrophilicity, the flip side of the coin, is used in the cleaning of roof tiles and windows, in mist-free mirrors and in photochemical degradation, to name but a few.<sup>7</sup> The inspiration for designing and developing new self-cleaning materials comes from nature;<sup>1</sup> the *Lotus* effect, which results in super-hydrophobicity and very high water repellence, as exhibited by the leaves of sacred Lotus (*Nelumbo nucifera*), was first reported by Barthlott and Neinhuis.<sup>8,9</sup> Apart from this, there is a wide variety of biological species exhibiting amazing wettability properties, like rice leaves, rose petals, the strider's legs, gecko feet, shark skin, mosquito compound eye, spider silks, cicada and butterfly wings, etc.<sup>10</sup>

The most common way to generate effective super-hydrophobic surfaces is to build multiscale hierarchical roughness. One way this can be achieved is by micro/nano-structuring a surface utilizing ultrafast lasers, which creates dual scale roughness in an one-step

process.<sup>3,11</sup> The first conical microstructures with multiscale roughness were reported by Her and Mazur<sup>12</sup> in 1998. Since then, femtosecond laser has proved to be a promising method for fabricating hierarchical structures with multiscale roughness.<sup>13</sup> For example, Zorba *et al.* produced artificially structured surfaces possessing controlled dual-scale roughness, which exhibited the water repellent characteristics of the natural Lotus leaf.<sup>3,14,15</sup>

Moreover, there is a continuously increasing demand for multifunctional surfaces with reversible characteristics. This can be achieved by using “smart” coatings, which can respond to external stimuli, such as light,<sup>16–20</sup> temperature,<sup>16,21–23</sup> electric field,<sup>16,23–25</sup> pH<sup>16,26,27</sup> or solvent selectivity.<sup>16,28</sup> Among the “smart” coatings found in the literature, the wetting properties of ZnO have been widely studied, since it can reversibly switch from super-hydrophilic to super-hydrophobic in response to UV irradiation and heating or dark storage, respectively.<sup>29–31</sup> For example, Papadopoulou *et al.*, reported the preparation of photoreversible ZnO hierarchical surfaces prepared by irradiating Si substrates with femtosecond laser and decorating them with ZnO nanoprotusions using pulsed laser deposition.<sup>30</sup>

ZnO, besides its well-known reversible self-cleaning properties, has been extensively studied for its photocatalytic behavior. In order to enhance its photocatalytic activity, research efforts have focused on the development of ZnO surfaces with a high surface to volume ratio. ZnO, with probably the largest variety of different nanostructures, has attracted much attention within the scientific community as a “material of the future.” Its range includes one- (1D), two- (2D), and three-dimensional (3D) structures. One-dimensional structures include nanowires, -needles, -helixes, -springs, -rings, -ribbons, -tubes, -belts, and -combs.<sup>32,33</sup> Examples of ZnO 2D structures are the nanoplates and the nanopellets.<sup>33,34</sup> 3D ZnO structures, reported in literature, are flowers, dandelion, snowflakes, coniferous urchin-like.<sup>33,35–37</sup>

Nanostructured ZnO materials have received broad attention due to their distinguished performance in electronics, optics and photonics. For example, ZnO nanoparticles have been utilized for the development of ultraviolet (UV) photodetectors, for commercial, military, and space applications.<sup>38-40</sup> Moreover, they are widely used in sunscreens and cosmetics.<sup>39,41</sup> On the other hand, ZnO nanoflowers were used for Li-ion batteries.<sup>39,42</sup> Nanocombs and nanosaws have been also fabricated from Hashimoto *et al.*<sup>43,44</sup> ZnO nanorings, nanohelices and nanospirals have been reported for micro- and nano-electromechanical systems and biomedical sensing.<sup>43,45,46</sup> Other ZnO nanostructures, like nanocages could be of interest for drug delivery.<sup>43,47</sup> ZnO nanowires and nanotubes have been used to detect biological molecules in aqueous solutions. Popular ones include pH sensors, glucose biosensors, and cholesterol biosensors.<sup>48</sup> Apart from ZnO nanowires, nanofibers, flower-like and nanoflakes have also been utilized as enzyme biosensors.<sup>49</sup> Additionally, ZnO nanoribbons and nanowires are popular for optoelectronics applications.<sup>48,50</sup> In general, ZnO nanostructures, are of interest for biomedical applications as well as gas, optical and electrical sensors. Alternative applications reported are for photocatalysis and dye degradations.<sup>39,51-57</sup> New applications of ZnO nanostructures in energy storage and hydrogen storage have also attracted growing interest.<sup>48</sup>

However, most of the work cited above suffers from the disadvantage of producing low stability specimens, which cannot be easily adopted for large scale synthesis and, thus, for industrial applications.

Thus, a critical issue related to ZnO nanostructures is the achievement of reproducible, fast and inexpensive patterning techniques. Moreover for all applications, controlling the shape of the semiconductor nanostructures is still a significant technological challenge. Several research groups have been working with ZnO nanostructures along with polymers in order to either control their properties and/or make them functionable to several applications.

Panigrahy and his co-workers prepared a variation of ZnO nanostructures by using polymers like Poly(ethylene glycol), PEG and Poly(vinyl pyrrolidinone), PVP in order to control the magnetic and optical properties.<sup>58</sup> Polymers with pyridine units have been widely studied due to their reactive nitrogen heteroatom.<sup>59</sup> Kumar *et al.* took advantage of the pH-response of Poly(4-vinyl pyridine), P4VP, which was utilized as a template for polymer / ZnO nanocomposites.<sup>59</sup> The combination of ZnO nanostructures and polymers could be advantageous for sensing applications.<sup>60</sup> For example Poly(methylmethacrylate), PMMA, microfibers, coated with Al-doped ZnO nanostructures have been fabricating for the detection of uric acid.<sup>61</sup> Polymers have been used for the development of highly oriented, aligned ZnO nanorods, for advanced optical devices.<sup>62</sup> Furthermore Polystyrene-block-poly(2-vinylpyridine)-gold nanoparticles hybrid nanotubes, with pH-responsive properties, found applications in microfluidic systems.<sup>63</sup>

In this work, ZnO nanowires were developed with enhanced stability and high photocatalytic behavior using polymeric stabilizers. First, ZnO nanowires were grown on ZnO pre-coated glass substrates via aqueous solution growth.<sup>64</sup> Afterwards, the samples were coated with polymers with the spin coating method. Poly(methylmethacrylate), PMMA and Poly(2-vinylpyridine), P2VP were utilized for this purpose. Samples were characterized with Scanning Electron Microscopy and were tested for their photocatalytic behavior using Fourier Transform Infrared Spectroscopy (FTIR). Stearic acid was utilized as a test organic pollutant. Samples were also tested for their wettability. ZnO nanowires were also coated with dichlorodimethylsilane for comparison reasons.

In parallel, ZnO coatings exhibiting reversible wettability and photocatalytic activity were developed, following an environmental friendly approach. The as-grown samples are prepared following a two-step fabrication process. First, silicon (Si) wafers are irradiated with femtosecond (fs) laser pulses in order to produce Si surfaces with dual scale roughness (Si

spikes).<sup>3,14,15</sup> Then, the rough Si samples are coated with a ZnO film prepared by a simple sol-gel process.<sup>51,64,65</sup> The artificial surfaces exhibit reversible wettability from super-hydrophilic (upon UV irradiation) to super-hydrophobic (upon heating), while the as-grown samples revealed high photocatalytic activity investigated by means of the decolorization of methylene blue as a model.<sup>66-68</sup> Moreover, the reproducibility and sustainability of the system is thoroughly studied.

### 2.1.1. Basic properties and applications of ZnO

Zinc oxide has been widely studied since 1935<sup>69</sup> due to the attractive applications and it has been characterized from the researchers as the “material of the future”.<sup>70,71</sup> ZnO, with a wide bandgap of 3.4eV, is quite important for blue and ultraviolet optical devices, including light-emitting diodes, laser diodes and photodetectors.<sup>43,71</sup> ZnO has several advantages with the most important being its large exciton binding energy<sup>43</sup> (60meV at room temperature) and the ability to grow single crystal substrates.<sup>43,71</sup> Other favorable aspects of ZnO include its broad chemistry leading to many opportunities for wet chemical etching, low power threshold for optical pumping, radiation hardness and biocompatibility.<sup>70</sup> The unique properties of ZnO mentioned above make it an ideal candidate for a variety of devices ranging from sensors to ultra-violet laser diodes and nanotechnology-based devices such as displays.<sup>71</sup>

ZnO crystallizes in the wurtzite (B4 type) structure, at ambient pressure and temperature. This tetrahedral coordination gives rise to polar symmetry along the hexagonal axis, which is responsible for a number of the properties of ZnO, including its piezoelectricity and spontaneous polarization, and is also a key factor in crystal growth, etching and defect generation.<sup>71</sup> The epitaxy of ZnO films on native substrates can result in ZnO layers with reduced concentration of extended defects and, consequently, better performance in

electronic and photonic devices.<sup>70,72</sup> One can see the hexagonal wurtzite crystal structure of ZnO in Figure 2.1.<sup>73</sup>

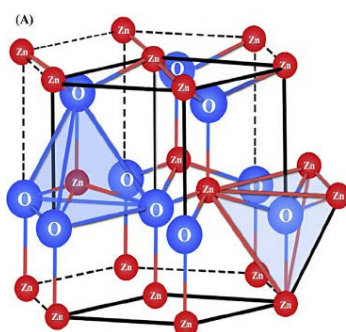


**Figure 2.1.** Hexagonal wurtzite crystal structure of ZnO.

Due to a strong luminescence in the green-white region of the spectrum, ZnO can exhibit enhanced properties including luminescence and phosphorescence compared to bulk materials making them ideal for solid state lighting and optical,<sup>43,71,73</sup> providing an emission spectrum with a peak at 495nm and a very broad half-width of 0.4eV.

Furthermore, the n-type conductivity of ZnO makes it appropriate for applications in vacuum fluorescent displays and field emission displays.<sup>70</sup> The origin of the luminescence center and the luminescence mechanism are frequently attributed to oxygen vacancies or zinc interstitials, without any clear evidence.<sup>70</sup>

In addition, the high thermal conductivity of ZnO, makes it useful as an additive.<sup>70</sup> For example, ZnO is added to rubber in order to increase the thermal conductivity of tires. High thermal conductivity translates into high efficiency of heat removal during device operation.<sup>70</sup>

The unique properties of ZnO make it dominant in many industrial manufacturing processes including paints, cosmetics, pharmaceuticals, plastics, batteries, electrical equipment, rubber, soap, textiles, floor coverings to name just a few. With improvements in growth technology

of ZnO nanostructures, epitaxial layers, single crystals and nanoparticles, we are now moving into an era where ZnO devices will become increasingly functional and exotic.<sup>71</sup>

Thus, ZnO, whilst already possessing a wide application base, has enormous opportunities for society and industry due to its unique properties. The future in which, ZnO devices become part of our everyday lives, is already on approaching reality.<sup>71</sup>

The basic material properties of ZnO are being summarized in the Table 2.1.<sup>74</sup>

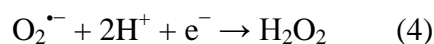
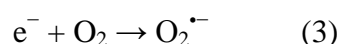
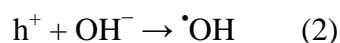
**Table 2.1.** Key properties of ZnO.

Property	Value
Lattice parameters at 300 K:	
$a_0$	0.32495 nm
$c_0$	0.52069 nm
$a_0/c_0$	1.602 (1.633 for ideal hexagonal structure)
$u$	0.345
Density	5.606 g/cm <sup>3</sup>
Stable phase at 300 K	Wurtzite
Melting point	1975°C
Thermal conductivity	0.6, 1-1.2
Linear expansion coefficient (/°C)	$a_0 : 6.5 \times 10^{-6}$ , $c_0 : 3.0 \times 10^{-6}$
Static dielectric constant	8.656
Refractive index	2.008, 2.029
Energy gap	3.4 eV (direct)
Intrinsic carrier concentration	$< 10^6/\text{cm}^3$
Exciting binding energy	60 meV
Electron effective mass	0.24
Electron Hall mobility at 300 K for low $n$ -type conductivity	200 cm <sup>2</sup> /V·s
Hole effective mass	0.59

### 2.1.2. ZnO mediated heterogeneous photocatalysis

Heterogeneous photocatalysis can be described as the acceleration of photoreaction in the presence of a catalyst. In the context of history and research, interest in heterogeneous photocatalysis can be traced back to many decades when Fujishima and Honda discovered the photochemical splitting of water into hydrogen and oxygen in the presence of TiO<sub>2</sub> back in 1972. From that time, extensive research, much of it published, has been carried out to produce hydrogen from water in oxidation reduction reactions using a variety of semiconductor catalyst materials.<sup>75,76</sup> Some notable examples of semiconductor solids used in environmental heterogeneous photocatalysis include TiO<sub>2</sub>, ZnO, CdS, WO<sub>3</sub>, SnO<sub>2</sub>, ZnS, CdTe, α-Fe<sub>2</sub>O<sub>3</sub>, AgNbO<sub>3</sub> and SrTiO<sub>3</sub>, to name but a few.<sup>76</sup>

The overall process of heterogeneous photocatalysis can be decomposed into four independent steps.<sup>77,78</sup> ZnO absorbs light with less than 388 nm in wavelength and promotes the valence band electrons up to the conduction band, leaving holes in valence band as in Equation (1). The holes produced could subsequently react with hydroxide ions (OH<sup>-</sup>) or water molecules in aqueous solution to form powerful oxidants such as hydroxyl radicals (·OH) in Equation (2). The electrons on conduction band transform the dissolved oxygen to superoxide in Equation (3) and further to hydrogen peroxide in Equation (4). These strong oxidants could be used to remove organic pollutants from wastewater.<sup>78</sup>



The general mechanism of the photocatalysis with ZnO is described schematically in Figure 2.2.<sup>79</sup>

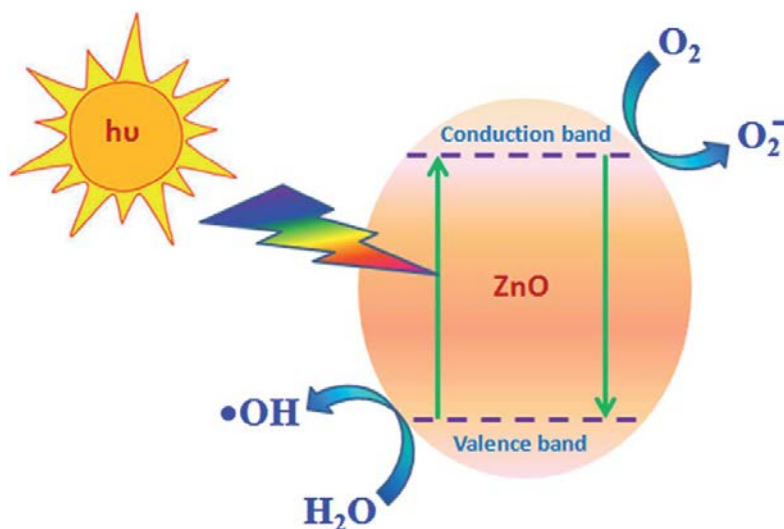


**Figure 2.2.** Schematic mechanism of ZnO, acting as photocatalyst.

### Photocatalytic degradation of stearic acid

Stearic acid ( $C_{18}H_{36}O_2$ ) is a saturated fatty acid with an 18-carbon chain and has the IUPAC name octadecanoic acid. The chemical structure of the stearic acid is depicted in Figure 2.3.

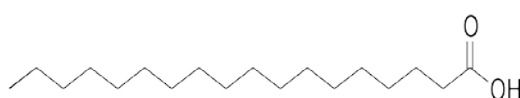
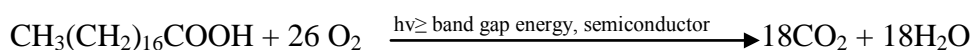


**Figure 2.3.** Chemical structure of stearic acid.

Among fatty acids, stearic acid, has desirable characteristics including negligible super cooling through a phase change, thermal and chemical stability, outstanding phase transition performance and non-toxicity.<sup>80</sup> Furthermore, the melting point of stearic acid is above room temperature,  $69.3^{\circ}C$ , and it forms solid films when deposited on surfaces,<sup>81,82</sup> while SA is very easily laid down from chloroform or methanol solutions.<sup>81</sup>

Taking advantage of this property, a thin layer of stearic acid is commonly employed as test organic pollutant in the characterization of semiconductor films for photocatalysis.<sup>51,53,80–83</sup>

This happens because, such solid compounds can simulate the type of solid organic film that deposits on indoor glass and ceramic surfaces.<sup>81,82</sup> Another property of stearic acid that makes it appropriate for photocatalytic measurements is that it is very stable under UV illumination, in the absence of a semiconductor. In addition, the degradation of stearic acid is usually simple and zero-order, and as a result, the SA film thickness does not affect the photocatalytic activity.<sup>81</sup> The photocatalytic degradation of the stearic acid can be described as follows<sup>83</sup>:



The most common way for studying the above reaction is by calculating the decomposition of stearic acid using infrared absorption spectroscopy, since it absorbs strongly in the region 2700-3000  $\text{cm}^{-1}$ .<sup>51,53,81–83</sup> Specifically, the characteristic absorption peaks of the stearic acid, are the asymmetric C–H stretching mode of the  $\text{CH}_3$  group at  $2958\text{cm}^{-1}$  and the asymmetric and symmetric C–H stretching modes of the  $\text{CH}_2$  group at  $2923\text{cm}^{-1}$  and  $2853\text{cm}^{-1}$ , respectively.<sup>53,81</sup>

### Photocatalytic degradation of methylene blue

Colour is the first contaminant to be recognized in water and has to be removed from wastewater before discharging it into water bodies. Most of the industries, textile, paper, printing, leather, food, cosmetics, etc. use dyes to colour their final product. Colour impedes light penetration, decelerates photosynthetic activity, inhibits the growth of biota and also has a tendency to form metal ions which produce micro-toxicity to fish and other organisms.<sup>66,84</sup>

The application of semiconductors in water treatment via photocatalysis of various pollutants

has attracted much attention from researchers. In this work, photocatalytic degradation of methylene blue was studied experimentally using ZnO via ultraviolet-visible spectroscopy (UV-Vis) in absorbance mode.

Methylene blue (MB), also known as methylthioninium chloride, is a cationic dye (Figure 2.4), with a chemical formula  $C_{16}H_{18}ClN_3S$ , which forms face-to-face dimers in dilute aqueous solutions and higher aggregates at increasing dye concentration.<sup>85</sup>

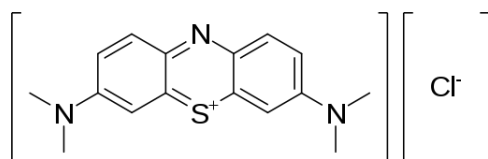


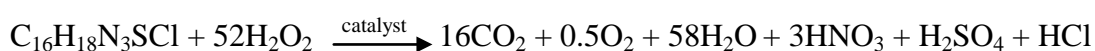
**Figure 2.4.** Structural formula of methylene blue.

The dye is sensitive to changes in the polarity of its surroundings. A summary of its spectral properties is given in Table 2.2. The maximum absorption of light is around 670 nm. The specifics of absorption depend on a number of factors, including protonation, adsorption to other materials, and metachromasy - the formation of dimers and higher-order aggregates depending on concentration and other interactions.<sup>85</sup>

**Table 2.2.** Band positions ( $\lambda$ ) and extinction coefficients ( $\epsilon$ ) of methylene blue.

Species	Absorption peak	Extinction coefficient ( $\text{dm}^3/\text{mole}\cdot\text{cm}$ )
$\text{MB}^+$ (solution)	664	95000
$\text{MBH}_2^+$ (solution)	741	76000
$(\text{MB}^+)_2$ (solution)	605	132000
$(\text{MB}^+)_3$ (solution)	580	110000
$\text{MB}^+$ (adsorbed on clay)	673	116000
$\text{MBH}_2^+$ (adsorbed on clay)	763	86000
$(\text{MB}^+)_2$ (adsorbed on clay)	596	80000
$(\text{MB}^+)_3$ (adsorbed on clay)	570	114000

As described above, during photocatalysis by ZnO, strong oxidants like hydrogen peroxide are produced. The stoichiometric equation describing the degradation of methylene blue is shown below.<sup>67</sup>



### 2.1.3. The mechanism of ZnO reversible wettability

It is well known that surface roughness and crystallinity are two main factors governing the surface wettability of ZnO. XRD patterns show that the crystallinity does not change appreciably among the thin films with different annealing temperature. Therefore, variation of the initial contact angle of the thin films should be primarily attributed to the difference in their surface roughness.<sup>86</sup>

The mechanism of light-induced wettability of ZnO nanostructure has been investigated by many researchers.<sup>29,30,86,87</sup> It has been reported that UV illumination will generate electron–hole pairs in the ZnO surface. Some of the holes can react with lattice oxygen to form surface oxygen vacancies, while some of the electrons react with lattice metal ions ( $\text{Zn}^{2+}$ ) to form  $\text{Zn}^+$  defective sites (surface trapped electrons). Meanwhile, water and oxygen may compete to dissociatively adsorb on these defective sites. The defective sites are kinetically more favorable for hydroxyl adsorption than oxygen adsorption. As a result, the surface hydrophilicity is improved, and the water contact angle is significantly reduced.<sup>86,88</sup> After the hydroxyl adsorption, the surface becomes energetically unstable. Because oxygen adsorption is thermodynamically favored, it is more strongly bonded on the defect sites than on the hydroxyl groups. Consequently, the hydroxyl groups adsorbed on the defective sites can be replaced gradually by oxygen atoms when the UV-irradiated films were placed in the dark. Heat treatment can accelerate the elimination of surface hydroxyl groups.<sup>86,89</sup> As a result, the surface reverts back to its original state (before UV irradiation) by means of dark storage (or heat treatment), and the wettability is reconverted from hydrophilicity to hydrophobicity. The magnitude of the reversible change between hydrophobic and hydrophilic states is connected with both surface chemical composition and roughness.<sup>86,90</sup>

#### 2.1.4. ZnO nanowires: growth and applications

ZnO nanowires have attracted the interest of the research community, since they can be prepared by a variety of physical or chemical methods.<sup>39</sup> Their growth can be achieved by physical vapor deposition, chemical vapor deposition, metal-organic chemical vapor deposition and by hydrothermal chemical approach<sup>91</sup>. The advantages and drawbacks of these methods have been discussed by Gomez *et al.*<sup>48</sup> Photolithography has been utilized by Tak and his co-workers for the development of ZnO nanowires.<sup>39,92</sup> Atomic force

microscopy<sup>39,93</sup>, electron beam lithography<sup>39,94,95</sup> and laser interference patterning techniques<sup>39,62,95</sup> are also among ZnO nanowires grown methods.

ZnO nanowires find applications in solar cells<sup>96</sup>, such as dye-sensitized solar cells (DSSCs)<sup>97</sup> or polymer-based solar cells<sup>39</sup>, while they are possible candidates for ultraviolet (UV) photodetectors.<sup>38,39</sup> Moreover, ZnO nanowires have been used to detect biological molecules in aqueous solutions,<sup>48</sup> while several applications include pH sensors, glucose biosensors, and cholesterol biosensors.<sup>48</sup> The photoluminescence properties of ZnO nanowires have been widely studied by Li *et al.*<sup>98</sup>

Finally, ZnO nanowires have been mainly studied for the photocatalytic decomposition of volatile organic compounds.<sup>51,53,99</sup> Shao *et al.* fabricated flexible ZnO carbon nanowires for efficient photocatalytic applications.<sup>100,101</sup> Baruah and his co-workers presented ZnO nanowires, grown on paper prepared from wood pulp, whose behavior was studied by the photodegradation of methylene blue,<sup>102</sup> while the photocatalytic behavior of ZnO nanowires have been also investigated by Wang *et al.*<sup>103</sup> Furthermore, photocatalytic spinning disc reactors enriched with ZnO nanorods, were also designed for large scale water treatment.<sup>104</sup>

### 2.1.5. Properties of Poly(methyl methacrylate), PMMA

Poly (methyl methacrylate), PMMA, having the IUPAC name of poly [1-(methoxy carbonyl)-1-methyl ethylene] from the hydrocarbon standpoint and poly (methyl 2-methyl-propenoate) from the ester standpoint, is a synthetic polymer from the methyl methacrylate monomer. PMMA was discovered in the early 1930s by British chemists, Rowland Hill and John Crawford, followed by its first application by a German chemist, Otto Rohm, in 1934.<sup>105</sup>

The chemical structure of the carboxy Terminated Poly(methyl methacrylate) is depicted in Figure 2.5.

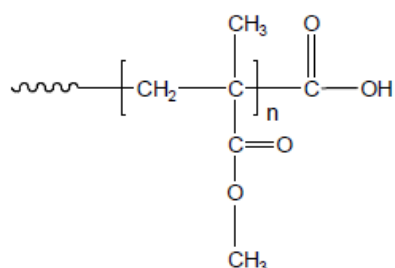


**Figure 2.5.** Chemical structure of carboxy terminated Poly(methyl methacrylate).

PMMA is an amorphous transparent thermoplastic with promising applications in optical fibers, optical disks and lenses.<sup>106</sup> Moreover it has been recognized as an excellent candidate for sensors and conductive devices.<sup>105,107,108</sup> PMMA has also been used in molecular separation, in the area of biomedical applications, as a gel polymer electrolyte for lithium and magnesium batteries, in the preparation of bone cements for drug delivery/release and cranioplasty.<sup>105,108</sup>

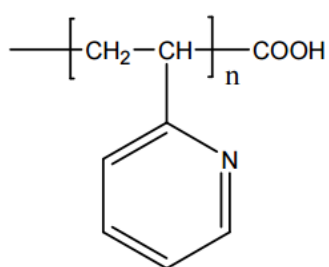
The diverse applications of PMMA originate from its outstanding properties. Among them, are that it is non-toxic, lightweight, it has high impact strength and weather, fracture and scratch resistance.<sup>105</sup> Other interesting properties attributed to PMMA are low cost, compatibility, ease of modification and processability. Physical and mechanical properties of PMMA are summarized in Table 2.3.<sup>105</sup>

**Table 2.3.** Physical and mechanical properties of PMMA.

Property	PMMA
Color	Courless
Density (g/cm <sup>3</sup> )	1.18
Melting point (°C)	220-240
Surface Hardness (Rockwell)	M92, M90-M100
Glass Transition Temperature (T <sub>g</sub> )	110-120
Linear Thermal Expansion (× 10 <sup>-5</sup> mm/mm.k)	6.3
Thermal Expansion Coefficient 20°C (× 10 <sup>-4</sup> K <sup>-1</sup> )	1.8
Thermal Expansion Coefficient 40°C (× 10 <sup>-4</sup> K <sup>-1</sup> )	2.2
Thermal Expansion Coefficient 20°C (× 10 <sup>-5</sup> bar <sup>-1</sup> )	2.7
Thermal Expansion Coefficient 40°C (× 10 <sup>-5</sup> bar <sup>-1</sup> )	2.9
Mold shrinkage (%)	0.3-0.6
Water Absorption (%)	0.3
Oxygen Index (%)	19, 17, 19
Thermal conductivity at 20°C (k(W/mK))	0.12, 0.17
Tensile Strength (MPa)	72
Tensile Modulus (GPa)	3.10
Elongation at Break (%)	5

### 2.1.6. Properties of Poly(2-vinylpyridine), P2VP

Poly(2-vinyl pyridine), P2VP is a non-toxic and water soluble polymer. The chemical structure of the carboxyl terminated P2VP is shown in Figure 2.6.

**Figure 2.6.** Chemical structure of carboxy terminated Poly(2-vinyl pyridine).

P2VP, a weak cationic polyelectrolyte with pH-dependent swelling properties, undergoes a phase transition under pH 5 owing to protonation of pyridine groups.<sup>109,110</sup>

P2VP has been utilized for the fabrication of microporous polymer membranes, which find applications in industry and medicine for separation and concentration of particles, colloids, proteins and cells.<sup>109</sup> Moreover, P2VP has been used as an electrolyte additive in lithium-ion batteries for improving their performances<sup>111</sup> and for the fabrication of photonic gels.<sup>112,113</sup>

Photonic crystals with tunability in the visible or near-infrared region are of interest for controlling and processing light for active components of display, sensory or telecommunication devices.<sup>113</sup>

## **A) Development of Si spikes covered with ZnO coating, exhibiting both photocatalytic behavior and reversible wettability**

### **2.1. Introduction**

In this work, the development of ZnO coatings exhibiting reversible wettability and photocatalytic activity is reported, following an environmental friendly approach. The as-grown samples are prepared following a two-step fabrication process. First, silicon (Si) wafers are irradiated with femtosecond (fs) laser pulses in order to produce Si surfaces with dual scale roughness (Si spikes).<sup>3,14,15</sup> Then, the rough Si samples are coated with a ZnO film prepared by a simple sol-gel process.<sup>51,64,65</sup> The artificial surfaces exhibit reversible wettability from super-hydrophilic (upon UV irradiation) to super-hydrophobic (upon heating), while the as-grown samples revealed high photocatalytic activity investigated by

means of the decolorization of methylene blue as a model.<sup>66–68</sup> Moreover, the reproducibility and sustainability of the system is thoroughly studied.<sup>90</sup>

## 2.2. Experimental Part

### 2.2.1. Surface manufacturing with fs laser

For the microstructuring of Si wafers, a Yb:KGW laser with a pulse duration of 170 fs at a wavelength of 1026 nm, was utilized. First, single crystal *n*-type Si (100) wafers with a resistivity of  $\rho = 2\text{--}8 \text{ L} \cdot \text{cm}$  were placed in a vacuum chamber evacuated down to a residual pressure  $10^{-2}$  mbar by means of a rotary pump. A micro valve system attached to the chamber enabled a precise backfilling of reactive gas ( $\text{SF}_6$ ) atmosphere. The parameters, like laser pulse, laser fluence, gas pressure, repetition rate and irradiation step, were investigated for the optimization of the system. The laser fluence was varied by using filters or attenuators. The laser beam was focused with a quartz lens on the sample, mounted to a sample holder inside the vacuum processing chamber. The laser beam entered the chamber through a quartz entrance window, while the irradiation process could be monitored through a Plexiglas window, which was laterally mounted on the vacuum chamber. The chamber was mounted on a high precision X-Y translational stage and the sample surface was kept perpendicular to the incident laser beam. The stage motion was synchronized with a mechanical shutter in order to provide a uniform exposure of a  $100 \text{ mm}^2$  area to an average of 500 laser pulses per spot. After that, the samples were cleaned with a 10% HF aqueous solution in order to remove the silicon oxide grown on the surface.<sup>3,20,90</sup> The experimental set up for the fabrication of Si spikes is shown in Figure 2.7. The surfaces were characterized by field emission Scanning Electron Microscopy (FE-SEM).

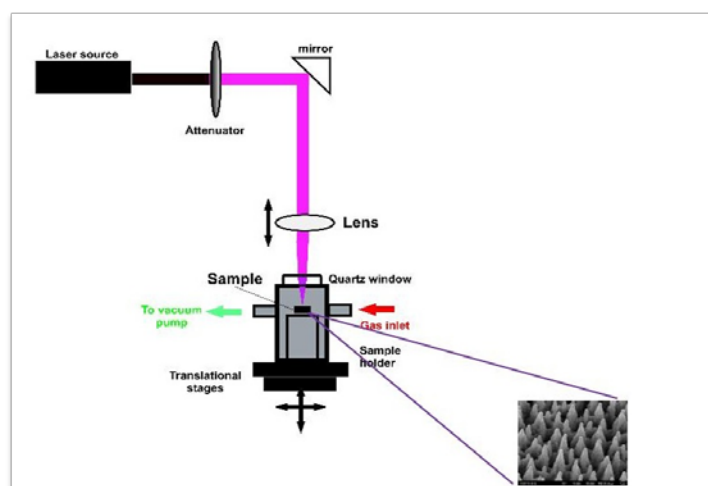


**Figure 2.7.** Experimental set up of fs laser.

### 2.2.2. Deposition of ZnO films on Si spikes

After rinsing several times with ethanol and bi-distilled water in order to remove any remains, the surfaces were coated by a ZnO film using a simple sol-gel process.<sup>114,115</sup> For this purpose, Zinc acetate dihydrate  $[(\text{Zn}(\text{CH}_2\text{COO})_2 \cdot 2\text{H}_2\text{O})$ , Sigma-Aldrich, 99.99%] was dissolved in 2-methoxy ethanol  $[(\text{CH}_3\text{OCH}_2\text{CH}_2\text{OH})$ , Sigma-Aldrich,  $\geq 99.55\%$ ] at a concentration of 0.75 mol/L. Monoethanolamine  $[(\text{HOCH}_2\text{CH}_2\text{NH}_2)$ , Sigma-Aldrich,  $\geq 99.0\%$ ] was also added as a stabilizer and the molar ratio of zinc acetate to ethanolamine was kept at 1:1. The resultant solution was stirred for 1h at 60°C in order to become clear and homogeneous. Subsequently, 30  $\mu\text{L}$  of the solution were dropped on the laser irradiated Si samples, which were rotated at 3000 rpm for 20 sec. After coating, the samples were heated at 350°C for 10 min to evaporate the solvent and remove any organic residuals. This procedure was repeated for four (4 $\times$ ) times. Finally, the samples were annealed in air at 500°C for 1h. In parallel with the deposition of the ZnO coatings on Si spikes, ZnO films on flat silicon wafers were grown as well. This way, reference specimens of ZnO on flat silicon were created for reference and comparison reasons.<sup>90</sup>

The surface morphology of flat Si substrates coated with ZnO films was investigated using an atomic force microscope (AFM) in tapping mode (Digital instruments- Nanoscope IIIa). The grain size and the roughness (rms) of the ZnO films on flat Si wafers were determined using the scanning probe image processing software (SPIP, v. 3.3.5.0, Image Metrology) for nano- and micro-scale microscopy, while the thickness of the ZnO film was measured with a stylus profilometer (alpha-step 100, Tencor). The morphology of laser irradiated Si surfaces, with and without the ZnO coating, was studied using a field emission scanning electron microscope (FE-SEM, JEOL JSM-7000F), while the crystalline structure of all samples was determined by X-ray diffraction (XRD) utilizing a Rigaku (RINT 2000) diffractometer with Cu K $\alpha$  radiation with a wavelength  $\lambda=1.54 \text{ \AA}$ . The schematic presentation of the overall procedure of the deposition of ZnO on Si spikes, is depicted in Figure 2.8.

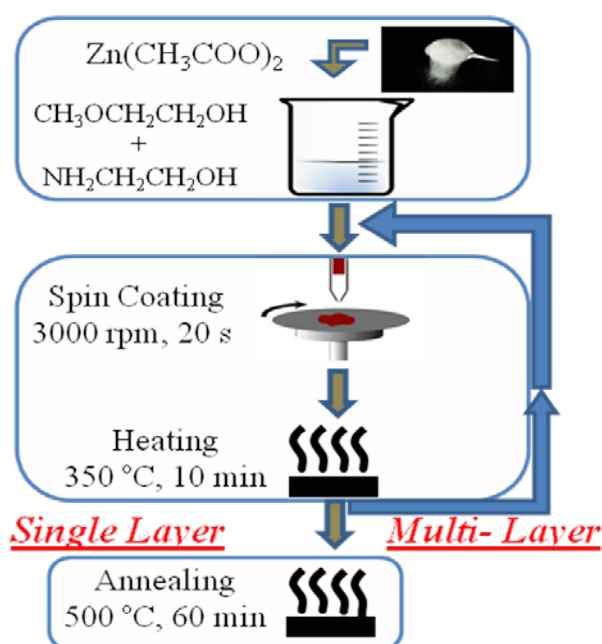


**Figure 2.8.** Schematic presentation of ZnO deposition on Si spikes.

### 2.2.3. Photocatalytic behavior of the developed surfaces

The photocatalytic activity of the samples was quantified by means of the decolorization of methylene blue (MB) in aqueous solution at an initial concentration of  $5.4 \times 10^{-7}$  mol/L (20 ppm), which is a typical potent cationic dye that has been widely used as a model organic probe to test the photocatalytic performance of photocatalysts.<sup>81,90,114,116,117</sup> The studied samples (both ZnO coated and bare Si spikes) were placed in a custom made quartz cell, and the whole setup was illuminated for up to 60 min using a UV lamp centered at 365 nm (Philips HPK 125 W) with a light intensity of  $\sim 10$  mW/cm<sup>2</sup>. The general set up is depicted in Figure 2.9.

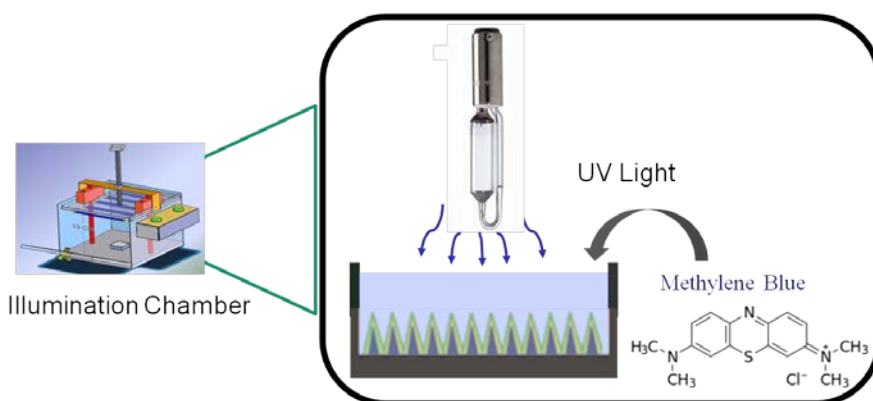


**Figure 2.9.** Custom made set up for the UV illumination of the studied samples.

The MB concentration was monitored during decolorization by UV-Vis spectroscopy in absorption mode, using a Perkin-Elmer (Lambda 950) spectrophotometer over the wavelength range of 250-1100 nm.

In addition, an apparent rate constant ( $k$ ) has been calculated as the basic kinetic parameter for the comparison of the photocatalytic activities. The rate constant  $k$  was obtained by fitting the concentration data to an equation  $\ln(C_t / C_0) = -k t$ , where  $k$  is apparent rate constant,  $C_t$  is the actual concentration at time  $t$  and  $C_0$  the initial concentration of MB. Since methylene blue has a strong absorption peak at  $\lambda_{\max} = 665$  nm, a series of MB aqueous solutions of

known concentration were prepared first in order to build a calibration curve. Photolysis experiments were also performed using bare Si substrates and bare Si spikes, under exactly the same conditions applied for the ZnO coated surfaces.<sup>90</sup>

### 2.3. Wettability of the prepared samples

Wettability tests were performed using a surface tensiometer (OCA-35, Dataphysics) utilizing the sessile drop method.<sup>118</sup> A drop of 5  $\mu\text{L}$  was deposited on the surface of each substrate after exposure to the UV lamp or heating at 200°C and the contact angle was measured in each case. Digital images of the water droplets were taken and the water contact angle was calculated by the Laplace-Young fitting.

## 2.4. Results and Discussion

### 2.4.1. Surface characterization

An AFM image of a 4 $\times$  layered ZnO film on a flat Si wafer is shown in Figure 2.10 a, with a scanned surface area of 1 $\times$ 1  $\mu\text{m}^2$ . The thickness of the film was  $\sim$ 80 nm estimated with the stylus profilometer. The determined rms roughness of the film is  $\sim$ 9.5 nm while the grain size is estimated as  $\sim$ 36.5  $\pm$  2 nm. Figure 2.10 b depicts a typical X-ray diffraction pattern of the ZnO thin films deposited on Silicon by the sol-gel/spin-coating technique after 4 spinning cycles and annealing at 500°C. XRD pattern reveals a strong (002) peak at a diffraction angle of  $2\theta = 34.42^\circ$  and two more at  $31.78^\circ$  and  $16.20^\circ$ , which correspond to the (100) and (101) planes, respectively, in good agreement with the JCPDS card (No. 36-1451) for a typical hexagonal wurtzite type ZnO crystal.<sup>64</sup> No other characteristic peaks corresponding to possible impurities, such as zinc nitrate or zinc hydroxide, are observed in the XRD patterns.

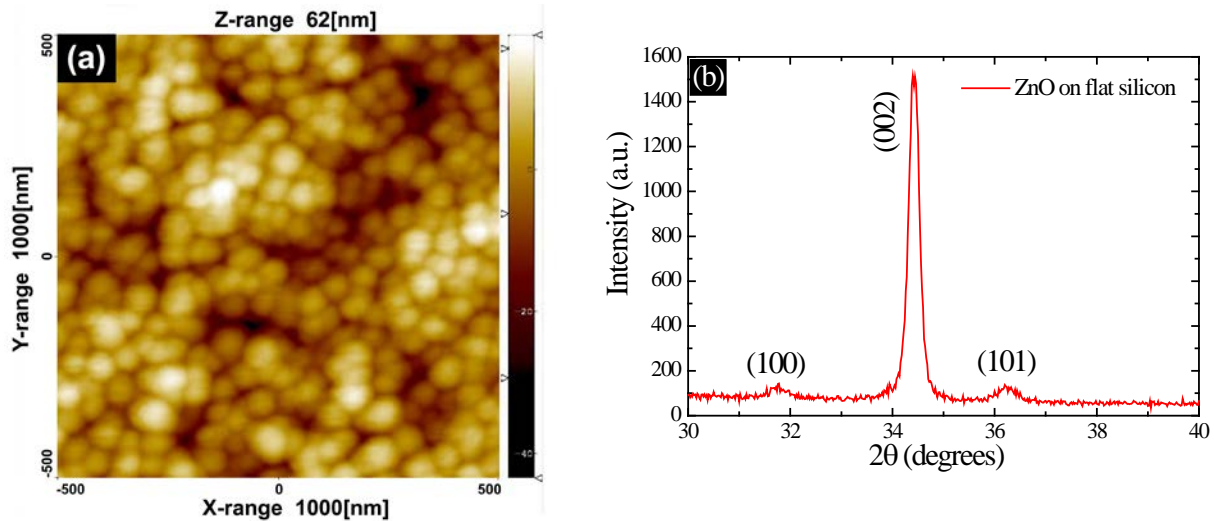


**Figure 2.10.** AFM image (scan size  $1\mu\text{m}\times 1\mu\text{m}$ ; z-range $\sim 62\text{nm}$ ), (a), and X-ray diffractogram, (b), of a  $\sim 80\text{nm}$  thick ZnO film on a flat Silicon substrate.

The fabrication of Si spikes with a ZnO coating was achieved following a two-step process: Si wafers were placed in a vacuum chamber under a pressure of  $10^{-2}$  mbar (which is drained with a reactive gas ( $\text{SF}_6$ ) atmosphere at a pressure of 500 Torr) and irradiated using a Yb:KGW laser with a repetition rate of 1 KHz and a pulse duration of 170 fs at a wavelength of 1026 nm, while the laser pulse fluence was maintained at  $0.65\text{ J/cm}^2$ . Afterwards, the samples were coated with ZnO, according to the procedure described in the experimental part. Figure 2.11 shows the SEM micrographs of the laser irradiated Si substrates before and after the ZnO coating. Careful examination of Figure 2.11 a and Figure 2.11 b makes clear that the ZnO coating did not affect the hierarchical micro- and nano-structure of the artificial surface; in both images, silicon spikes are clearly visible and distinct. This is reasonable since the roughness introduced by the ZnO layer is on the order of a few tens of nanometers while the spike dimensions are in the order of tens of microns (the peak of the spikes alone is close to  $1\mu\text{m}$  wide) and their nano-roughness is in order of 100nm. Therefore, the used quantity of ZnO is sufficient to create a very thin film on the surface of each spike but not in excess that would submerge them and make the roughness inefficient.

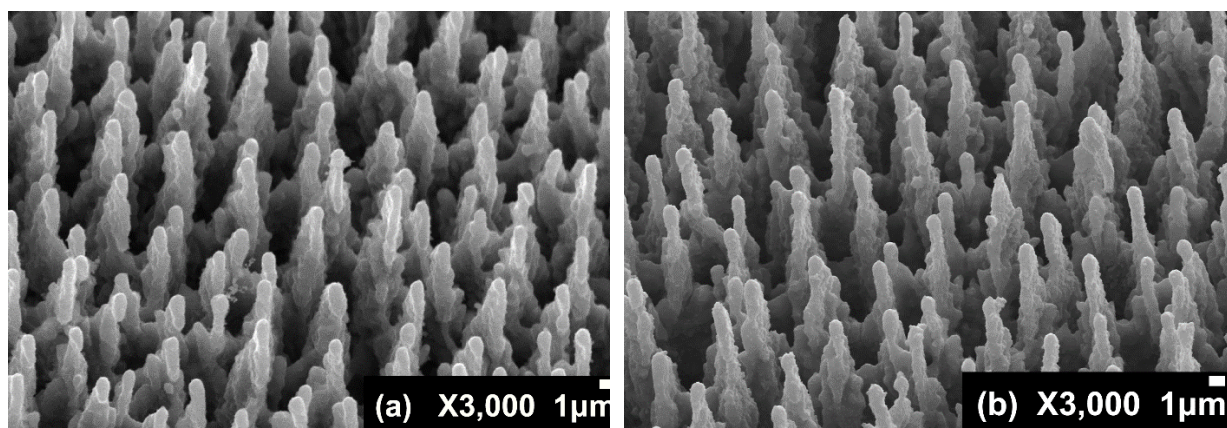


**Figure 2.11.** FE-SEM micrographs of bare Si spikes prepared by fs Laser irradiation on Silicon (a) and coated with ZnO by the sol-gel/spin-coating process (b).

In an attempt to correlate the structural and morphological properties of the ZnO coated samples with their photocatalytic activity, different structures of spikes were developed, by utilizing different laser conditions. Figure 2.12 shows the SEM micrographs of the laser irradiated Si substrates after ZnO coating. The parameters at which these surfaces, were developed, are shown in Table 2.4.

**Table 2.4.** Parameters of the fs laser used for the fabrication of ZnO coated Si spikes.

Sample	Power (mW)	Gas pressure (bar)	Irradiation step ( $\mu\text{m}$ )
A	10	0.65	16
B	50	No gas	16
C	50	0.65	16
D	100	0.65	16

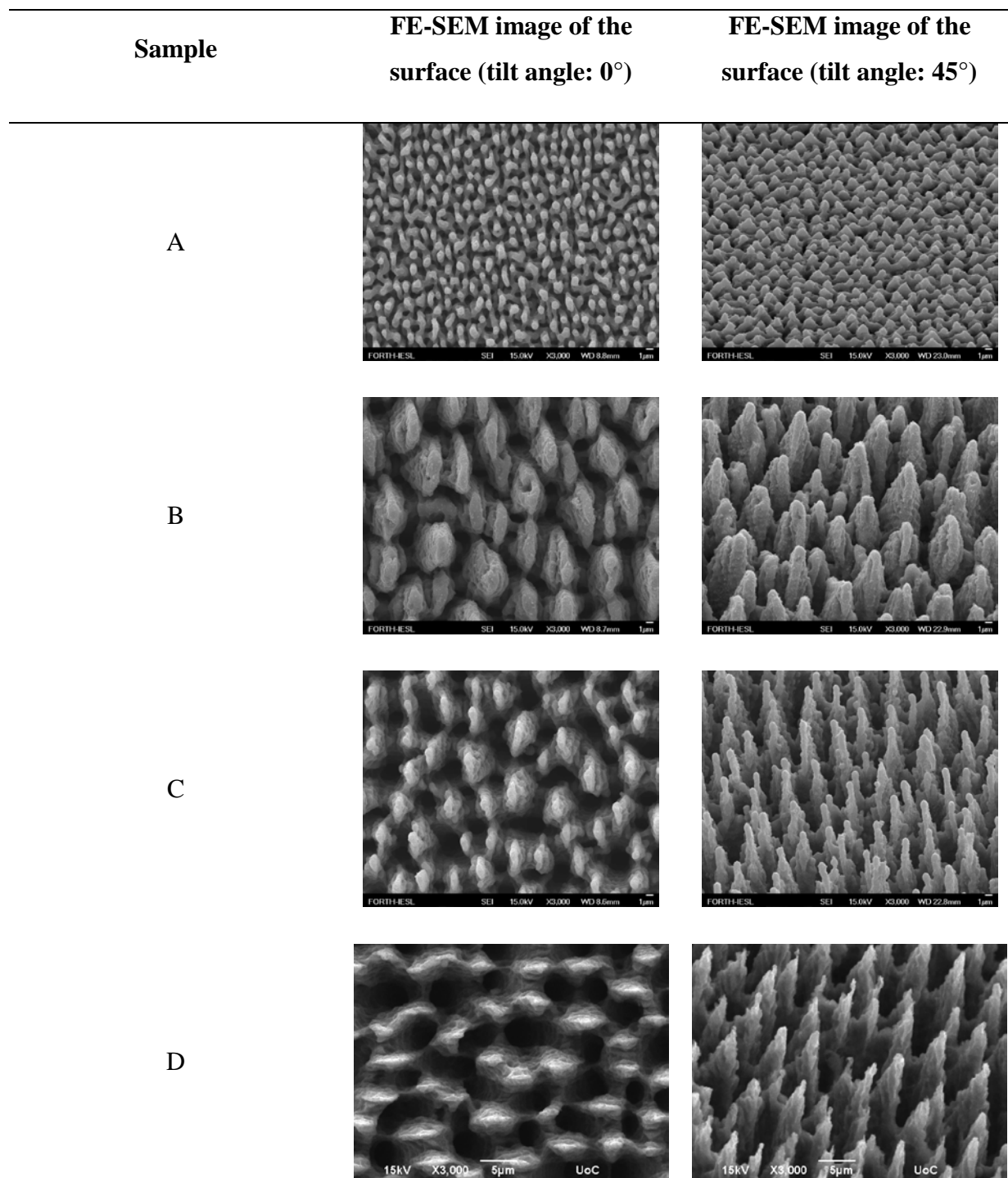


**Figure 2.12.** SEM micrographs of the Laser irradiated Si substrates after ZnO coating.

Comparing the SEM images of Figure 2.12, it can be observed that there are differences in the shape, size and density of the spikes. In sample A, the spikes are shorter but they are more close-packed. The sample B has taller spikes, but comparing to the C, they are wider and

bare, without the nano-roughness. This is due to the absence of the SF<sub>6</sub> gas. Comparing the samples C and D, it seems that in the latter case, the density of the spikes is lower and the spikes seem to have broader shape. All these parameters should influence both the photocatalytic activity and the wettability of the surfaces.

### 2.4.2. Photocatalytic activity

The photocatalytic mechanism of ZnO has been reported in previous works.<sup>31,64,115</sup> UV-Vis spectroscopy was utilized to evaluate the photocatalytic behavior of the rough surfaces with the ZnO film coating as well as of the various controls. A custom made cuvette was used that brought in contact the aqueous solution of methylene blue and the coated or non-coated surfaces during UV illumination. The absorbance as a function of wavelength for various UV illumination time intervals was monitored for each specimen; Figure 2.13 shows the absorption spectra for the specimen with the ZnO coating on top of the silicon spikes.

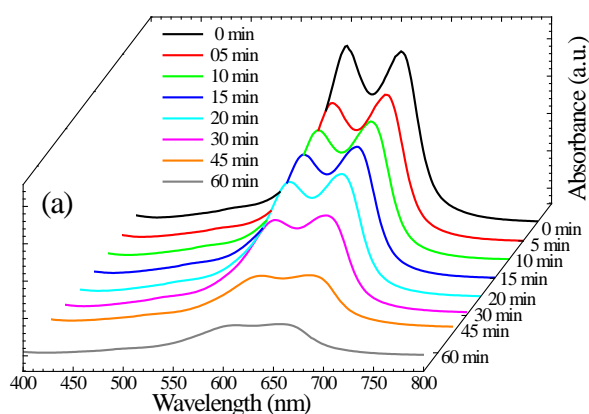


**Figure 2.13.** UV-Vis absorption spectra of aqueous solution of methylene blue in contact with a surface with a ZnO coating on top of silicon spikes following UV irradiation for various times.

The normalized integrated areas were calculated below such absorbance curves at the peak wavelength and the data are shown in Figure 2.14 as a function of the UV illumination time.

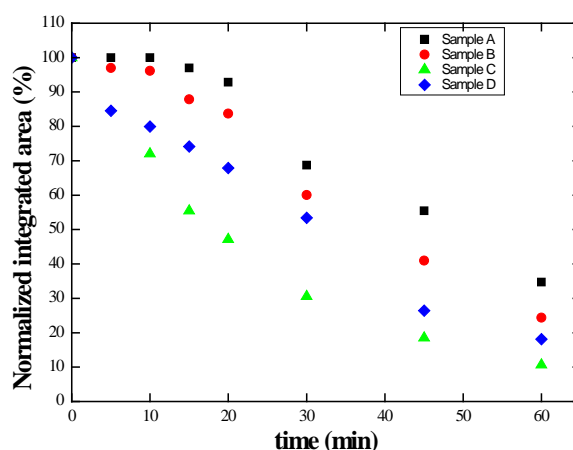


**Figure 2.14.** Normalized absorption of aqueous solutions of methylene blue at  $\lambda_{\max}=665\text{nm}$  under UV light irradiation, for Samples A, B, C and D.

Figure 2.14 shows that all the samples exhibit high photocatalytic activity with more than 60% of degradation of the organic dye. The highest decolorization of methylene blue was observed for the Sample C (more than 90% of methylene blue decolorization), which was attributed to the high surface to volume ratio.

In parallel, the photocatalytic behavior of flat Si substrates, both bare and with a ZnO coating, along with the hierarchical surfaces (silicon spikes) both bare and with a ZnO coating, were examined. The results are depicted in Figure 2.15.

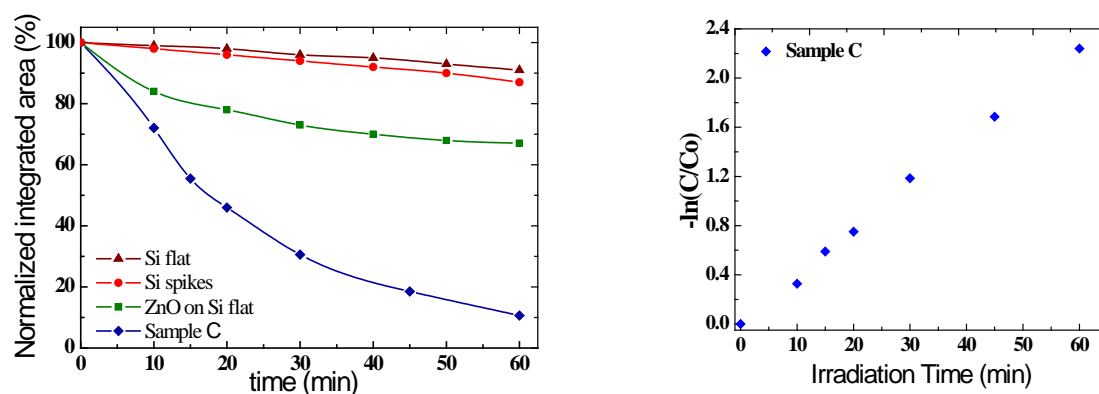
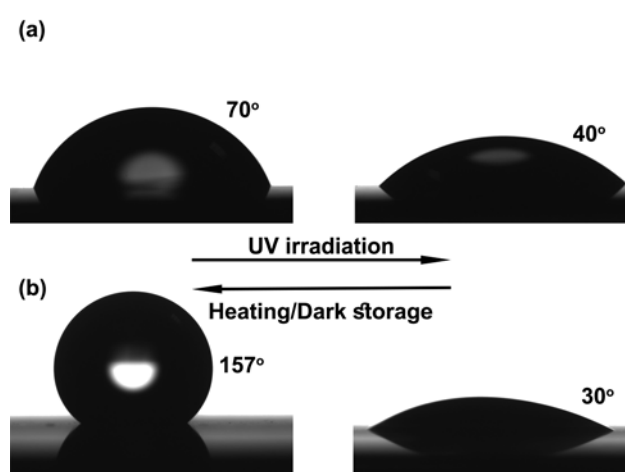


**Figure 2.15.** Normalized absorption of aqueous solutions of methylene blue at  $\lambda_{\max}=665\text{nm}$  under UV light irradiation for flat Si substrate (triangles), Si spikes (circles),  $4\times\text{ZnO}$  coating on flat silicon (squares) and  $4\times\text{ZnO}$  coating on silicon spikes (left) and plot of  $-\ln(C/C_0)$  vs irradiation time for photodegradation for Sample C (right).

The ZnO coated silicon spikes exhibit high photocatalytic activity when compared to a ZnO film on flat silicon. For the ZnO on the spikes, the degradation of MB reaches about 90% in only 60 min (even  $\sim 70\%$  degradation in only 30 min), while for a ZnO on flat silicon the degradation is only  $\sim 30\%$  after 60 min. This can be attributed to the high surface-to-volume-ratio of the ZnO coated on the silicon spikes, in agreement with research results reported in the literature.<sup>64,116,119</sup> The integrated area is proportional to the MB concentration; thus, analysis of the data of Figure 2.15 with the equation  $\ln(I_t/I_0) = \ln(C_t/C_0) = -k t$  (see Experimental section) can be used to extract an apparent rate constant. The data in Figure 2.15 (especially for the ZnO film on silicon spikes) give a good linear fit, thus confirming that the photodegradation of MB over the studied photocatalysts follows first-order kinetics. The calculated apparent rate constant for the ZnO coated silicon spikes was  $0.016\text{ min}^{-1}$ , which is close to the values recorded in the literature.<sup>51,81</sup> Reference samples (flat Si substrate and Si spikes) without ZnO coatings were also characterized in terms of MB decolorization by means of UV-Vis absorption and showed that their photocatalytic activity was negligible.

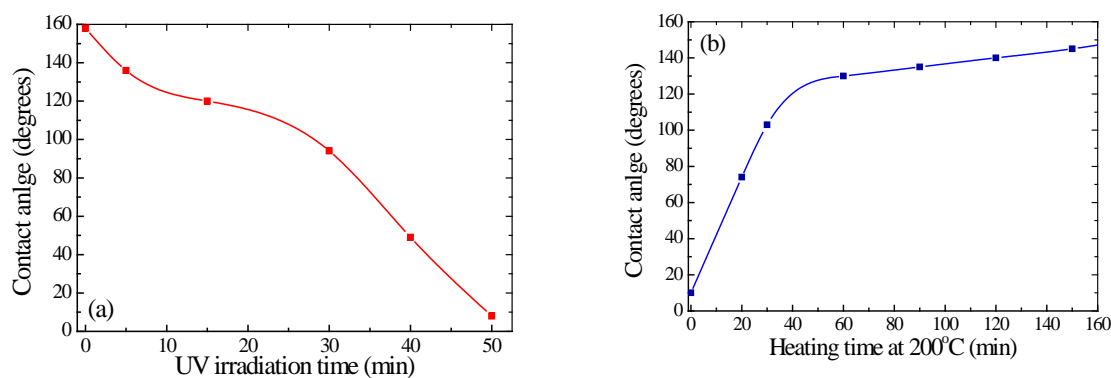
### 2.4.3. Wettability

Figure 2.16 shows representative water drop images for the specimen with a ZnO coating onto a flat silicon surface (Fig. 16 a) and onto Sample C, micro/nano-structured surface of silicon spikes, (Fig. 16 b) following a cycle of UV irradiation and of subsequent heating. It can be clearly seen that, as the samples are exposed to UV illumination, they both become hydrophilic, while when the same samples are heated at 200°C for 3h, an increase in their contact angle is recorded. It should be noted that the hydrophobic behavior of the specimens can also be achieved by storing them in dark, although this process requires time of the order of days.<sup>29,30</sup> The contact angle of water on the ZnO coated flat silicon surfaces is measured at ~70° after heating while that on the ZnO coated silicon spikes give values of ~157°, illustrating super-hydrophobic behavior. The difference in the contact angle measurements between these two ZnO surfaces is due to the enhanced hierarchical roughness in the latter case.



**Figure 2.16.** Photographs of representative water drops and the respective equilibrium contact angles on specimens with (a) ZnO coating onto a flat Si substrate and (b) ZnO coating onto a surface with silicon spikes. Drops are shown for the specimens following UV irradiation (on the right) and after thermal treatment at 200°C (on the left).

Figure 2.17 shows the water contact angles as a function of time of UV illumination (Fig. 2.17 a) and heating (Fig. 2.17 b), respectively, for a specimen with a ZnO coating onto a micro/nano-structured surface of silicon spikes. When the surface is illuminated with UV lamp (centered at 365 nm with a light intensity of  $\sim 10 \text{ mW} / \text{cm}^2$ ), the contact angle decreases slowly with time, until it reaches the superhydrophilic regime after about 50 min. On the other hand, when the same surface is heated at  $200^\circ\text{C}$ , an apparently two-stage process is observed. The contact angle increases at a faster rate for early times reaching  $\sim 120^\circ$  after  $\sim 50$  minutes whereas it, then, increases with a slower rate until it reaches a superhydrophobic state after  $\sim 160$  min of exposure to heat. Other temperatures were also tested. Lower temperatures caused a rapid decrease in efficiency while higher temperatures did not make the process much faster or more efficient. This makes the whole process affordable in energy cost and convenient since it does not require any sophisticated equipment for heating.



**Figure 2.17.** Dependence of the water contact angle on a surface with a ZnO coating on top of the silicon spikes following (a) UV irradiation and (b) heating at  $200^\circ\text{C}$  for various times.

#### 2.4.4. Stability test

In order to study the reproducibility and the stability of the system, specimens have been subjected to at least five cycles of UV irradiation and thermal heating and their wettability is investigated (Figure 2.18). The water contact angle data are shown for the specimens with a

ZnO coating onto a surface with silicon spikes and the one with a ZnO coating onto a flat silicon substrate for five cycles of UV illumination and heating. A responsive behavior is observed for the case of the ZnO coated flat specimen with contact angle values fluctuating within a narrow region between 40° and 70°. On the contrary, the ZnO coated hierarchically roughened specimen exhibits a very wide range in responsiveness ranging from around 20° to a region very close to 150°. Both reversibility and reproducibility prove the efficiency and endurance of the surfaces, which is very important for practical applications.

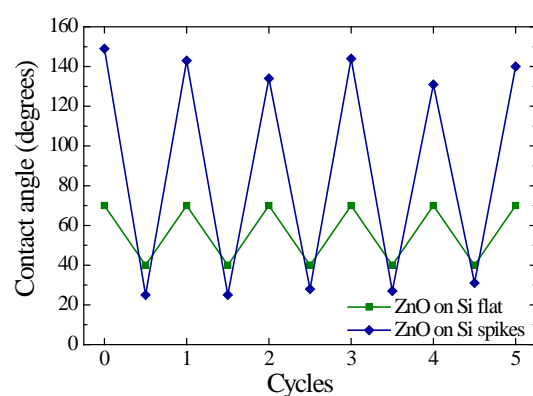


**Figure 2.18.** Average contact angle values of water droplets situated on specimens with ZnO coating onto a flat Si substrate (squares) and ZnO coating onto a surface with silicon spikes (diamonds) for five irradiation cycles of UV irradiation (UV lamp centered at 365 nm with a light intensity of  $\sim 10 \text{ mW} / \text{cm}^2$ ) for 50 min and 3h thermal heating at 200°C.

It has been reported that there is a possibility for photocorrosion under UV irradiation of the ZnO catalyst;<sup>115</sup> this is more prone to happen for ultrathin (20-70 nm) films of ZnO. Thus, we have performed tests of the present system for the stability and reproducibility of the photocatalytic behavior. For that, cycles of both wettability and photocatalysis measurements were performed and the performance is illustrated in Table 2.5.

**Table 2.5.** Repeatability of the specimen performance.

	Wettability		Photocatalysis		
	After heating in 200°C	After UV irradiation	% Degradation of methylene blue		Reaction constant (k)
			After 20min irradiation	After 60min irradiation	
1 <sup>st</sup> cycle	157°	10°	22	86	0.016 s <sup>-1</sup>
2 <sup>nd</sup> cycle	151°	20°	21	84	0.016 s <sup>-1</sup>

According to the results the surface maintains the reversible wettability behavior after photocatalysis as well as its superhydrophobic features. Furthermore, the second cycle of photocatalysis proved to be as efficient as the first one, without any reduction of the reaction rate constant. Therefore, the system maintained its efficiency after repeated wettability-photocatalysis cycles proving its reproducibility and stability. Such a bi-responsive structure could be the basis for a variety of applications in the future.

## 2.5. Conclusions

A multi-functional surface with a ZnO coating deposited onto a hierarchically roughened surface has been fabricated with a two-step process. The wettability and the photocatalytic activity of the surfaces have been investigated in detail as a function of time. High photocatalytic activity is achieved with a ~90% decolorization of a model dye in ~60 min. The systems exhibit a reversible wettability behavior from superhydrophilic (upon UV irradiation) to superhydrophobic (upon heating). The stability of the behavior is investigated extensively and the system proves to be quite stable. To the best of our knowledge, this is the first work on the development of surfaces with both high photocatalytic activity and reversible wettability behavior from superhydrophobic to superhydrophilic. The combination

of photocatalysis with reversible wettability with a single coating makes the system appropriate for a variety of applications, such as self-cleaning surfaces, air purification, marine coatings or fog-proofing.

## **B) Development of polymer brush ZnO nanowires exhibiting high photocatalytic behavior**

### **2.6. Introduction**

In this work, ZnO nanowires with enhanced stability and high photocatalytic behavior were developed using polymeric stabilizers. First, ZnO nanowires were grown on ZnO pre-coated glass substrates via aqueous solution growth.<sup>64</sup> Afterwards, the samples were coated with polymers with the spin coating method. Poly(methyl methacrylate), PMMA and Poly(2-vinyl pyridine), P2VP were utilized for this purpose. Samples were characterized with Scanning Electron Microscopy and were tested for their photocatalytic behavior using Fourier Transform Infrared Spectroscopy (FTIR). Stearic acid was utilized as a test organic pollutant. Samples were also tested for their wettability. In parallel, ZnO nanowires were coated with dichlorodimethylsilane for comparison.

### **2.7. Experimental Part**

#### **2.7.1. Deposition of ZnO seed layers and nanowires**

The development of ZnO nanowires consisted of two steps. Initially ZnO seed layers were prepared by a sol-gel / spin coating method on glass substrates (Corning Eagle 2000

Borosilicate Glass, Specialty Glass Products). Prior to ZnO deposition, all substrates used were cleaned using a Piranha solution ( $\text{H}_2\text{SO}_4/\text{H}_2\text{O}_2$ : 3/1), rinsed with MilliQ water and dried under  $\text{N}_2$  gas flow. Initially, Zinc acetate dihydrate [ $(\text{Zn}(\text{CH}_2\text{COO})_2 \cdot 2\text{H}_2\text{O})$ , Sigma-Aldrich, 99.99%] was dissolved in 2-methoxy ethanol [ $(\text{CH}_3\text{OCH}_2\text{CH}_2\text{OH})$ , Sigma-Aldrich,  $\geq 99.55\%$ ] at a concentration of 0.75 mol/L. Monoethanolamine [ $(\text{HOCH}_2\text{CH}_2\text{NH}_2)$ , Sigma-Aldrich,  $\geq 99.0\%$ ] was also added as a stabilizer and the molar ratio of zinc acetate to ethanolamine was kept at 1:1. The resultant solution was stirred for 1 h at  $60^\circ\text{C}$  to yield a homogeneous, clear, and transparent solution using a magnetic stirrer. The resultant solution was stirred for 1h at  $60^\circ\text{C}$  in order to become homogeneous. Subsequently, 30  $\mu\text{L}$  of the solution were dropped on the glass substrates, which were rotated at 3000 rpm for 20 sec. After coating, the samples were heated at  $350^\circ\text{C}$  for 10min to evaporate the solvent and remove any organic residuals. This procedure was repeated for four (4 $\times$ ) times.<sup>51,53,64,90,120,121</sup> The films were then annealed in air at  $500^\circ\text{C}$  for 60min.

Afterwards, ZnO nanowires were grown on Corning glass substrates from an equimolar (0.01M) aqueous solution of zinc nitrate hexahydrate ( $\text{Zn}(\text{NO}_3)_2 \cdot 6\text{H}_2\text{O}$ ) and methanamine ( $\text{C}_6\text{H}_{12}\text{N}_4$ ). For this purpose, laboratory Pyrex glass bottles with polypropylene autoclavable screw caps were filled with the above solution. Then, the glass substrates, coated with ZnO seed layers, were placed in the bottles facing downwards and heated at a constant temperature of  $95^\circ\text{C}$  for 2h in a regular laboratory oven (EV 018 Vacuum Oven, NÜVE). Finally, the samples were dipped into MilliQ (18.2  $\text{M}\Omega\cdot\text{cm}$ ) water to eliminate residual salts or amino complexes, and dried in air at the same temperature.<sup>120-122</sup>

### 2.7.2. Deposition of polymer films on ZnO nanorods

As already stated the main drawback of the ZnO nanorods is their instability, which limits their practical applications. In order to protect them, ZnO nanowires were covered with a thin

polymer film. Specifically, carboxy terminated PMMA (Polymer Source,  $M_n = 31000 \text{ g}\cdot\text{mol}^{-1}$ ) and carboxy terminated P2VP (Polymer Source,  $M_n = 53000 \text{ g}\cdot\text{mol}^{-1}$ ) were utilized.

Initially, glass substrates with ZnO nanowires were exposed to UV irradiation in order to become hydrophilic. Afterwards, the samples were covered with either PMMA or P2VP with the spin coating method. Spin coating is a procedure used to deposit homogeneous thin films to substrates. A small amount of coating material is applied on the center of the sample, which is being rotated at low or high speed.<sup>123</sup> Polymer films were spun from chloroform or toluene solutions (0.01 wt % and 0.001 wt %, respectively) onto 1-cm diameter glass substrates, deposited with ZnO nanowires. In order to optimize the system, samples were prepared with different quantities of polymer drop; 10, 20, 30, 50 and 70  $\mu\text{L}$ . Spinning speeds ranged from 500 to 3000 rpm. Acceleration times were less than 2 s and total spin times were 20 s.

Then, the samples were annealed at average sample temperatures, above the glass transition temperature in the laboratory oven under vacuum, in order for the carboxy end-groups to find the ZnO surface and react with the  $-\text{OH}$  groups forming end-anchored polymer chains. The effect of heating time was also studied from 4 to 12h. Finally, the samples were dipped into chloroform to remove the un-grafted polymer.

### 2.7.3. Silane-modified ZnO nanorods

Alternatively, the surfaces with the ZnO nanostructures were silanized with dichlorodimethylsilane ( $(\text{CH}_3)_2\text{SiCl}_2$ , DMDCS, Sigma-Aldrich) which can assemble into high quality coatings, resulting in a material with a low surface energy. The silanized samples exhibit hydrophobic properties, which can be maintained for long periods of time over a wide temperature range.<sup>3,124</sup>

The samples were deposited in a custom designed holder, which was then placed in laboratory Pyrex glass bottles, containing 0.5 mL of the silane. The sample was facing downwards without being in contact with the silane reagent. The vapor-phase reaction was carried out for approximately 18h at room temperature. The silanized samples were dipped into toluene (two aliquots), water (two aliquots), ethanol (two aliquots), and then water (three aliquots) and were then dried in a clean oven at 120°C for about 45min.<sup>3,125</sup>

#### 2.7.4. Photocatalytic behavior of the developed surfaces

For all photocatalytic performance measurements, stearic acid was used as the organic material. It has been suggested that stearic acid is an appropriate model pollutant for the organic solid films that deposit on (exterior) window glass surfaces.<sup>120</sup>

The samples were spin coated using a droplet of 30  $\mu\text{L}$  of a 0.1M stearic acid solution in chloroform, for 30 s with a rotation speed of 500 rpm. The surfaces were illuminated in a box reactor with a UV lamp, centered at 365nm (Philips HPK 125W, 10mW/cm<sup>2</sup>) at certain time intervals. The degradation of the stearic acid was calculated by Fourier Transform Infrared Spectroscopy (FT-IR, IRPrestige-21, Shimadzu) through the monitoring of the asymmetric C–H stretching mode of the CH<sub>3</sub> group at 2958cm<sup>-1</sup> and the asymmetric and symmetric C–H stretching modes of the CH<sub>2</sub> group at 2923cm<sup>-1</sup> and 2853cm<sup>-1</sup>, respectively. The integrated area of the C–H stretching peaks (2800–3000cm<sup>-1</sup>) measured at each irradiation time interval was normalized to the initial integrated area (prior to the irradiation) in order to calculate the percentage of stearic acid remaining as a function of irradiation time. The decomposition of stearic acid (mol/min) and the formal quantum efficiency (FQE) for all samples were calculated according to the methodology of Mills and Wang.<sup>51,53,81,99,120</sup>

The photocatalytic activity experiments on the samples for the degradation of stearic acid, were performed at ambient temperature. Blank experiments (photolysis) were also performed using bare substrates under exactly the same conditions as used for the ZnO samples.

### 2.7.5. Wettability of the prepared samples

Wettability tests were performed using a surface tensiometer (OCA-35, Dataphysics) utilizing the sessile drop method.<sup>118</sup> A drop of 5  $\mu\text{L}$  was deposited on the surface of each substrate and the contact angle was measured in each case. Contact angle was measured before and after immersing in different pH solutions and subsequently drying in the case of P2VP coated ZnO nanowires, before and after silanization of the ZnO nanostructures. Digital images of the water droplets were taken and the water contact angle was calculated by Laplace-Young Fitting.

## 2.8. Results and Discussion

### 2.8.1. Surface characterization

The surface morphology was studied by means of a field emission scanning electron microscope (FE-SEM, JEOL JSM-7000F). Figure 2.19 illustrates SEM images of ZnO nanowires deposited on Corning glass substrates, pre-coated with 4 $\times$  ZnO seed layer, for 2h. As it can be observed, the substrates were covered with quite dense and uniform ZnO nanostructures. The ZnO nanorods are growing perpendicular to the surface with a very good alignment. This has been attributed to the polar nature of the ZnO surface and the matching lattice structure.<sup>64,99,126</sup> The detailed surface characterization of the bare ZnO nanowires, developed with aqueous solution growth procedure, has been reported in previous works.<sup>31,99,120,121</sup>

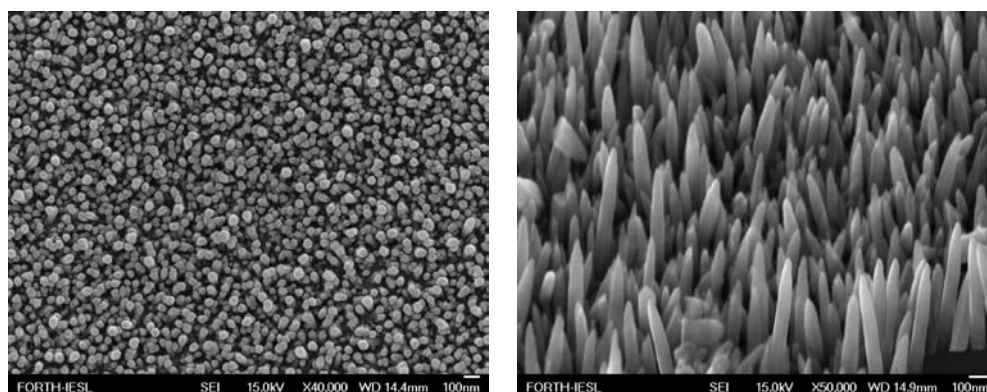


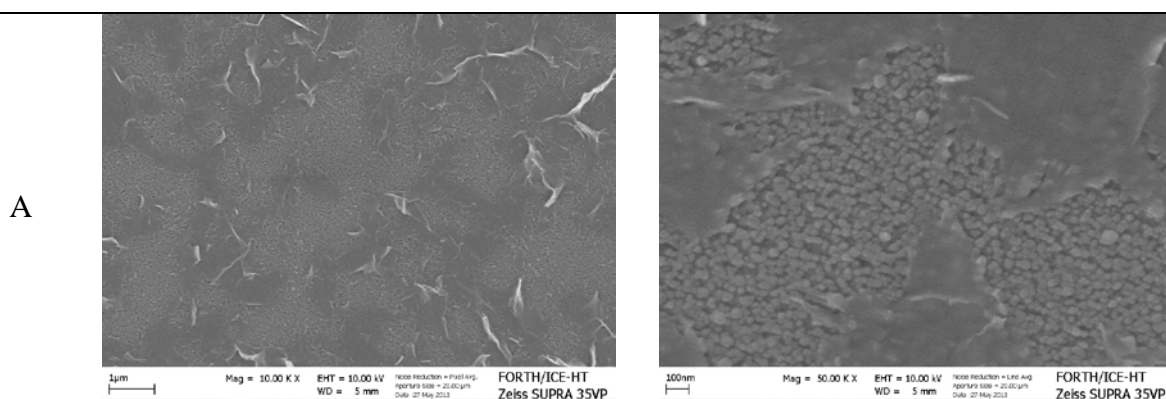
**Figure 2.19.** FE-SEM micrographs of ZnO nanowires grown on Corning glasses, top view (left) and side view (right).

As it has been noted in the introduction, the main drawback of these structures is the lack of stability. Thus, in this work, the ZnO nanowires were initially covered with Poly(methyl methacrylate), PMMA brushes, as a way to protect them and to enhance their robustness. The high photocatalytic activity of the ZnO nanowires has been attributed to their particularly high surface-to-volume ratio. As a result, the thickness of the polymer film should not affect the roughness of the ZnO nanostructures. For this purpose, the effect of polymer concentration, the heating temperature and the time of annealing were studied. PMMA films were spun from toluene solution (0.01 wt % and 0.001 wt %, respectively) onto 1-cm diameter glass substrates, containing the ZnO nanowires. 30  $\mu\text{L}$  of the above solutions, were dropped in the glass substrate, containing the ZnO nanowires, and the sample was spin coated for 20s with a rotation speed of 3000 rpm. Samples prepared are summarized in Table 2.6.

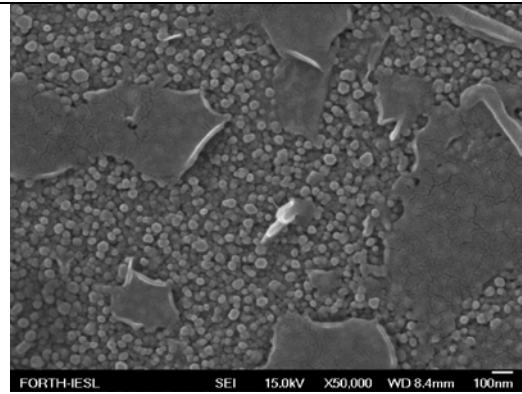
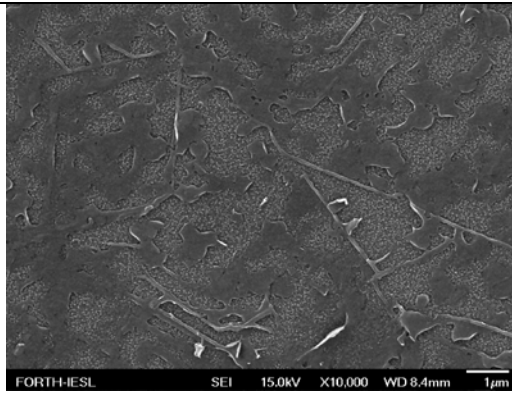
**Table 2.6.** Parameters of the PMMA film coating on ZnO nanowires.

Sample	PMMA in toluene (wt %)	Annealing temperature (°C) under vacuum	Annealing time (h)
A	0.01	130	4
B	0.01	130	12
C	0.01	180	4
D	0.01	180	12
E	0.001	130	4
F	0.001	130	12
G	0.001	180	4
H	0.001	180	12

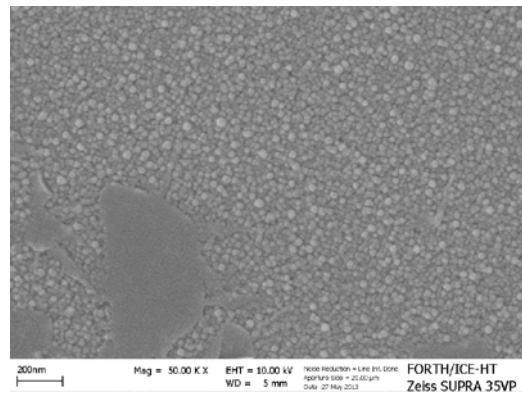
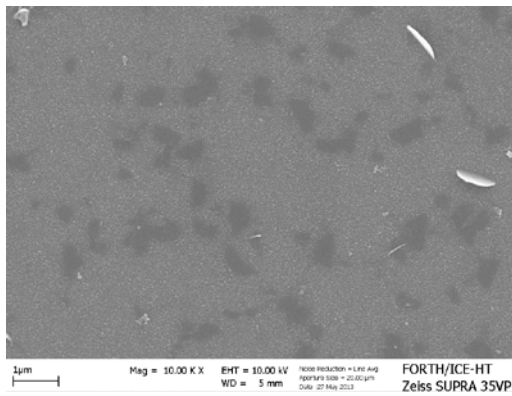
The surface characterization of the samples described above, was performed with scanning electron microscope. The FE-SEM images of the samples in different magnifications are depicted in Figure 2.20.

**Sample**      **FE-SEM micrographs of ZnO nanowires coated with PMMA film**

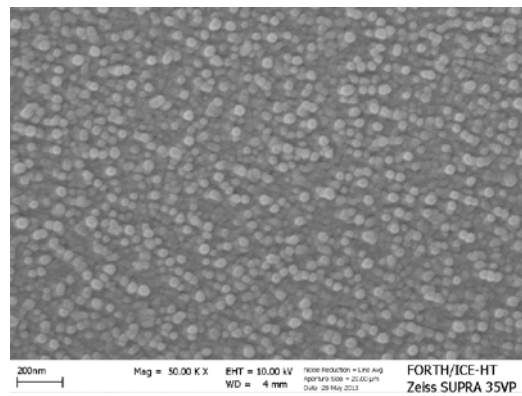
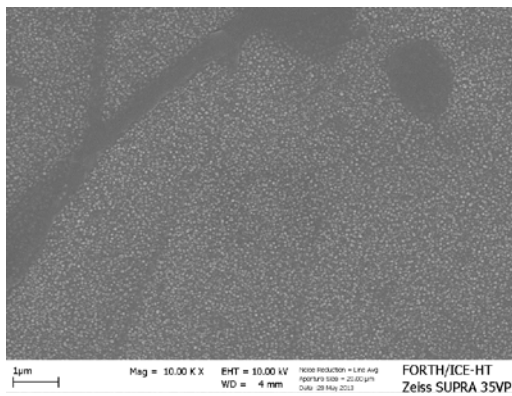
B



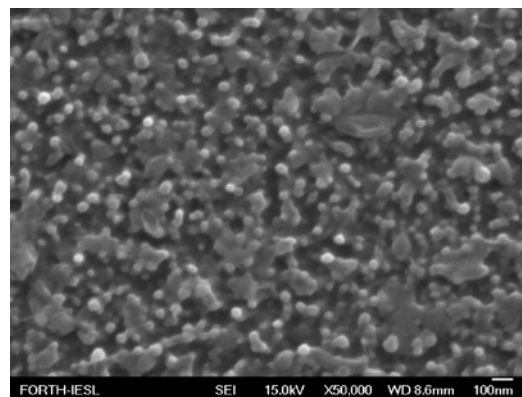
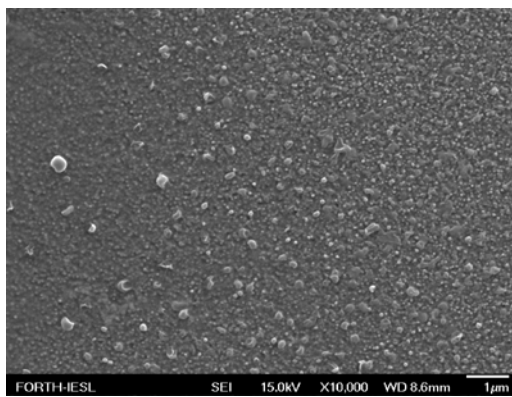
C



D



E



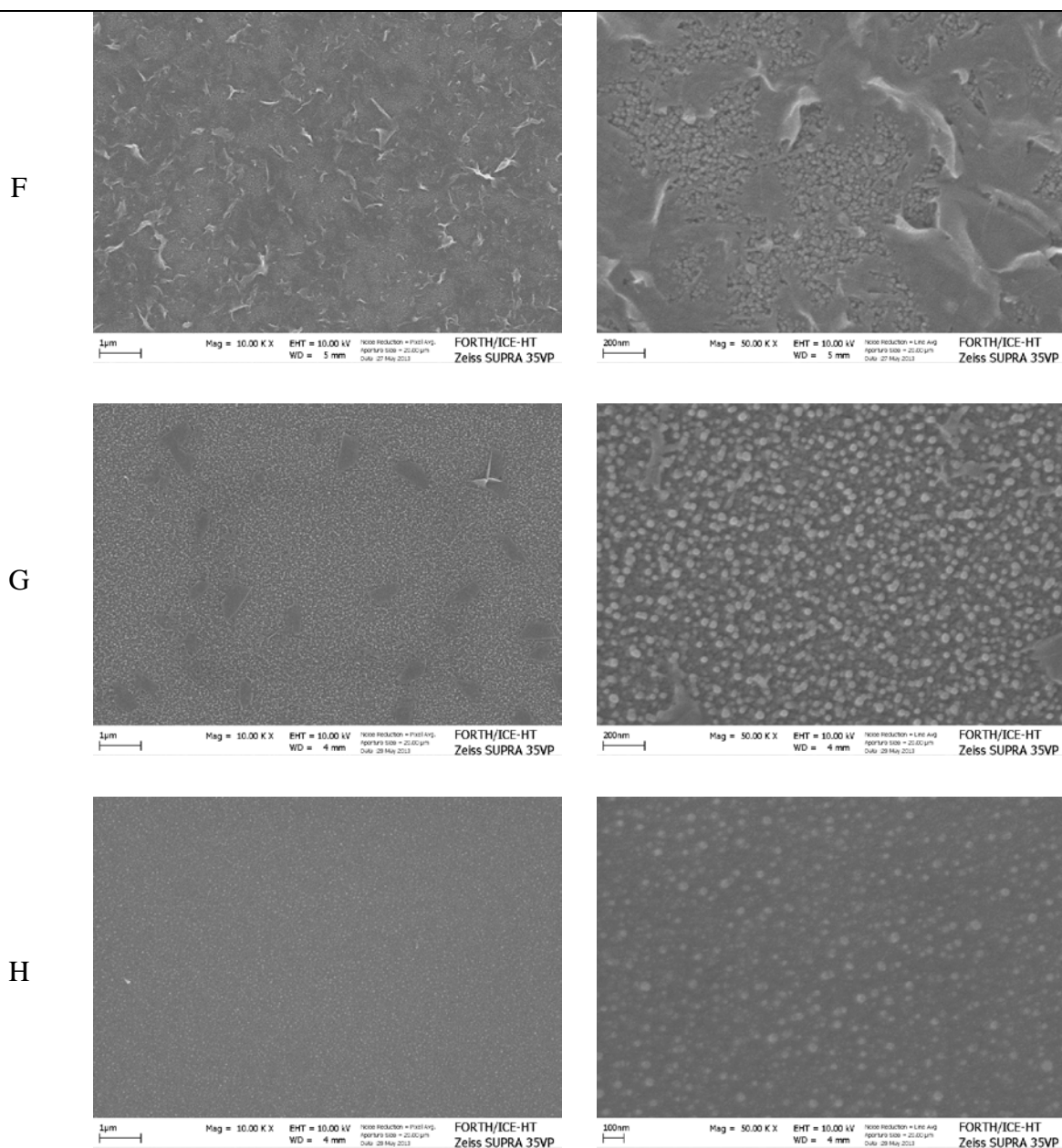


**Figure 2.20.** FE-SEM micrographs of ZnO nanowires coated with PMMA film.

Comparing samples A-D with E-H, one cannot really observe any specific difference due to the concentration of the polymer solution. However, there is a noticeable change upon increasing the annealing temperature from 130°C to 180°C. By comparing samples A with C, B with D, E with G and F with H, it can be concluded that at higher temperatures, the samples are more homogeneous. The polymer chains have penetrated the ZnO nanorods and

there are less chains on the tip of them. This happens because, through thermal annealing the chain mobility increases, allowing movement for the chains to orient in such a way for the maximum amount of contact with the surface. In the case that the heating time is examined, it can be observed by comparing the samples C and D or G and H, that by increasing the heating time a more uniform polymer film is developed. With longer periods of annealing time the polymer chains are able to move around and bind to the surface; however, at shorter time periods the chains don't have enough time to attach to the maximum amount of locations. Based on these results it can be concluded that annealing at higher temperatures for longer annealing times will let the PMMA film have the best chance of binding to the surface, since there will be better chain mobility at longer periods of time allowing optimum chain movement.

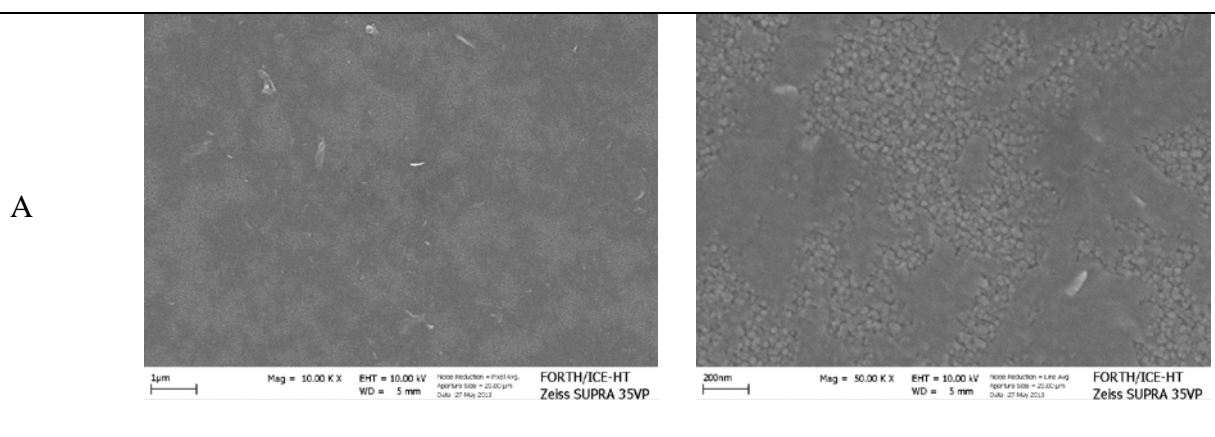
Taking into account the above observations, it can be concluded that at higher concentrations, lower temperatures and shorter time periods, the polymer film is too thick and the ZnO nanostructures have been covered. However, at lower concentrations and longer time periods (samples G and H), polymer brushes are formed and the thin film that does not affect the features of the ZnO nanostructures.

In parallel, carboxy-terminated P2VP was grafted to the ZnO nanorods. In order to optimize the grafting procedure, for the reasons mentioned before, the effect of polymer solution, annealing time and annealing temperature were studied in this case as well. P2VP films were spin coated from toluene solution (0.01 wt % and 0.001 wt %) onto 1-cm-diameter glass substrates, contained the ZnO nanowires. 30  $\mu\text{L}$  of the above solutions, were dropped in the glass substrate, containing the ZnO nanowires, and the sample was spin coated for 20 s with a rotation speed of 3000 rpm. Samples prepared are summarized in Table 2.7.

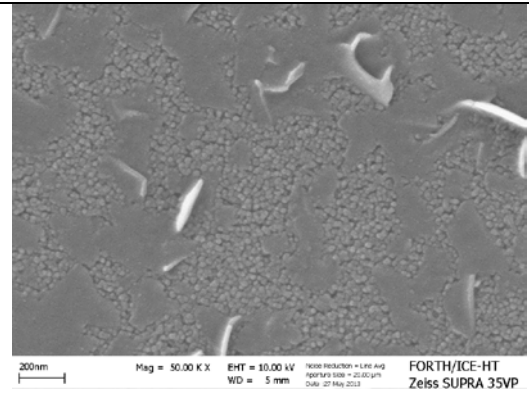
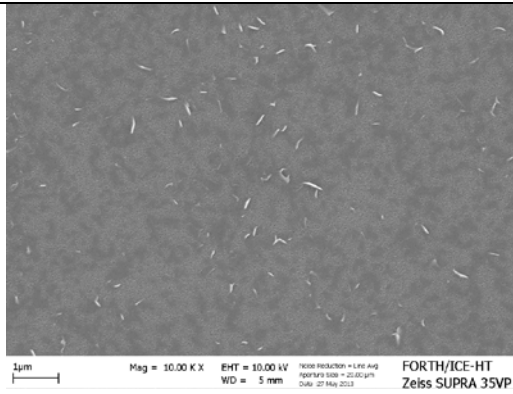
**Table 2.7.** Parameters of the P2VP film coating on ZnO nanowires.

Sample	P2VP in chloroform (wt %)	Annealing temperature (°C) under vacuum	Annealing time (h)
A	0.01	130	4
B	0.01	130	12
C	0.01	180	4
D	0.01	180	12
E	0.001	130	4
F	0.001	130	12
G	0.001	180	4
H	0.001	180	12

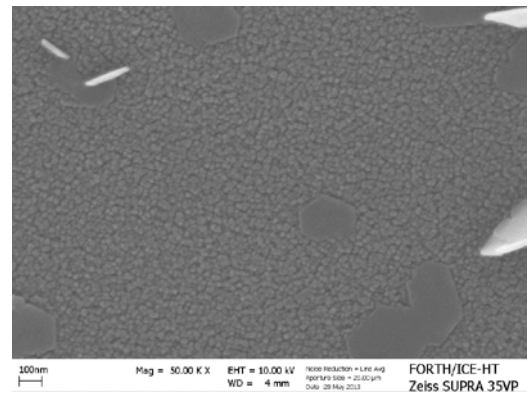
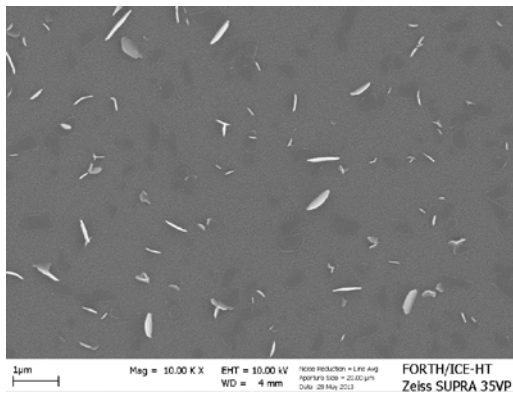
The surface characterization of the samples described above, was performed with scanning electron microscope. The FE-SEM images of the samples in different magnifications are depicted in Figure 2.21.

**Sample FE-SEM micrographs of ZnO nanowires coated with P2VP film**

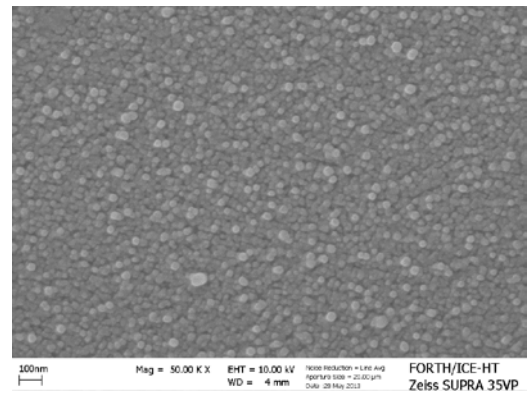
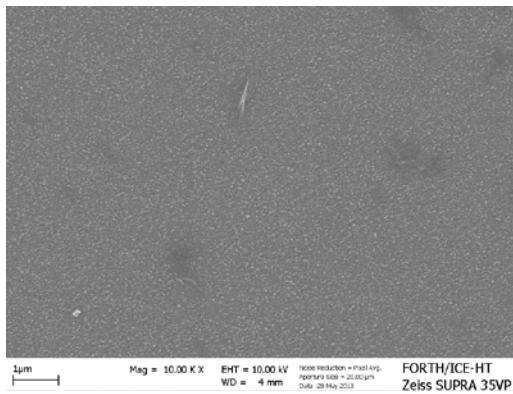
B



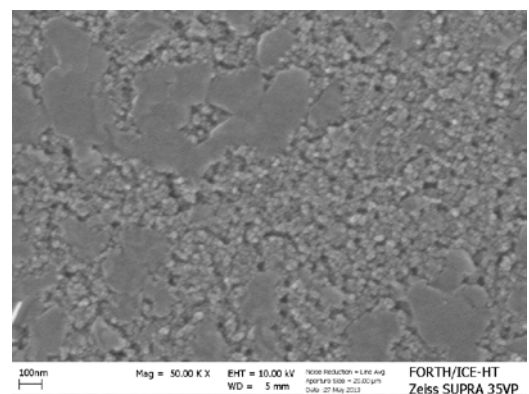
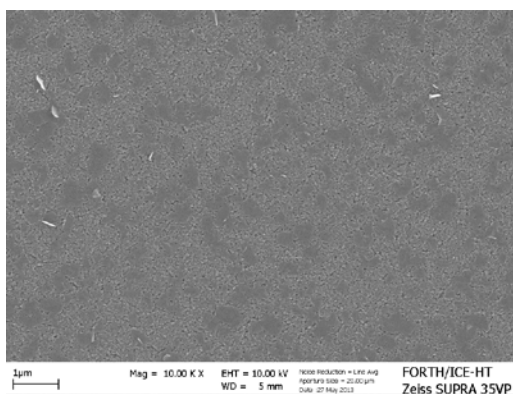
C



D



E



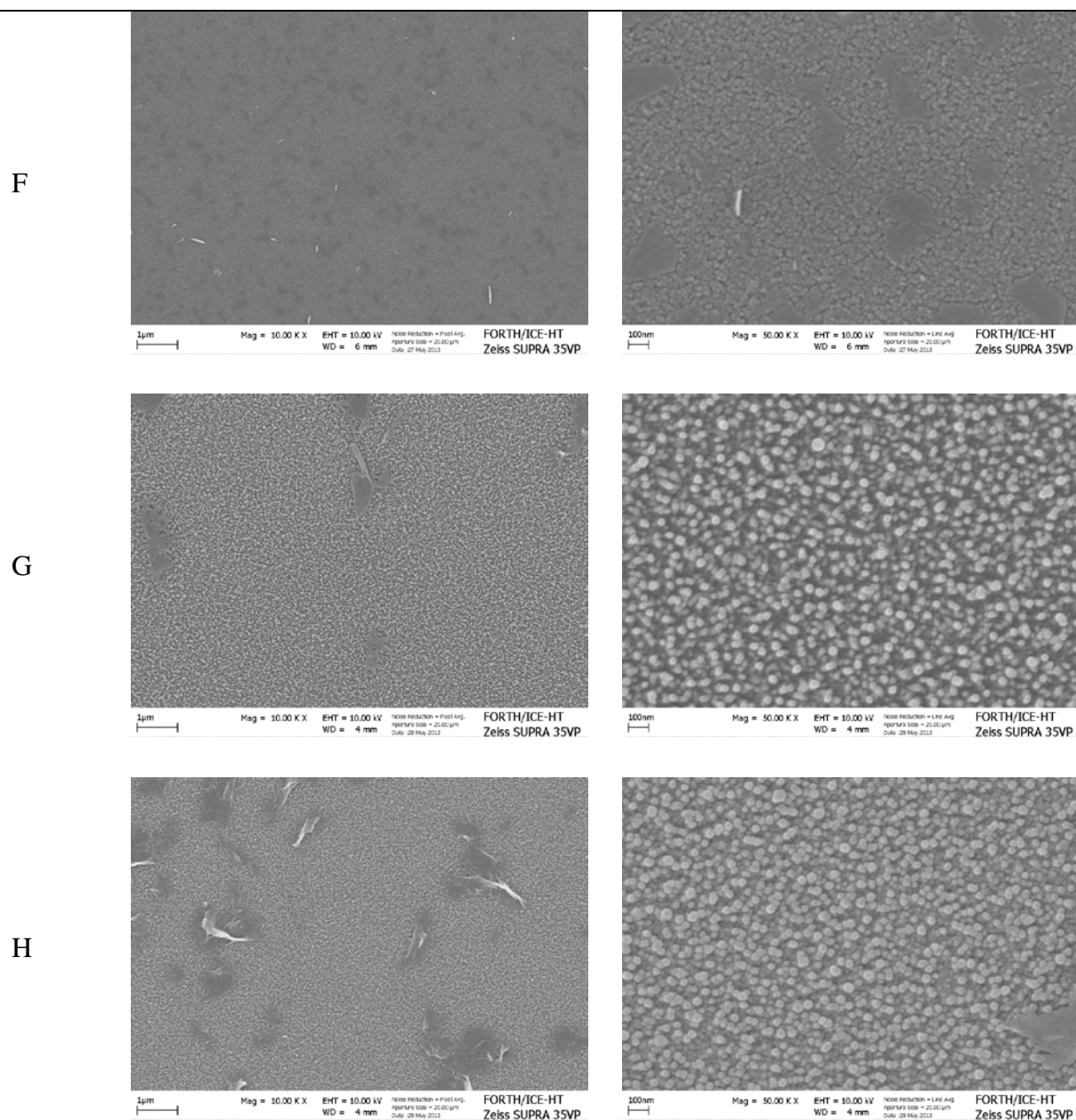


**Figure 2.21.** FE-SEM micrographs of ZnO nanowires coated with P2VP film.

According to the above images, P2VP grafted ZnO nanowires did not present obvious differences, referring to the concentration of the polymer solution. This is not the same by increasing the annealing temperature from 130°C to 180°C. By comparing the samples A with C, B with D, E with G and F with H, it can be concluded that in higher temperatures, the samples are more uniform. Upon thermal annealing the polymer chains gained mobility to

move between nanostructures. Not only the annealing temperature, but also the annealing time of the polymer chains, can lead to better distribution of polymer chains. By comparing the samples C and D or G and H, it can be noticed, that by increasing the heating time a more uniform polymer film is developed. Based on these results, it can be concluded, that both heating temperature and heating time, affect the grafting of the P2VP film.

Specifically, it can be concluded that at higher concentrations, lower temperatures and shorter time periods, the polymer film is too thick and the ZnO nanostructures have been covered. However, at lower concentrations and longer time periods (samples G and H), polymer brushes are formed and the thin film that does not affect the features of the ZnO nanostructures.

For the photocatalytic measurements, the samples, before and after the polymer grafting, were covered with stearic acid. Figure 2.22 depicts the FE-SEM images of the ZnO nanorods, with P2VP (sample G), covered with stearic acid.

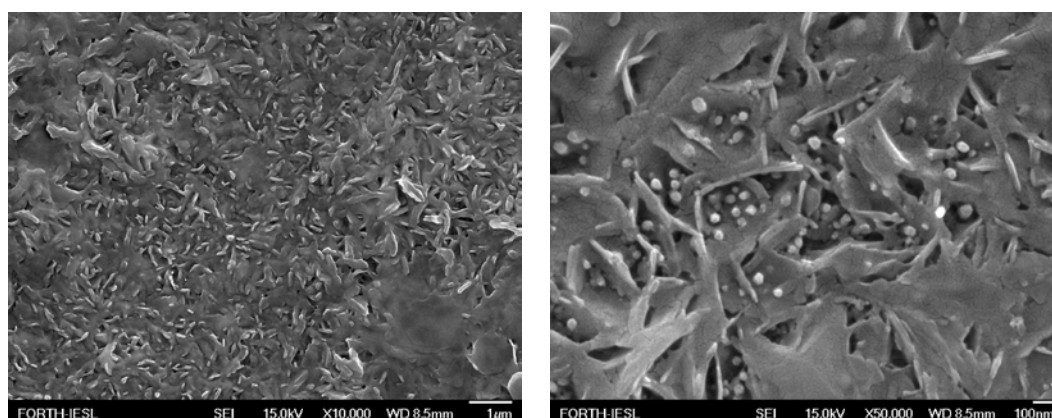


**Figure 2.22.** FE-SEM images of ZnO nanowires grafted with P2VP (sample G) and covered with stearic acid.

Figure 2.23 depicts the ZnO nanowires after the silanization process.

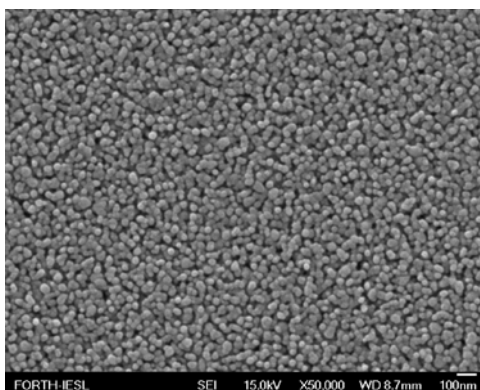


**Figure 2.23.** FE-SEM micrograph of silanized ZnO nanowires.

Careful examination of Figure 2.19 and Figure 2.23 makes clear that the dichlorodimethylsilane did not affect the nano-structures of the artificial surface. This is reasonable since the quantity of the silane reagent is sufficient to create a very thin film on the surface of each nanorod, but not in excess that would submerge them and make the roughness inefficient.

### 2.8.2. Photocatalytic activity

The photocatalytic mechanism of ZnO has been reported in previous works.<sup>31,64,115</sup> FT-IR spectroscopy was utilized to evaluate the photocatalytic behavior of the surfaces with the ZnO nanorods, coating with polymers, as well as of the various controls. For this purpose, the samples were coated with a thin layer of the model compound stearic acid and its photocatalytic degradation was monitored as a function of time.

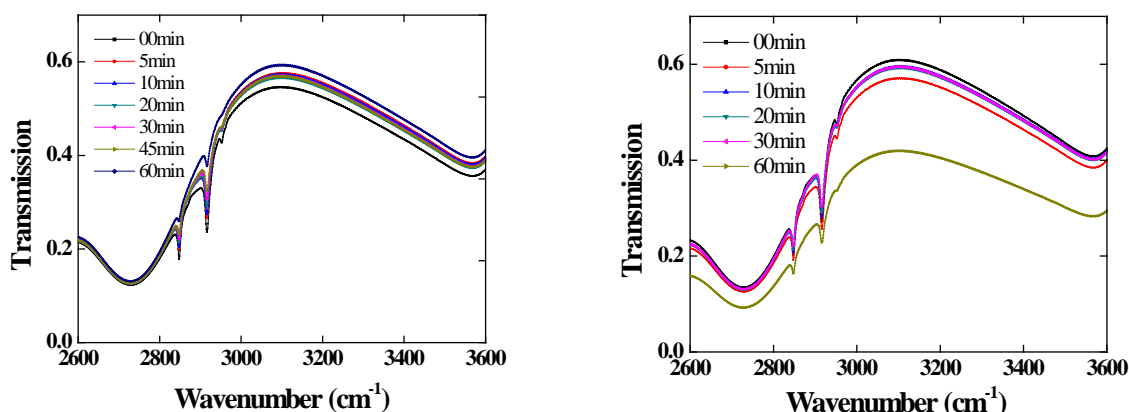


**Figure 2.24.** FT-IR transmittance versus wavenumber spectra demonstrating the degradation of stearic acid vs. irradiation time: (left) on the ZnO nanowires covered with PMMA (0.1 wt % in toluene) and (right) on the ZnO nanowires covered with PMMA (0.01 wt % in toluene).

The normalized integrated areas were calculated from such absorbance curves at the peak wavelength and the data are shown in Figure 2.25 as a function of the UV illumination time.

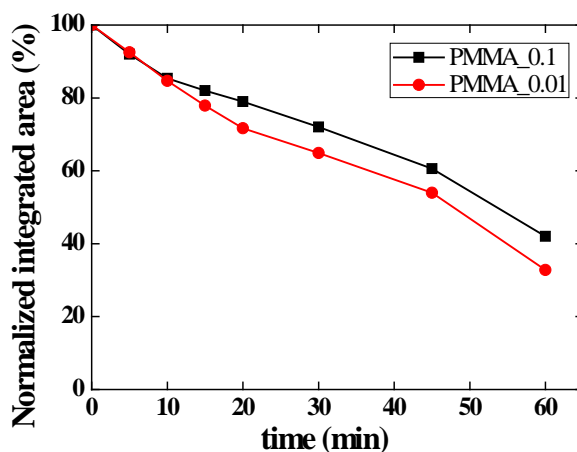


**Figure 2.25.** Normalized absorption of chloroform solutions of stearic acid under UV light irradiation for PMMA coated ZnO nanowires in concentrations 0.01 wt % (circles) and 0.1 wt % (squares).

Figure 2.25 shows that, both samples, ZnO nanowires covered with PMMA in concentrations 0.01 wt % and 0.1 wt %, exhibited photocatalytic activity being able to catalyze the degradation of the model compound down to 67.2 and 58 % respectively, within 60 min. According to

literature, the photocatalytic behavior of bare ZnO nanowires is up to 90 % of degradation of stearic acid.<sup>64,99,120</sup> The difference can be attributed to the fact, that the surface-to-volume ratio is lower in the case of the covered ZnO nanowires.

In parallel, P2VP coated ZnO nanowires were measured for their photocatalytic behavior. For this purpose, samples with ZnO nanowires were spin coated with toluene solutions of P2VP, 0.001, 0.01 and 0.1 wt %. The results are summarized in the Figure 2.26.

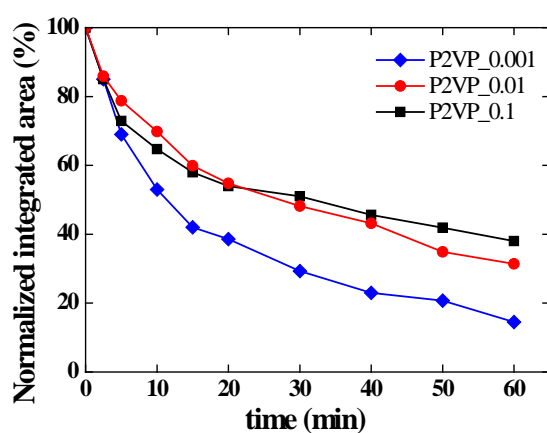


**Figure 2.26.** Normalized absorption of chloroform solutions of stearic acid under UV light irradiation for P2VP coated, 0.001 wt % (diamonds), 0.01 (circles) wt % and 0.1 wt % (squares), ZnO nanowires.

According to the results, all three samples found to be photocatalytically active. This behavior, however, was enhanced by decreasing the polymer concentration. This result was expected, as the active surface-to-volume ratio was decreased in the case of a thick polymer film.

Comparing the results from PMMA and P2VP coated surfaces for the representative concentration, there are no significant differences. In the case of the 0.1 wt % coated ZnO nanowires, the photocatalytic degradation of stearic acid, was found 58% for the PMMA and 62% for the P2VP coated surfaces after 60 min. In the case of 0.01 wt % coated ZnO

nanowires, the respective results were 67% and 69%. It is noticeable, however, that in the case of the 0.001 wt % P2VP coated ZnO nanowires, the photocatalytic degradation of stearic acid, was found to be 85.5% after 60 min. According to the literature, the bare ZnO nanowires exhibit better photocatalytic activity, with up to 93% degradation of stearic acid after 30 min.<sup>53</sup> This can be explained by the fact the active surface area of ZnO in the latter case, is higher.

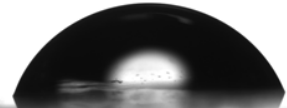
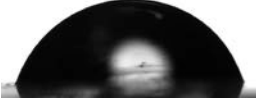
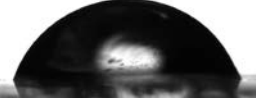
### **2.8.3. Wettability of the developed surfaces**

#### **Wettability of the P2VP coated ZnO nanowires**

The P2VP coated ZnO nanorods were tested for their wettability by the sessile drop method. In order to examine how the parameters of the spin coating affect the wettability of the surfaces different samples were prepared. The effect of rotation speed, the concentration and drop size of the polymer solution were tested.

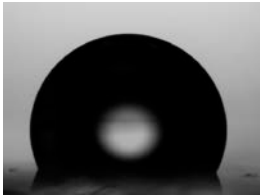
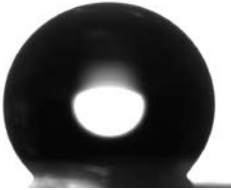
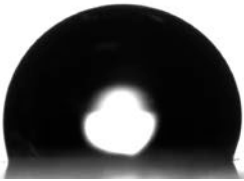
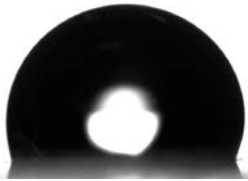
In order to study the effect of the surface chemistry in the wettability, samples were prepared, with ZnO nanowires covered with P2VP (1 and 0.01 wt % in toluene). Table 2.8 and table 2.9 are summarizing the results for both concentrations.

**Table 2.8.** Average contact angle values of P2VP (0.01 wt % in toluene) coated nanorods on glass surfaces.

Rotation speed (rpm)	Drop of P2VP (0.01 wt % in toluene) applied to ZnO nanorods on glass surfaces ( $\mu\text{L}$ )		
	30	50	70
500	63°	89°	66°
			
1000	68°	66°	83°
			
2000	71°	72°	71°
			

The contact angle value in the case of ZnO nanowires, covered with P2VP (0.01 wt % in toluene), was fluctuating from 63° to 89°, which are slightly higher to the contact angle of the bare ZnO nanostructures. By changing the rotation speed or the quantity of the polymer applied, no systematic change of the contact angle can be observed.

**Table 2.9.** Average contact angle values of P2VP (1 wt % in toluene) coated ZnO nanorods on glass surfaces.

Drop of P2VP (1 wt % in toluene) applied to ZnO nanorods on glass surfaces ( $\mu\text{L}$ )			
Rotation speed (rpm)	30	50	70
500	115°	125°	125°
			
1000	137°	112°	112°
			
2000	124°	106°	125°
			

By increasing the concentration of the polymer in the toluene solution, there is a clear increment in the hydrophobicity of the surfaces. The contact angle value in this case, is varying from 106° to 137°. The outcome of the above results, is that the thickness of the polymer film grafted to the ZnO nanowires, depends mainly on the polymer solution and not on the parameters of the spin coating. It seems that, when 0.01 wt % P2VP solution in toluene

was applied, the polymer grafted was inadequate to affect the wettability of the surfaces. However, this was not the same in the case that a solution with higher concentration in P2VP was utilized.

P2VP coated ZnO nanowires, were tested also for their pH responsiveness. P2VP is a pH-responsive polymer, exhibiting hydrophilic behavior at  $\text{pH} < \text{pK}_a$  and hydrophobic at  $\text{pH} > \text{pK}_a$ .<sup>127</sup> So, the stability and the wettability of the samples in different pH environment was studied. For this purpose, P2VP coated ZnO nanowires, were immersed in basic (pH 12) and acidic (pH 2) aqueous solutions for approximately 20 s. Subsequently, the contact angle was measured in each case. Figure 2.27 depicts representative water drops on glass substrates with ZnO nanorods covered with P2VP (0.01 wt % in toluene) after immersion in pH 2 and pH 12.

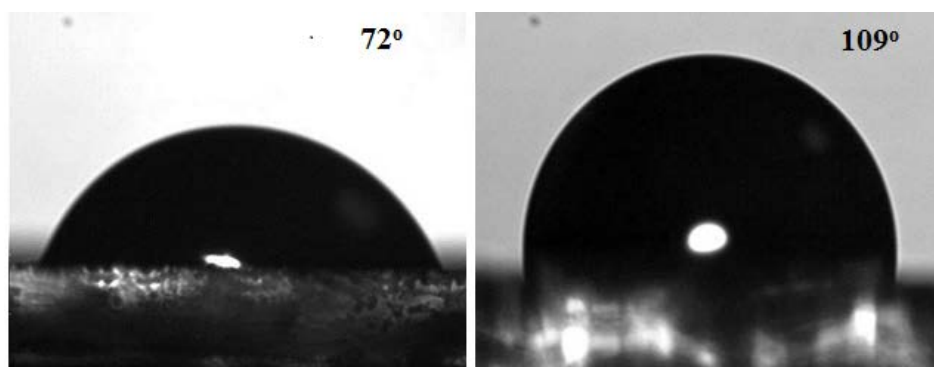


**Figure 2.27.** Photographs of representative water drops and the respective equilibrium contact angles on glass substrates with ZnO nanorods covered with P2VP (0.01 wt % in toluene) after immersion in pH 2 (left) and pH 12 (right).

Figure 2.27 shows the switchable wetting behavior of the samples from  $72^\circ$  (at pH 2) to  $109^\circ$  (at pH 12). The surfaces are not switching from superhydrophilicity to superhydrophobicity and there is a slight increase in the hydrophobicity upon immersion in high pH solution.

In order to study the reproducibility and stability of the system, samples were subjected to at least five cycles of immersion in high and low pH successively and the wettability was investigated (Figure 2.28).

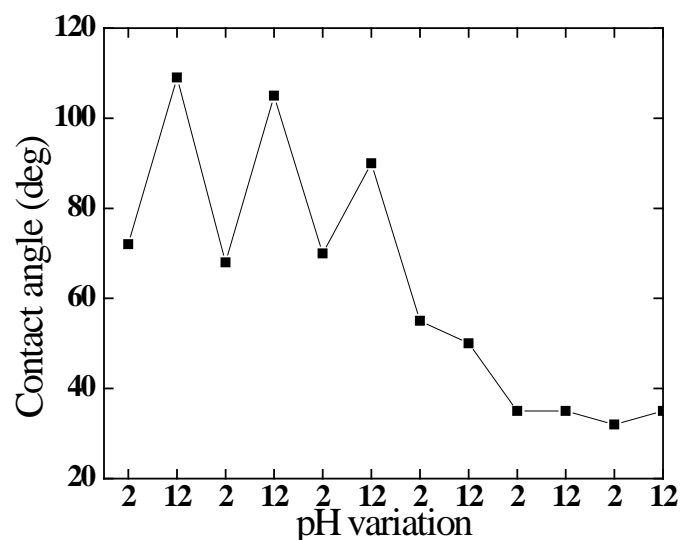


**Figure 2.28.** Average contact angle values of water droplets onto ZnO nanorods coated with P2VP brushes, for 6 cycles of pH environment changes.

Figure 2.28 shows that the samples maintained their responsiveness for 3 cycles. That happens because the ZnO nanorods are being removed with the repetitive immersion in acidic conditions.<sup>128</sup>

### Wettability of the silane-modified ZnO nanorods

In Figure 2.29, there are the images of the representative water drops and the respective equilibrium contact angles on glass substrates with ZnO nanorods, before (left) and after the silanization process (right).

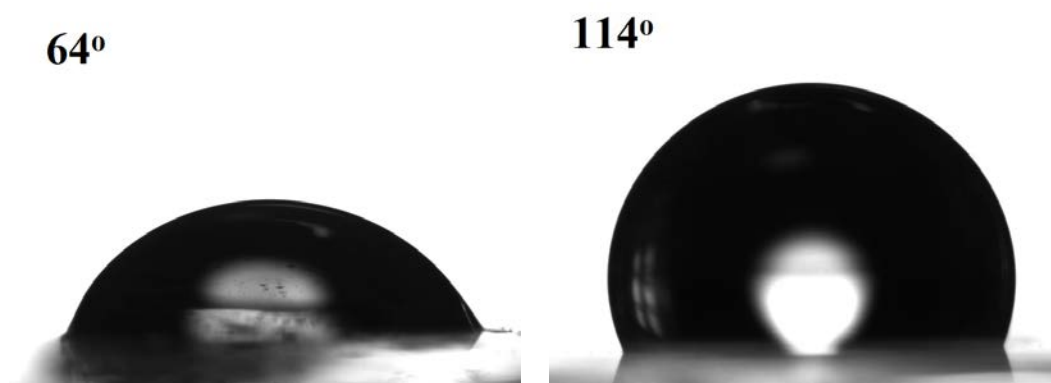


**Figure 2.29.** Photographs of the representative water drops and the respective equilibrium contact angles on glass substrates with ZnO nanowires, before (left) and after the silanization process (right).

The coating of the ZnO nanowires with dichlorodimethylsilane, resulted in samples with a low surface energy. Thus, the silanized samples exhibit hydrophobic properties, with a contact angle to be  $114^\circ$ , which can be maintained for long periods of time and for a wide temperature range.

## 2.9. Conclusions

In this work, ZnO nanowires with enhanced stability and high photocatalytic behavior were developed. In order to achieve this, initially ZnO nanowires were grown on ZnO pre-coated glass substrates via aqueous solution growth. Afterwards the samples were coated with polymers with the spin coating method. Poly(methylmethacrylate), PMMA and Poly(2-vinyl pyridine), P2VP were utilized for this purpose. The parameters of the spin coating technique were studied further. Samples were successfully characterized with Scanning Electron Microscopy and were tested for their photocatalytic behavior with Fourier Transform Infrared Spectroscopy (FTIR). Stearic acid was utilized as a test organic pollutant. Samples were also tested for their wettability. In parallel ZnO nanowires were coated with dichlorodimethylsilane for comparison reasons.

All samples exhibited photocatalytic activity, with this behavior depending on the thickness of the polymer film. The highest photocatalytic degradation of the model dye achieved was found to be ~85%, for the thinnest polymer film. This was attributed to the higher surface-to-volume ratio, i.e. to the fact that the polymer did not cover the nanowires fully.

Taking into consideration the wettability results, it should be noted that the contact angle of ZnO nanowires covered with P2VP, was higher compared to the bare ZnO nanostructures. This behavior was enhanced by increasing the concentration of the polymer in the toluene solution. The contact angle value was varied from  $63^\circ$  to  $137^\circ$ , depending on the coating conditions.

P2VP coated ZnO nanowires were also tested for their pH responsiveness and the samples maintained their reversible behavior for 3 cycles (switching from  $72^\circ$  at pH 2 to  $109^\circ$  at pH 12). That happened because the ZnO nanorods are being removed with the repetitive immersion in acidic conditions.

To conclude, ZnO nanostructures covered with polymers, exhibited photocatalytic activity with enhanced hydrophobicity. Depending on the application, the parameters of the system have to be selected, because by increasing the thickness of the polymer film, the nanowires are more stable but the photocatalytic activity is being decreased. So the optimum conditions have to be chosen in every case.

## 2.10. References

- (1) Anastasiadis, S. H. Development of Functional Polymer Surfaces with Controlled Wettability. *Langmuir* **2013**, *29* (30), 9277–9290.
- (2) Bhushan, B.; Jung, Y. C.; Koch, K. Micro-, Nano- and Hierarchical Structures for Superhydrophobicity, Self-Cleaning and Low Adhesion. *Philos. Trans. A. Math. Phys. Eng. Sci.* **2009**, *367* (1894), 1631–1672.
- (3) Zorba, V.; Stratakis, E.; Barberoglou, M.; Spanakis, E.; Tzanetakis, P.; Anastasiadis, S. H.; Fotakis, C. Biomimetic Artificial Surfaces Quantitatively Reproduce the Water Repellency of a Lotus Leaf. *Adv. Mater.* **2008**, *20* (21), 4049–4054.
- (4) Blossey, R. Self-Cleaning Surfaces--Virtual Realities. *Nat. Mater.* **2003**, *2* (5), 301–306.
- (5) Callies, M.; Quéré, D. On Water Repellency. *Soft Matter* **2005**, *1* (1), 55.
- (6) Nakajima, A.; Fujishima, A.; Hashimoto, K.; Watanabe, T. Preparation of Transparent Superhydrophobic Boehmite and Silica Films by Sublimation of Aluminum Acetylacetonate. *Adv. Mater.* **1999**, *11* (16), 1365–1368.
- (7) Ueda, E.; Levkin, P. a. Emerging Applications of Superhydrophilic-Superhydrophobic Micropatterns. *Adv. Mater.* **2013**, *25* (9), 1234–1247.
- (8) Barthlott, W.; Neinhuis, C. Purity of the Sacred Lotus, or Escape from Contamination in Biological Surfaces. *Planta* **1997**, *202* (1), 1–8.
- (9) Füstner, R.; Barthlott, W.; Neinhuis, C.; Walzel, P. Wetting and Self-Cleaning Properties of Artificial Superhydrophobic Surfaces. *Langmuir* **2005**, *21*, 956–961.
- (10) Liu, K.; Jiang, L. Bio-Inspired Design of Multiscale Structures for Function Integration. *Nano Today* **2011**, *6* (2), 155–175.
- (11) Hsu, S.-T.; Wang, H.; Satoh, G.; Yao, Y. L. Applications of Surface Structuring with Lasers. *Icaleo* **2011**, 1095–1104.
- (12) Her, T.-H.; Finlay, R. J.; Wu, C.; Deliwala, S.; Mazur, E. Microstructuring of Silicon with Femtosecond Laser Pulses. *Appl. Phys. Lett.* **1998**, *73* (12), 1673.
- (13) Zhang, D.; Chen, F.; Yang, Q.; Yong, J.; Bian, H.; Ou, Y.; Si, J.; Meng, X.; Hou, X. A Simple Way to Achieve Pattern-Dependent Tunable Adhesion in Superhydrophobic Surfaces by a Femtosecond Laser. *ACS Appl. Mater. Interfaces* **2012**, *4* (9), 4905–4912.
- (14) Zorba, V.; Persano, L.; Pisignano, D.; Athanassiou, a; Stratakis, E.; Cingolani, R.; Tzanetakis, P.; Fotakis, C. Making Silicon Hydrophobic: Wettability Control by Two-Lengthscale Simultaneous Patterning with Femtosecond Laser Irradiation. *Nanotechnology* **2006**, *17* (13), 3234–3238.
- (15) Barberoglou, M.; Zorba, V.; Stratakis, E.; Spanakis, E.; Tzanetakis, P.; Anastasiadis, S. H.; Fotakis, C. Bio-Inspired Water Repellent Surfaces Produced by Ultrafast Laser Structuring of Silicon. *Appl. Surf. Sci.* **2009**, *255* (10), 5425–5429.
- (16) Wang, S.; Song, Y.; Jiang, L. Photoresponsive Surfaces with Controllable Wettability. *J. Photochem. Photobiol. C Photochem. Rev.* **2007**, *8* (1), 18–29.
- (17) Feng, X.; Jiang, L. Design and Creation of Superwetting/antiwetting Surfaces. *Adv.*

- Mater.* **2006**, *18* (23), 3063–3078.
- (18) Rosario, R.; Gust, D.; Hayes, M.; Jahnke, F.; Springer, J.; Garcia, A. a. Photon-Modulated Wettability Changes on Spiropyran-Coated Surfaces. *Langmuir* **2002**, *18* (21), 8062–8069.
- (19) Liu, H.; Feng, L.; Zhai, J.; Jiang, L.; Zhu, D. Reversible Wettability of a Chemical Vapor Deposition Prepared ZnO Film between Superhydrophobicity and Superhydrophilicity. *Langmuir* **2004**, *20* (14), 5659–5661.
- (20) Irie, H.; Ping, T. S.; Shibata, T.; Hashimoto, K. Reversible Control of Wettability of a TiO<sub>2</sub> Surface by Introducing Surface Roughness. *Electrochem. Solid-State Lett.* **2005**, *8* (9), D23.
- (21) Crevoisier, G. D. Switchable Tackiness and Wettability of a Liquid Crystalline Polymer. *Science* (80-. ). **1999**, *285* (5431), 1246–1249.
- (22) Fu, Q.; Rao, G. V. R.; Basame, S. B.; Keller, D. J.; Artyushkova, K.; Fulghum, J. E.; Lopez, G. P. Reversible Control of Free Energy and Topography of Nanostructured Surfaces. *J. Am. Chem. Soc.* **2004**, *126* (29), 8904–8905.
- (23) Sun, T.; Wang, G.; Feng, L.; Liu, B.; Ma, Y.; Jiang, L.; Zhu, D. Reversible Switching between Superhydrophilicity and Superhydrophobicity. *Angew. Chemie - Int. Ed.* **2004**, *43* (3), 357–360.
- (24) Lahann, J.; Mitragotri, S.; Tran, T.-N.; Kaido, H.; Sundaram, J.; Choi, I. S.; Hoffer, S.; Somorjai, G. a; Langer, R. A Reversibly Switching Surface. *Science* **2003**, *299* (5605), 371–374.
- (25) Krupenkin, T. N.; Taylor, J. A.; Schneider, T. M.; Yang, S. From Rolling Ball to Complete Wetting: The Dynamic Tuning of Liquids on Nanostructured Surfaces. *Langmuir* **2004**, *20* (10), 3824–3827.
- (26) Yu, X.; Wang, Z.; Jiang, Y.; Shi, F.; Zhang, X. Reversible pH-Responsive Surface: From Superhydrophobicity to Superhydrophilicity. *Adv. Mater.* **2005**, *17* (10), 1289–1293.
- (27) Stratakis, E.; Mateescu, A.; Barberoglou, M.; Vamvakaki, M.; Fotakis, C.; Anastasiadis, S. H. From Superhydrophobicity and Water Repellency to Superhydrophilicity: Smart Polymer-Functionalized Surfaces. *Chem. Commun.* **2010**, *46* (23), 4136.
- (28) Minko, S.; Müller, M.; Motornov, M.; Nitschke, M.; Grundke, K.; Stamm, M. Two-Level Structured Self-Adaptive Surfaces with Reversibly Tunable Properties. *J. Am. Chem. Soc.* **2003**, *125* (13), 3896–3900.
- (29) Papadopoulou, E. L.; Barberoglou, M.; Zorba, V.; Manousaki, A.; Pagkozidis, A.; Stratakis, E.; Fotakis, C. Reversible Photoinduced Wettability Transition of Hierarchical ZnO Structures. *J. Phys. Chem. C* **2009**, *113* (7), 2891–2895.
- (30) Papadopoulou, E. L.; Zorba, V.; Pagkozidis, a.; Barberoglou, M.; Stratakis, E.; Fotakis, C. Reversible Wettability of ZnO Nanostructured Thin Films Prepared by Pulsed Laser Deposition. *Thin Solid Films* **2009**, *518* (4), 1267–1270.
- (31) Kenanakis, G.; Stratakis, E.; Vlachou, K.; Vernardou, D.; Koudoumas, E.; Katsarakis, N. Light-Induced Reversible Hydrophilicity of ZnO Structures Grown by Aqueous Chemical Growth. *Appl. Surf. Sci.* **2008**, *254* (18), 5695–5699.
- (32) Sahu, D. R.; Liu, C. P.; Wang, R. C.; Kuo, C. L.; Huang, J. L. Growth and Application

- of ZnO Nanostructures. *Int. J. Appl. Ceram. Technol.* **2013**, *10* (5), 814–838.
- (33) Kolodziejczak-Radzimska, A.; Jesionowski, T. Zinc Oxide—from Synthesis to Application: A Review. *Materials (Basel)*. **2014**, *7* (4), 2833–2881.
- (34) Chiu, W. S.; Khiew, P. S.; Cloke, M.; Isa, D.; Tan, T. K.; Radiman, S.; Abd-Shukor, R.; Hamid, M. A. A.; Huang, N. M.; Lim, H. N.; et al. Photocatalytic Study of Two-Dimensional ZnO Nanopellets in the Decomposition of Methylene Blue. *Chem. Eng. J.* **2010**, *158* (2), 345–352.
- (35) Xie, Q.; Dai, Z.; Liang, J.; Xu, L.; Yu, W.; Qian, Y. Synthesis of ZnO Three-Dimensional Architectures and Their Optical Properties. *Solid State Commun.* **2005**, *136* (5), 304–307.
- (36) Liu, J.; Huang, X.; Li, Y.; Sulieman, K. M.; Sun, F.; He, X. Selective Growth and Properties of Zinc Oxide Nanostructures. *Scr. Mater.* **2006**, *55* (9), 795–798.
- (37) Bitenc, M.; Crnjak Orel, Z. Synthesis and Characterization of Crystalline Hexagonal Bipods of Zinc Oxide. *Mater. Res. Bull.* **2009**, *44* (2), 381–387.
- (38) Soci, C.; Zhang, A.; Xiang, B.; Dayeh, S. A.; Aplin, D. P. R.; Park, J.; Bao, X. Y.; Lo, Y. H.; Wang, D. ZnO Nanowire UV Photodetectors with High Internal Gain. *Nano Lett.* **2007**, *7* (4), 1003–1009.
- (39) Djurišić, A. B.; Chen, X.; Leung, Y. H.; Man Ching Ng, A. ZnO Nanostructures: Growth, Properties and Applications. *J. Mater. Chem.* **2012**, *22* (14), 6526.
- (40) Jin, Y.; Wang, J.; Sun, B.; Blakesley, J. C.; Greenham, N. C. Solution-Processed Ultraviolet Photodetectors Based on Colloidal ZnO Nanoparticles. *Nano Lett.* **2008**, *8* (6), 1649–1653.
- (41) Nohynek, G. J.; Lademann, J.; Ribaud, C.; Roberts, M. S. Grey Goo on the Skin? Nanotechnology, Cosmetic and Sunscreen Safety. *Crit. Rev. Toxicol.* **2007**, *37* (3), 251–277.
- (42) Ahmad, M.; Yingying, S.; Nisar, A.; Sun, H.; Shen, W.; Wei, M.; Zhu, J. Synthesis of Hierarchical Flower-like ZnO Nanostructures and Their Functionalization by Au Nanoparticles for Improved Photocatalytic and High Performance Li-Ion Battery Anodes. *J. Mater. Chem.* **2011**, *21* (December 2015), 7723.
- (43) Wang, Z. L. Zinc Oxide Nanostructures: Growth, Properties and Applications. *J. Phys. Condens. Matter* **2004**, *16*, R829–R858.
- (44) Hashimoto, S.; Yamaguchi, A. Growth Morphology and Mechanism of a Hollow ZnO Polycrystal. *J. Am. Ceram. Soc.* **1996**, *79* (4), 1121–1123.
- (45) Kong, X. Y.; Wang, Z. L. Polar-Surface Dominated ZnO Nanobelts and the Electrostatic Energy Induced Nanohelices, Nanosprings, and Nanospirals. *Appl. Phys. Lett.* **2004**, *84* (6), 975–977.
- (46) Kong, X. Y.; Wang, Z. L. Spontaneous Polarization-Induced Nanohelices, Nanosprings, and Nanorings of Piezoelectric Nanobelts. *Nano Lett.* **2003**, *3* (12), 1625–1631.
- (47) Gao, P. X.; Wang, Z. L. Mesoporous Polyhedral Cages and Shells Formed by Textured Self-Assembly of ZnO Nanocrystals. *J. Am. Chem. Soc.* **2003**, *125* (37), 11299–11305.
- (48) Gomez, J. L.; Tigli, O. Zinc Oxide Nanostructures: From Growth to Application. *J. Mater. Sci.* **2013**, *48* (2), 612–624.

- (49) Zhang, Y.; Kang, Z.; Yan, X.; Liao, Q. ZnO Nanostructures in Enzyme Biosensors. *Sci. China Mater.* **2015**, *58* (1), 60–76.
- (50) Djuriić, A. B.; Ng, A. M. C.; Chen, X. Y. ZnO Nanostructures for Optoelectronics: Material Properties and Device Applications. *Prog. Quantum Electron.* **2010**, *34* (4), 191–259.
- (51) Kenanakis, G.; Katsarakis, N. ZnO Nanowires on Glass via Chemical Routes: A Prospective Photocatalyst for Indoors Applications. *J. Environ. Chem. Eng.* **2014**, *2* (3), 1416–1422.
- (52) Chen, D.; Wang, Z.; Ren, T.; Ding, H.; Yao, W.; Zong, R.; Zhu, Y. Influence of Defects on the Photocatalytic Activity of ZnO. *Journal of Physical Chemistry C*. 2014, pp 15300–15307.
- (53) Kenanakis, G.; Katsarakis, N. Light-Induced Photocatalytic Degradation of Stearic Acid by c-Axis Oriented ZnO Nanowires. *Appl. Catal. A Gen.* **2010**, *378* (2), 227–233.
- (54) Rashad, M. M.; Ismail, A. A.; Osama, I.; Ibrahim, I. A.; Kandil, A. H. T. Photocatalytic Decomposition of Dyes Using ZnO Doped SnO<sub>2</sub> Nanoparticles Prepared by Solvothermal Method. *Arab. J. Chem.* **2014**, *7* (1), 71–77.
- (55) Xu, T.; Zhang, L.; Cheng, H.; Zhu, Y. Significantly Enhanced Photocatalytic Performance of ZnO via Graphene Hybridization and the Mechanism Study. *Appl. Catal. B Environ.* **2011**, *101* (3–4), 382–387.
- (56) Cao, Y.-Q.; Chen, J.; Zhou, H.; Zhu, L.; Li, X.; Cao, Z.-Y.; Wu, D.; Li, A.-D. Photocatalytic Activity and Photocorrosion of Atomic Layer Deposited ZnO Ultrathin Films for the Degradation of Methylene Blue. *Nanotechnology* **2015**, *26* (2), 24002.
- (57) Mohan, R.; Krishnamoorthy, K.; Kim, S.-J. Enhanced Photocatalytic Activity of Cu-Doped ZnO Nanorods. *Solid State Commun.* **2012**, *152* (5), 375–380.
- (58) Panigrahy, B.; Aslam, M.; Misra, D. S.; Bahadur, D. Polymer-Mediated Shape-Selective Synthesis of ZnO Nanostructures Using a Single-Step Aqueous Approach. *CrystEngComm* **2009**, *11* (9), 1920.
- (59) Kumar, S.; Lee, H.-J.; Yoon, T.-H.; Murthy, C. N.; Lee, J.-S. Morphological Control over ZnO Nanostructures from Self-Emulsion Polymerization. *Cryst. Growth Des.* **2016**, *16* (7), 3905–3911.
- (60) Aga, R.; Mu, R. Doping of Polymers with ZnO Nanostructures for Optoelectronic and Sensor Applications. *Nanowires Sci. Technol.* **2010**, No. February.
- (61) Irawati, N.; Harun, S. W.; Adwan, S.; Alnowami, M.; Ahmad, H. PMMA Microfiber Coated with Al-Doped ZnO Nanostructures for Detecting Uric Acid. *Microw. Opt. Technol. Lett.* **2015**, *57* (10), 2455.
- (62) Kim, K. S.; Jeong, H.; Jeong, M. S.; Jung, G. Y. Polymer-Templated Hydrothermal Growth of Vertically Aligned Single-Crystal ZnO Nanorods and Morphological Transformations Using Structural Polarity. *Adv. Funct. Mater.* **2010**, *20* (18), 3055–3063.
- (63) Chang, S.; Singamaneni, S.; Kharlampieva, E.; Young, S. L.; Tsukruk, V. V. Responsive Hybrid Nanotubes Composed of Block Copolymer and Gold Nanoparticles. *Macromolecules* **2009**, *42* (15), 5781–5785.
- (64) Kenanakis, G.; Vernardou, D.; Katsarakis, N. Light-Induced Self-Cleaning Properties of ZnO Nanowires Grown at Low Temperatures. *Applied Catalysis A: General*. 2012,

- pp 7–14.
- (65) Kenanakis, G.; Pervolaraki, M.; Giapintzakis, J.; Katsarakis, N. The Use of Pulsed Laser Deposited Seed Layers for the Aqueous Solution Growth of Highly Oriented ZnO Nanowires on Sapphire Substrates at 95°C: Study of Their Photocatalytic Activity in Terms of Octadecanoic (Stearic) Acid Degradation. *Appl. Catal. A Gen.* **2013**, *467*, 559–567.
- (66) Garg, V. K.; Amita, M.; Kumar, R.; Gupta, R. Basic Dye (Methylene Blue) Removal from Simulated Wastewater by Adsorption Using Indian Rosewood Sawdust: A Timber Industry Waste. *Dye. Pigment.* **2004**, *63* (3), 243–250.
- (67) Salem, I. A.; El-Maazawi, M. S. Kinetics and Mechanism of Color Removal of Methylene Blue with Hydrogen Peroxide Catalyzed by Some Supported Alumina Surfaces. *Chemosphere* **2000**, *41* (8), 1173–1180.
- (68) Rahimi, R.; Shokrayian, J.; Rabbani, M. Photocatalytic Removing of Methylene Blue by Using of Cu-Doped ZnO, Ag-Doped ZnO and Cu,Ag-Codoped ZnO Nanostructures. *Proc. 17th Int. Electron. Conf. Synth. Org. Chem.* **2013**, b019.
- (69) Bunn, B. Y. C. W. The Lattice-Dimensions of Zinc Oxide.
- (70) Anderson, J.; Chris, G. V. de W. Fundamentals of Zinc Oxide as a Semiconductor. *Reports Prog. Phys.* **2009**, *72* (12), 126501.
- (71) Coleman, V. A.; Jagadish, C. Basic Properties and Applications of ZnO. *Zinc Oxide Bulk, Thin Film. Nanostructures* **2006**, No. December, 1–20.
- (72) Nickel, N.; TerukovEvgenii. *Zinc Oxide—A Material for Micro- and Optoelectronic Applications*; Netherlands, 2005.
- (73) Kamble, A. S.; Sinha, B. B.; Chung, K.; Gil, M. G.; Burungale, V.; Park, C. J.; Kim, J. H.; Patil, P. S. Effect of Hydroxide Anion Generating Agents on Growth and Properties of ZnO Nanorod Arrays. *Electrochim. Acta* **2014**, *149* (October), 386–393.
- (74) Norton, D. P.; Heo, Y. W.; Ivill, M. P.; Ip, K.; Pearton, S. J.; Chisholm, M. F.; Steiner, T. ZnO: Growth, Doping & Processing. *Mater. Today* **2004**, *7* (6), 34–40.
- (75) Ibhaddon, A.; Fitzpatrick, P. Heterogeneous Photocatalysis: Recent Advances and Applications. *Catalysts* **2013**, *3* (1), 189–218.
- (76) Gaya, U. I. *Heterogeneous Photocatalysis Using Inorganic Semiconductor Solids*; 2014; Vol. 9789400777.
- (77) Herrmann, J. Heterogeneous Photocatalysis: Fundamentals and Applications to the Removal of Various Types of Aqueous Pollutants. *Catal. Today* **1999**, *53* (1), 115–129.
- (78) Whang, T.-J.; Hsieh, M.-T.; Chen, H.-H. Visible-Light Photocatalytic Degradation of Methylene Blue with Fe Doped CdS Nanoparticles. *Appl. Surf. Sci.* **2013**, *270* (7), 655–660.
- (79) Adhikari, S.; Sarkar, D.; Madras, G. Synthesis and Photocatalytic Performance of Ag<sub>3</sub>PO<sub>4</sub>/AgCl Hybrids. *Optoelectron. Lett.* **2014**, *10* (2), 119–122.
- (80) Tahan Latibari, S.; Mehrli, M.; Mehrli, M.; Afifi, A. B. M.; Mahlia, T. M. I.; Akhiani, A. R.; Metselaar, H. S. C. Facile Synthesis and Thermal Performances of Stearic Acid/titania Core/shell Nanocapsules by Sol-Gel Method. *Energy* **2015**, *85*, 635–644.

- (81) Mills, A.; Wang, J. Simultaneous Monitoring of the Destruction of Stearic Acid and Generation of Carbon Dioxide by Self-Cleaning Semiconductor Photocatalytic Films. *J. Photochem. Photobiol. A Chem.* **2006**, *182* (2), 181–186.
- (82) Mills, A.; Lee, S.-K.; Lepre, A.; Parkin, I. P.; O'Neill, S. a. Spectral and Photocatalytic Characteristics of TiO<sub>2</sub> CVD Films on Quartz. *Photochem. Photobiol. Sci.* **2002**, *1* (11), 865–868.
- (83) Mills, A.; Elliott, N.; Hill, G.; Fallis, D.; Durrant, J. R.; Willis, R. L. Preparation and Characterisation of Novel Thick Sol-Gel Titania Film Photocatalysts. *Photochem. Photobiol. Sci.* **2003**, *2* (5), 591–596.
- (84) McKay, G.; Otterburn, M. S.; Sweeney, A. G. The Removal of Colour from Effluent Using Various Adsorbents. III. Silica: Rate Processes. *Water Res.* **1980**, *14* (1), 15–20.
- (85) Cenens, J.; Schoonheydt, R. A. Visible Spectroscopy of Methylene Blue on Hectorite, Laponite B, and Barasym in Aqueous Suspension. *Clays Clay Miner.* **1988**, *36* (3), 214–224.
- (86) Lü, J.; Huang, K.; Chen, X.; Zhu, J.; Meng, F.; Song, X.; Sun, Z. Reversible Wettability of Nanostructured ZnO Thin Films by Sol-Gel Method. *Appl. Surf. Sci.* **2010**, *256* (14), 4720–4723.
- (87) Sun, R.-D.; Nakajima, A.; Fujishima, A.; Watanabe, T.; Hashimoto, K. Photoinduced Surface Wettability Conversion of ZnO and TiO<sub>2</sub> Thin Films. *J. Phys. Chem. B* **2001**, *105* (10), 1984–1990.
- (88) Sun, R.-D.; Nakajima, A.; Fujishima, A.; Watanabe, T.; Hashimoto, K. Photoinduced Surface Wettability Conversion of ZnO and TiO<sub>2</sub> Thin Films. *J. Phys. Chem. B* **2001**, *105* (10), 1984–1990.
- (89) Miyauchi, M.; Kieda, N.; Hishita, S.; Mitsuhashi, T.; Nakajima, A.; Watanabe, T.; Hashimoto, K. Reversible Wettability Control of TiO<sub>2</sub> Surface by Light Irradiation. *Surf. Sci.* **2002**, *511* (1–3), 401–407.
- (90) Frysali, M. A.; Papoutsakis, L.; Kenanakis, G.; Anastasiadis, S. H. Functional Surfaces with Photocatalytic Behavior and Reversible Wettability: ZnO Coating on Silicon Spikes. *J. Phys. Chem. C* **2015**, *119* (45), 25401–25407.
- (91) Baruah, S.; Dutta, J. Hydrothermal Growth of ZnO Nanostructures. *Sci. Technol. Adv. Mater.* **2009**, *10* (1), 13001.
- (92) Tak, Y.; Yong, K. Controlled Growth of Well-Aligned ZnO Nanorod Array Using a Novel Solution Method. **2005**, 19263–19269.
- (93) He, J. H.; Hsu, J. H.; Wang, C. W.; Lin, H. N.; Chen, L. J.; Wang, Z. L. Pattern and Feature Designed Growth of {ZnO} Nanowire Arrays for Vertical Devices. **2006**, *110* (1), 50–53.
- (94) Ding, Y.; Zhang, F.; Wang, Z. L. Deriving the Three-Dimensional Structure of ZnO Nanowires/nanobelts by Scanning Transmission Electron Microscope Tomography. *Nano Res.* **2013**, *6* (4), 253–262.
- (95) Xu, S.; Wei, Y.; Kirkham, M.; Liu, J.; Mai, W.; Davidovic, D.; Snyder, R. L.; Zhong, L. W. Patterned Growth of Vertically Aligned ZnO Nanowire Arrays on Inorganic Substrates at Low Temperature without Catalyst. *J. Am. Chem. Soc.* **2008**, *130* (45), 14958–14959.
- (96) Greene, L. E.; Law, M.; Goldberger, J.; Kim, F.; Johnson, J. C.; Zhang, Y.; Saykally,

- R. J.; Yang, P. Low-Temperature Wafer-Scale Production of ZnO Nanowire Arrays. *Angew. Chemie - Int. Ed.* **2003**, *42* (26), 3031–3034.
- (97) Zhang, Q.; Dandeneau, C. S.; Zhou, X.; Cao, G. ZnO Nanostructures for Dye-Sensitized Solar Cells. *Adv. Mater. (Weinheim, Ger.)* **2009**, *21* (41), 4087–4108.
- (98) Li, G. H.; Zhang, X. Y.; Wang, X. F. Ordered Semiconductor ZnO Nanowire Arrays and Their Photoluminescence Properties. *Appl. Phys. Lett.* **2000**, *76* (15), 2011–2013.
- (99) Kenanakis, G.; Vernardou, D.; Katsarakis, N. Light-Induced Self-Cleaning Properties of ZnO Nanowires Grown at Low Temperatures. *Appl. Catal. A Gen.* **2012**, *411–412*, 7–14.
- (100) Adnan, M.; Julkapli, N. M.; Bee, S.; Hamid, A. Review on ZnO Hybrid Photocatalyst : Impact on Photocatalytic Activities of Water Pollutant Degradation. **2016**.
- (101) Shao, D. L.; Sun, H. T.; Gao, J.; Xin, G. Q.; Aguilar, M. A.; Yao, T. K.; Koratkar, N.; Lian, J.; Sawyer, S. Flexible, Thorn-like ZnO-Multiwalled Carbon Nanotube Hybrid Paper for Efficient Ultraviolet Sensing and Photocatalyst Applications. *Nanoscale* **2014**, *6* (22), 13630–13636.
- (102) Baruah, S.; Jaisai, M.; Imani, R.; Nazhad, M. M.; Dutta, J. Photocatalytic Paper Using Zinc Oxide Nanorods. *Sci. Technol. Adv. Mater.* **2010**, *11* (5), 55002.
- (103) Wang, G.; Chen, D.; Zhang, H.; Zhang, J. Z.; Li, J. Tunable Photocurrent Spectrum in Well-Oriented Zinc Oxide Nanorod Arrays with Enhanced Photocatalytic Activity. *J. Phys. Chem. C* **2008**, *112* (24), 8850–8855.
- (104) Chen, Y. L.; Kuo, L.-C.; Tseng, M. L.; Chen, H. M.; Chen, C.-K.; Huang, H. J.; Liu, R.-S.; Tsai, D. P. ZnO Nanorod Optical Disk Photocatalytic Reactor for Photodegradation of Methyl Orange. *Opt. Express* **2013**, *21* (6), 7240–7249.
- (105) Ali, U.; Karim, K. J. B. A.; Buang, N. A. A Review of the Properties and Applications of Poly (Methyl Methacrylate) (PMMA). *Polym. Rev.* **2015**, *55* (4), 678–705.
- (106) Lee, L.; Chen, W. High-Refractive-Index Thin Films Prepared from Trialkoxysilane-Capped Poly ( Methyl Methacrylate ) -Titania Materials. *Chem. Mater.* **2001**, *13* (15), 1137–1142.
- (107) Adhikari, B.; Majumdar, S. Polymers in Sensor Applications. *Prog. Polym. Sci.* **2004**, *29* (7), 699–766.
- (108) Hashim, H.; Adam, N. I.; Zaki, N. H. M.; Mahmud, Z. S.; Said, C. M. S.; Yahya, M. Z. A.; Ali, A. M. M. Natural Rubber-Grafted with 30% Poly(methylmethacrylate) Characterization for Application in Lithium Polymer Battery. *CSSR 2010 - 2010 Int. Conf. Sci. Soc. Res.* **2010**, No. Csr, 485–488.
- (109) Orlov, M.; Tokarev, I.; Scholl, A.; Doran, A.; Minko, S. pH-Responsive Thin Film Membranes from Poly ( 2-Vinylpyridine ): Water Vapor-Induced Formation of a Microporous Structure pH-Responsive Thin Film Membranes from Poly ( 2-Vinylpyridine ): Water Vapor-Induced Formation of a Microporous Structure. *Macromolecules* **2007**, *40*, 2086–2091.
- (110) Chen, J. K.; Chang, C. J. Fabrications and Applications of Stimulus-Responsive Polymer Films and Patterns on Surfaces: A Review. *Materials (Basel)*. **2014**, *7* (2), 805–875.
- (111) Komaba, S.; Itabashi, T.; Ohtsuka, T.; Groult, H.; Kumagai, N.; Kaplan, B.; Yashiro, H. Impact of 2-Vinylpyridine as Electrolyte Additive on Surface and Electrochemistry

- of Graphite for C/LiMn<sub>2</sub>O<sub>4</sub> Li-Ion Cells. *J. Electrochem. Soc.* **2005**, *152* (5), A937.
- (112) Nadgorny, M.; Xiao, Z.; Chen, C.; Connal, L. A. 3D-Printing of pH-Responsive and Functional Polymers on an Affordable Desktop Printer. *ACS Appl. Mater. Interfaces* **2016**, acsami.6b07388.
- (113) Kang, Y.; Walish, J. J.; Gorishnyy, T.; Thomas, E. L. Broad-Wavelength-Range Chemically Tunable Block-Copolymer Photonic Gels. *Nat. Mater.* **2007**, *6* (12), 957–960.
- (114) Kenanakis, G.; Katsarakis, N. Chemically Grown TiO<sub>2</sub> on Glass with Superior Photocatalytic Properties. *J. Environ. Chem. Eng.* **2014**, *2* (3), 1748–1755.
- (115) Cao, Y.-Q.; Chen, J.; Zhou, H.; Zhu, L.; Li, X.; Cao, Z.-Y.; Wu, D.; Li, A.-D. Photocatalytic Activity and Photocorrosion of Atomic Layer Deposited ZnO Ultrathin Films for the Degradation of Methylene Blue. *Nanotechnology* **2015**, *26* (2), 24002.
- (116) Hong, R.; Pan, T.; Qian, J.; Li, H. Synthesis and Surface Modification of ZnO Nanoparticles. *Chem. Eng. J.* **2006**, *119* (2–3), 71–81.
- (117) Houas, a. Photocatalytic Degradation Pathway of Methylene Blue in Water. *Appl. Catal. B Environ.* **2001**, *31* (2), 145–157.
- (118) Anastasiadis, S. H.; Hatzikiriakos, S. G. The Work of Adhesion of Polymer/wall Interfaces and Its Association with the Onset of Wall Slip. *J. Rheol. (N. Y. N. Y.)* **1998**, *42* (4), 795.
- (119) Chen, L. J.; Ma, H.; Chen, K. C.; Fan, W.; Cha, H. R.; Lee, Y. I.; Qian, D. J.; Hao, J.; Liu, H. G. Synthesis and Assembly of Catalytically Active Platinum-Doped Polymer Nanocomposites at the Liquid/liquid Interface. *Colloids Surfaces A Physicochem. Eng. Asp.* **2011**, *386* (1–3), 141–150.
- (120) Kenanakis, G.; Giannakoudakis, Z.; Vernardou, D.; Savvakis, C.; Katsarakis, N. Photocatalytic Degradation of Stearic Acid by ZnO Thin Films and Nanostructures Deposited by Different Chemical Routes. *Catal. Today* **2010**, *151* (1–2), 34–38.
- (121) Kenanakis, G.; Vernardou, D.; Koudoumas, E.; Katsarakis, N. Growth of c-Axis Oriented ZnO Nanowires from Aqueous Solution: The Decisive Role of a Seed Layer for Controlling the Wires' Diameter. *J. Cryst. Growth* **2009**, *311* (23–24), 4799–4804.
- (122) Vayssieres, L. Growth of Arrayed Nanorods and Nanowires of ZnO from Aqueous Solutions. *Adv. Mater.* **2003**, *15* (5), 464–466.
- (123) Hall, D. B.; Underhill, P.; Torkelson, J. M. Spin Coating of Thin and Ultrathin Polymer Films. *Polym. Eng. Sci.* **1998**, *38* (12), 2039–2045.
- (124) Ashurst, W. R.; Carraro, C.; Maboudian, R. Vapor Phase Anti-Stiction Coatings for MEMS. *IEEE Trans. Device Mater. Reliab.* **2003**, *3* (4), 173–178.
- (125) Öner, D.; McCarthy, T. J. Ultrahydrophobic Surfaces. Effects of Topography Length Scales on Wettability. *Langmuir* **2000**, *16* (20), 7777–7782.
- (126) Wang, Z. L. Nanostructures of Zinc Oxide. *Mater. Today* **2004**, *7* (6), 26–33.
- (127) Uhlmann, P.; Ionov, L.; Houbenov, N.; Nitschke, M.; Grundke, K.; Motornov, M.; Minko, S.; Stamm, M. Surface Functionalization by Smart Coatings: Stimuli-Responsive Binary Polymer Brushes. *Prog. Org. Coatings* **2006**, *55* (2), 168–174.
- (128) Na, S.-I.; Kim, S.-S.; Hong, W.-K.; Park, J.-W.; Jo, J.; Nah, Y.-C.; Lee, T.; Kim, D.-Y.

Fabrication of TiO<sub>2</sub> Nanotubes by Using Electrodeposited ZnO Nanorod Template and Their Application to Hybrid Solar Cells. *Electrochim. Acta* **2008**, 53 (5), 2560–2566.

## Chapter 3

### 3. Dual pH- thermo responsive surfaces

#### 3.1. Introduction

Nowadays the main focus of the research community is on the fabrication of responsive surfaces with controllable wettability. Such surfaces can alter their wetting properties in response to external stimuli, like pH, light, solvent quality, electric field, heating, magnetic field, etc.<sup>1-7</sup> A number of smart material surfaces have been reported, which can switch between superhydrophobicity and superhydrophilicity in response to an appropriate external stimulus, with promising applications as switchable valves,<sup>8</sup> biosensors,<sup>2</sup> selective separation,<sup>4</sup> tunable microlenses<sup>9</sup> and “lab-on-a chip” devices<sup>10</sup>. Among them, the wetting properties of responsive polymers have been widely studied.<sup>11</sup> Polymer functionalized pH-responsive surfaces based on poly(2-(diisopropyl- amino)ethyl methacrylate), PDPAEMA, brushes synthesized onto hierarchically roughened inorganic surfaces, have been previously developed, which can reversibly switch between superhydrophilicity at low pH and superhydrophobicity and water repellency at pH>8.<sup>10</sup> A dual-responsive material with tunable wettability and ability to respond to both temperature and pH, based on poly(N-isopropyl acrylamide)-co-poly(acrylic acid), P(NIPAAm-co-AAc), films, was investigated by Xia, *et al.*<sup>5</sup> Despite the wide range of works reported, the fabrication of stimuli-responsive surfaces is still a challenging issue.

The investigation of the wettability of plant surfaces revealed another interesting

phenomenon, the so-called rose-petal effect.<sup>12</sup> Unlike the lotus leaf, where superhydrophobicity is accompanied by water repellency, i.e., by very low adhesion, rose petals, scallions and garlic exhibit superhydrophobic behavior with high adhesion.<sup>13,14</sup> Although the origin of high contact angle hysteresis has not been fully understood, it appears that the main factors affecting the surface adhesion are the height and density of the protrusions as well as the chemical defects.<sup>13–15</sup> In the literature, there are numerous works attempting to imitate the “adhesive” superhydrophobic behavior of these species.<sup>16–19</sup>

Besides the “sticky” superhydrophobic species, another remarkable category of plants are the so-called “parahydrophobic” plants, which exhibit high contact angles, but not above 150°, with high adhesion. An important family among this kind of species are most of the thermogenic plants, which can raise their temperature above the ambient.<sup>13</sup> Although the role of thermogenesis is still controversial, the most accepted theory is that heat attracts insect pollinators to the plants. Skunk cabbage is one of the most studied thermogenic plant, known for its ability to melt its way through frozen ground, while there is still snow and ice on the ground. The abaxial surface of the leaf has hierarchical roughness with an advancing angle of 110° and a contact angle hysteresis of 27°. The high adhesion in this case is attributed to hydrophobic defects, due to diallyl disulfide.<sup>13</sup> Leaf wettability is a determining factor for pollutant deposition, like acid rain, for plant disease and photosynthesis.<sup>20</sup> Plants with “adhesive” hydrophobicity, usually exist in regions with dry conditions as a way to minimize the water losses.<sup>21</sup> Other plants that belong to this category are the banana leaf, the red-veined prayer plant<sup>22</sup>, the oak leaves<sup>23</sup>, the ceratonia siliqua<sup>21</sup>, the majority of hairy leaves<sup>24</sup> and many others.<sup>25–27</sup> Adhesive hydrophobic materials can find applications as barrier materials, micromanipulators and oil-water separators.<sup>28</sup>

In this work, responsive surfaces with “parahydrophobic” behavior were developed, inspired by nature. For this reason poly(2-vinylpyridine), P2VP, and poly(N-isopropylacrylamide),

PNIPAm, were selected for the development of responsive surfaces. P2VP is pH responsive polymer with an effective pKa of the protonated P2VP  $\sim 5$ ,<sup>29</sup> while PNIPAm is a thermoresponsive one with a lower critical solution temperature (LCST) of approximately 32°C.<sup>4,30,31</sup> Silicon wafers were initially treated with femtosecond (fs) laser pulses in order to produce the hierarchically micro/nano-structured surfaces, the so-called Si spikes.<sup>10,32,33</sup> Organic coatings, P2VP or PNIPAm, were subsequently introduced by anchoring end-functionalized polymer chains utilizing the "grafting-to" method. The main drawback of this method is that the anchoring density of the polymer chains, which is determined by the polymer molecular weight and the strength of the end-group – surface interaction, cannot be very high as the attached polymer chains prevent the anchoring of more chains.<sup>34</sup> However, in this work this apparent disadvantage turns into an advantage as the low density lead to chemical nano-defects, which resulted to high adhesion. Moreover, the responsive behavior of the two polymers, P2VP and PNIPAm, end-anchored onto the same surface was achieved. So, a dual pH- and thermo-responsive surface, with high adhesion was developed, utilizing a mixed P2VP / PNIPAm brush. To the best of our knowledge this is the first work referring to pH/thermo responsive surfaces with “adhesive” hydrophobicity on hierarchically rough surfaces.

Finally, the Si surfaces produced using fs laser (Si spikes) with different wetting properties, and the Si spikes coated with P2VP and PNIPAm were seeded with 3T3 fibroblasts in order to examine the cell response on these substrates. Thus cell attachment and proliferation were examined for different surface wetting properties, roughness and chemistry for 7 days of cell culture.

### 3.1.1. Applications of smart polymers with reversible wettability

Stimuli-responsive polymers, also known as smart systems, are polymers which are responsive to one or more external stimuli, physical or chemical. Ionic species, pH, metabolites have been reported as chemical stimulus, while temperature, light, pressure, electricity belong to the physical signals.<sup>35</sup>

Smart polymers can be utilized for drug delivery, bio-separation, protein purification, industrial coatings, oil exploration, surface modification, microfluidic devices and water remediation.<sup>36</sup> Photoresponsive polymers, which exhibit conformation changes in response to light, have been widely studied for applications referring to photo-optical media, photo-switches, micropatterning, photo-mechanical systems, sensing, actuating and non-linear optical media.<sup>35,37-41</sup> Thermosensitive polymers have attracted the interest of the research community, due to their applications in many fields, such as functional materials<sup>42,43</sup>, drug delivery and release<sup>42</sup>, chromatography, artificial muscles<sup>44</sup>, nanotechnology,<sup>35,45</sup> tissue engineering<sup>46,47</sup> and surface modifiers.<sup>35,48</sup> Another category of smart polymers that have gained the attention are pH-sensitive polymers. These polymers have been applied for the controllable release of model compounds, drugs and proteins.<sup>41,49,50</sup> Almeida and his co-workers have reported how the temperature and pH responsive polymers can be applied in anticancer therapy.<sup>51</sup> On the other hand, electro-responsive polymeric systems have been widely studied in medicine, mechanical engineering, drug delivery, contact lenses, artificial muscles, mechanical grippers and sensors.<sup>41,52,53</sup>

Multi-responsive surfaces have also been reported in the literature. These can be achieved by synthesizing either polymers with more than one responsive functional groups or diblock copolymers, or by modifying the surfaces with more than one polymer. Kulawardana *et al.* synthesized thermo-responsive PNIPAm hydrogels, modified with pendent groups sensitive

to UV-light.<sup>54</sup> Temperature- and light- sensitive polymers have also been reported by synthesizing a thermo-responsive polymer with azobenzene<sup>55,56</sup> or spirobenzopyran<sup>57</sup> as a functional group. Furthermore dual pH and thermo sensitive polymeric systems have been developed based on PNIPAm and chitosan.<sup>58,59</sup> Guo and his co-workers fabricated a dual responsive system by the covalent attachment of poly-L-lysine on surfaces.<sup>4</sup> Tunable reversible wettability with responsivity to both temperature and pH was also achieved by grafting poly(N-isopropyl acrylamide-*co*-acrylic acid) [(P(NIPAAm-*co*-PAAc)] on both flat and rough surfaces.<sup>5</sup>

### 3.1.2. Covalent bonding of polymers on surfaces

Generally, polymer films can be deposited on solid surfaces by spin coating, precipitation, Langmuir-Blodgett, physisorption and covalent attachment (chemical grafting)<sup>60</sup>. The simplest way to immobilize polymers on surfaces is through physisorption. In this case, the one block of a block copolymer interacts strongly with the surface and the other weakly.<sup>61</sup> However such adsorbed polymer brushes can be unstable under certain conditions.<sup>34</sup> Covalently attached polymer chains can be prepared by either the “grafting to” or the “grafting from” method.<sup>34,61,62</sup> By utilizing the “grafting to” method, the functionalized polymers are reacting with functional groups located on the surfaces. Although it is a simple method, it faces the drawback of leading to low grafting densities. It has been reported that by the “grafting to” method, the previously attached chains impede the attachment of the new ones, leading to low density of polymer brushes.<sup>34</sup> In cases where high grafting density is required, the “grafting from” method can be utilized. This procedure involves the *in situ* polymerization of the monomer on an initiator functionalized surface.<sup>34</sup>

The schematic presentation of the methods for polymer chains immobilization onto solid surfaces, are depicted in Figure 3.1.

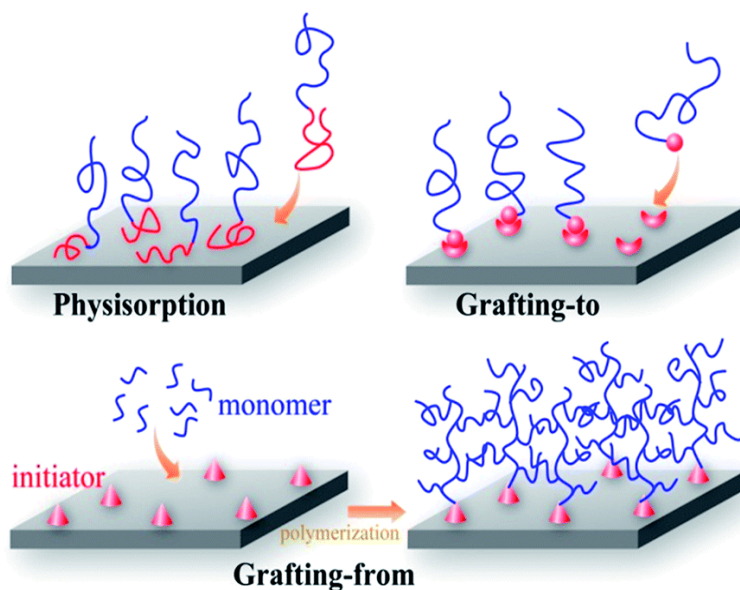


**Figure 3.1.** Schematic presentation of methods for polymer chains immobilization.

### 3.1.3. Properties of poly(N-isopropylacrylamide) ,PNIPAM

Poly(N-isopropylacrylamide) is a thermo-responsive polymer, which was first appeared in the literature in 1956.<sup>63</sup> The chemical structure of the carboxy terminated PNIPAm is depicted in Figure 3.2.

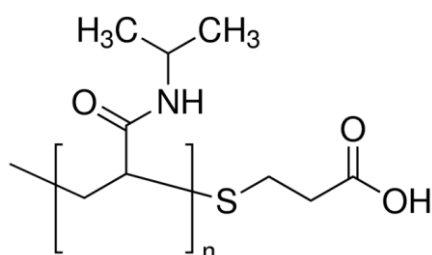


**Figure 3.2.** Chemical structure of carboxy terminated PNIPAm.

PNIPAm is probably the most popular polymer with reversible solubility upon heating, as it undergoes a sharp phase transition close to physiological temperature. The lower critical solution temperature (LCST) of PNIPAm has been determined experimentally at 30-35°C, depending on the structure of the macromolecule.<sup>63</sup> Below the LCST, enthalpic gain from intermolecular hydrogen bonding between PNIPAM and water molecules dominates the solvation; above the LCST, entropic effects resulting from the intramolecular hydrogen bonding between the carboxyl and amide groups of PNIPAM lead to water expulsion.<sup>31</sup> This phenomenon can be explained as follows.

The liquid water forms a three-dimensional, hydrogen-bonded network. The molecules which cannot participate in hydrogen bonding with water perturb the local structure of water around them and this leads to a decrease in entropy. As a result, the water is locally more ordered by the presence of foreign molecules and this leads to an increase in the free energy.

Gibbs equation:  $\Delta G = \Delta H - T\Delta S$  (G: Gibbs free energy, H: enthalpy and S: entropy)

In case that two foreign molecules are brought closer together, the extra ordering is reduced, leading to an effective attractive interaction. This interaction is known as hydrophobic interaction.<sup>63-65</sup>

Thermosensitive polymers have been widely studied due to their applications in many fields, such as functional materials<sup>42,43</sup>, drug delivery and release<sup>42</sup>, chromatography, artificial muscles<sup>44</sup>, nanotechnology<sup>35,45</sup> and surface modifiers<sup>35,48</sup>. As the LCST of PNIPAm is around the body temperature, it can be applied for controlled release of anti-cancer drugs<sup>66</sup>.

### 3.1.4. Effect of surface characteristics on cell attachment and proliferation

Cell – materials interaction is very important for materials that will be used for biomedical applications since biological integration is required.<sup>67</sup> Cells are inherently sensitive to surface characteristics; thus, the surface properties of a material play a very important role on cell attachment, proliferation and differentiation.<sup>68</sup> Cell-surface interactions are crucial in order to promote a new tissue formation since surface properties influence the initial cellular events at the cell – material interface.<sup>69,70</sup> These initial events between a solid material surface and a biological environment include oriented adsorption of a variety of biomolecules, since all organized biological systems have the ability to recognize foreign objects at molecular dimensions.<sup>71</sup> The nature of the adsorbed biomolecules affects cell recruitment, growth and differentiation.<sup>72</sup>

Cell adhesion on a surface is a very complicated process. When a material comes in contact with a biological environment, almost immediately, proteins are absorbed on its surface. The sequence of events occurring after the protein absorption is strongly dependent on the type, composition and amount of these proteins. When proteins are successfully absorbed they recruit the cells which attach, spread, migrate, proliferate and differentiate on the substrate.<sup>73</sup> On the other hand, when cells are placed in an external environment, the receptors on the cell membrane are covered with extracellular matrix (ECM) proteins which interact with the proteins that have already been absorbed on the substrate using specific ligands. Since both cell membrane and materials surface are covered by biomolecules they can exchange many different substances and form a complex and dynamic interface.<sup>71</sup>

As mentioned before, the surface of a material determines the cellular response; however, often the surface properties do not meet the requirements for specific biomedical applications and , thus, surface modification is required. The most important surface characteristics that

influence cell behavior are the surface chemistry,<sup>74,75</sup> topography and wettability. Such properties can be tailored alone or in combination to satisfy the needs for the new tissue formation.<sup>76</sup>

Several studies have shown that the surface chemistry of a material influences the binding of proteins such as immunoglobulins, vitronectin, fibrinogen and fibronectin and thus the binding of cells onto the surface.<sup>77</sup> Keselowsky *et al.* have studied the influence of well-defined chemistries such as -CH<sub>3</sub>, -OH, -COOH and -NH<sub>2</sub> and they showed that the hydrophilic -OH functionality supports highest level protein recruitment, NH<sub>2</sub> and COOH intermediate levels and CH<sub>3</sub> lowest levels.<sup>78</sup> Lee *et al.* functionalized polyethylene sheets with different functional groups (-COOH, -CH<sub>2</sub>OH, -CONH<sub>2</sub>, and -CH<sub>2</sub>NH<sub>2</sub>) groups and investigated their effect on cell adhesion. They concluded that the surfaces with amine groups were the best for cell attachment.<sup>79</sup>

Surface topography, independently of surface chemistry significantly affects cellular behavior.<sup>80</sup> Cells are very sensitive to substrates with specific nano- and micro-scale topography, for example cellular interactions with nano-micro-scale features result in alteration of cell adhesion, morphology, orientation and phagocytotic activity.<sup>81,82</sup> Cliffs, groves, ridges, hills, pits, tubes and tunnels, fibres, spikes or even random roughness are some of the most known surface structures that have been proved to influence the behavior of a variety of cells type such as fibroblasts, macrophages, osteocytes, endothelial and muscle cells.<sup>83-85</sup> In the literature, it has been reported that topographical features when inserted on a surface they enhance cell proliferation. For example osteoblasts attachment and growth has been favored when the surface they attach is textured with 100µm cavities,<sup>86</sup> epithelial cells spreading has been proved to increase with the increase of protrusions on silicon wafers,<sup>87</sup> osteoprogenitor cells proliferation has be shown to increase on electrospun polymeric fibers

compared to smooth surfaces, etc.<sup>88</sup> Several methods have been used to create micro – or nano-structured surfaces such as photolithography, microstamping, microfluidic patterning, laser irradiation, etc.<sup>89,90</sup>

Finally, surface wettability is another parameter that has been proved to affect cells fate since protein absorption is strongly dependent on surface hydrophilicity. Generally, it is believed that cells do prefer to adhere on surfaces which present moderate wettability with water contact angles between 40-70°.<sup>91</sup> Lee *et al.* have shown that surface wettability affects the growth of neurites from PC-12 cells, since the neuronal phenotype is mostly expressed at water contact angle of about 55°.<sup>92</sup> Altankov *et al.* have seeded with cells materials with different contact angles varying from 25°-111° and they concluded that fibronectin focal adhesions and actin fibers are formed mostly on hydrophilic surfaces.<sup>93</sup> However, surface wettability cannot be considered independently to surface chemistry and roughness since it is correlated to both.<sup>94,95</sup>

## 3.2. Experimental Part

### 3.2.1. Surface Modification with fs laser

Single crystal *n*-type Si(100) wafers with a resistivity of  $\rho = 2-8 \Omega\cdot\text{cm}$  were utilized as substrates for the fabrication of silicon spikes. Micro/nano-structuring of Si surfaces was performed by femtosecond (fs) laser (Yb:KGW) irradiation under a reactive gas ( $\text{SF}_6$ ) atmosphere at a pressure 500 Torr. The irradiation source with wavelength of 1026 nm and pulse duration of 170 fs was adjusted at a repetition rate of 1 kHz. The laser pulse fluences tested were 0.53, 1.4 and 2.1  $\text{J}\cdot\text{cm}^{-2}$ , and the fluence 1.4  $\text{J}\cdot\text{cm}^{-2}$  was selected as the optimum for this work. The samples were kept in a chamber, mounted on a high precision X-Y translational stage, perpendicular to the incident laser beam.<sup>50,96</sup>

### 3.2.2. Silanization and thermal oxide growth process on Silicon

In order to develop superhydrophobic surfaces, the irradiated silicon surfaces were silanized with dichlorodimethylsilane ( $(\text{CH}_3)_2\text{SiCl}_2$ , DMDCS, Sigma-Aldrich) which can assemble into high quality coatings, resulting in a material with a low surface energy. The silanized samples exhibit hydrophobic properties, which can be maintained for long periods of time and for a wide temperature range.<sup>33,97</sup>

The samples were deposited in a custom designed holder, which was then placed in laboratory Pyrex glass bottles, containing 0.5 mL of the silane. The sample was facing downwards without being in contact with the silane reagent. The vapor-phase reaction was carried out for approximately 18h at room temperature. The silanized samples were dipped into toluene (two aliquots), water (two aliquots), ethanol (two aliquots), and then water (three aliquots) and were then dried in a clean oven at 120°C for about 45min.<sup>33,98</sup>

In cases that superhydrophobicity was required, the irradiated silicon samples were placed in a box furnace and heated at 1000 °C for 45 min in air, resulting in a thick oxide layer.

### 3.2.3. End-Grafted PNIPAm and P2VP Thin Films

The laser irradiated Si substrates were initially cleaned with chloroform in a ultrasonic bath for 30 min and then placed in piranha solution (sulfuric acid and hydrogen peroxide, 3:1) for 1h. Following that, the samples were rinsed with MilliQ water and dried with a nitrogen flow.<sup>7,99,100</sup> Subsequently, the samples were heated at 1000°C for 1h at a heating rate of 25°C/min in order to achieve the formation of native oxide on the surface. After cooling, a 0.002% w/v solution of Poly(glycidyl methacrylate) (PGMA) with an average molecular weight of  $M_n \sim 20,000 \text{ g}\cdot\text{mol}^{-1}$  in chloroform, was spin coated onto the substrates and the samples were heated for 10 min at 120°C. The thin film of PGMA was utilized to enable the

formation of robust chemical bonds between the oxidized silicon substrate and the carboxy or hydroxy end-functionalized polymer chains, due to the very active epoxy groups.<sup>101–103</sup> Carboxy terminated poly(2-vinyl pyridine), P2VP ( $M_n = 10,000 \text{ g}\cdot\text{mol}^{-1}$ , PDI = 1.08 and  $53,000 \text{ g}\cdot\text{mol}^{-1}$ , PDI = 1.06), hydroxy terminated P2VP ( $M_n = 80,500 \text{ g}\cdot\text{mol}^{-1}$ , PDI = 1.17 and  $172,000 \text{ g}\cdot\text{mol}^{-1}$ , PDI = 2.3) and carboxy terminated poly(N-isopropylacrylamide), PNIPAm ( $M_n = 30,000$ ,  $43,000$  (PDI = 1.25),  $80,000$  (PDI = 1.2) and  $130,000 \text{ g}\cdot\text{mol}^{-1}$  (PDI = 1.3)), dissolved in chloroform solutions (2% w/v), were spin coated onto the samples and the coated surfaces were annealed under vacuum at  $150^\circ\text{C}$  for 24 h in order to form the layer of grafted polymer chains. To remove the ungrafted polymer chains, the samples were ultrasonicated in chloroform for 30 min. Furthermore flat Si wafers were also coated with polymers to be used as reference materials.

In order to combine the pH- and thermo-responsiveness of P2VP and PNIPAm, respectively, on one surface, a 50/50 solution of carboxy-terminated P2VP and carboxy-terminated PNIPAM in chloroform was prepared. The solution of mixed polymers was subsequently spin coated onto laser micro/nano-structured silicon samples, cleaned and functionalized with PGMA. The same procedure was repeated with 30/70 and 70/30 solutions of carboxy-terminated P2VP/PNIPAm for comparison reasons.

#### 3.2.4. Surface characterization

Silicon substrates, irradiated at a laser fluence of  $1.4 \text{ J}\cdot\text{cm}^{-2}$ , before and after the polymer anchoring, were characterized by Field Emission Scanning Electron Microscopy (FE-SEM, JEOL JSM-7000F). The thickness of the polymer films prepared on flat silicon substrates was measured by ellipsometry. Attenuated total reflection Fourier Transform Infrared (ATR-FTIR) spectra were recorded to investigate the interaction of the flat silicon surfaces with the polymer chains. A Bruker Vertex 70v FTIR spectrometer equipped with an A225/Q Platinum

attenuated total reflection (ATR) integrating sphere with single reflection diamond crystal was employed.

### 3.2.5. Wettability of the prepared samples

Wettability tests were performed using a surface tensiometer (OCA-40, Dataphysics) utilizing the sessile drop method.<sup>104</sup> Contact angle measurements of P2VP coated samples were performed after immersion of the surfaces in different pH solutions and PNIPAm coated samples after heating at different temperatures. The pH solutions were prepared by dissolving bases or acids in distilled water and the pH was measured by a pH meter (Crison, GLP21). A water drop of 2  $\mu\text{L}$  was deposited onto the sample in each case and digital images of the water droplets were taken. Sessile contact angle measurements were repeated five times for each sample. The contact angle hysteresis was defined as the difference between the advancing and receding contact angles for a contact line moving to an opposite direction.<sup>105–</sup>

107

### 3.2.6. Cell culture experiments

Laser irradiated Si surfaces coated with PNIPAm and P2VP were seeded with 3T3 fibroblasts for 7 days in order to examine the effect of the topography induced using laser and the effect of chemistry induced via the two different polymers.

All chemicals for cellular studies were purchased from Sigma-Aldrich UK. For the cell culture, the standard 3T3 embryonic murine mouse fibroblast cell line was used, and the standard protocol for the cell culture was followed. Firstly, the cell culture was prepared and afterwards the cells were seeded on the samples. The cells were cultured in S-DMEM (supplemented- DMED). The medium was supplemented with 10% foetal bovine serum (FBS), 2.4% L-glutamine, 2.4% 4-(2-hydroxyethyl)-1-piperazineethanesulfonic acid

(HEPES) buffer and 1% penicillin/streptomycin. Cells were passaged using Trypsin on the 7th day after culture in S-DMEM after they had reached approximately 70% confluency.

All samples were sterilized prior to the cell seeding using autoclave for 15 minutes at 121°C. The sterilized samples were placed in 12 well-plates and the cells together with S-DMEM were added to each well at a seeding density of 25.000 cells per sample. The cell seeded surfaces were replenished with an additional 2 mL S-DMEM and incubated at 37°C at 5% CO<sub>2</sub> and 100% relative humidity. The medium in each sample was changed every 3 days.

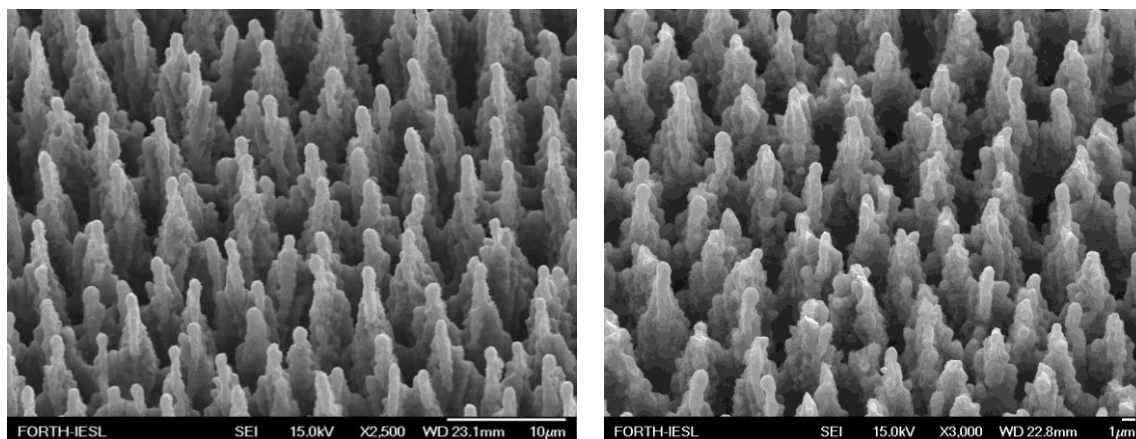
The cell seeded surfaces were visualized using SEM. The operating voltage was 10 kV, the working distance was 10 mm and the spot size was 3. Prior to testing, the cell seeded samples were chemically fixed using 2.5% glutaraldehyde for 24 h and dehydrated with ethanol. Afterwards, the samples were washed in 70, 90 and 100% aqueous ethanol solutions for 30 min followed by 100% dried ethanol for additional 30 min. The samples were then placed in liquid CO<sub>2</sub> at 1070 psi and 31°C for 60 min. Finally, the specimens were Pt coated by a sputtering method using 25 mA and 1.5 kV and the thickness of sputtered Au was between 10-12 nm.

### 3.3. Results and Discussion

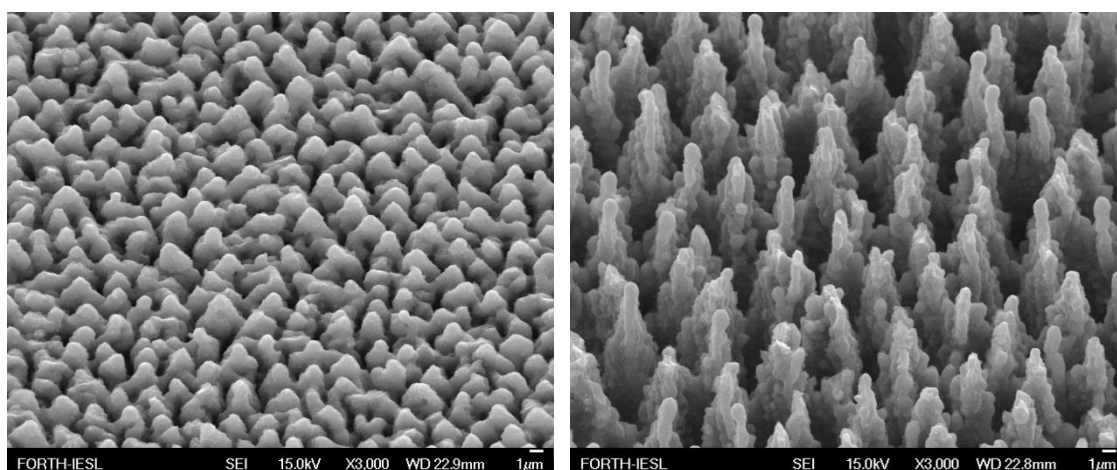
#### 3.3.1. Surface characterization of polymer coated surfaces

Figure 3.3 depicts the SEM micrographs of the Si substrates, irradiated at a laser fluence of 1.4 J·cm<sup>-2</sup>, before and after the coating with the end-anchored polymer. Comparison of the two samples, without and with the carboxy terminated grafted P2VP ( $M_n = 53,000$  g·mol<sup>-1</sup>), leads to the conclusion that the procedure for the formation of the polymer brushes did not affect the hierarchical micro- and nano-structure of the artificial surface. According to ellipsometry results, the thickness of the respective P2VP film onto a flat Si substrate was

found to be  $8 \pm 2$  nm. Similar were the results for the surfaces with PNIPAm chains ( $M_n = 43,000$  g·mol<sup>-1</sup>). The anchoring density,  $\sigma$ , of the P2VP brushes was found to be 0.1 chains·nm<sup>-2</sup> and for the PNIPAm brushes 0.12 chains·nm<sup>-2</sup>. For comparison reasons, the surface characterization procedure was repeated for samples, irradiated of 0.5 and 2.1 J·cm<sup>-2</sup> (Figure 3.4).



**Figure 3.3.** Micro/nano-structured Si substrate by fs-laser irradiation (at 1.4 J·cm<sup>-2</sup> fluence) under reactive SF<sub>6</sub> atmosphere before (left) and after (right) coating with P2VP brushes.



**Figure 3.4.** Microstructured Si surface by fs-laser irradiation under reactive SF<sub>6</sub> atmosphere irradiated at 0.5 (left) and 2.1 J·cm<sup>-2</sup> (right) after coating with P2VP brushes.

Figure 3.5 shows the FTIR-ATR spectra of the respective flat silicon substrates coated with end-anchored PNIPAM ( $M_n = 43,000 \text{ g}\cdot\text{mol}^{-1}$ ) and P2VP ( $M_n = 53,000 \text{ g}\cdot\text{mol}^{-1}$ ) chains as well as with the grafted 50/50 mixture of P2VP and PNIPAm chains.

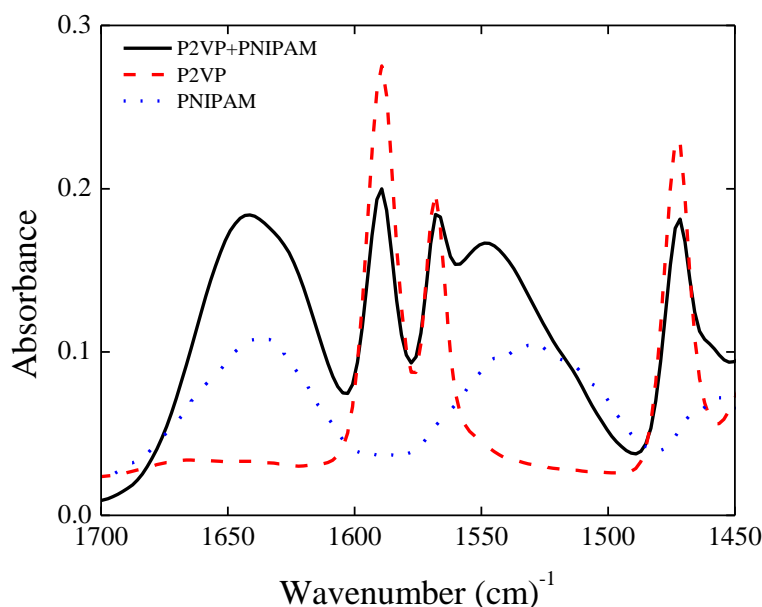


**Figure 3.5.** ATR-FTIR spectra of the P2VP brush, the PNIPAm brush and the 50/50 mixed P2VP/PNIPAm brush.

The characteristic absorption bands of P2VP due to pyridine group are evident at 1475, 1570 and 1590  $\text{cm}^{-1}$  in the spectra for the P2VP brush, while the amide bands of PNIPAm at 1530 and 1645  $\text{cm}^{-1}$  are evident in the spectra for the PNIPAm brush. In the case of the mixed brush, the characteristic peaks of both the amide and pyridine groups were identified,<sup>108</sup> which proves the successful anchoring of both polymers. Comparing the spectra of the mono and mixed brushes, a shift of the amide band was observed from 1530 to 1550  $\text{cm}^{-1}$ , probably due to interactions between the two polymers.

### 3.3.2. Wettability of polymer coated surfaces

#### Wettability of P2VP coated surfaces

P2VP brushes present switching properties upon exposure to different pH values. For low pH, the chains exhibit a hydrophilic behavior due to protonation of the pyridine nitrogen, while, for high pH, the chains turn back to hydrophobic. Carboxy-terminated P2VP ( $M_n = 53,000 \text{ g}\cdot\text{mol}^{-1}$ ) coated samples were immersed for 20 min in aqueous solution of pH 2 and pH 9 and the contact angles were measured. Figure 3.6 depicts the results after the exposure of the surface in the different pH solutions.

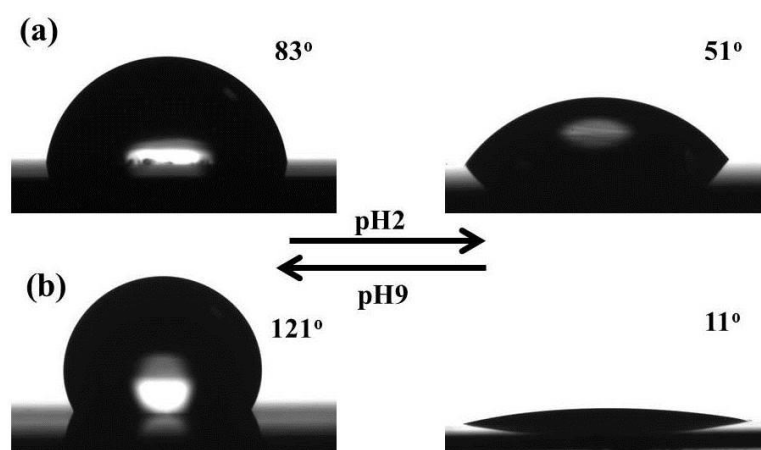


**Figure 3.6.** Photographs of representative water drops and the respective contact angles on (a) flat Si and (b) laser micro/nano-structured Si substrates ( $1.4 \text{ J}\cdot\text{cm}^{-2}$ ) coated with P2VP brushes ( $M_n = 53,000 \text{ g}\cdot\text{mol}^{-1}$ ) following immersion in high and low pH solutions (pH 9 and pH 2, respectively).

The contact angle of the water on the coated flat silicon substrate was measured at  $\sim 83^\circ$  after immersion in a pH 9 solution and  $\sim 51^\circ$  in a pH 2 solution. In the case of the hierarchically roughened surface, the difference between the static contact angle measurements after the immersion in pH 2 and pH 9 solutions was higher ( $11^\circ$  and  $121^\circ$ , respectively), due to the

micro/nano-structuring of the surface. The irradiated silicon sample coated with P2VP was found to be superhydrophilic at low pH and hydrophobic at pH 9 with a contact angle hysteresis of  $\sim 27^\circ$ , representing the behavior of skunk cabbage leaf.<sup>13</sup> It should be mentioned that Si substrates, irradiated under identical conditions and coated with dichlorodimethylsilane (a hydrophobic silane), were found to be superhydrophobic, with contact angles of  $\sim 160^\circ$ , with a very low contact angle hysteresis (Figure 3.7). Once more, this proves that the hierarchical roughness requires the appropriate chemistry in order to lead to superhydrophobicity and superhydrophilicity.

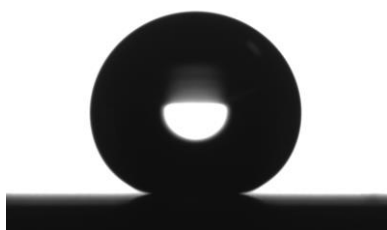


**Figure 3.7.** Photograph of representative water drop Si Laser irradiated substrate coated with dichlorodimethylsilane.

In order to study the reproducibility and stability of the system, samples were subjected to cycles of immersion in high and low pH successively and the wettability was investigated (Figure 3.8). According to the results, both systems, Si flat and Si spikes coated with P2VP, proved to be reproducible and stably responsive in the change of the pH environment.

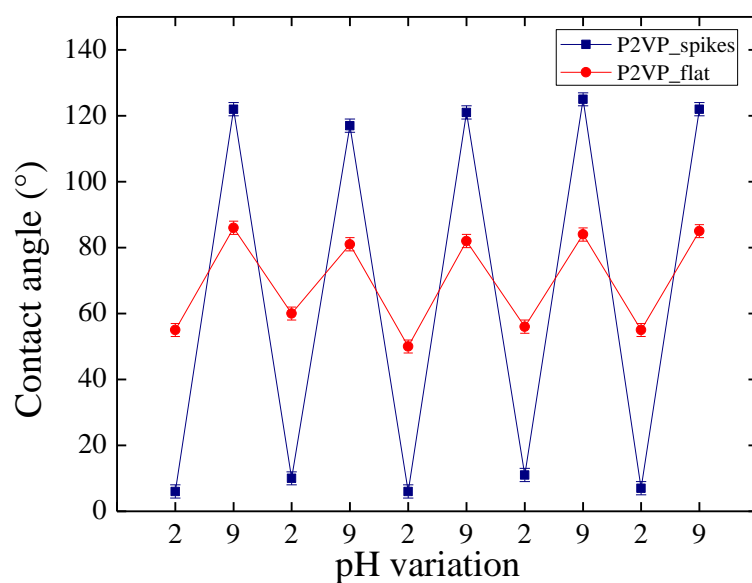


**Figure 3.8.** Average contact angle values of water droplets onto flat Si substrate and Si spikes (irradiated at  $1.4 \text{ J}\cdot\text{cm}^{-2}$ ) coated with P2VP brushes ( $M_n = 53,000 \text{ g}\cdot\text{mol}^{-1}$ ), for 5 cycles of pH environment changes.

Wettability tests were also performed on P2VP-coated substrates which were irradiated at different laser fluences. For a higher fluence ( $2.1 \text{ J}\cdot\text{cm}^{-2}$ ), there was no difference in the results while, for a lower fluence ( $0.53 \text{ J}\cdot\text{cm}^{-2}$ ), the results were reproducible but with a lower contact angle value variation (Figure 3.9).

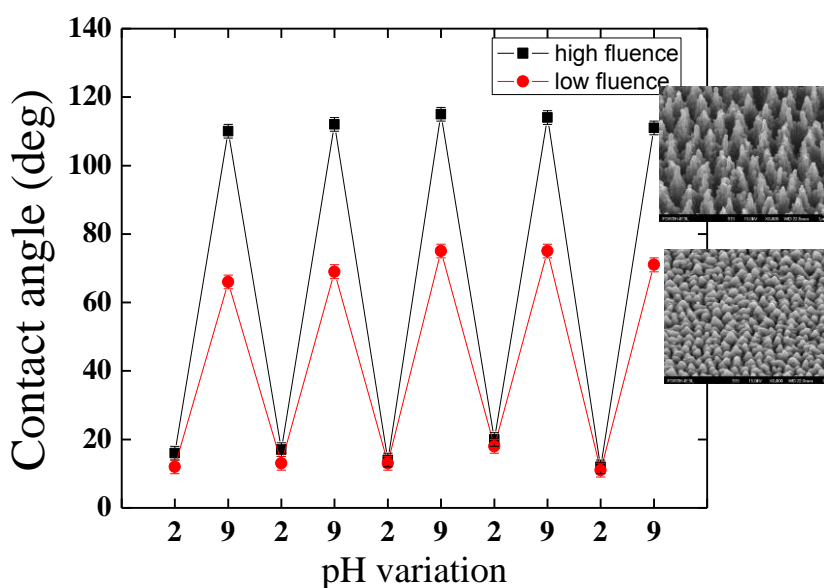


**Figure 3.9.** Average contact angle values of water droplets onto Si spikes coated with P2VP brushes ( $M_n = 53,000 \text{ g}\cdot\text{mol}^{-1}$ ), irradiated at 0.5 (circles) and 2.1  $\text{J}\cdot\text{cm}^{-2}$  (squares), for 3 cycles of pH environment changes. Insets are SEM images of the micro-structured Si surfaces coated with P2VP brushes, irradiated at 0.5 and 2.1  $\text{J}\cdot\text{cm}^{-2}$  respectively.

The same procedure was repeated for P2VP brushes with different molecular weights. In the case of carboxy-terminated P2VP with  $M_n = 10,000 \text{ g}\cdot\text{mol}^{-1}$ , there was no responsive behavior observed. It has been reported that the molecular weight affects the charge density per molecule; a polymer with lower molecular weight shows lower charge density for the polyelectrolyte.<sup>109</sup>

In contrast, responsive behavior was detected for the laser irradiated silicon substrates functionalized with hydroxyl-terminated P2VP of  $M_n = 80,500$  and  $172,000 \text{ g}\cdot\text{mol}^{-1}$ . In both cases, the contact angle values were fluctuating between  $\sim 110^\circ$  following immersion in a pH 9 solution to  $\sim 20^\circ$  following immersion in a pH 2 one, with a hysteresis of  $\sim 28^\circ$  (Figures 3.10 and 3.11). The small difference of  $\sim 10^\circ$ , compared to the lower molecular weight, is probably attributed to the lower mobility of the chains.<sup>110</sup>

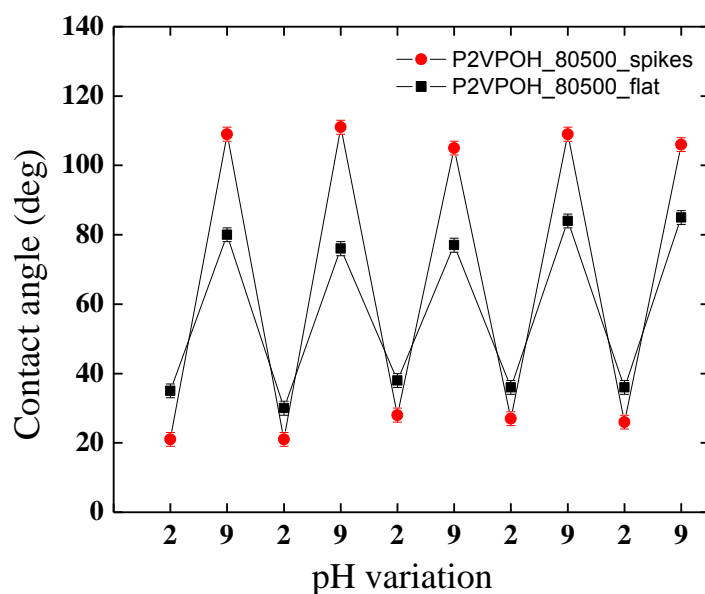


**Figure 3.10.** Average contact angle values of water droplets onto flat Si substrate (squares) and Si spikes (circles) coated with hydroxyl terminated P2VP brushes ( $M_n = 80,500 \text{ g}\cdot\text{mol}^{-1}$ ), for 5 cycles of pH environment changes.

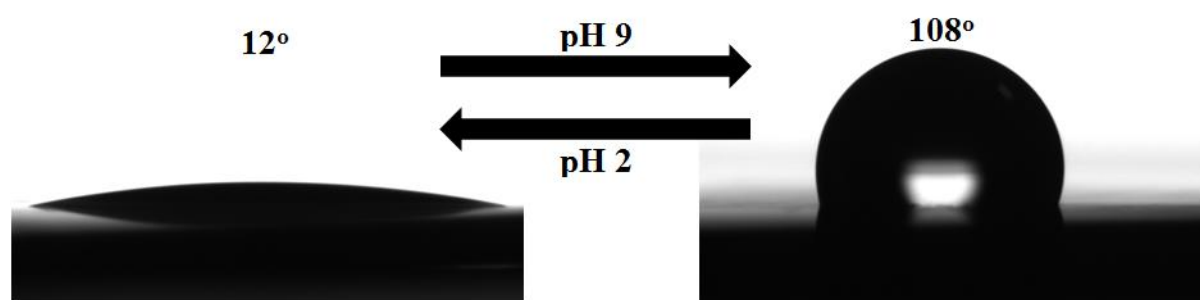


**Figure 3.11.** Representative water droplets onto flat Si substrate and Si spikes coated with hydroxyl terminated P2VP brushes ( $M_n = 172,000 \text{ g}\cdot\text{mol}^{-1}$ ), after immersion in high and low pH solutions.

### Wettability of PNIPAm coated surfaces

At temperatures below the lower critical solution temperature, LCST, of the PNIPAm solutions, the PNIPAm brushes are arranged into a swollen and hydrated conformation, while at temperatures above 32°C, the chains are hydrophobic and, thus, collapsed.<sup>111-113</sup> Carboxy-terminated PNIPAm chains ( $M_n = 43,000 \text{ g}\cdot\text{mol}^{-1}$ ) were end-grafted onto the silicon surfaces according to the procedure described in the experimental part. The wettability of the PNIPAm coated samples was investigated at ambient temperature (25°C) and at 40°C. The heating of the samples was performed with a heating rate of 0.2°C/min under nitrogen flow and the samples remained at 40°C for 4h before measuring. It has been found that humidity affects the characteristic properties of the polymer and the water absorption dynamics, so the nitrogen flow played an important role for the reproducibility of the experimental conditions during the procedure of the contact angle measurements;<sup>31</sup> exposure to different humidity conditions has been shown to be a stimulus that can modify the surface behavior of polymer films as well.<sup>114</sup> Figure 3.12 shows images of water droplets on flat and laser irradiated silicon substrates, coated with end-anchored PNIPAm chains ( $M_n = 43,000 \text{ g}\cdot\text{mol}^{-1}$ ), following temperature treatments at 25°C and 40°C.

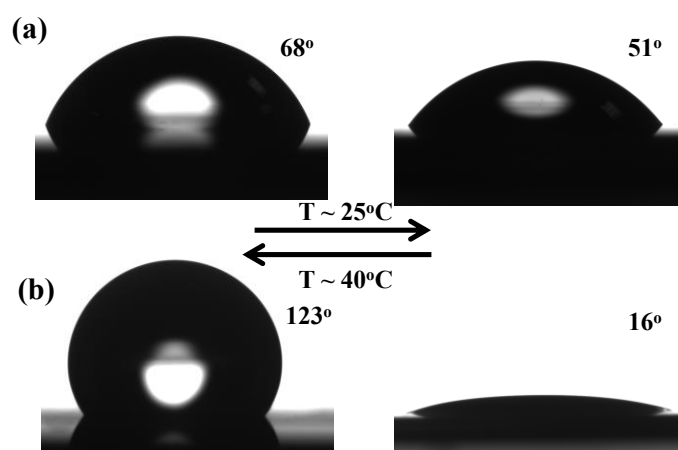


**Figure 3.12.** Photographs of representative water drops and the respective contact angles on (a) flat silicon and (b) laser micro/nano-structured silicon substrates (at  $1.4 \text{ J}\cdot\text{cm}^{-2}$  fluence) coated with PNIPAm brushes ( $M_n = 43,000 \text{ g}\cdot\text{mol}^{-1}$ ) following temperature treatments at  $25^\circ\text{C}$  and  $40^\circ\text{C}$ .

In case of the laser irradiated silicon substrate, the static contact angles were measured as  $16^\circ$  (at  $25^\circ\text{C}$ ) and  $123^\circ$  (at  $40^\circ\text{C}$ ), behavior similar to that of the pH-responsive surface described above. A significant contact angle hysteresis of approximately  $29^\circ$  was measured for the hydrophobic state, which is in agreement with literature.<sup>115,116</sup> Flat silicon substrates, similarly coated with the same PNIPAm chains, were also measured as reference and the contact angles were measured to change from  $\sim 51^\circ$  (at  $25^\circ\text{C}$ ) to  $\sim 68^\circ$  (at  $40^\circ\text{C}$ ). Comparison of the flat and the laser irradiated surfaces illustrates the influence of the laser micro/nano-structuring of the surfaces on the amplification of the effects of surface chemistry. The stability of the systems was investigated through ten repeated cycles of contact angle measurements after heating and cooling of the specimens. Figure 3.13 shows the results for 5 cycles.

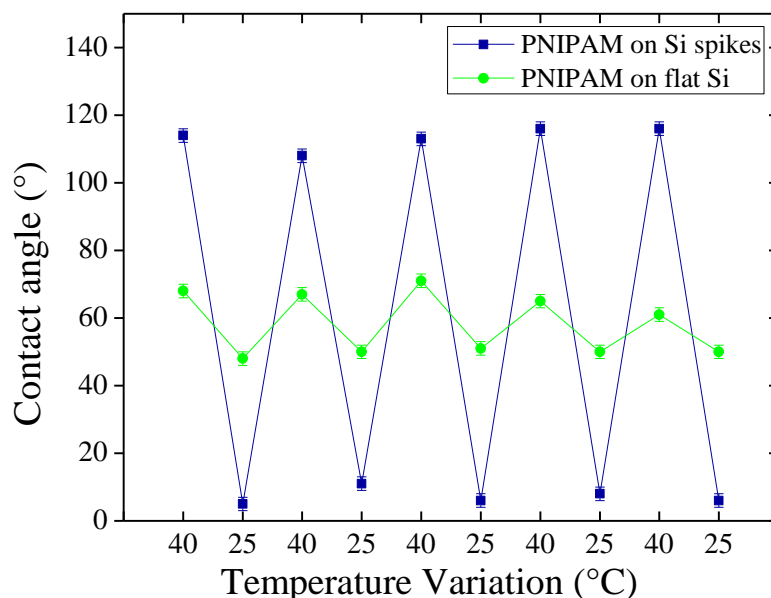


**Figure 3.13.** Average contact angle values of water droplets onto flat Si substrates (circles) and Si spikes (squares), irradiated at  $1.4 \text{ J}\cdot\text{cm}^{-2}$  and coated with PNIPAm brushes ( $M_n = 43,000 \text{ g}\cdot\text{mol}^{-1}$ ), for 5 cycles of temperature changes.

In parallel, surfaces were prepared with end-anchoring of PNIPAm chains of different molecular weights. According to literature, low-molecular weight PNIPAm chains do not collapse above the LCST.<sup>112,115</sup> Indeed, when the same procedure was repeated for carboxy-terminated PNIPAm chains ( $M_n = 30,000 \text{ g}\cdot\text{mol}^{-1}$ ) end-anchored onto irradiated silicon substrates at the same fluence, the results were slightly different, with a contact angle of  $\sim 85^\circ$  (at  $40^\circ\text{C}$ ). In contrast, when PNIPAm chains with  $M_n = 80,000 \text{ g}\cdot\text{mol}^{-1}$  and  $130,000 \text{ g}\cdot\text{mol}^{-1}$  were end-anchored onto the substrates, the results were almost the same with the case in Figs. 3.12 - 3.13. The systems were stable and reproducible with the contact angle fluctuating from  $\sim 10^\circ$  (at  $25^\circ\text{C}$ ) to  $\sim 120^\circ$  (at  $40^\circ\text{C}$ ) (Figure 3.14 and 3.15).

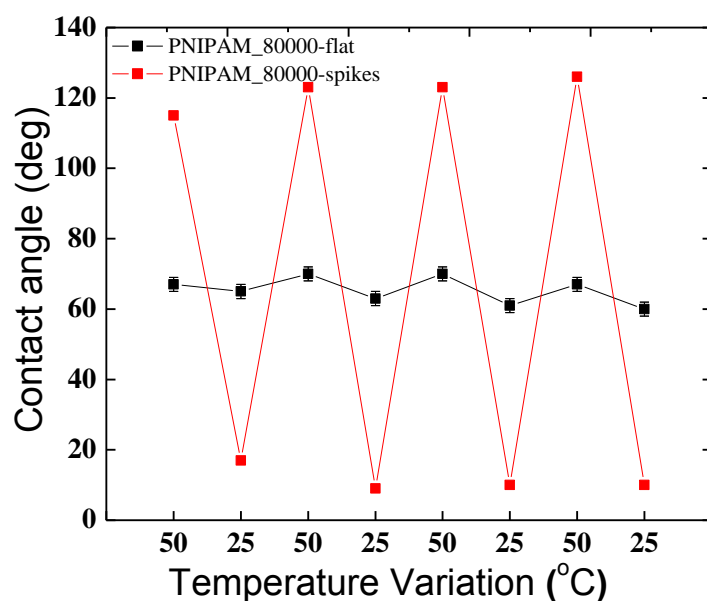


**Figure 3.14.** Average contact angle values of water droplets onto flat Si substrate (squares) and Si spikes (circles) coated with PNIPAm brushes ( $M_n = 80,000 \text{ g}\cdot\text{mol}^{-1}$ ), for 5 cycles of temperature change.

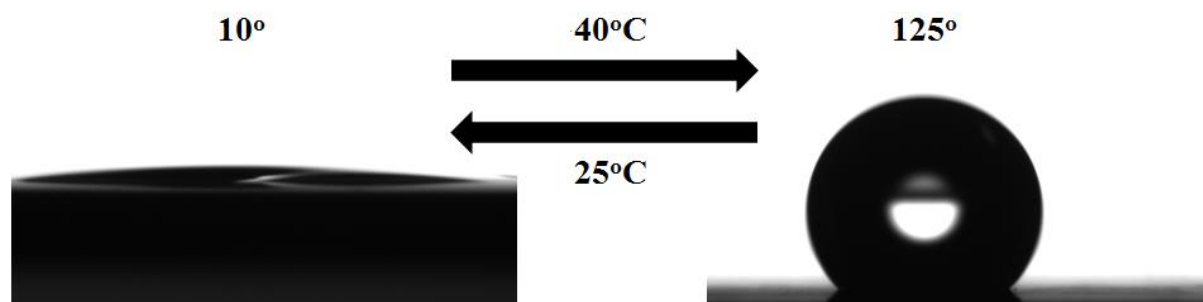


**Figure 3.15.** Representative water droplets onto flat Si substrate and Si spikes coated with hydroxyl terminated PNIPAm brushes ( $M_n = 130,000 \text{ g}\cdot\text{mol}^{-1}$ ), before and after heating.

### Wettability of P2VP/PNIPAm mixed coated surfaces

In order to achieve a multi-responsive system and to combine the pH- and thermo-responsiveness in one surface, samples were fabricated with mixed brushes of P2VP ( $M_n = 53,000 \text{ g}\cdot\text{mol}^{-1}$ ) and PNIPAm ( $M_n = 43,000 \text{ g}\cdot\text{mol}^{-1}$ ). For this purpose solutions in chloroform with composition ratios 30/70, 50/50 and 70/30 of the above polymers were prepared. These solutions were spin coated onto the laser irradiated micro/nano-structured silicon substrates, after the anchoring of the PGMA, according to the procedure described in the experimental part. The samples were tested for their wettability in response to pH and temperature variations. Table 3.1 presents the results from the contact angle measurements. At 25°C and pH 2, the PNIPAm are hydrophilic and the P2VP ones are positively charged, which means that the surfaces are superhydrophilic independently of the polymer composition. In the opposite scenario, at 40°C and pH 9, when both polymers are in a hydrophobic state, high hydrophobicity is expected. In the case of 25°C and pH 9, the PNIPAm chains are hydrophilic whereas the P2VP ones are hydrophobic. So, the contact angle values are expected to increase gradually with increasing the ratio of the P2VP chains in the brush layer; indeed, the contact angle values increase from 64°, when the P2VP/PNIPAm ratio is 30/70, to 95°, when the ratio is 50/50, and to 110°, when the P2VP/PNIPAm ratio is 70/30. The opposite behavior is observed for the conditions of 40°C and pH 2, where the P2VP chains are charged and, thus, hydrophilic, whereas the PNIPAm chains are hydrophobic, with the contact angles being higher for high ratios of PNIPAm brushes (82°, when the P2VP/PNIPAm ratio is 30/70, and 115-112°, when the ratio is 50/50 and 70/30).

**Table 3.1.** Average contact angle values of water droplets onto micro/nano-structured silicon substrates coated with mixed P2VP/PNIPAm brushes of three different P2VP/PNIPAm ratios: 30/70, 50/50 and 70/30.

Temperature (°)	pH	Contact angle values(°)		
		P2VP/PNIPAm: 30/70	P2VP/PNIPAm: 50/50	P2VP/PNIPAm: 70/30
25	2	17	20	14
	9	64	95	130
40	2	82	115	112
	9	127	125	135

It should be mentioned here that, when one compares the results from the samples coated with mono-functional brushes with the ones coated with the mixed brush, the surfaces coated with mixed brush are more hydrophobic, probably due to interactions between the two kinds of chains.<sup>101</sup> In contrast, no significant difference was observed in the calculation of hysteresis values (28°).

To illustrate further the effect of pH and temperature on the wettability of the dual responsive surface, the contact angles were measured as a function of pH and temperature for the sample with a mixed 50/50 P2VP/PNIPAm brush and the results are summarized in the following Figure 3.16.

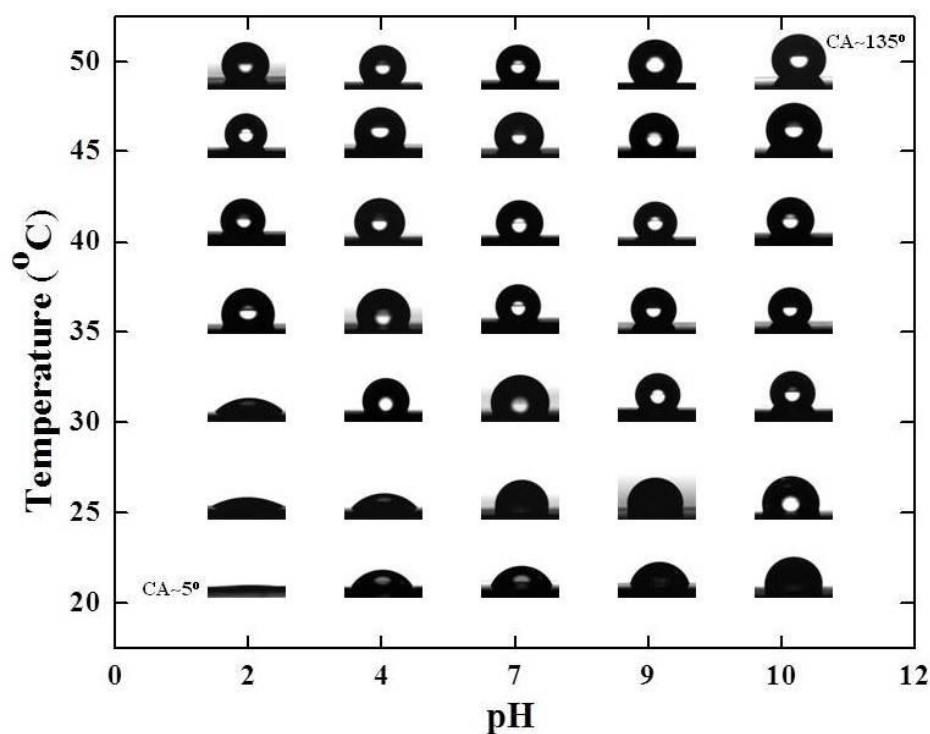


**Figure 3.16.** Photographs of representative water drops and the respective contact angle values for a hierarchically roughened silicon substrate coated with a mixed 50/50 P2VP/PNIPAm brush exposed to immersion to solutions of different pH and exposure to different temperatures.

At temperatures below 30°C, the contact angle values increase from ~5° to ~90° by increasing the solution pH from 2 to 10. However, for the case of a constant pH 2 and by increasing temperature from 20°C to 50°C, the contact angle value increase from ~5° to ~123°. This means that probably the hydrophobicity of the PNIPAm chains dominate in the competition between the two polymers and the temperature effect is more pronounced than the pH effect. At 30°C, which is close to the LCST of PNIPAm, the contact angle values measured by increasing the solution pH changed from ~20° to ~125°, with a rapid increase at pH 4 (~95°), which is close to the pKa of P2VP. At temperatures above the LCST of PNIPAm, there is no obvious change in the wettability results, which also supports the hypothesis that the influence of the PNIPAm chains is stronger in comparison to that of the P2VP ones.

The dually responsive surfaces were subjected to pH/thermo cycles in order to test their stability. Figure 3.17 shows the results following 5 cycles of immersion in a pH 2 solution and exposure to 25 °C vs. immersion in a pH 10 solution and exposure to 50°C.

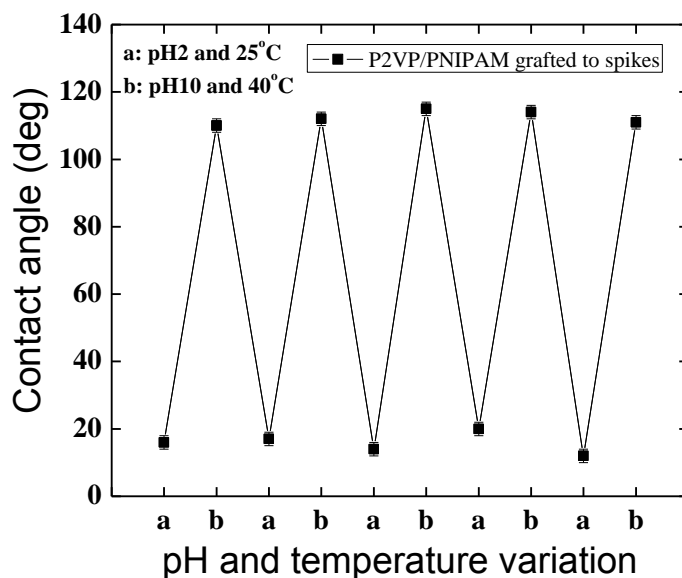


**Figure 3.17.** Average contact angle values of water droplets onto Si spikes (irradiated at 1.4 J·cm<sup>-2</sup>) coated with a mixed 50/50 P2VP/PNIPAm brush, for 5 cycles of pH / temperature variation.

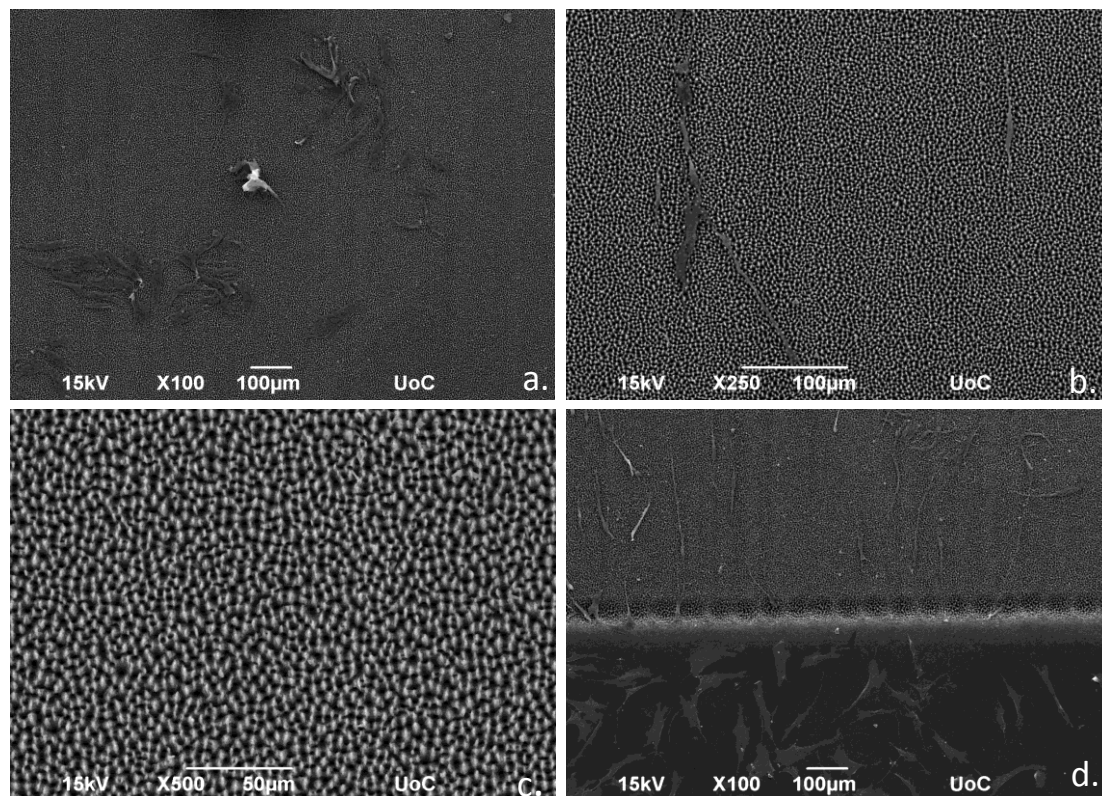
The sample with the P2VP/PNIPAm brushes proved to be stable with controllable and reproducible wettability changes. The average contact angle value were measured as ~15°, when the samples were immersed in solutions with pH 2 at 25°C and ~120° when the samples were immersed in solutions with pH 10 at 50°C, i.e., when both polymers are hydrophobic and collapsed.

### 3.3.3. Cell adhesion to polymer surfaces

Bare laser irradiated Si substrates with different wetting properties, and laser irradiated Si substrates coated with P2VP and PNIPAm were seeded with 3T3 fibroblasts for 7 days. The behavior of the cells on the bare and polymer coated substrates as well as the effect of the topographical features, were examined using SEM for days 1 and 7 of the cell culture.

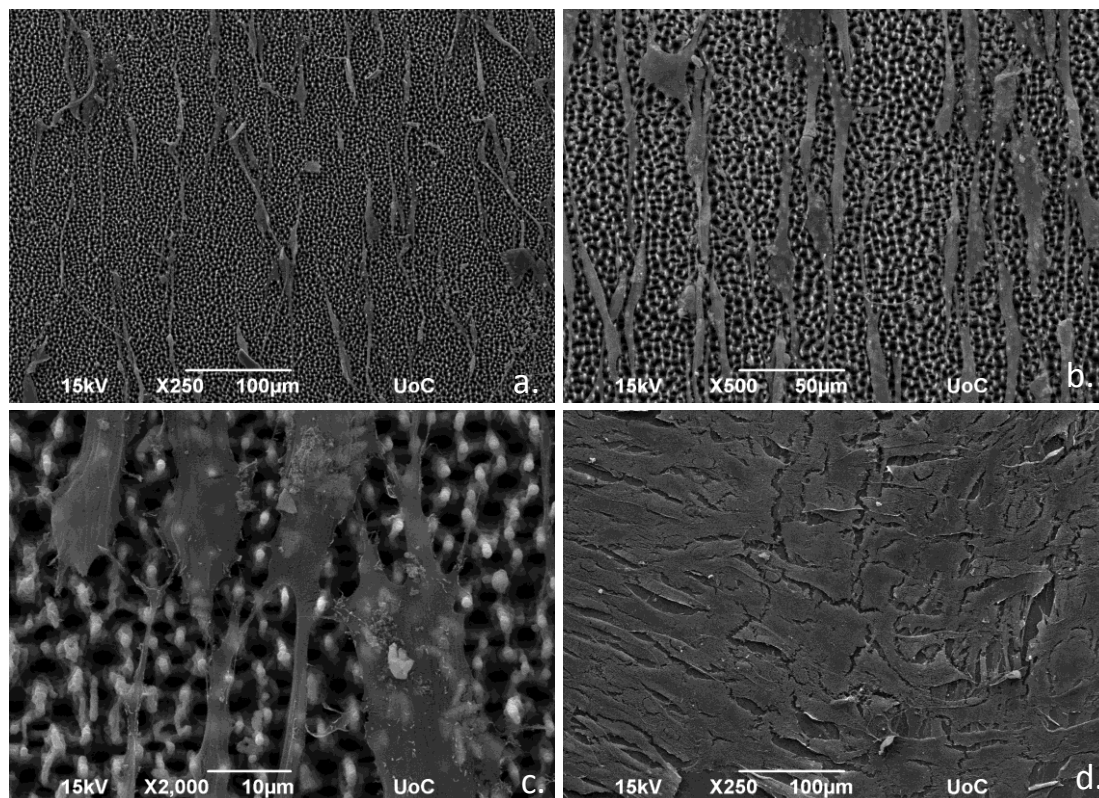
#### Cell seeding on surfaces with different wetting behavior

Figures 3.18 – 3.20 show fibroblasts seeded on laser irradiated Si substrates with different wettability for 7 days of cell culture. Figure 3.18 shows different magnifications of the bare Si surfaces after thermal oxidation, seeded with fibroblasts for 7 days. In this case, the water contact angle was  $8^\circ$ . Figures 3.18 a – 3.18 c show that very few cells were attached on the hydrophobic surface, and thus no proliferation or cell adhesion occurred. Figure 3.18 d, where we can see the border between the surface with spikes and the surface without spikes, shows clearly that cells grow, attach and proliferate on the untreated surface. So, the area treated with laser together with the super-hydrophilic character induced by the thermal oxidation process, inhibits cell attachment.



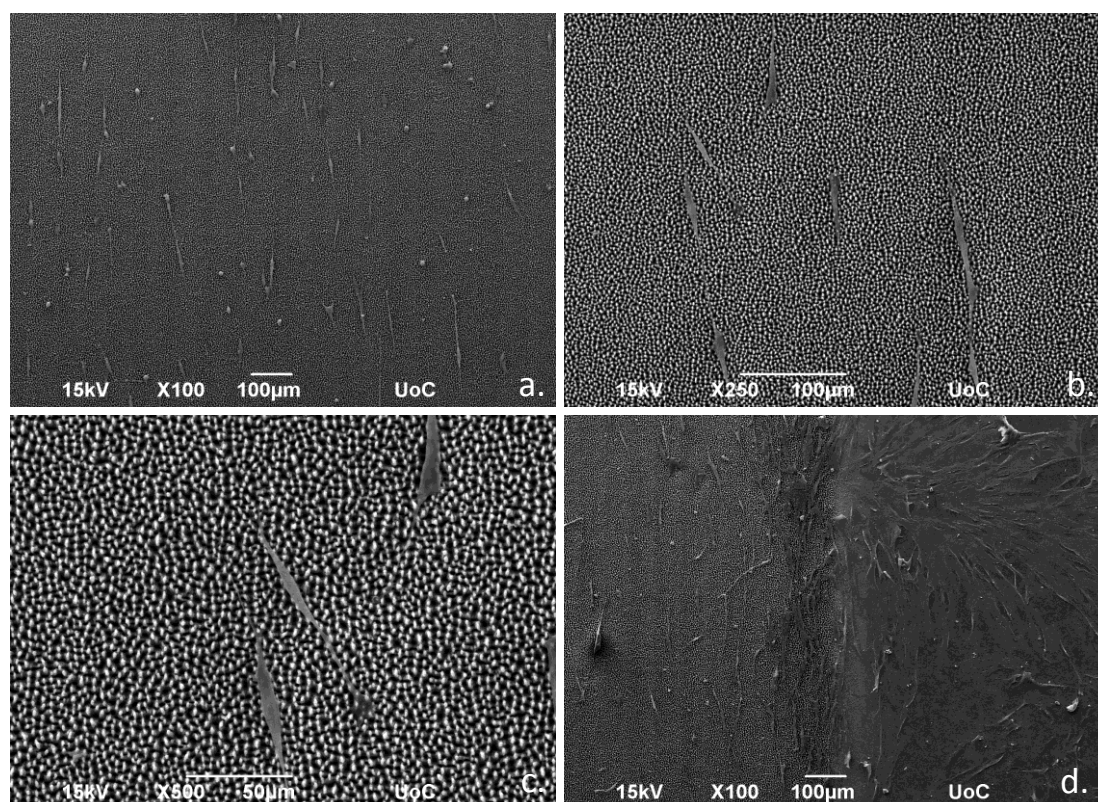
**Figure 3.18.** A, B, C) Different magnifications of the micro-structured Si surface irradiated with  $1.4 \cdot \text{J cm}^{-2}$  after thermal oxidation and seeded with fibroblasts for 7 days. D) Border between the surface with spikes and the surface without spikes, after thermal oxidation and seeded with fibroblasts for 7 days.

Figure 3.19 shows different magnifications of the cell seeded bare Si irradiated surface without any treatment. In this case, the Si irradiated surface has a contact angle of  $80^\circ$ . Figures 3.19 a-c shows that cells grow and proliferate after 7 days of culture. They also appear to grow with a specific directionality, being elongated in one direction, the direction of the laser irradiation. Figure 3.19 c shows that cells not only grow on the surface with the spikes but they are also interconnected and their cytoplasmic projections also follow the direction of the spikes. Figure 3.19.d shows the area of the same sample without spikes. There the cell proliferation is much higher, and within 7 days of culture cells have already formed layers.



**Figure 3.19.** A, B, C) Different magnifications of the micro-structured Si surface irradiated with  $1.4 \cdot \text{J cm}^{-2}$ , without treatment, seeded with fibroblasts for 7 days. D) Bare silicon substrate without spikes seeded with fibroblasts for 7 days.

Figure 3.20 shows different magnifications of the cell seeded Si surface irradiated with  $1.4 \cdot \text{J cm}^{-2}$  and treated with dichlorodimethylsilane. In this case the contact angle of the Si spikes is  $155^\circ$ , while for the Si substrate without spikes is  $70^\circ$ . Similarly to Figure 3.18, here there is not significant cell attachment or proliferation. The superhydrophobic character of the surface induced by the silane, do not favor cell growth. This is clear from figure 3.20 a-c, where very few cells can be observed on the surface of the spikes; however, on the surface without spikes for the same sample that cells grow and proliferate, as it can be seen in Figure 3.19 d.



**Figure 3.20.** A, B, C) Different magnifications of the micro-structured Si surface irradiated with  $1.4 \cdot \text{J cm}^{-2}$ , treated with dichlorodimethylsilane and seeded with fibroblasts for 7 days. D) Border between the surface with spikes and the surface without spikes, after treatment with dichlorodimethylsilane and seeded with fibroblasts for 7 days.

The SEM images of the surfaces with different water contact angles that were seeded with fibroblasts showed clearly that cells do not prefer to adhere and proliferate on the superhydrophobic or superhydrophilic surfaces, on the contrary their preference is to grow on the surface with contact angle  $80^\circ$ . These results are in agreement with the literature. The wettability of a surface when placed in a biological environment is responsible for the initial adsorption of proteins. As more proteins are absorbed on a surface, more cells are attaching and grow.<sup>117</sup> Generally, high levels of protein absorption have been found on surfaces with moderate water contact angles with a preference on hydrophilic surfaces, and as a consequence cellular response on these surfaces is more positive.<sup>95,118</sup> Lee *et al.* have studied the adhesion of different cell types and the absorption of serum proteins on surfaces with

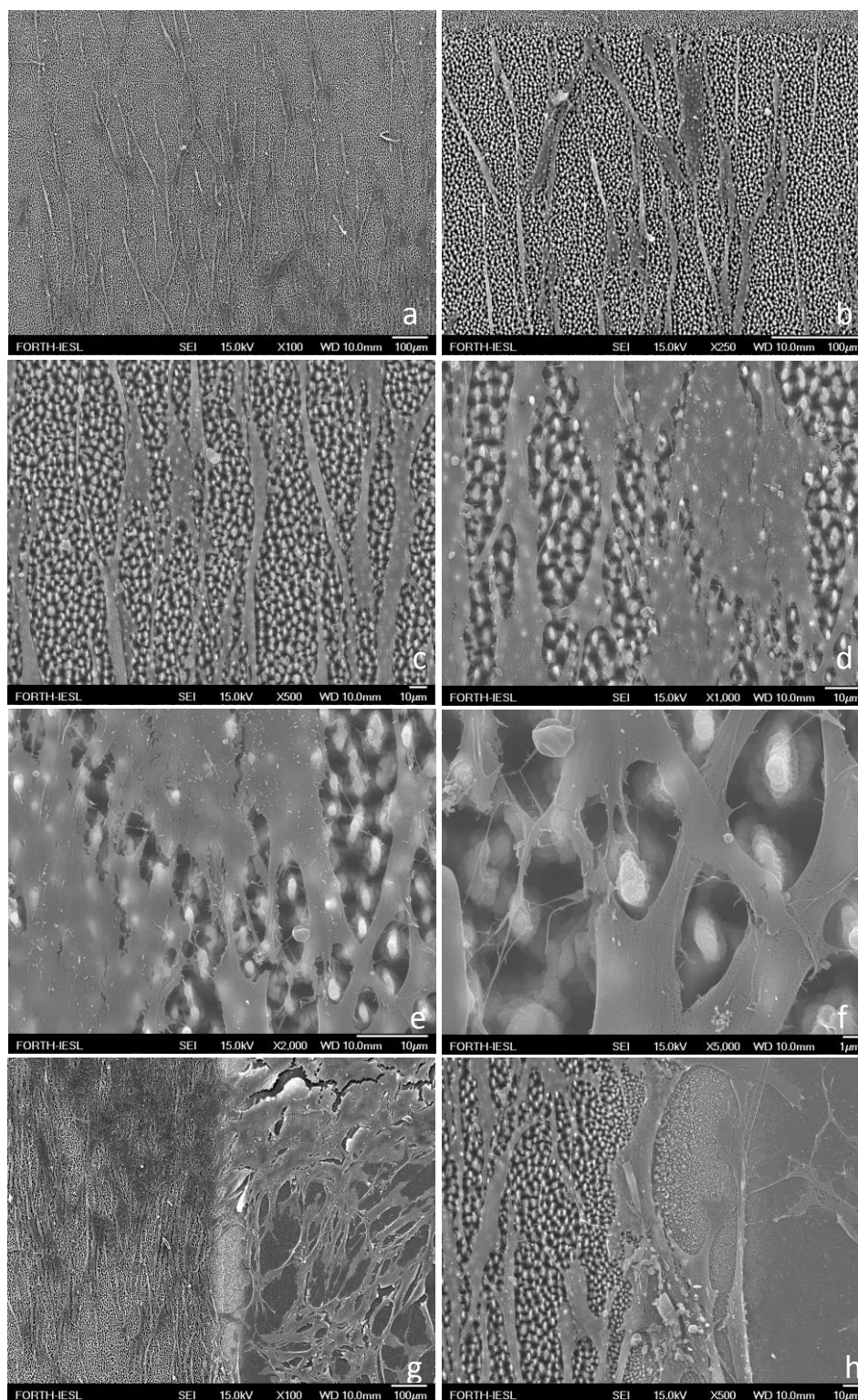
wettability gradient. They observed that cells, independently on their type, adhered and proliferated on the surfaces with moderate hydrophilicity, this observation was in accordance with the protein adsorption on the surfaces with similar wetting characteristics.<sup>119</sup> Similarly, Dowling *et al.* studied cell attachment on surfaces with water contact angles in the range of 12-122°. The optimum contact angle for the cell behavior was found at 64°.<sup>120</sup> Since the wettability of a surface is strongly dependent on the surface chemistry and structure, the cellular behavior is always considered as a result of both parameters.<sup>121,122</sup> Commonly the effect of the surface wettability is explained in terms of free energy of adhesion or is related to the ability of the surface to absorb the proteins responsible for cells attraction.<sup>123</sup>

### **Cell seeding on Si laser irradiated surfaces coated with P2VP an PNIPAm**

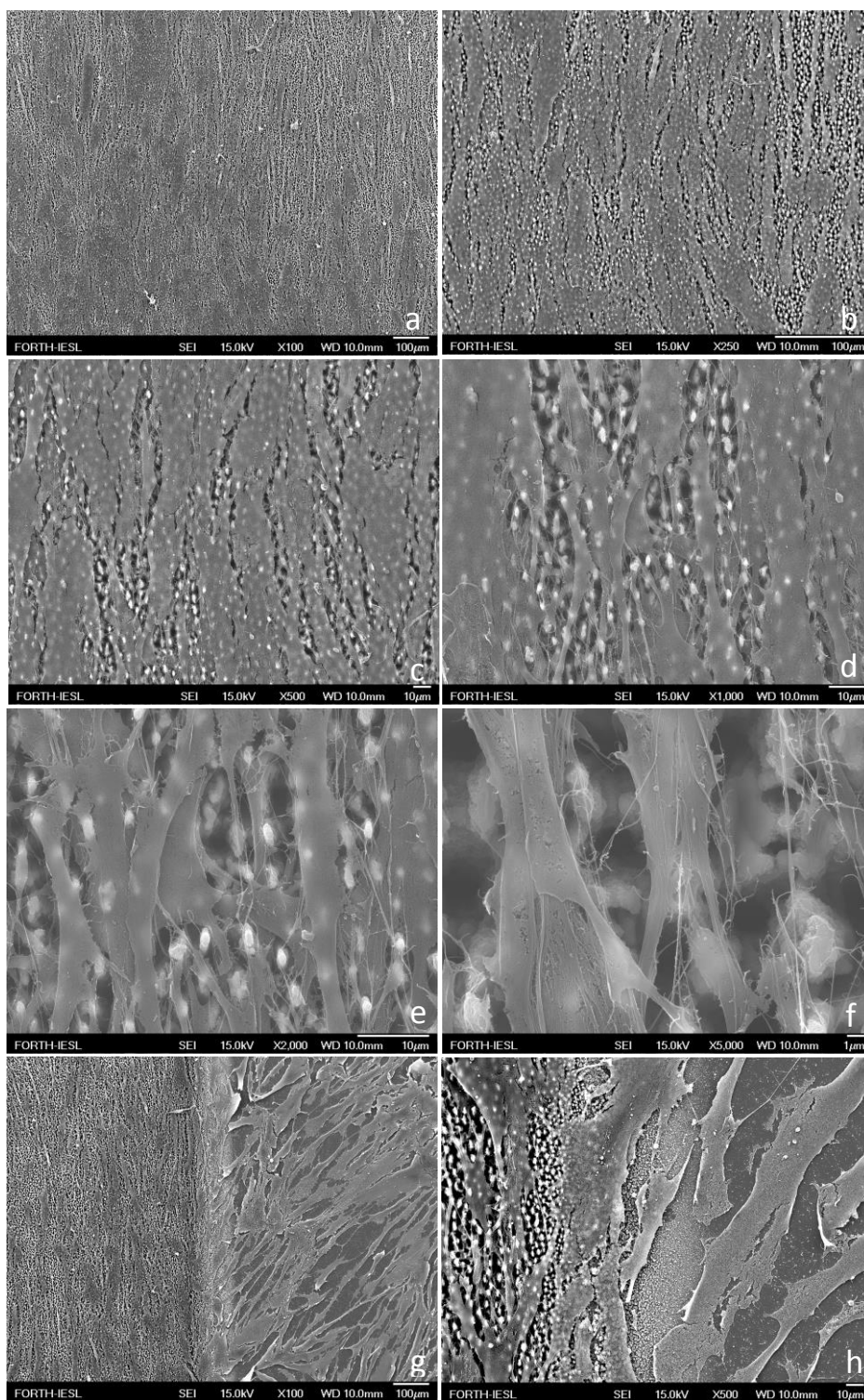
Figures 3.9-3.12 show fibroblasts seeded on Si laser irradiated surfaces coated with P2VP (Figures 3.9-3.10) and PNIPAm (Figures 3.11-3.12) for days 1 and 7 of cell culture respectively. Figure 3.9 shows that fibroblasts attach and proliferate on the P2VP coated surface already after 24 hours after seeding. The cells that are attached on the spikes appear to have an elongated shape following the directionality of the spikes. Figure 3.9 g-h where one can see the border between the surface with spikes and the surface without the spikes, cells proliferation is seen to be in the area without spikes but without the elongated shape. It is evident that the number of cells attached on the area with the spikes is less compared to the number of cells on the flat surface. It is assumed that the surface topographical features are very intense for the cells, however, they do not inhibit the cell attachment. Moreover, the cells that attach on the spikes grow on the same direction with the laser irradiated spikes and this is evident not only from the shape of the individual cells but also from the parallel position between them. This kind of directionality does not facilitate the communication and connection between the cells, compared to the area without spikes, however the cells do grow and their cytoplasmic projections are directed towards the cell communication sites.

Figure 3.10 shows the fibroblasts seeded on the P2VP coated surface for day 7 of the cell culture. After 7 days of culture the surface seems to be fully coated with cells. The cell number has increased significantly, and cells continue to grow in the same direction as the spikes. Here, isolated cells cannot be observed since they attach to each other and form clusters. Figures 3.10 g and h show the interface between the area with and without spikes where it can be seen that cells proliferate covering the surface without spikes but without directionality.

To our knowledge, so far in the literature, cellular response on P2VP surfaces has not been reported. P2VP has been used in combination with other polymers such as polystyrene, PS or poly(acrylic acid), PAA in the form of block copolymer to produce polymeric substrates for cell seeding.<sup>124</sup> For example, PS-b-P2VP co-polymer has been used for the production of thin films with nanopattern characteristics for the seeding of fibroblasts and mesenchymal stem cells. It has been found that the presence of P2VP in the PS-b-P2VP block copolymer enhances cell proliferation.<sup>125</sup> PS-b-P2VP co-polymer has also been used in the form of micelles in order to induce topographical features on surfaces. Osteoblast seeding on these substrates showed enhanced osteogenic behavior attributed to both the chemistry and topography of the substrate.<sup>126</sup> In our case, P2VP appears to favor cell attachment and proliferation within 7 days of culture. Together with the topographical features induced with the laser treatment, directionality of the attached cells has been also achieved. The specific surface geometry has been reported by Stratakis *et al.* where Si substrates irradiated with laser were used for the directionality of neuronal network outgrowth.<sup>90</sup>



**Figure 3.21.** A-F) Different magnifications of the micro-structured Si surface irradiated with  $1.4 \text{ J cm}^{-2}$  after coating with P2VP and seeded with fibroblasts for one day. G-H) Border between the P2VP coated surface with spikes and the surface without spikes and seeded with fibroblasts for one day.



**Figure 3.22.** A-F) Different magnifications of the micro-structured Si surface irradiated with  $1.4 \text{ J cm}^{-2}$  after coating with P2VP and seeded with fibroblasts for 7 days. G-H) Border between the P2VP coated surface with spikes and the surface without spikes and seeded with fibroblasts for 7 days.

Figure 3.11 shows the fibroblasts seeded on the PNIPAm coated surface for day 1 of the cell culture. Very few cells can be observed on the PNIPAm coated surface. For day 7 of the same sample (Figure 3.12) a slight higher proliferation can be observed with a few cells to grow and attach on the surface exhibiting a directionality in the direction of the spikes.

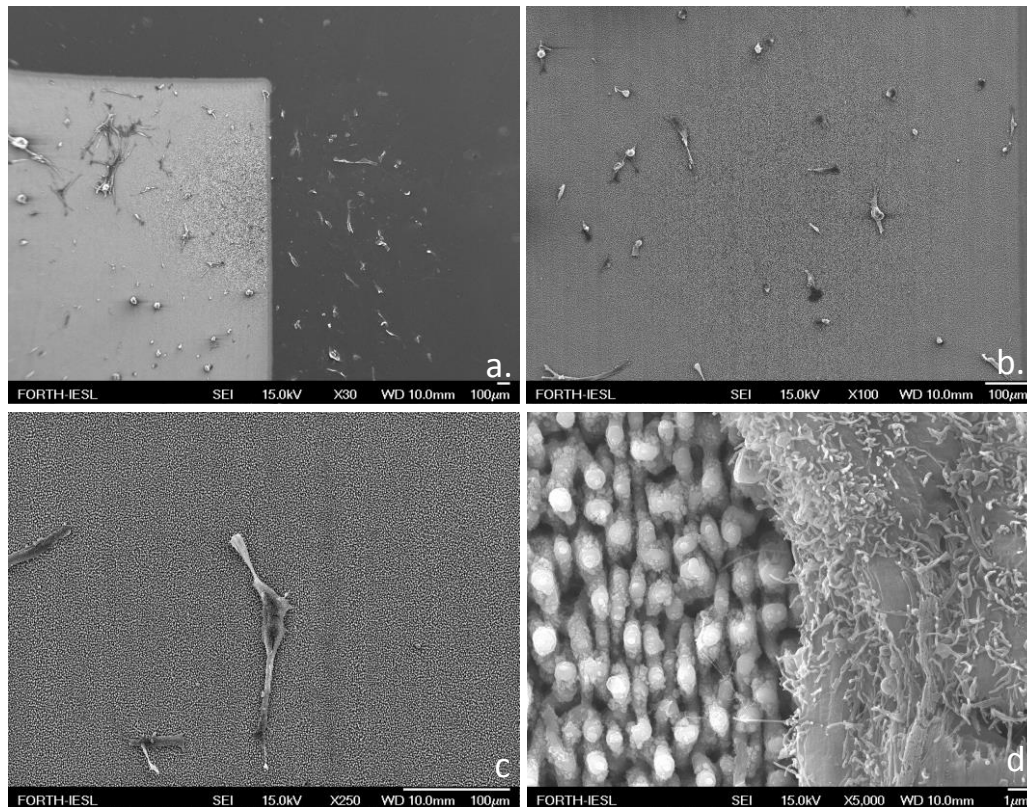


**Figure 3.23.** A) Border between the PNIPAm coated surface with spikes and the surface without spikes and seeded with fibroblasts for one day. B-D) Different magnifications of the micro-structured Si surface irradiated with  $1.4 \cdot \text{J cm}^{-2}$  after coating with PNIPAm and seeded with fibroblasts for one day.

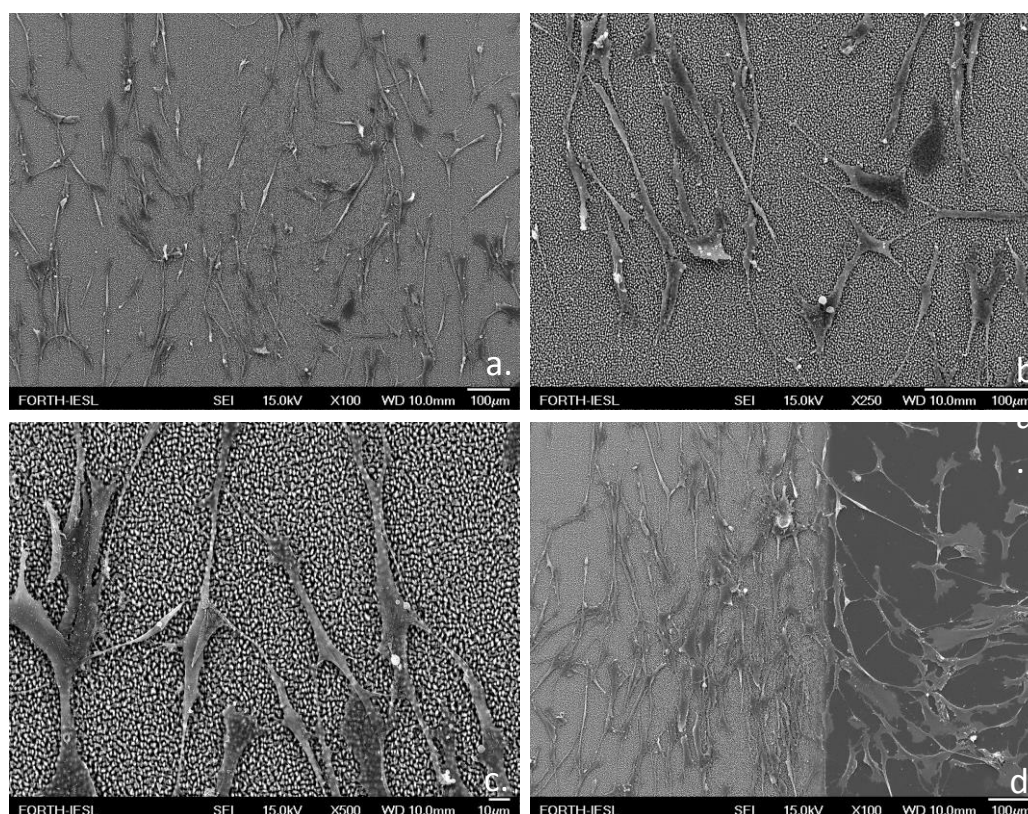


**Figure 3.24.** A-C) Different magnifications of the micro-structured Si surface irradiated with  $1.4 \cdot \text{J cm}^{-2}$  after coating with PNIPAm and seeded with fibroblasts for 7 days. D) Border between the PNIPAm coated surface with spikes and the surface without spikes and seeded with fibroblasts for 7 days.

PNIPAm, as a thermoresponsive polymer, has been reported in the literature as a means for cell detachment and harvesting.<sup>127,128</sup> The thermo-reversible nature of PNIPAm makes it an ideal material for attachment/detachment of proteins, mammalian cells and bacterial cells.<sup>129</sup> When cells are seeded onto the surface of PNIPAm they do attach and grow at a temperature of 37-38°C, which is the physiological temperature for cells to survive. When the temperature is lowered below 32°C, the polymer becomes hydrophilic; this increase on hydrophilicity leads to the detachment of extracellular matrix, ECM proteins and, thus, detachment of the cells. In this case cells, detach as a sheet and not individually.<sup>130</sup> In our case, it is believed that cells were initially attached onto the substrate coated with PNIPAm. However, due to the fixation process, which was used to prepare the samples for SEM imaging, where

glutaraldehyde at a low temperature (9°C) was used, we assume that the cell layer that was formed detached from the surface since the temperature was far below the transition temperature of the polymer (32°C). This explains why there were very few cells observed with the SEM. Thus, the PNIPAm coated Si surfaces are not representative and conclusive for the cell seeding.

### 3.4. Conclusions

In summary, hierarchically roughened surfaces micro/nano-structured utilizing fs laser irradiation of silicon substrates were fabricated and were functionalized using end-anchoring of end-functional P2VP or PNIPAm chains utilizing the “grafting to” method. The effect of molecular weight of the polymers on the wettability results was investigated and the results found to be reproducible in all cases. The same method applied successfully for both carboxy- and hydroxyl-terminated polymers. Furthermore, multi-responsive surfaces were developed utilizing a mixture of P2VP/PNIPAm chains “grafted to” the hierarchical surfaces. “Sticky” highly hydrophobic surfaces were achieved, with reversible and controllable wetting characteristics, imitating plant leaves with “parahydrophobic” behavior. These surfaces can be successfully applied in industry as switchable valves, biosensors, tunable microlenses and for selective liquid separation.

In our case, P2VP and PNIPAm coated surfaces were applied for cell seeding. To our knowledge, so far in the literature, cellular response on P2VP surfaces has not been reported. P2VP appears to favor cell attachment and proliferation within 7 days of culture. Together with the topographical features induced with the laser treatment, directionality of the attached cells has been also achieved. As for the PNIPAM coated surfaces, cells were initially attached onto the substrate. However, due to the fixation process, which was used to prepare the samples for SEM imaging, we assume that the cell layer that was formed detached from the

surface because the temperature was far below the transition temperature of the polymer (32°C). This explains why there were very few cells observed with the SEM. Thus, the PNIPAm coated Si surfaces are not representative and conclusive for the cell seeding.

### 3.5. References

- (1) Caputo, G.; Cortese, B.; Nobile, C.; Salerno, M.; Cingolani, R.; Gigli, G.; Cozzoli, P. D.; Athanassiou, A. Reversibly Light-Switchable Wettability of Hybrid Organic/inorganic Surfaces with Dual Micro-/ Nanoscale Roughness. *Adv. Funct. Mater.* **2009**, *19* (8), 1149–1157.
- (2) Caputo, G.; Nobile, C.; Kipp, T.; Blasi, L.; Grillo, V.; Carlino, E.; Manna, L.; Cingolani, R.; Cozzoli, P. D.; Athanassiou, A. Reversible Wettability Changes in Colloidal TiO Nanorod Thin-Film Coatings under Selective UV Laser Irradiation Reversible Wettability Changes in Colloidal TiO<sub>2</sub> Nanorod Thin-Film Coatings under Selective UV Laser Irradiation. **2008**, 701–714.
- (3) Genzer, J.; Efimenko, K. Recent Developments in Superhydrophobic Surfaces and Their Relevance to Marine Fouling: A Review. *Biofouling* **2006**, *22* (5–6), 339–360.
- (4) Guo, Y.; Xia, F.; Xu, L.; Li, J.; Yang, W.; Jiang, L. Switchable Wettability on Cooperative Dual-Responsive Poly-L-Lysine Surface. *Langmuir* **2010**, *26* (2), 1024–1028.
- (5) Xia, F.; Feng, L.; Wang, S.; Sun, T.; Song, W.; Jiang, W.; Jiang, L. Dual-Responsive Surfaces That Switch between Superhydrophilicity and Superhydrophobicity. *Adv. Mater.* **2006**, *18* (4), 432–436.
- (6) Frysali, M. A.; Papoutsakis, L.; Kenanakis, G.; Anastasiadis, S. H. Functional Surfaces with Photocatalytic Behavior and Reversible Wettability: ZnO Coating on Silicon Spikes. *J. Phys. Chem. C* **2015**, *119* (45), 25401–25407.
- (7) Ionov, L.; Houbenov, N.; Sidorenko, A.; Stamm, M.; Minko, S. Stimuli-Responsive Command Polymer Surface for Generation of Protein Gradients. *Biointerphases* **2009**, *4* (2), FA45-9.
- (8) Chunder, A.; Etcheverry, K.; Londe, G.; Cho, H. J.; Zhai, L. Conformal Switchable Superhydrophobic/hydrophilic Surfaces for Microscale Flow Control. *Colloids Surfaces A Physicochem. Eng. Asp.* **2009**, *333* (1–3), 187–193.
- (9) Fujii, S.; Kameyama, S.; Armes, S. P.; Dupin, D.; Suzaki, M.; Nakamura, Y. pH-Responsive Liquid Marbles Stabilized with poly(2-Vinylpyridine) Particles. *Soft Matter* **2010**, *6* (3), 635.
- (10) Stratakis, E.; Mateescu, A.; Barberoglou, M.; Vamvakaki, M.; Fotakis, C.; Anastasiadis, S. H. From Superhydrophobicity and Water Repellency to Superhydrophilicity: Smart Polymer-Functionalized Surfaces. *Chem. Commun.* **2010**, *46* (23), 4136.
- (11) Chen, J. K.; Chang, C. J. Fabrications and Applications of Stimulus-Responsive Polymer Films and Patterns on Surfaces: A Review. *Materials (Basel)*. **2014**, *7* (2), 805–875.
- (12) Bhushan, B. *Biomimetics*. **2016**, 23–34.
- (13) Ramachandran, R.; Nosonovsky, M. Surface Micro/nanotopography, Wetting Properties and the Potential for Biomimetic Icephobicity of Skunk Cabbage *Symplocarpus Foetidus*. *Soft Matter* **2014**, *10* (39), 7797–7803.
- (14) Chang, F. M.; Hong, S. J.; Sheng, Y. J.; Tsao, H. K. High Contact Angle Hysteresis of

- Superhydrophobic Surfaces: Hydrophobic Defects. *Appl. Phys. Lett.* **2009**, *95* (6), 2012–2015.
- (15) Sun, M.; Liang, A.; Watson, G. S.; Watson, J. A.; Zheng, Y.; Ju, J.; Jiang, L. Influence of Cuticle Nanostructuring on the Wetting Behaviour/states on Cicada Wings. *PLoS One* **2012**, *7* (4), 1–8.
- (16) Liu, X.; Liang, Y.; Zhou, F.; Liu, W. Extreme Wettability and Tunable Adhesion: Biomimicking beyond Nature? *Soft Matter* **2012**, *8* (7), 2070.
- (17) Lai, Y.; Lin, C.; Huang, J.; Zhuang, H.; Sun, L.; Nguyen, T. Markedly Controllable Adhesion of Superhydrophobic Spongelike Nanostructure TiO<sub>2</sub> Films. *Langmuir* **2008**, *24* (8), 3867–3873.
- (18) Lai, Y.; Gao, X.; Zhuang, H.; Huang, J.; Lin, C.; Jiang, L. Designing Superhydrophobic Porous Nanostructures with Tunable Water Adhesion. *Adv. Mater.* **2009**, *21* (37), 3799–3803.
- (19) Jin, M.; Feng, X.; Feng, L.; Sun, T.; Zhai, J.; Li, T.; Jiang, L. Superhydrophobic Aligned Polystyrene Nanotube Films with High Adhesive Force. *Adv. Mater.* **2005**, *17* (16), 1977–1981.
- (20) Wang, H.; Shi, H.; Wang, Y. The Wetting of Leaf Surfaces and Its Ecological Significances.
- (21) Kolyva, F.; Stratakis, E.; Rhizopoulou, S.; Chimona, C.; Fotakis, C. Leaf Surface Characteristics and Wetting in *Cerantia Siliqua* L. *Flora Morphol. Distrib. Funct. Ecol. Plants* **2012**, *207* (8), 551–556.
- (22) Gilet, T.; Bourouiba, L. Rain-Induced Ejection of Pathogens from Leaves: Revisiting the Hypothesis of Splash-on-Film Using High-Speed Visualization. *Integr. Comp. Biol.* **2014**, *54* (6), 974–984.
- (23) Fernández, V.; Sancho-Knapik, D.; Guzmán, P.; Peguero-Pina, J. J.; Gil, L.; Karabourniotis, G.; Khayet, M.; Fasseas, C.; Heredia-Guerrero, J. A.; Heredia, A.; et al. Wettability, Polarity and Water Absorption of *Quercus Ilex* Leaves: Effect of Leaf Side and Age. *Plant Physiol.* **2014**, *166* (September), 168–180.
- (24) Kortekamp, A.; Wind, R.; Zyprian, E. The Role of Hairs on the Wettability of Grapevine (*Vitis* Spp.) Leaves. *Vitis* **1999**, *38* (3), 101–105.
- (25) Haines, B. L.; Jernstedt, J. A.; Neufeld, H. S. Direct Foliar Effects of Simulated Acid-Rain .2. Leaf Surface Characteristics. *New Phytol.* **1985**, *99* (3), 407–416.
- (26) Hall, D. M.; Burke, W. Wettability of Leaves of a Selection of New Zealand Plants. *New Zeal. J. Bot.* **1974**, *12* (3), 283–298.
- (27) Guo, H. Bio-Inspired Surface Engineering for Hydrophobicity. *Thesis* **2014**.
- (28) Guo, Z. G.; Liu, W. M. Sticky Superhydrophobic Surface. *Appl. Phys. Lett.* **2007**, *90* (22).
- (29) Stavrouli, N.; Katsampas, I.; Aggelopoulos, S.; Tsitsilianis, C. pH/thermosensitive Hydrogels Formed at Low pH by a PMMA-PAA-P2VP-PAA-PMMA Pentablock Terpolymer. *Macromol. Rapid Commun.* **2008**, *29* (2), 130–135.
- (30) Tafti, E. Y.; Londe, G.; Chunder, A.; Zhai, L.; Kumar, R.; Cho, H. J. Wettability Control and Flow Regulation Using a Nanostructure-Embedded Surface. *J. Nanosci. Nanotechnol.* **2011**, *11* (2), 1417–1420.
- (31) Chhabra, A.; Kanapuram, R. R.; Kim, T. J.; Geng, J.; da Silva, A. K.; Bielawski, C. W.; Hidrovo, C. H. Humidity Effects on the Wetting Characteristics of Poly(N-Isopropylacrylamide) during a Lower Critical Solution Transition. *Langmuir* **2013**, 130605123642004.
- (32) Papadopoulou, E. L.; Barberoglou, M.; Zorba, V.; Manousaki, A.; Pagkozidis, A.; Stratakis, E.; Fotakis, C. Reversible Photoinduced Wettability Transition of Hierarchical ZnO Structures. *J. Phys. Chem. C* **2009**, *113* (7), 2891–2895.

- (33) Zorba, V.; Stratakis, E.; Barberoglou, M.; Spanakis, E.; Tzanetakis, P.; Anastasiadis, S. H.; Fotakis, C. Biomimetic Artificial Surfaces Quantitatively Reproduce the Water Repellency of a Lotus Leaf. *Adv. Mater.* **2008**, *20* (21), 4049–4054.
- (34) Li, D.; Zheng, Q.; Wang, Y.; Chen, H. Combining Surface Topography with Polymer Chemistry: Exploring New Interfacial Biological Phenomena. *Polym. Chem.* **2014**, *5* (1), 14.
- (35) Dai, S.; Ravi, P.; Tam, K. C. Thermo- and Photo-Responsive Polymeric Systems. *Soft Matter* **2009**, 2513–2533.
- (36) Anastasiadis, S. H.; Lygeraki, M. I.; Athanassiou, A.; Farsari, M.; Pisignano, D. Reversibly Photo-Responsive Polymer Surfaces for Controlled Wettability. *J. Adhes. Sci. Technol.* **2008**, *22* (15), 1853–1868.
- (37) Guo, C.; Zhou, L.; Lv, J. Effects of Expandable Graphite and Modified Ammonium Polyphosphate on the Flame-Retardant and Mechanical Properties of Wood Flour-Polypropylene Composites. *Polym. Polym. Compos.* **2013**, *21* (7), 449–456.
- (38) Wang, S.; Choi, M. S.; Kim, S. H. Multiple Switching Photochromic poly(N-Isopropylacrylamide) with Spiroanthoxazine Hydrogel. *Dye. Pigment.* **2008**, *78* (1), 8–14.
- (39) Wang, S.; Choi, M. S.; Kim, S. H. Bistable Photoswitching in poly(N-Isopropylacrylamide) with Spiroanthoxazine Hydrogel for Optical Data Storage. *J. Photochem. Photobiol. A Chem.* **2008**, *198* (2–3), 150–155.
- (40) Yu, Y.; Ikeda, T. Soft Actuators Based on Liquid-Crystalline Elastomers. *Angew. Chemie - Int. Ed.* **2006**, *45* (33), 5416–5418.
- (41) Kulawardana, E. U. Stimuli-Responsive Polymers. *Intell. Macromol. Smart Devices From ...* **2010**, No. December.
- (42) Yan, N.; Zhang, J.; Yuan, Y.; Chen, G.-T.; Dyson, P. J.; Li, Z.-C.; Kou, Y. Thermoresponsive Polymers Based on Poly-Vinylpyrrolidone: Applications in Nanoparticle Catalysis. *Chem. Commun. (Camb).* **2010**, *46* (10), 1631–1633.
- (43) Hu, Z. B.; Chen, Y. Y.; Wang, C. J.; Zheng, Y. D.; Li, Y. Polymer Gels with Engineered Environmentally Responsive Surface Patterns. *Nature* **1998**, *393* (6681), 149–152.
- (44) Nakabo, Y. Mukai, T. Asaka, K. *Electroactive Polymers for Robotics Applications*; 2010.
- (45) Zhu, M. Q.; Wang, L. Q.; Exarhos, G. J.; Li, A. D. Q. Thermosensitive Gold Nanoparticles. *J. Am. Chem. Soc.* **2004**, *126* (9), 2656–2657.
- (46) da Silva, R. M. P.; Mano, J. F.; Reis, R. L. Smart Thermoresponsive Coatings and Surfaces for Tissue Engineering: Switching Cell-Material Boundaries. *Trends Biotechnol.* **2007**, *25* (12), 577–583.
- (47) Ista, L. K.; Mendez, S.; Lopez, G. P. Attachment and Detachment of Bacteria on Surfaces with Tunable and Switchable Wettability. *Biofouling* **2010**, *26* (1), 111–118.
- (48) Saunders, J. M.; Saunders, B. R. Temperature-Triggered Capture of Dispersed Particles Using a Laponite-poly(NIPAM) Temperature-Responsive Surface. *J. Macromol. Sci. Part B Phys.* **2007**, *46 B* (3), 547–559.
- (49) Carreira, A. S.; Gonçalves, F. A. M. M.; Mendonça, P. V.; Gil, M. H.; Coelho, J. F. J. Temperature and pH Responsive Polymers Based on Chitosan: Applications and New Graft Copolymerization Strategies Based on Living Radical Polymerization. *Carbohydr. Polym.* **2010**, *80* (3), 618–630.
- (50) Stratakis, E.; Mateescu, A.; Barberoglou, M.; Vamvakaki, M.; Fotakis, C.; Anastasiadis, S. H. From Superhydrophobicity and Water Repellency to Superhydrophilicity: Smart Polymer-Functionalized Surfaces. *Chem. Commun.* **2010**, *46* (23), 4136.

- (51) Almeida, H.; Amaral, M. H.; Lobão, P. Temperature and pH Stimuli-Responsive Polymers and Their Applications in Controlled and Selfregulated Drug Delivery. *J. Appl. Pharm. Sci.* **2012**, *2* (6), 01–10.
- (52) Kim, S. J.; Kim, H. II; Park, S. J.; Kim, I. Y.; Lee, S. H.; Lee, T. S.; Kim, S. I. Behavior in Electric Fields of Smart Hydrogels with Potential Application as Bio-Inspired Actuators. *Smart Mater. Struct.* **2005**, *14* (4), 511–514.
- (53) Ahn, S.; Kasi, R. M.; Kim, S.-C.; Sharma, N.; Zhou, Y. Stimuli-Responsive Polymer Gels. *Soft Matter* **2008**, *4* (6), 1151.
- (54) Kulawardana, E. U.; Kuruwita-Mudiyanselage, T.; Neckers, D. Dual Responsive Poly(N-Isopropylacrylamide) Hydrogels Having Spironaphthoxazines as Pendant Groups. *Am. Chem. Soc. Polym. Prepr. Div. Polym. Chem.* **2008**, *49* (1), 511–512.
- (55) Jochum, F. D.; Borg, L. Zur; Roth, P. J.; Theato, P. Thermo- and Light-Responsive Polymers Containing Photoswitchable Azobenzene End Groups. *Macromolecules* **2009**, *42* (20), 7854–7862.
- (56) Yuan, W.; Jiang, G.; Wang, J.; Wang, G.; Song, Y.; Jiang, L. Temperature/light Dual-Responsive Surface with Tunable Wettability Created by Modification with an Azobenzene-Containing Copolymer. *Macromolecules* **2006**, *39* (3), 1300–1303.
- (57) Sumaru, K.; Kameda, M.; Kanamori, T.; Shinbo, T. Characteristic Phase Transition of Aqueous Solution of Poly(N-Isopropylacrylamide) Functionalized with Spirobenzopyran. *Macromolecules* **2004**, *37* (13), 4949–4955.
- (58) Verestiuc, L.; Ivanov, C.; Barbu, E.; Tsibouklis, J. Dual-Stimuli-Responsive Hydrogels Based on poly(N-Isopropylacrylamide)/ Chitosan Semi-Interpenetrating Networks. *Int. J. Pharm.* **2004**, *269* (1), 185–194.
- (59) Marques, N. D. N.; Maia, A. M. da S.; Balaban, R. de C. Development of Dual-Sensitive Smart Polymers by Grafting Chitosan with Poly (N-Isopropylacrylamide): An Overview. *Polimeros* **2015**, *25* (3), 237–246.
- (60) Stamm, M. *Polymer Surfaces and Interfaces*; 2008.
- (61) Zhao, B.; Brittain, W. J. Polymer Brushes: Surface-Immobilized Macromolecules. *Prog. Polym. Sci.* **2000**, *25* (5), 677–710.
- (62) Brittain, W. J.; Minko, S. A Structural Definition of Polymer Brushes. *J. Polym. Sci. Part A Polym. Chem.* **2007**, *45* (16), 3505–3512.
- (63) Schild, H. G. Poly ( N-Isopropylacrylamide ): Experiment , Theory and Application. *Prog. Polym. Sci.* **1992**, *17*, 163–249.
- (64) Ward, M. A.; Georgiou, T. K. Thermoresponsive Polymers for Biomedical Applications. *Polymers (Basel)*. **2011**, *3* (3), 1215–1242.
- (65) Jones, R. A. . *Soft Condensed Matter*; Oxford University Press, 2002.
- (66) Meyer, D. E.; Shin, B. C.; Kong, G. A.; Dewhirst, M. W.; Chilkoti, A. Drug Targeting Using Thermally Responsive Polymers and Local Hyperthermia. *J. Control. Release* **2001**, *74* (1), 213–224.
- (67) Kaklamani, G.; Bowen, J.; Mehrban, N.; Dong, H.; Grover, L. M.; Stamboulis, A. Active Screen Plasma Nitriding Enhances Cell Attachment to Polymer Surfaces. *Appl. Surf. Sci.* **2013**, *273*, 787–798.
- (68) Stevens, M. M.; George, J. H. Exploring and Engineering the Cell Surface Interface. *Mater. Biol.* **2005**, *310*, 1135–1138.
- (69) Jäger, M.; Zilkens, C.; Zanger, K.; Krauspe, R. Significance of Nano- and Microtopography for Cell-Surface Interactions in Orthopaedic Implants. *J. Biomed. Biotechnol.* **2007**, 2007.
- (70) Boyan, B. D.; Hummert, T. W.; Dean, D. D.; Schwartz, Z. Role of Material Surfaces in Regulating Bone and Cartilage Cell Response. *Biomaterials* **1996**, *17* (2), 137–146.
- (71) Kasemo, B. Biological Surface Science.pdf. No. Figure 1, 451–459.

- (72) Anselme, K. Osteoblast Adhesion on Biomaterials. *Biomaterials* **2000**, *21* (7), 667–681.
- (73) Carré, A.; Lacarrière, V. How Substrate Properties Control Cell Adhesion. A Physical–Chemical Approach. *J. Adhes. Sci. Technol.* **2010**, *24* (October 2014), 815–830.
- (74) Mrksich, M. A Surface Chemistry Approach to Studying Cell Adhesion. *Chem. Soc. Rev.* **2000**, *29* (4), 267–273.
- (75) Mrksich, M. What Can Surface Chemistry Do for Cell Biology? *Curr. Opin. Chem. Biol.* **2002**, *6* (6), 794–797.
- (76) Ismail, F. S. M.; Rohanizadeh, R.; Atwa, S.; Mason, R. S.; Ruys, A. J.; Martin, P. J.; Bendavid, A. The Influence of Surface Chemistry and Topography on the Contact Guidance of MG63 Osteoblast Cells. *J. Mater. Sci. Mater. Med.* **2007**, *18* (5), 705–714.
- (77) Keselowsky, B. G.; Collard, D. M.; Garci, J. Surface Chemistry Modulates Fibronectin Conformation and Directs Integrin Binding and Specificity to Control Cell Adhesion. **2002**.
- (78) Keselowsky, B. G.; Collard, D. M. Surface Chemistry Modulates Focal Adhesion Composition and Signaling through Changes in Integrin Binding. **2004**, *25*, 5947–5954.
- (79) Lee, J. H.; Jung, H. W.; Kang, I.-K.; Lee, H. B. Cell Behaviour on Polymer Surfaces with Different Functional Groups. *Biomaterials* **1994**, *15* (9), 705–711.
- (80) Martínez, E.; Engel, E.; Planell, J. A.; Samitier, J. Effects of Artificial Micro- and Nano-Structured Surfaces on Cell Behaviour. *Ann. Anat.* **2009**, *191* (1), 126–135.
- (81) Andersson, A. S.; Bäckhed, F.; Von Euler, A.; Richter-Dahlfors, A.; Sutherland, D.; Kasemo, B. Nanoscale Features Influence Epithelial Cell Morphology and Cytokine Production. *Biomaterials* **2003**, *24* (20), 3427–3436.
- (82) Wong, J. Y.; Leach, J. B.; Brown, X. Q. Balance of Chemistry, Topography, and Mechanics at the Cell-Biomaterial Interface: Issues and Challenges for Assessing the Role of Substrate Mechanics on Cell Response. *Surf. Sci.* **2004**, *570* (1–2), 119–133.
- (83) Curtis, A.; Wilkinson, C. Topographical Control of Cells. *Biomaterials* **1997**, *18* (24), 1573–1583.
- (84) Flemming, R.; Murphy, C.; Abrams, G.; Goodman, S.; Nealey, P. Effects of Synthetic Micro-and Nano-Structured Surfaces on Cell Behavior. *Biomaterials* **1999**, *20* (1999), 573–588.
- (85) Anderson, D. G.; Putnam, D.; Lavik, E. B.; Mahmood, T. A.; Langer, R. Biomaterial Microarrays: Rapid, Microscale Screening of Polymer-Cell Interaction. *Biomaterials* **2005**, *26* (23), 4892–4897.
- (86) Condie, R.; Bose, S.; Bandyopadhyay, A. Bone Cell-Materials Interaction on Si Microchannels with Bioinert Coatings. *Acta Biomater.* **2007**, *3* (4), 523–530.
- (87) Andersson, A. S.; Brink, J.; Lidberg, U.; Sutherland, D. S. Influence of Systematically Varied Nanoscale Topography on the Morphology of Epithelial Cells. *IEEE Trans. Nanobioscience* **2003**, *2* (2), 49–57.
- (88) Badami, A. S.; Kreke, M. R.; Thompson, M. S.; Riffle, J. S.; Goldstein, A. S. Effect of Fiber Diameter on Spreading, Proliferation, and Differentiation of Osteoblastic Cells on Electrospun Poly(lactic Acid) Substrates. *Biomaterials* **2006**, *27* (4), 596–606.
- (89) Folch, A.; Toner, M. Microengineering of Cellular Interactions. *Annu. Rev. Biomed. Eng.* **2000**, 227–256.
- (90) Simitzi, C.; Efstathopoulos, P.; Kourgiantaki, A.; Ranella, A.; Charalampopoulos, I.; Fotakis, C.; Athanassakis, I.; Stratakis, E.; Gravanis, A. Laser Fabricated Discontinuous Anisotropic Microconical Substrates as a New Model Scaffold to Control the Directionality of Neuronal Network Outgrowth. *Biomaterials* **2015**, *67*,

- 115–128.
- (91) Arima, Y.; Iwata, H. Effect of Wettability and Surface Functional Groups on Protein Adsorption and Cell Adhesion Using Well-Defined Mixed Self-Assembled Monolayers. *Biomaterials* **2007**, *28* (20), 3074–3082.
- (92) Lee, S. J.; Khang, G.; Lee, Y. M.; Lee, H. B. The Effect of Surface Wettability on Induction and Growth of Neurites from the PC-12 Cell on a Polymer Surface. *J. Colloid Interface Sci.* **2003**, *259* (2), 228–235.
- (93) Altankov, G.; Grinnell, F.; Groth, T. Studies on the Biocompatibility of Materials: Fibroblast Reorganization of Substratum-Bound Fibronectin on Surfaces Varying in Wettability. *J. Biomed. Mater. Res.* **1996**, *30* (3), 385–391.
- (94) Lampin, M.; Warocquier-Clérout, R.; Legris, C.; Degrange, M.; Sigot-Luizard, M. F. Correlation between Substratum Roughness and Wettability, Cell Adhesion, and Cell Migration. *J. Biomed. Mater. Res.* **1997**, *36* (1), 99–108.
- (95) Webb, K.; Hlady, V.; Tresco, P. A. Relative Importance of Surface Wettability and Charged Functional Groups on NIH 3T3 Fibroblast Attachment, Spreading, and Cytoskeletal Organization. **1998**.
- (96) Zorba, V.; Persano, L.; Pisignano, D.; Athanassiou, A.; Stratakis, E.; Cingolani, R.; Tzanetakis, P.; Fotakis, C. Making Silicon Hydrophobic: Wettability Control by Two-Lengthscale Simultaneous Patterning with Femtosecond Laser Irradiation. *Nanotechnology* **2006**, *17* (13), 3234–3238.
- (97) Ashurst, W. R.; Carraro, C.; Maboudian, R. Vapor Phase Anti-Stiction Coatings for MEMS. *IEEE Trans. Device Mater. Reliab.* **2003**, *3* (4), 173–178.
- (98) Öner, D.; McCarthy, T. J. Ultrahydrophobic Surfaces. Effects of Topography Length Scales on Wettability. *Langmuir* **2000**, *16* (20), 7777–7782.
- (99) Ionov, L.; Sapra, S.; Synytska, A.; Rogach, A. L.; Stamm, M.; Diez, S. Fast and Spatially Resolved Environmental Probing Using Stimuli-Responsive Polymer Layers and Fluorescent Nanocrystals. *Adv. Mater.* **2006**, *18* (11), 1453–1457.
- (100) Synytska, A.; Stamm, M.; Diez, S.; Ionov, L. Simple and Fast Method for the Fabrication of Switchable Bicomponent Micropatterned Polymer Surfaces. **2007**, No. 19, 5205–5209.
- (101) Bittrich, E.; Burkert, S.; Eichhorn, K.; Stamm, M.; Uhlmann, P. Control of Protein Adsorption and Cell Adhesion by Mixed Polymer Brushes Made by the “Grafting-To” Approach. *Preteins Interfaces III State Art* **2012**, 179–193.
- (102) Draper, J.; Luzinov, I.; Ionov, L.; Minko, S.; Sunil, K. WETTABILITY AND MORPHOLOGY OF A MIXED POLYMER. **2003**, *44* (1), 570–571.
- (103) Haider, I.; Siddiq, M.; Shah, S. M.; ur Rehman, S. Synthesis and Characterization of Multi-Responsive Poly (NIPAm-Co-AAc) Microgels. *IOP Conf. Ser. Mater. Sci. Eng.* **2014**, *60*, 12046.
- (104) Anastasiadis, S. H.; Hatzikiriakos, S. G. The Work of Adhesion of Polymer/wall Interfaces and Its Association with the Onset of Wall Slip. *J. Rheol. (N. Y. N. Y.)* **1998**, *42* (4), 795.
- (105) Choi, W.; Tuteja, A.; Mabry, J. M.; Cohen, R. E.; McKinley, G. H. A Modified Cassie-Baxter Relationship to Explain Contact Angle Hysteresis and Anisotropy on Non-Wetting Textured Surfaces. *J. Colloid Interface Sci.* **2009**, *339* (1), 208–216.
- (106) Bracco, G.; Holst, B. *Surface Science Techniques*; 2013; Vol. 51.
- (107) Eral, H. B.; Mannetje, D. J. C. M.; Oh, J. M. Contact Angle Hysteresis: A Review of Fundamentals and Applications. *Colloid Polym. Sci.* **2013**, *291* (2), 247–260.
- (108) Koenig, M.; Magerl, D.; Philipp, M.; Eichhorn, K.-J.; Müller, M.; Müller-Buschbaum, P.; Stamm, M.; Uhlmann, P. Nanocomposite Coatings with Stimuli-Responsive

- Catalytic Activity. *RSC Adv.* **2014**, *4* (34), 17579.
- (109) Choi, S. P H Sensitive Polymers for Novel Conformance Control and Polymer Flooding Applications. 2008.
- (110) Zdyrko, B.; Varshney, S. K.; Luzinov, I. Effect of Molecular Weight on Synthesis and Surface Morphology of High-Density Poly(ethylene Glycol) Grafted Layers. *Langmuir* **2004**, *20* (16), 6727–6735.
- (111) Seeber, M.; Zdyrko, B.; Burtovvy, R.; Andruk, T.; Tsai, C.-C.; Owens, J. R.; Kornev, K. G.; Luzinov, I. Surface Grafting of Thermoresponsive Microgel Nanoparticles. *Soft Matter* **2011**, *7* (21), 9962.
- (112) Zhu, X.; Yan, C.; Winnik, F. M.; Leckband, D. End-Grafted Low-Molecular-Weight PNIPAM Does Not Collapse above the LCST. *Langmuir* **2007**, *23* (1), 162–169.
- (113) Burmistrova, A. Temperature-Induced Swelling / Shrinking Behavior of Adsorbed PNIPAM Microgels, Berlin, 2011.
- (114) Anastasiadis, S. H.; Retsos, H.; Pispas, S.; Hadjichristidis, N.; Neophytides, S. Smart Polymer Surfaces. *Macromolecules* **2003**, *36* (6), 1994–1999.
- (115) Plunkett, K. N.; Zhu, X.; Moore, J. S.; Leckband, D. E. PNIPAM Chain Collapse Depends on the Molecular Weight and Grafting Density. *Langmuir* **2006**, *22* (9), 4259–4266.
- (116) Feng, X.; Liu, J.; Rieke, P. C.; Fryxell, G. E. Reversible Surface Properties of Glass Plate and Capillary Tube Grafted by Photopolymerization of N -Isopropylacrylamide. *Macromolecules* **1998**, *31* (22), 7845–7850.
- (117) Wei, J.; Igarashi, T.; Okumori, N.; Igarashi, T.; Maetani, T.; Liu, B.; Yoshinari, M. Influence of Surface Wettability on Competitive Protein Adsorption and Initial Attachment of Osteoblasts. *Biomed. Mater.* **2009**, *4*, 45002.
- (118) Gittens, R. A.; Olivares-Navarrete, R.; Cheng, A.; Anderson, D. M.; McLachlan, T.; Stephan, I.; Geis-Gerstorfer, J.; Sandhage, K. H.; Fedorov, A. G.; Rupp, F.; et al. The Roles of Titanium Surface Micro/nanotopography and Wettability on the Differential Response of Human Osteoblast Lineage Cells. *Acta Biomater.* **2013**, *9* (4), 6268–6277.
- (119) Lee, J.; Khang, G.; Lee, J.; Lee, H. Interaction of Different Types of Cells on Polymer Surfaces with Wettability Gradient. *J. Colloid Interface Sci.* **1998**, *205* (2), 323–330.
- (120) Dowling, D. P.; Miller, I. S.; Ardhaoui, M.; Gallagher, W. M. Effect of Surface Wettability and Topography on the Adhesion of Osteosarcoma Cells on Plasma-Modified Polystyrene. *J. Biomater. Appl.* **2011**, *26* (3), 327–347.
- (121) Choe, J.-H.; Lee, S. J.; Lee, Y. M.; Rhee, J. M.; Lee, H. B.; Khang, G. Proliferation Rate of Fibroblast Cells on Polyethylene Surfaces with Wettability Gradient. *J Appl Polym Sci* **2004**, *92*, 599–606.
- (122) Wachem, P. B. Van; Hogt, a H.; Beugeling, T.; Bantjes, a; Aken, W. Van. A ~ Esion of Caned H ~ an Endotherm Cells onto Methacrylate Polymers with Vaqying Surface Wettabi & Y and Charge. **1987**, *8*, 323–328.
- (123) Dewez, J. L.; Lhoest, J. B.; Detrait, E.; Berger, V.; Dupont-Gillain, C. C.; Vincent, L. M.; Schneider, Y. J.; Bertrand, P.; Rouxhet, P. G. Adhesion of Mammalian Cells to Polymer Surfaces: From Physical Chemistry of Surfaces to Selective Adhesion on Defined Patterns. *Biomaterials* **1998**, *19* (16), 1441–1445.
- (124) Kelley, E. G.; Albert, J. N. L.; Sullivan, M. O.; Epps III, T. H. Stimuli-Responsive Copolymer Solution and Surface Assemblies for Biomedical Applications. *Chem. Soc. Rev.* **2013**, *42* (17), 7057–7071.
- (125) Khor, H. L.; Kuan, Y.; Kukula, H.; Tamada, K.; Knoll, W.; Moeller, M.; Hutmacher, D. W. Response of Cells on Surface-Induced Nanopatterns : Fibroblasts and Mesenchymal Progenitor Cells Response of Cells on Surface-Induced Nanopatterns : Fibroblasts and Mesenchymal Progenitor Cells. *Society* **2007**, 1530–1540.

- (126) MacLaine, S. E.; Gadhari, N.; Pugin, R.; Meek, R. M. D.; Liley, M.; Dalby, M. J. Optimizing the Osteogenicity of Nanotopography Using Block Co-Polymer Phase Separation Fabrication Techniques. *J. Orthop. Res.* **2012**, *30* (8), 1190–1197.
- (127) Brun-Graepi, A. K. A. S.; Richard, C.; Bessodes, M.; Scherman, D.; Merten, O. W. Thermoresponsive Surfaces for Cell Culture and Enzyme-Free Cell Detachment. *Prog. Polym. Sci.* **2010**, *35* (11), 1311–1324.
- (128) Gil, E. S.; Hudson, S. M. Stimuli-Responsive Polymers and Their Bioconjugates. *Prog. Polym. Sci.* **2004**, *29* (12), 1173–1222.
- (129) Cole, M. A.; Voelcker, N. H.; Thissen, H.; Griesser, H. J. Stimuli-Responsive Interfaces and Systems for the Control of Protein-Surface and Cell-Surface Interactions. *Biomaterials* **2009**, *30* (9), 1827–1850.
- (130) Kim, J.; Hayward, R. C. Mimicking Dynamic in Vivo Environments with Stimuli-Responsive Materials for Cell Culture. *Trends Biotechnol.* **2012**, *30* (8), 426–439.

## *Chapter 4*

# 4. Anisotropic directionality on patterned surfaces

### 4.1. Introduction

The plant and animal kingdoms provide a large diversity of hierarchical structures with extraordinary wetting properties. One of the most well-known example, is the lotus leaf, with a water-repellent behavior, based on both surface roughness and chemistry.<sup>1-3</sup> Neinhuis and Barthlott reported 200 plants with similar wetting characteristics.<sup>4,5</sup> The term water-repellent is referred to the property of materials, which makes the water droplets to roll off the surface and bounce upon impacting.<sup>6</sup> So far, a vast number of superhydrophobic and water-repellent surfaces have been fabricated, owing to its great applications in self-cleaning, anti-icing, inkjet printing, agriculture and spray cooling.<sup>2,3,7-15</sup>

However, numerous micro/mechanical applications require novel surfaces with new properties. Besides the isotropic textures in nature, there are also directional structures, exhibiting both superhydrophobicity and anisotropic wetting.<sup>16,17</sup> Such examples are the butterfly wings,<sup>16-20</sup> the water striders,<sup>16,17</sup> the rice leaf,<sup>17,19</sup> the cicada wings<sup>10</sup> and the fish scale.<sup>17</sup> In each case, such surfaces comprise directional dependent geometrical structures, that produce anisotropic wetting.<sup>18</sup>

Many researchers derive their inspiration from nature in order to develop directional wetting surfaces. Jokinen and his co-workers developed directional wetting surfaces with triangular micropillars. The directionality achieved, was due to the asymmetry of the microstructures.<sup>21</sup> Inspired from butterfly wings, Malvadkar *et al.* developed hydrophobic surfaces with anisotropic adhesive wetting.<sup>18</sup> Unidirectional control of wetting was also achieved through surface modification of PDMS microstructures.<sup>22</sup> Furthermore, smart valves on microchannel, based on chemically patterned surfaces have been reported.<sup>23</sup> Moreover, substrates with periodic asymmetric patterns have been created, which induce droplet transport in response to mechanical or electric fields.<sup>24,25</sup> Such superhydrophobic surfaces with directional controllable wettability have led to advances in microfluidic devices,<sup>18,23,25,26</sup> medicine,<sup>17,18,26</sup> anti-fogging,<sup>17,26</sup> anti-fouling,<sup>26</sup> lab-on-a-chip devices,<sup>22,26</sup> microreactors,<sup>26</sup> and self-cleaning devices.<sup>17,25</sup>

However, the inspiration from nature is unlimited. Apart from the biological species mentioned above, high adhesive surfaces have attracted the attention of researchers, especially at hydrophobic and superhydrophobic surfaces.<sup>17</sup> Among the natural examples of such surfaces, the most well-known is the rose petal effect, with the ability to have water droplets pinned on the surfaces at any tilt angle.<sup>27-29</sup> Bhushan and co-workers fabricated superhydrophobic surfaces with high adhesion by replicating the rose petal.<sup>28</sup> Garlic and scallion leaves exhibit similar wetting properties with high contact angle hysteresis, due to chemical defects.<sup>30</sup> Another interesting phenomenon, revealed from the study of nature, is the gecko's feet. The special wetting properties of gecko's feet, arise from the keratinous hairs, called setae, in its structure.<sup>31</sup>

Inspired from gecko, scientists attempted to develop functional materials with adhesive properties. Such surfaces have many applications, such as in liquid transportation without loss

and in the analysis of very small volumes of liquid samples.<sup>17,31–33</sup> For example, highly adhesive superhydrophobic PS nanotubes have been successfully applied for the no lost transport of superparamagnetic droplets. Different nanostructures with similar wetting characteristics were also developed from Lai *et al.*<sup>34</sup> Additionally, they can be utilized for the analysis of liquid samples with small volumes and for the fabrication of new microfluidic devices.<sup>31</sup> Furthermore, possible applications are for the localized chemical or biological reactions, for the in situ detection of analytes and as blood-compatible surfaces.<sup>35</sup> Geim and his co-workers develop new “gecko tapes” by microfabrication of dense pillars.<sup>36</sup> Hybrid polymeric adhesives, have also been reported, combining gecko elements and mussel proteins.<sup>37</sup> Gecko-mimetic PDMS polymeric films have been developed by using controllable pore channels as template.<sup>31</sup>

In this work, three types of anisotropic surfaces were developed. Initially, superhydrophobic non-adhesive surfaces with unidirectional droplet roll-off behavior were successfully fabricated. For this purpose, Si wafers were treated with femto-second laser, not in a conventional way, but at a tilt angle. The substrate was tilted and, as a result, the laser beam was not pointed perpendicular to the surface. This procedure led to the formation of tilted periodic spikes. Such surfaces, after a silanization process, exhibit anisotropic superhydrophobic behavior with a droplet motion in the direction of the spikes. It was observed that the velocity of the droplet motion was different, depending on the chosen tilt angle. To the best of our knowledge, this is the first work, referring to tilted spikes prepared with fs-laser.

A third level of macro-structuring was also introduced by patterning the inorganic surfaces using photolithography in order to enhance the anisotropic wetting behavior. Si substrates, patterned with grooves, were irradiated with fs laser at a tilt angle. The effect of the

characteristics of the grooves on the final contact angle were investigated. These surfaces exhibit a superhydrophilic directionality, after thermal oxidation, or superhydrophobic directionality after silanization.

Finally, superhydrophobic surfaces with high unidirectional hysteresis were developed. For this purpose, the irradiation of Si wafers was performed at a tilt angle. The substrate was tilted and as a result, the laser beam was not pointed perpendicular to the surface. In order to achieve the high hysteresis, central wavelength of 800 nm was utilized and the different parameters of laser irradiation were investigated. This procedure led to the formation of tilted periodic spikes but with high contact angle hysteresis.

#### 4.1.1. Contact angle hysteresis

Contact angle hysteresis ( $\Delta\theta_h$ ), an important parameter for the surface wetting characterization, can be defined as the difference between the advancing contact angle ( $\theta_{adv}$ ) and the receding contact angle ( $\theta_{red}$ ) for a droplet on a solid surface.<sup>28</sup>

$$\Delta\theta_h = \theta_{adv} - \theta_{red}$$

The advancing angle is referred to the maximum contact angle, obtained by adding volume, while the receding is called the smallest possible angle upon removing volume.<sup>38</sup> The adhesion hysteresis,  $\Delta W$ , is related to the fact that the energy required for the liquid-solid separation is greater than the gain of the energy by their adhesion.<sup>29,39</sup>

$$\Delta W = (\cos\theta_{adv} - \cos\theta_{red}) \cdot \gamma_{LV}$$

Researchers have tried to understand the CA hysteresis by simulations.<sup>29,40</sup> However, models predicting the CA hysteresis are limited and the theoretical understanding is still unclear.<sup>41-43</sup>

CA hysteresis has been mainly attributed to adhesion hysteresis, chemical defects, contamination and roughness.<sup>29,39,40</sup> According to the literature, superhydrophobic surfaces can be defined as surfaces with contact angle above 150° and with small hysteresis.<sup>44</sup> However, recent studies have showed that a surface can be simultaneously superhydrophobic and strongly adhesive.<sup>29,32</sup> This phenomenon is known as “petal effect”.<sup>29,39</sup> As reported by Quere, in these cases the asymmetry in CA creates a difference in the Laplace pressure between the front and the rear, which is able to resist gravity.<sup>16</sup>

Real surfaces are actually rough with hydrophilic blemishes.<sup>38</sup> Bhushan and his co-workers had showed that both micro- and nano- structure, can affect the contact angle value and contact angle hysteresis.<sup>28</sup> For example, surfaces with large density and small microstructures combined with nanostructures with low density exhibit high adhesion and high static contact angle. On the other hand, high density of nanostructures may prevent the water impregnation and can lead to an increased air pocket formation with low adhesion.<sup>28</sup> Furthermore, by increasing the height of the protrusions at a constant density or decreasing the diameter at a constant height, the CA hysteresis increases.<sup>42</sup>

Apart from the structure, the surface chemistry also affects the contact angle hysteresis. Chang *et al.* showed that diallyl disulfide (DADS) is the key component for the high adhesion of garlic and scallion.<sup>38</sup> In this case, CA hysteresis is present due to hydrophobic defects. Diallyl disulfide is insoluble in water. As a result, superhydrophobic surfaces coated with DADS molecules, exhibit high adhesion due to the relative low surface energy between the water and the DADS defects.<sup>38</sup>

#### 4.1.2. Anisotropic wetting

Surface wettability is of paramount importance for the characterization of the surfaces. In case that the structures are uniform to all directions, the apparent contact angle measured

from both directions are similar and the surface is considered to be isotropic.<sup>45</sup> However, isotropic structures are not usually observed. Most surfaces, not only in nature but also in industry, are anisotropic with different contact angle by changing the direction. Usually, the contact angle value is smaller in the direction perpendicular to the surface structure.<sup>45</sup> The anisotropy in these cases has been attributed to dissimilarities in chemical or physical properties.<sup>26</sup> On chemically homogeneous surfaces, the droplets are elongated, while on superhydrophobic surfaces, the droplet rolls off anisotropically.<sup>21</sup>

Anisotropic wetting phenomena are of great interest due to their potential applications in cases that the liquid must be guided, like in microfluidic devices and self-cleaning coatings.<sup>22,46,47</sup> According to literature, anisotropy can be achieved either by directional patterns on surfaces or by chemical modification of the structures. So far, a lot of reports are referring to 1D groove structures, prepared with various techniques, like lithography and imprinting.<sup>22</sup> In parallel, several reports have addressed the effect of the chemical modification of grooves on their anisotropic wettability.<sup>22,46–56</sup> The combination of structural and chemical anisotropy can lead to surfaces with enhanced directional wetting properties.<sup>22,49,51,57</sup> For example, surfaces with gradient-based pathways structures, or chemical asperities, can lead to droplet motion in the preferred direction.<sup>58,59</sup>

### 4.1.3. Anisotropic wetting phenomena in nature with low hysteresis

In nature anisotropic wetting is observed in a variety of biological surfaces. For example, the butterfly wings present a directional adhesion due to the directional micro- and nano-structures.<sup>20</sup> The structure of the wings of the Blue Morpho didius is depicted in Figure 4.1.<sup>60</sup>

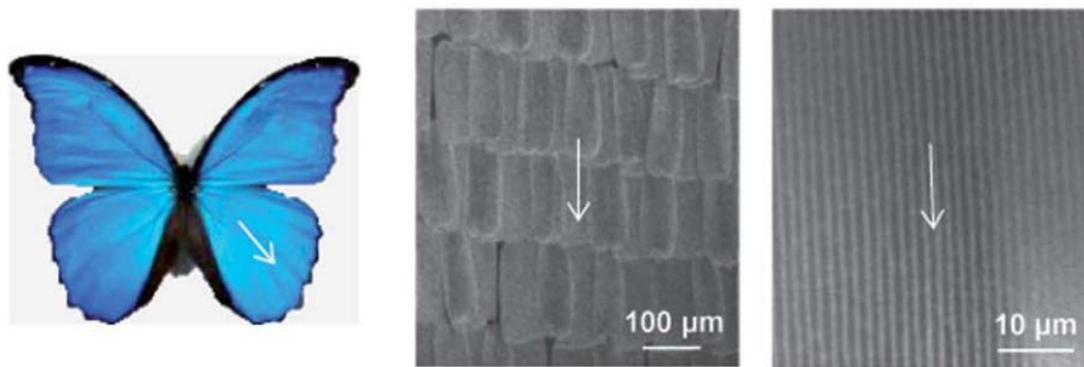


**Figure 4.1.** Digital photo and scanning electron microscope (SEM) images of butterfly wings.

Butterfly wings are covered by a large number of scales, which overlap each other to form a periodic hierarchy along the radial outward direction. Each scale is composed of well-oriented nanostructures, which are stacked stepwise by tilted periodic lamellae. Interestingly, the nanotips on the top of stripes tilt slightly upward.<sup>17</sup> As a result, the droplet rolls off the surface along the radial direction of the central axis, but it is pinned against the anisotropy.<sup>17,20,26</sup>

Another example of anisotropic behavior is the rice leaf, which have sinusoidal grooves.<sup>17,60</sup>

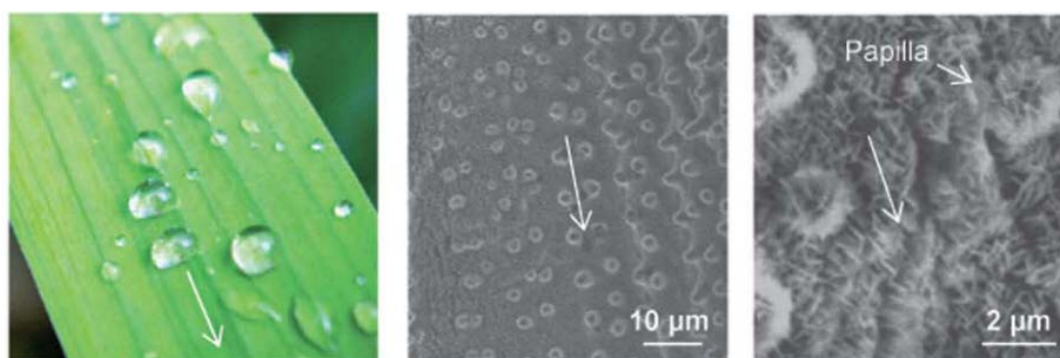


**Figure 4.2.** Digital photo and scanning electron microscope (SEM) images of rice leaf.

The quasi-one dimensional ordered hierarchically structured papillae of rice leaves provide a different energy barrier of wetting in the two directions.<sup>17,26</sup> Along the direction of the leaf edge, the sliding angle is  $5^\circ$ , while in a perpendicular direction, the respective value is  $9^\circ$ - $15^\circ$ .<sup>17</sup>

*Strelitzia reginae* leaves exhibit also unidirectional water spreading. (Figure 4.3)<sup>61</sup>



**Figure 4.3.** Photographs of the *Strelitzia reginae* plant and flower.

Mele and his co-workers found that the green and dried leaves of the plant are promising templates for the development of artificial surfaces with different wettability.<sup>61</sup>

Antifouling example in nature with directional wetting properties is the shark skin (Figure 4.4).<sup>17,60,62</sup> Controlling biofouling is accomplished through a variety of ways in medical, marine, and industrial applications. Thus, engineers have investigated the anisotropic mechanism of shark skin and have developed surfaces, imitating this behavior.<sup>17,60,63</sup>

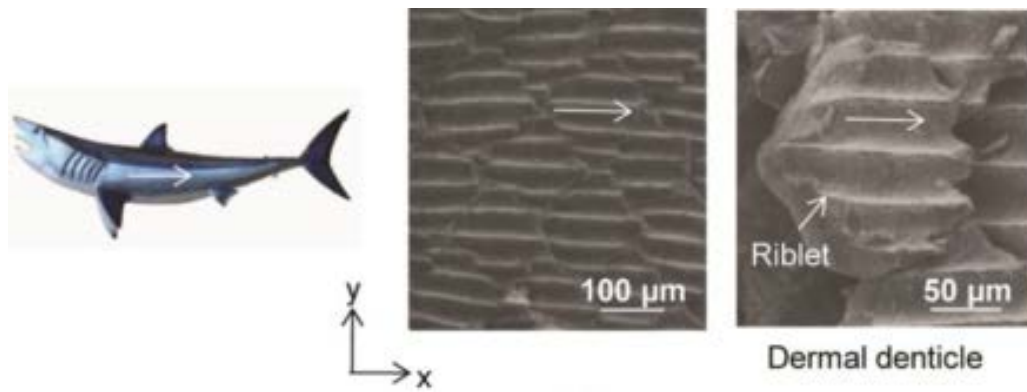


**Figure 4.4.** Digital photo and scanning electron microscope (SEM) images of shark skin.<sup>60</sup>

Anisotropic behavior of shark skin occurs due to the riblets aligned in the swimming direction, that control the turbulent flow.<sup>60</sup> The skin of fast swimming sharks is consisted of scales, known as dermal denticles, which are the reason for the shear stress and drag reduction.<sup>60</sup> The spacing between the denticles is such that prevents the aquatic organisms to adhere to the surface.<sup>63</sup>

Similar behavior exhibit the fish scale, with low drag and antifouling properties (Figure 4.5). Fishes are covered with well-oriented scales that direct the flow from head to tail. Both shark skin and fish scales, have been reported also as oil-repellent surfaces.<sup>60,63,64</sup>

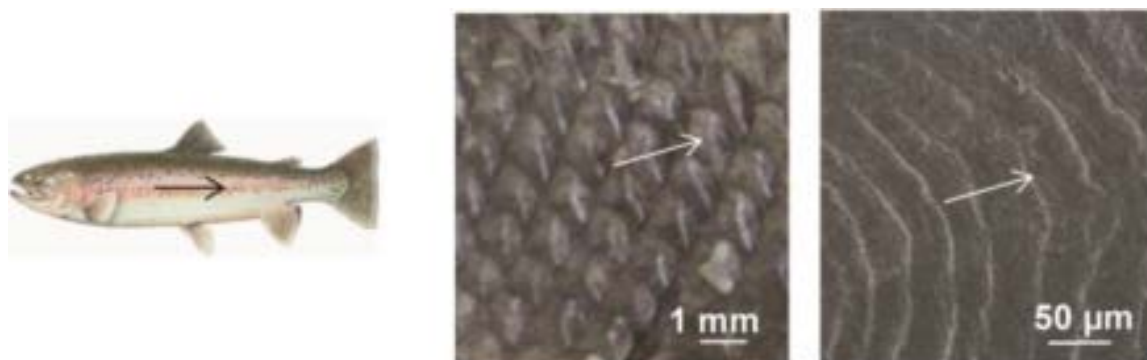


**Figure 4.5.** Digital photo and scanning electron microscope (SEM) images of fish scale.<sup>60</sup>

Engineered fish replicas have potential for many applications in an oil/water/solid system, such as marine antifouling, prevention of oil spills, microfluidic technology, and bioadhesion.<sup>17</sup> Furthermore, drag reduction is one of the main handicaps for aircrafts, ships, submarines and microfluidic devices.<sup>17</sup>

#### 4.1.4. High adhesive surfaces in nature

The natural examples of superhydrophobic surfaces with high adhesion are rare. The most well known example, is the rose petal effect. The “sticky” wetting behavior of rose petal can be explained as follows. The microstructures of the rose petals (Figure 4.6), are larger than the lotus leaf, resulting in impregnation of the water between the large scale grooves. However, the liquid are not allowed to enter into the smaller grooves and the droplets pin on the surface.<sup>17</sup> This phenomenon is known as Cassie impregnating wetting regime.<sup>38</sup> Feng *et al.* achieve to duplicate the microstructures of the “petal effect”.<sup>65</sup>

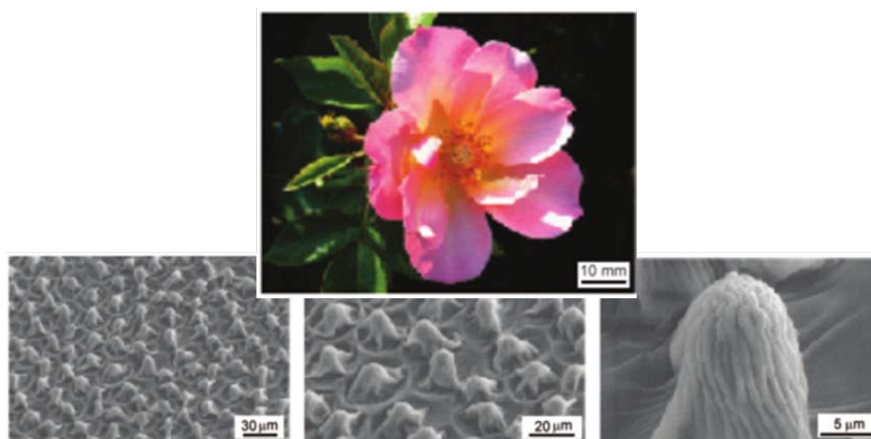


**Figure 4.6.** Rose petal with high adhesion.

Other petals exhibiting similar behavior, high CA with high adhesion, are the Chinese Kafir and the sunflower (Figure 4.7).<sup>65</sup>

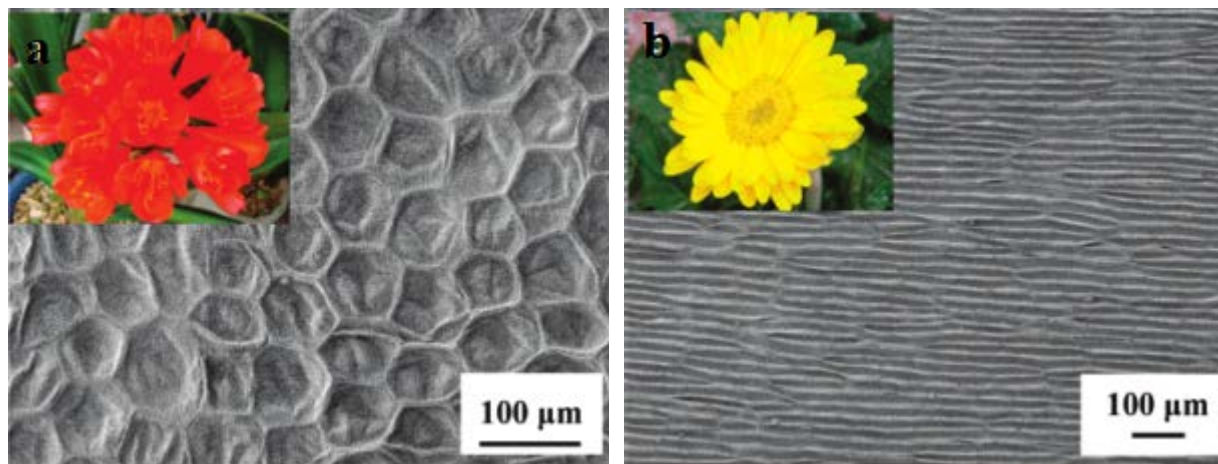


**Figure 4.7.** (a) Chinese Kafir and (b) sunflower petal.

The highly adhesive superhydrophobic behavior of the leaves of xerophate peanut (*Arachis hypogaea*) has been investigated by Yang and his co-workers<sup>66</sup> (Figure 4.8).

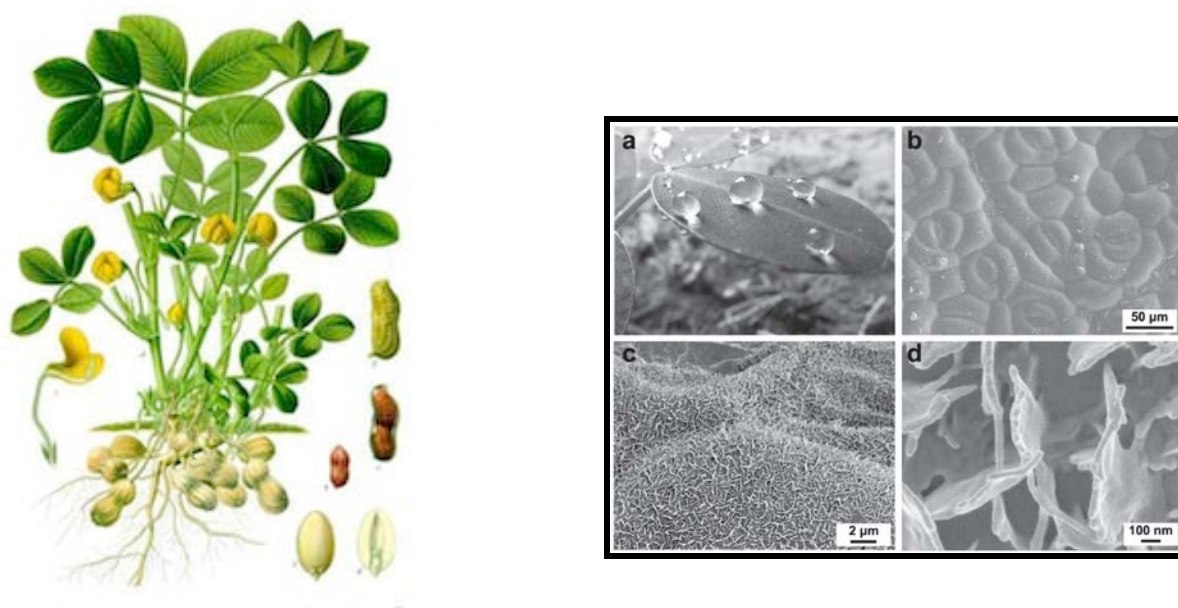


**Figure 4.8.** Peanut leaf (left) and surface wettability and structural hierarchy of peanut leaves (right).<sup>66</sup>

The peanut, due to its fog capture properties, survives in arid and semi-arid regions, characterized by high temperature and low rainfall.<sup>66</sup> The wetting behavior of the peanut leaf

has been attributed to the discontinuous of nanoscale and quasi-continuous at the microscale.<sup>66</sup>

Similar behavior exhibits the skunk cabbage leaf, which belong to the thermogenic plants (Figure 4.9). The surface of the skunk cabbage leaf is hydrophobic, but not above  $150^\circ$ , with high hysteresis.<sup>67</sup>

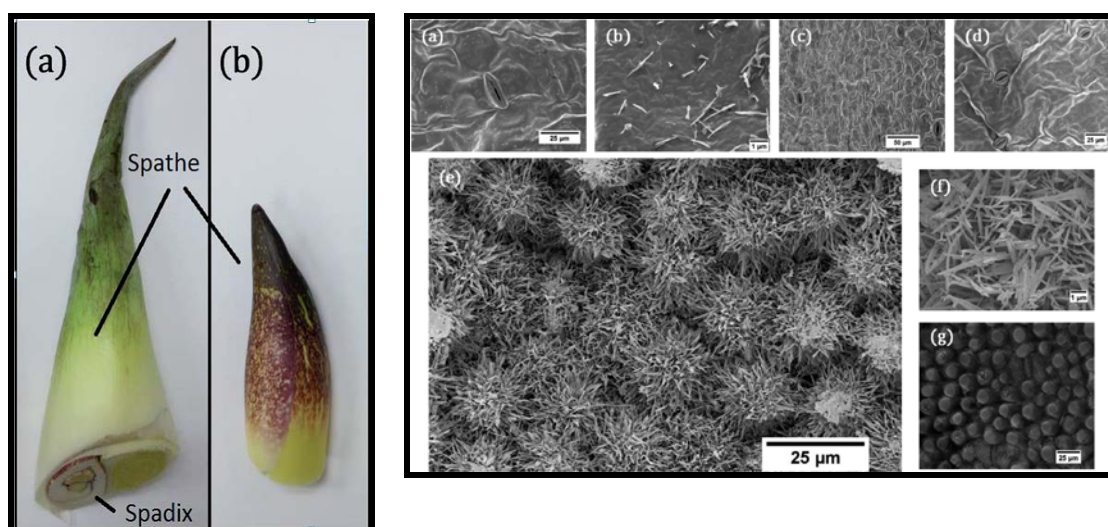


**Figure 4.9.** Skunk cabbage leaf (left) and surface wettability and structural hierarchy of the same leaf (right).<sup>67</sup>

Another interesting phenomenon in nature is gecko, known as the most effective adhesive in nature<sup>17</sup> (Figure 4.10). The special wetting properties of gecko's foot, arise from the keratinous hairs, called setae, in its structure.<sup>31</sup> The tips of setae contains smaller hairs, called spatula, provide a large surface area in close contact to the surface.<sup>31</sup>

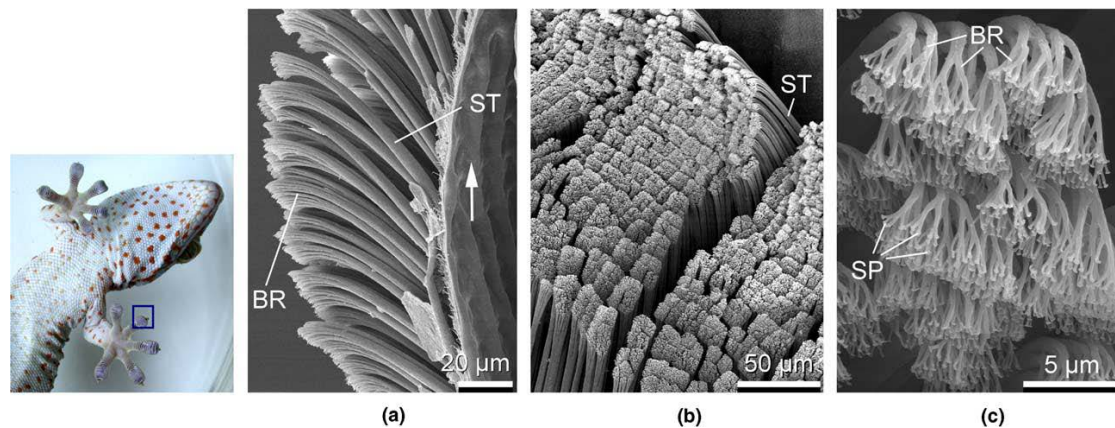


**Figure 4.10.** Hierarchical adhesive structures of Gecko. (a) A toe of gecko contains hundreds of thousands of setae and each seta contains hundreds of spatula, (b): scanning electron micrographs of rows of setae at different magnifications and (c): spatulae, the finest terminal branches of seta.<sup>68</sup>

Autumn *et al.* proved that the Van der Waals forces enable gecko to adhere to surfaces.<sup>69</sup> The toes of gecko are highly hydrophobic and can adhere well to both strongly hydrophobic and strongly hydrophilic surfaces.<sup>69</sup>

## A) Superhydrophobic non-adhesive surfaces with unidirectional droplet roll-off behavior

### 4.2. Introduction

Until now, there are few reports referring to single direction of liquid flows. In this work, superhydrophobic surfaces were developed, non-adhesive, with directional droplet roll-off behavior. For this purpose, Si substrates were treated with femto-second laser in order to achieve the dual-scale roughness. However, the irradiation was not performed in a

conventional way, but at a tilt angle. The substrate was tilted and as a result, the laser beam was not pointed perpendicular to the surface. This procedure led to the formation of tilted periodic spikes. Such surfaces after a silanization process exhibit anisotropic wettability, with a droplet motion on the direction of the spikes. It was observed that the velocity of the droplet motion was different, depending on the chosen tilt angle. To the best of our knowledge, this is the first work, referring to tilted spikes, treated with fs-laser.

### 4.3. Experimental Part

#### 4.3.1. Surface manufacturing with fs laser

Single crystal *n*-type Si (100) wafers with a resistivity of  $\rho = 2\text{-}8 \text{ }\Omega\text{-cm}$  were utilized as substrates for the fabrication of Si spikes. Microstructuring of Si surfaces was performed by femtosecond (fs) laser (Yb:KGW) under a reactive gas ( $\text{SF}_6$ ) atmosphere at a pressure 500 Torr. The conical spikes are sharper when silicon is processed in sulfur hexafluoride ( $\text{SF}_6$ ) because fluorine radicals react with silicon and etch away silicon at the surface.<sup>70</sup> The irradiation source was adjusted at a repetition rate of 1 kHz and pulse duration of 170 fs at a wavelength of 1026 nm. The samples were kept in a chamber, mounted on a high precision X-Y translational stage, on a tilted angle to the incident laser beam (Figure 4.11).

In case that the substrates are tilted during the irradiation process, the distance between the substrate and the central of the lens would not be the same. For this reason, the focus lens was mounted on a high precision X translational stage. So, the laser pulse travels in the +x-direction, step a distance in the y-direction and before travelling again in the -x-direction, the lens was moved in the +x axis. Through this process, the lens focus length was maintained during the irradiation process, in every step motion in +y axis. The step motion of the lens was calculated depending on the angle of the tilted substrate.

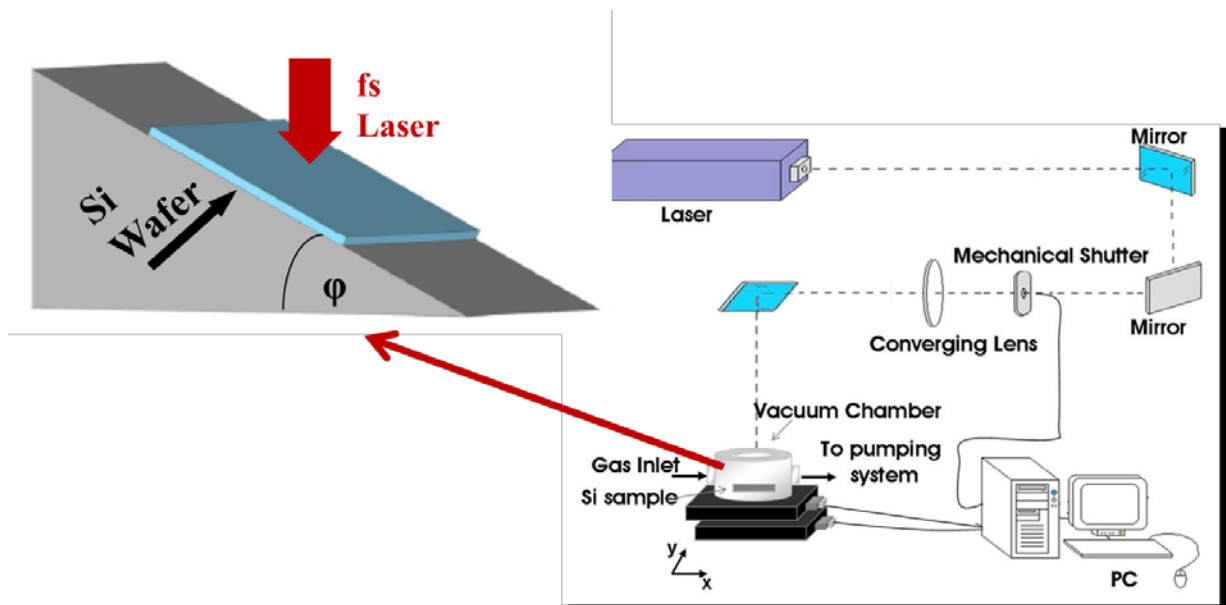


**Figure 4.11.** Schematic diagram of a femtosecond laser micromachining system for fabrication of tilted microstructures.

The experimental procedure for the femtosecond-laser microstructuring silicon involves several variable parameters. Among them, are the shot number, the fluence, the pulse duration, the ambient gas atmosphere, the laser wavelength, the polarization and propagation direction, the spot size and the substrate properties.<sup>71,72</sup> The effect of these parameters in the final morphology and chemical composition of the conventional microstructuring, has been reported in literature.<sup>71–73</sup>

As this is the first work referring to tilted spikes, the fundamental investigation of different parameters was needed. For this purpose, Si substrates were irradiated with fs laser at different tilt angles and the effect of fluence, step distance in the y-direction, repetition rate and the scanning speed were investigated.

#### 4.3.2. Making Si spikes superhydrophobic

Samples, after irradiation were cleaned in ultrasonic baths of trichloroethylene, acetone and methanol followed by a 10% HF v/v aqueous treatment in order to remove the oxide grown

on the surface.<sup>11</sup> Afterwards, the samples were placed in a flask containing 0.5 ml of dimethyldichlorosilane ((CH<sub>3</sub>)<sub>2</sub>SiCl<sub>2</sub>, DMDCS) reagent, which is a low surface energy coating. Hydrophobic DMDCS monolayers were subsequently deposited on the sample's surface through adsorption reactions. The vapor-phase reactions were carried out overnight at room temperature.<sup>2</sup> The hydrophobized surfaces were rinsed with toluene (two aliquots), ethanol (three aliquots), 1:1 ethanol/water (two aliquots), deionized water (two aliquots), ethanol (two aliquots), and deionized water (three aliquots) and were finally dried in a clean oven at 120°C for 45 minutes.<sup>11</sup>

### 4.3.3. Wettability of the prepared samples

Wettability tests were performed using a surface tensiometer (OCA-40, Dataphysics) utilizing the sessile drop method.<sup>74</sup> Sessile contact angle titrations were repeated five times for each sample.

Furthermore, the roll-off angle of sessile drop was measured. This was performed through a device unit, which allows the motor-driven and software controlled inclination of the instrument up to an angle of 90°. Advancing and receding contact angles were determined by adding / removing volume to the drop dynamically. The maximum angle achieved, by increasing the solid/liquid interfacial area, is the advancing contact angle. The receding contact angle is the smallest possible angle, without decreasing its solid/liquid interfacial area, determined by removing volume from the drop dynamically.<sup>16</sup> The contact angle hysteresis was defined as the difference between the advancing and receding contact angle for a contact line moving to an opposite direction.<sup>75-77</sup> In cases that drop bouncing occurred, the velocity of the droplet motion was also calculated.

## 4.4. Results and Discussion

### 4.4.1. Surface characterization

Si substrates were irradiated at different tilt angles under a reactive gas ( $\text{SF}_6$ ) atmosphere at a pressure 500 Torr. The irradiation source was adjusted at a repetition rate 1 kHz with pulse duration of 170 fs and at a wavelength of 1026 nm. The effect of fluence and the step distance in the y-direction were investigated through field emission scanning electron microscope (FE-SEM, JEOL JSM-7000F).

#### 4.4.1.1. Effect of fluence

In this section the morphology of the spikes was examined at different laser fluencies. Initially, samples were irradiated in a conventional way, with the laser beam perpendicular to the substrate, as reference materials. The irradiation source was adjusted at a repetition rate of 1 kHz and the step distance in the y-direction was 16  $\mu\text{m}$ . The characterization of the conventional spikes is depicted in Figure 4.12.

## Top-view SEM images. 45-degree-view SEM images.

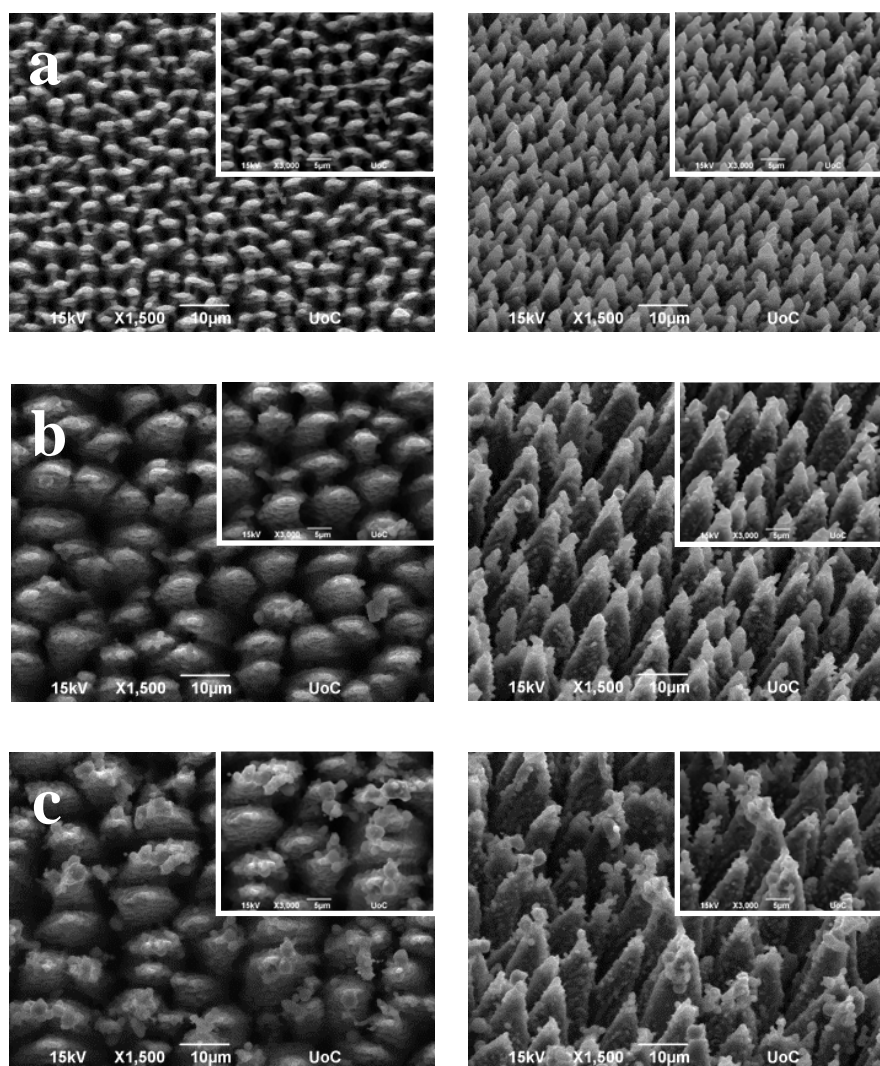
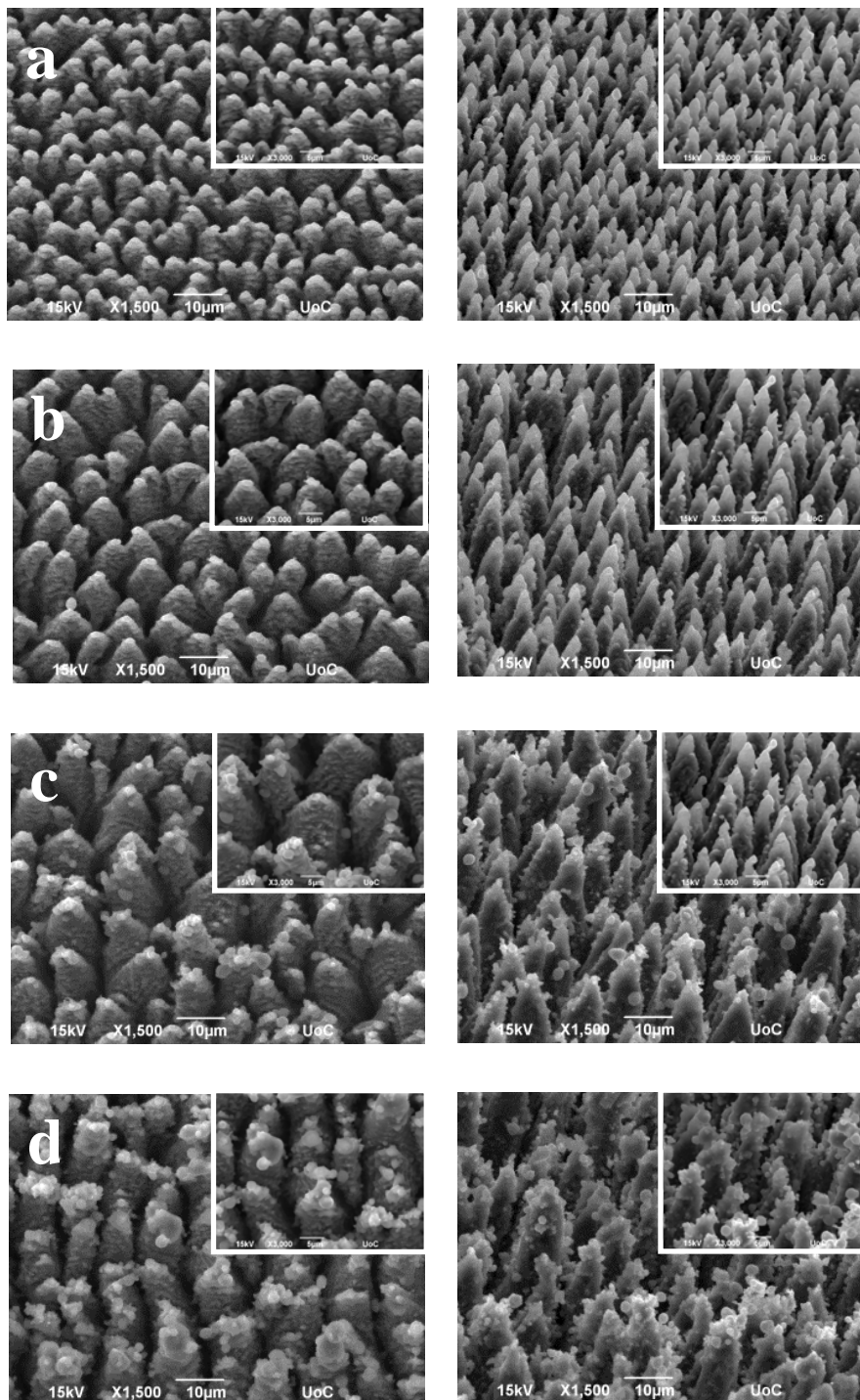


**Figure 4.12.** Top-view (left) and 45-degree view (right) scanning electron micrographs of a silicon surface after irradiation with laser pulses of fluence (a)  $0.5 \text{ J/cm}^2$ , (b)  $1 \text{ J/cm}^2$ , (c)  $1.5 \text{ J/cm}^2$ . Insets are higher magnification images from the same samples.

According to Figure 4.12, with increasing the fluence (at constant shot number) the morphology goes from laser induced periodic surface structures, to sharp microstructures. At a fluence of  $0.5 \text{ J} \cdot \text{cm}^{-2}$ , conical microstructures are developed. As the fluence increases from  $0.5$  to  $1.5 \text{ J} \cdot \text{cm}^{-2}$ , the height and the diameter of the spikes are increasing, while their density is lower.

As a next step, samples were irradiated at different tilt angles  $10^\circ$ ,  $20^\circ$ ,  $30^\circ$  and  $45^\circ$  with fluencies varying from  $0.5$  to  $2.8 \text{ J} \cdot \text{cm}^{-2}$ . Figure 4.13 shows the characterization of the surfaces, irradiated at  $10^\circ$  tilt angle.

**Top-view SEM images. 45-degree-view SEM images.**



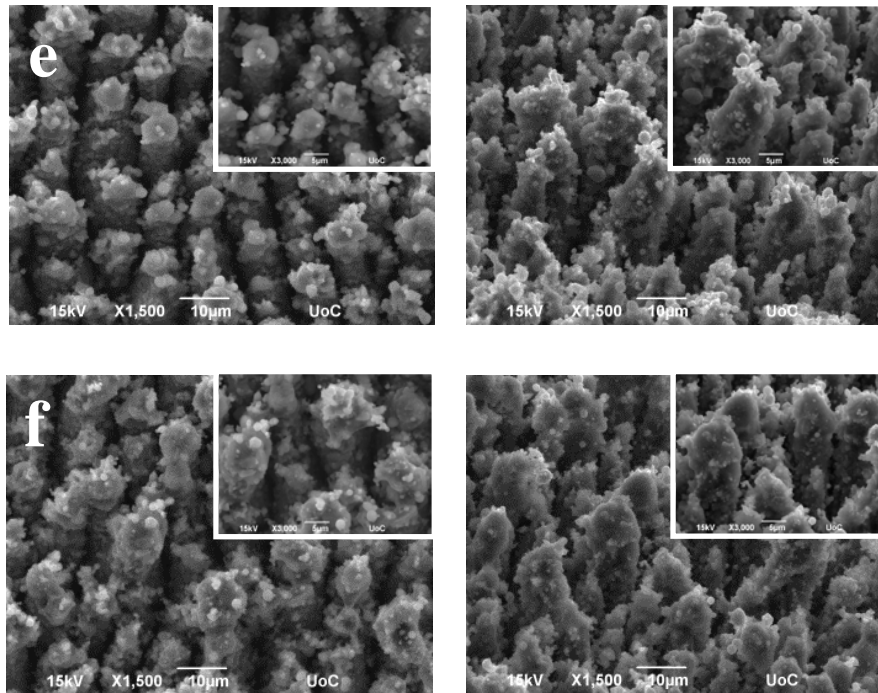
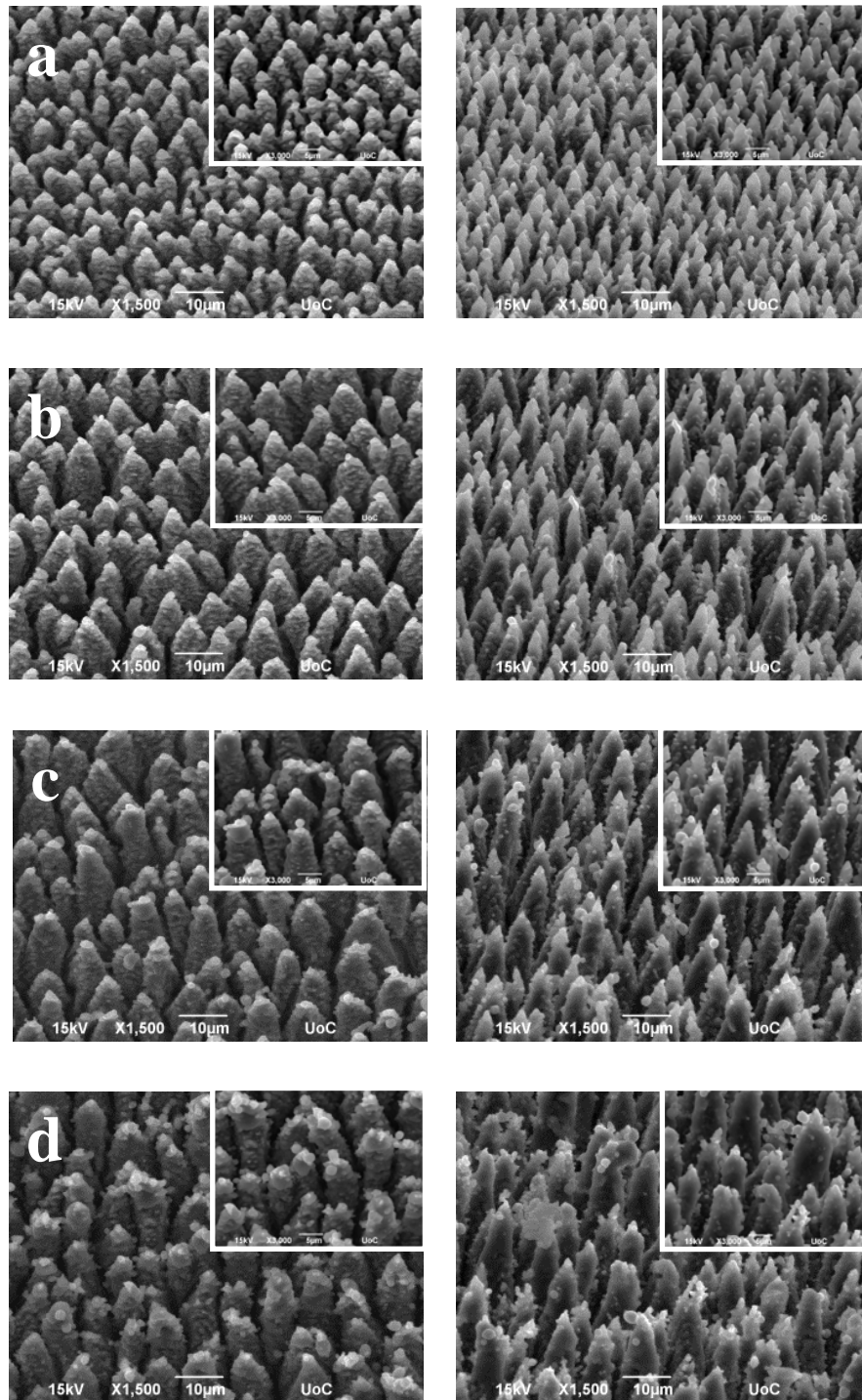


**Figure 4.13.** Top-view (left) and 45-degree view (right) scanning electron micrographs of a silicon surface after irradiation at a  $10^\circ$  tilt angle, with laser pulses with fluence: (a)  $0.5 \text{ J/cm}^2$ , (b)  $0.7 \text{ J/cm}^2$ , (c)  $1 \text{ J/cm}^2$ , d)  $1.5 \text{ J/cm}^2$  e)  $2 \text{ J/cm}^2$  and f)  $2.8 \text{ J/cm}^2$ . Insets are higher magnification images from the same samples.

According to Figure 4.13, the size and the morphology of  $10^\circ$  tilted spikes, depends on the selected fluence. At low fluencies, from  $0.5$  to  $0.7 \text{ J/cm}^2$ , the tilted spikes are formed and they have similar size and shape with the conventional spikes (Figure 4.12). Comparing the images 4.13 a and 4.13 c, it can be observed an increase in the height of the spikes without losing their conical structure. At  $1$  to  $1.5 \text{ J/cm}^2$  (Figure 4.13 c and d), the tilted spikes are not homogeneous and their structure and shape are not so well-defined. By utilizing higher fluencies, (above  $2 \text{ J/cm}^2$ ), spikes cannot be observed. The structures are heterogeneous with irregular shape and size.

Afterwards, samples were irradiated at  $20^\circ$  tilted angle with fluencies varying from  $0.5$  to  $2.8 \text{ J} \cdot \text{cm}^{-2}$ . Figure 4.14 shows the characterization of the surfaces, irradiated at  $20^\circ$  tilt angle.

## Top-view SEM images. 45-degree-view SEM images.



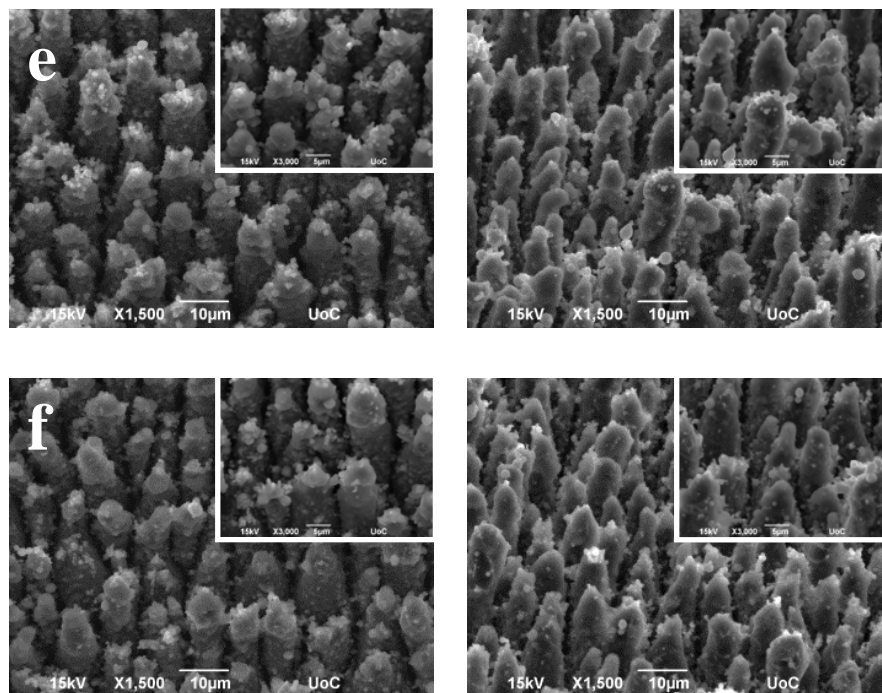


**Figure 4.14.** Top-view (left) and 45-degree view (right) scanning electron micrographs of a silicon surface after irradiation at a 20° tilt angle, with laser pulses with fluence: (a) 0.5 J/cm<sup>2</sup>, (b) 0.7 J/cm<sup>2</sup>, (c) 1 J/cm<sup>2</sup>, (d) 1.5 J/cm<sup>2</sup> e) 2 J/cm<sup>2</sup> and f) 2.8 J/cm<sup>2</sup>. Insets are higher magnification images from the same samples.

From fluencies 0.5 to 1 J/cm<sup>2</sup>, spikes are etched out of the surface and both height and density of the microstructures are increased. At higher fluencies (1.5 - 2.8 J/cm<sup>2</sup>), material removal becomes extreme and instead of clear conical structures, there are spikes covered with particles 1-2 µm in diameter. Comparing the results of 10° and 20° tilted spikes in respective fluencies, (Figures 4.13, 4.14) there are no noticeable differences in the morphology, the size and the shape of the microstructures.

In parallel, samples were irradiated at 30° tilt angle with fluencies varying from 0.5 to 1.5 J·cm<sup>-2</sup>. Figure 4.15 shows the characterization of the surfaces, irradiated at 30° tilt angle.

## Top-view SEM images. 45-degree-view SEM images.

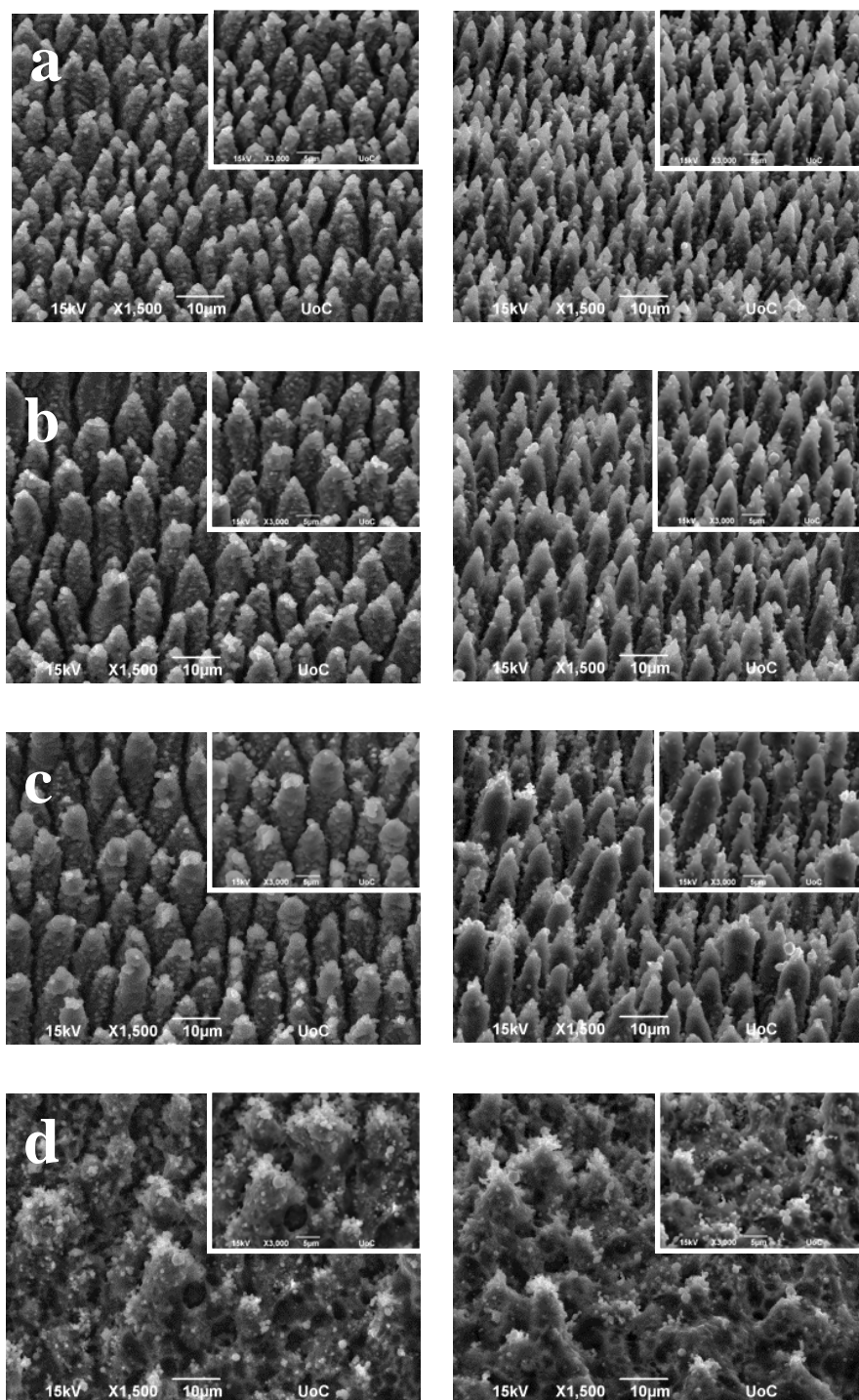
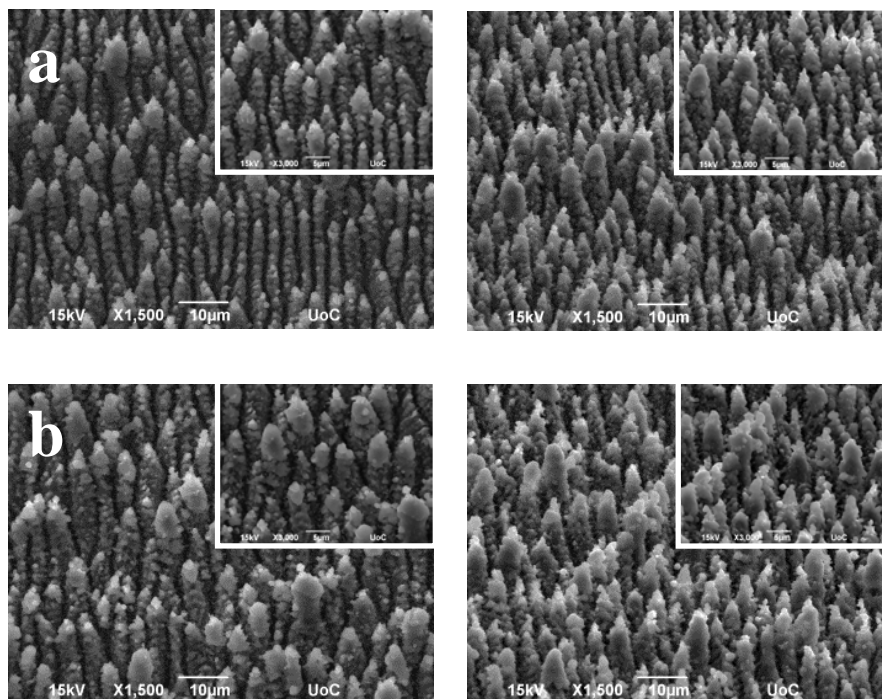


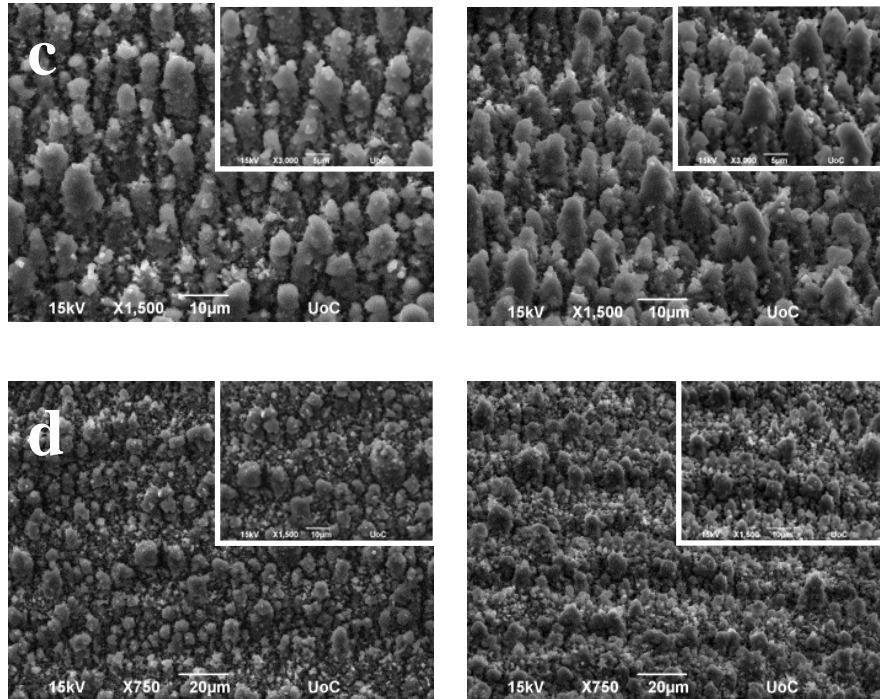
**Figure 4.15.** Top-view (left) and 45-degree view (right) scanning electron micrographs of a silicon surface after irradiation at a  $30^\circ$  tilt angle, with laser pulses with fluence: (a)  $0.5 \text{ J/cm}^2$ , (b)  $0.7 \text{ J/cm}^2$ , (c)  $1 \text{ J/cm}^2$  and d)  $1.5 \text{ J/cm}^2$ . Insets are higher magnification images from the same samples.

According to Figure 4.15, the  $30^\circ$  tilted spikes irradiated at fluencies from  $0.5$  to  $1 \text{ J/cm}^2$ , are well-ordered and uniform. At low fluencies ( $0.5 \text{ J/cm}^2$ ) the spikes are much smoother and in higher density. By increasing the fluence, their size and height is increasing, while more micro- and nano-particles are deposited on the surface of the microstructures. In fluencies above  $1.5 \text{ J/cm}^2$ , there no spikes formed, but only a rough surface with random structures. Comparing these results, with the  $10^\circ$  and  $20^\circ$  tilted spikes, it can be noticed that the spikes in the  $30^\circ$  tilted spikes are higher in low fluencies. Furthermore, in Figures 4.13 and 4.14, there are spikes in high fluencies, although they are not well-ordered.

Next, samples were irradiated at  $45^\circ$  tilt angle with fluencies varying from  $0.5$  to  $1.5 \text{ J}\cdot\text{cm}^{-2}$ . Figure 4.16 shows the characterization of the surfaces, irradiated at  $45^\circ$  tilt angle.

**Top-view SEM images. 45-degree-view SEM images.**



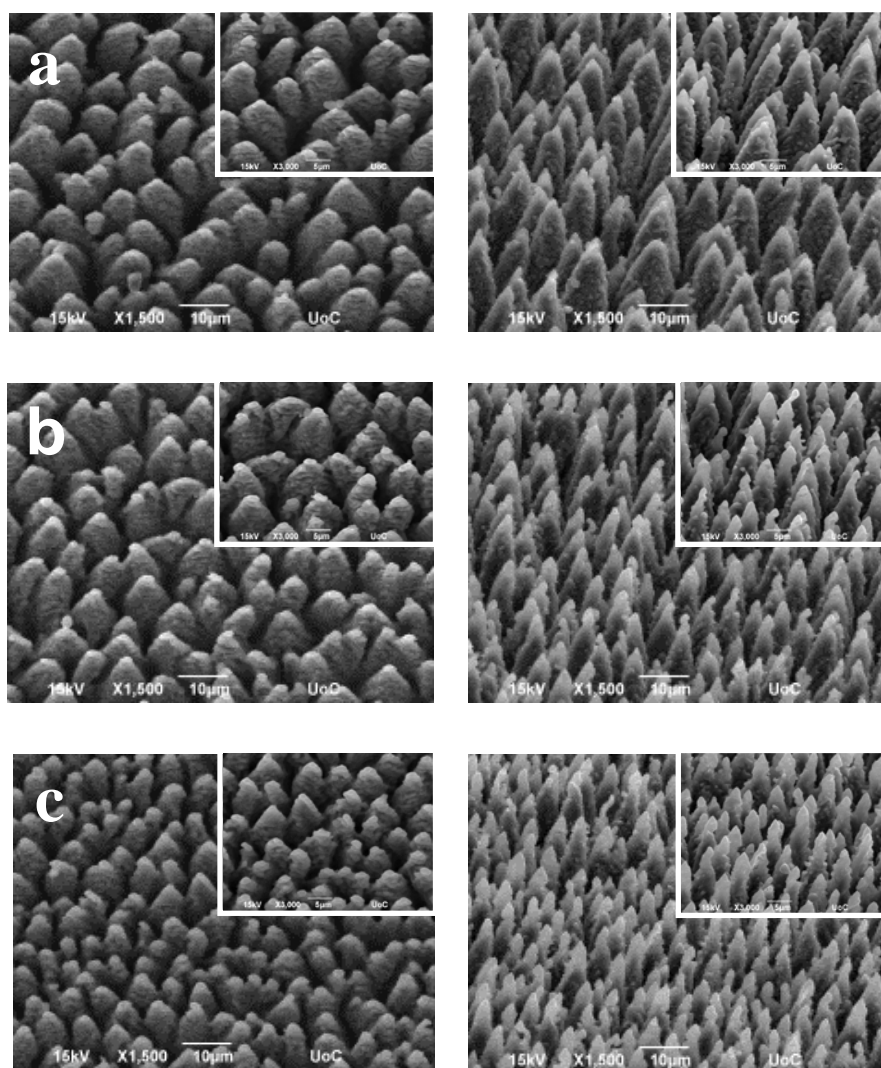


**Figure 4.16.** Top-view (left) and 45-degree view (right) scanning electron micrographs of a silicon surface after irradiation at  $45^\circ$  tilt angle, with laser pulses with fluence: (a)  $0.5 \text{ J/cm}^2$ , (b)  $0.7 \text{ J/cm}^2$ , (c)  $1 \text{ J/cm}^2$  and d)  $1.5 \text{ J/cm}^2$ . Insets are higher magnification images from the same samples.

Figure 4.16 shows the results for silicon surfaces after irradiation at a  $45^\circ$  tilt angle. In this case, spikes are not well-ordered even in low fluencies. The morphology of the structures resembles more ripples with tips than spikes. In high fluencies, structures cannot be distinguished. The surfaces are covered with damaged spikes.

#### 4.4.1.2. Effect of step distance in the y-direction

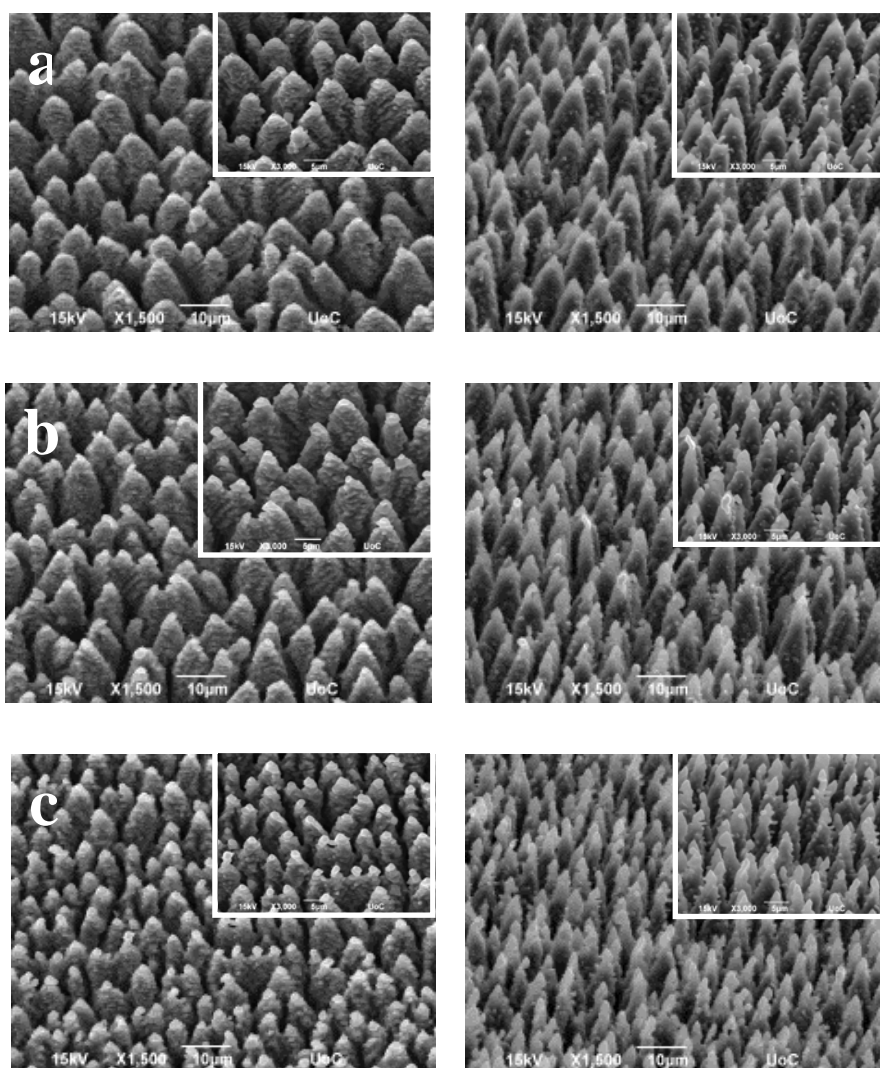
In this section the morphology of the spikes was examined at y step distances. The irradiation source was adjusted at a repetition rate of 1 kHz and the fluence at  $0.7 \text{ J/cm}^2$ . The characterization of the tilted spikes is depicted in Figures 4.17-4.19.

**Top-view SEM images. 45-degree-view SEM images.**

**Figure 4.17.** Top-view (left) and 45-degree view (right) scanning electron micrographs of a silicon surface after irradiation on a  $10^\circ$  tilt angle, with laser pulses with y step: (a)  $8\ \mu\text{m}$ , (b)  $16\ \mu\text{m}$  and (c)  $30\ \mu\text{m}$ . Insets are higher magnification images from the same samples.

According to the Figure 4.17, the y step distance affects the size and the density of the spikes. In all cases the spikes are ordered, uniform and they have conical shape. However, by increasing the y step distance, the density of the spikes is higher and structures are shorter and thinner.

The morphology of the  $20^\circ$  tilted spikes was also investigated, by altering the y step distance (Figure 4.18).

**Top-view SEM images. 45-degree-view SEM images.**

**Figure 4.18.** Top-view (left) and 45-degree view (right) scanning electron micrographs of a silicon surface after irradiation at a  $20^\circ$  tilt angle, with laser pulses with y step: (a)  $8\ \mu\text{m}$ , (b)  $16\ \mu\text{m}$  and (c)  $30\ \mu\text{m}$ . Insets are higher magnification images from the same samples.

The results for  $20^\circ$  tilted spikes, depending on the y step distance, are similar to the  $10^\circ$  tilted spikes. The size and the density of the spikes are changing by altering the y step.

The study was fulfilled with the effect of the y step in the morphology of the  $30^\circ$  tilted spikes (Figure 4.19).

**Top-view SEM images. 45-degree-view SEM images.**

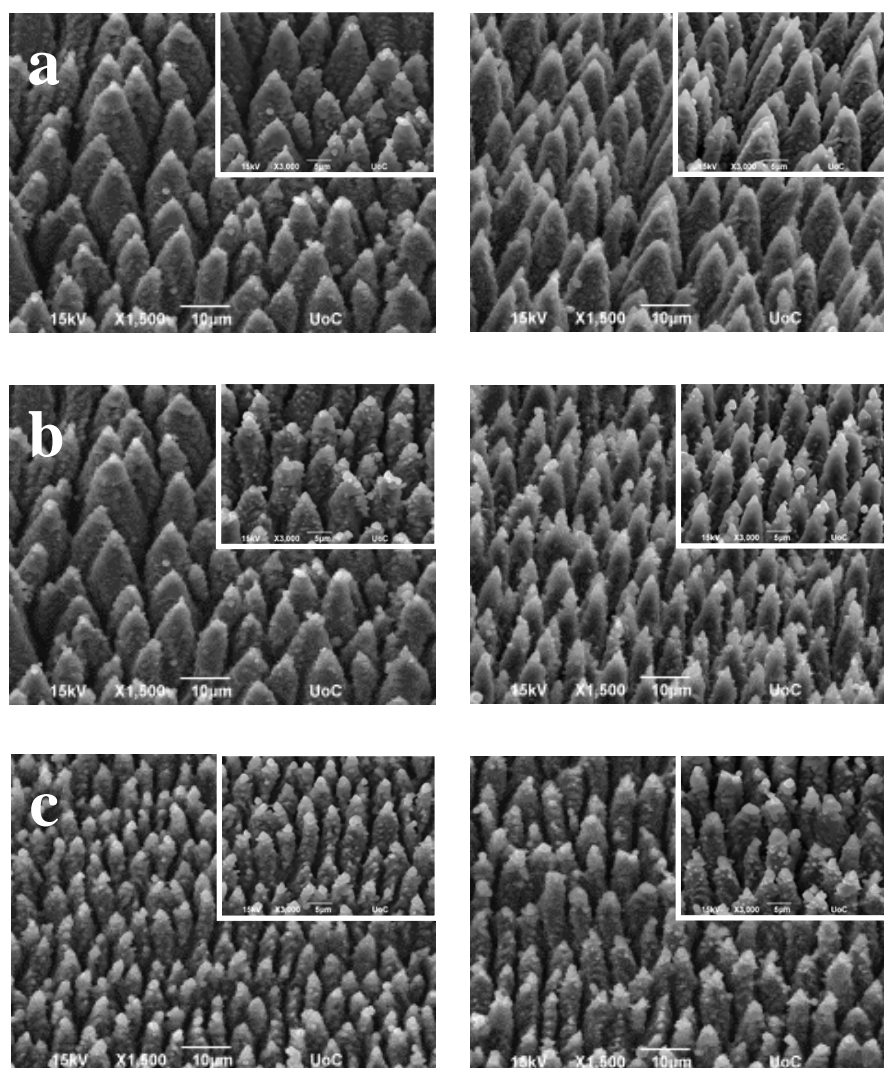


**Figure 4.19.** Top-view (left) and 45-degree view (right) scanning electron micrographs of a silicon surface after irradiation at a  $30^\circ$  tilt angle, with laser pulses with y step: (a)  $8\ \mu\text{m}$ , (b)  $16\ \mu\text{m}$  and (c)  $30\ \mu\text{m}$ . Insets are higher magnification images from the same samples.

According to the FE-SEM images for the  $30^\circ$  tilted spikes, the structures for low values of y step ( $8$  and  $26\ \mu\text{m}$ ), the morphology of the spikes is similar with the respective structures of  $10^\circ$  and  $20^\circ$  tilted spikes. However, for the case of  $30\ \mu\text{m}$ , the spikes resemble the structure of the  $45^\circ$  tilted spikes, irradiated with y step distance  $16\ \mu\text{m}$  (Figure 4.16 a).

#### 4.4.2. Wettability

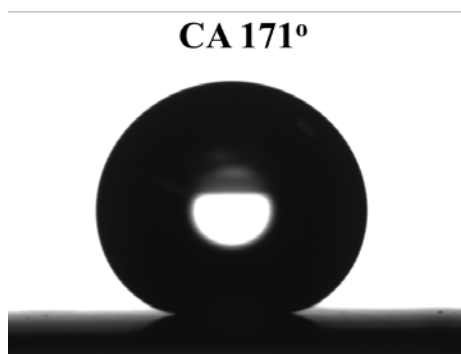
Si wafers, after irradiated with fs laser, were treated with dimethyldichlorosilane, as described in the experimental part. The fluence selected for the irradiation process, taking into account the surface characterization, was  $0.7 \text{ J/cm}^2$  and the  $y$  step distance was  $16 \text{ }\mu\text{m}$ .

Wettability tests were performed utilizing the sessile drop method.<sup>74</sup> The static measurement was performed by producing a specific drop volume (1-10 $\mu\text{L}$ ) that was still hanging from a syringe needle, which was then gently brought into contact with the solid. Distilled water (density  $\rho = 999 \text{ kg/m}^3$ , viscosity  $\eta = 889 \text{ }\mu\text{Pa s}$ , and surface tension  $\gamma = 72.8 \text{ mN/m}$ ) was used to measure the wettability of the surfaces. Usually, when the droplet contacts the surface, it will detach from the syringe and spread on the surface, decreasing the contact angle value from initially  $180^\circ$  (prior to contact) to the static (“equilibrium”) contact angle ( $\theta$ ). However, this is not the case for superhydrophobic surfaces with low hysteresis. As the droplet driving forces are the capillary forces, the low surface tension of the samples, prevent the attachment of the droplet to the surface, which remains on the syringe tip. On the other hand, when the droplet volume increases, influence of gravity becomes larger. In this work, droplets of  $10 \text{ }\mu\text{L}$  were utilized in order to achieve their gentle attachment on the surfaces. Sessile contact angle titrations were repeated five times for each sample.

The velocity of the water droplets motion was calculated as well as the restitution coefficient. The restitution coefficient, can be defined as the ratio of the centre of mass velocity just after impact, to that just before impact.<sup>11</sup>

##### 4.4.2.1. Wettability of surfaces with $10^\circ$ tilted spikes

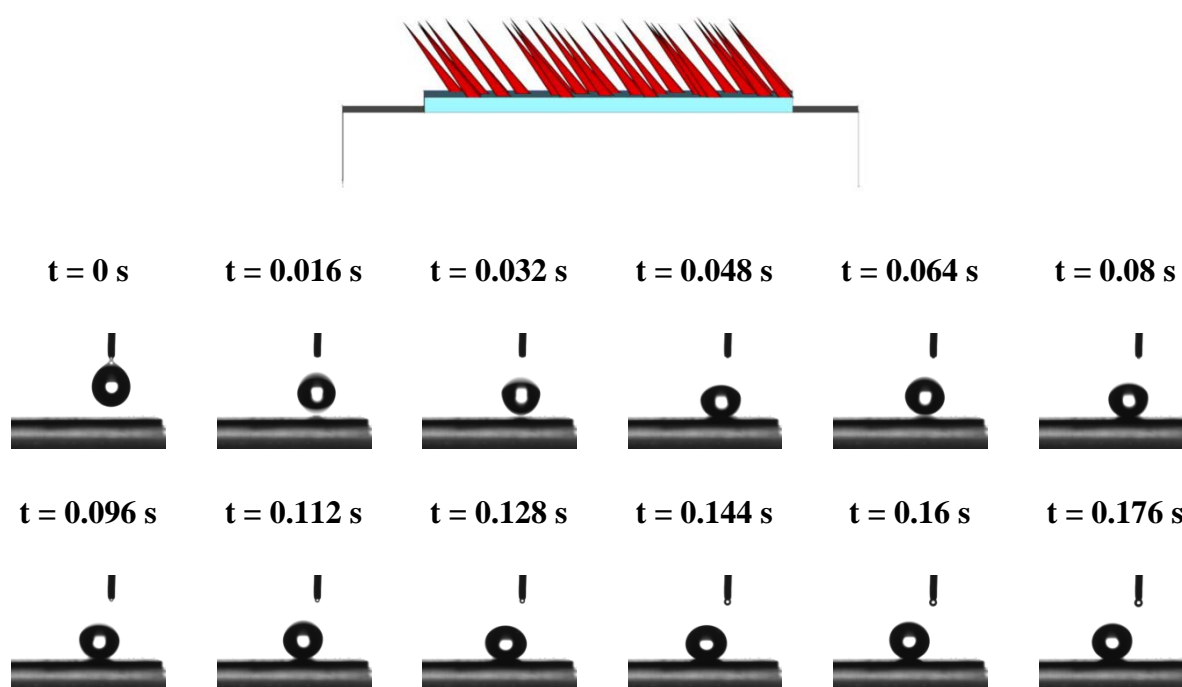
In this work, the CAH of the superhydrophobic surfaces was very low ( $2^\circ$ ) and the droplet could hardly stay on the surface during the experiment. Figure 4.20 shows a representative water drop contact angle for  $10^\circ$  tilted spikes.



**Figure 4.20.** Representative water drop contact angle for  $10^\circ$  tilted spikes.

The contact angle for Si tilted spikes with an angle of irradiation of  $10^\circ$ , was found to be  $171 \pm 2^\circ$ . It has to be mentioned here that the static contact angle and CAH of a lotus leaf are about  $164^\circ$  and  $3^\circ$ , respectively.<sup>78</sup>

Following the static contact angle measurements, bouncing droplet experiments were performed. For this purpose, a  $10 \mu\text{L}$  droplet fell on the surface from 4 mm height. In order to check if there is any directionality, droplets fell on different points of surface and by altering the orientation of the surface. Figure 4.21 shows snapshots of a droplet, bouncing on the surface with  $10^\circ$  tilted spikes, in the direction of the spikes.



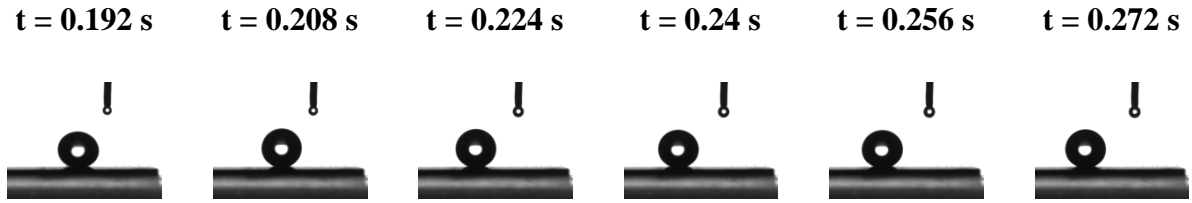


**Figure 4.21.** Selected snapshots of the impact and rebound of water drops on artificial surfaces of Si tilted spikes with an angle of irradiation of  $10^\circ$ .

According to Figure 4.21, the droplet hit the surface under an impact velocity of 0.28 m/s and then it started to roll off. The impact velocity was calculated just prior to the droplet hitting on the surface. Finally, the droplet sat on the surface, without running the whole irradiated surface and with high contact angle, which suggests the formation of solid-air-liquid interface. The velocity of the droplet motion was found to be 0.018 m/s and the restitution coefficient was 0.58.

Furthermore, it cannot be negligible the fact, that after repetition of the experiment, the droplet always was running unidirectional, following the orientation of the spikes. In order to prove this, the experiment was repeated with the droplet falling on the other side of the surface (Figure 4.22).

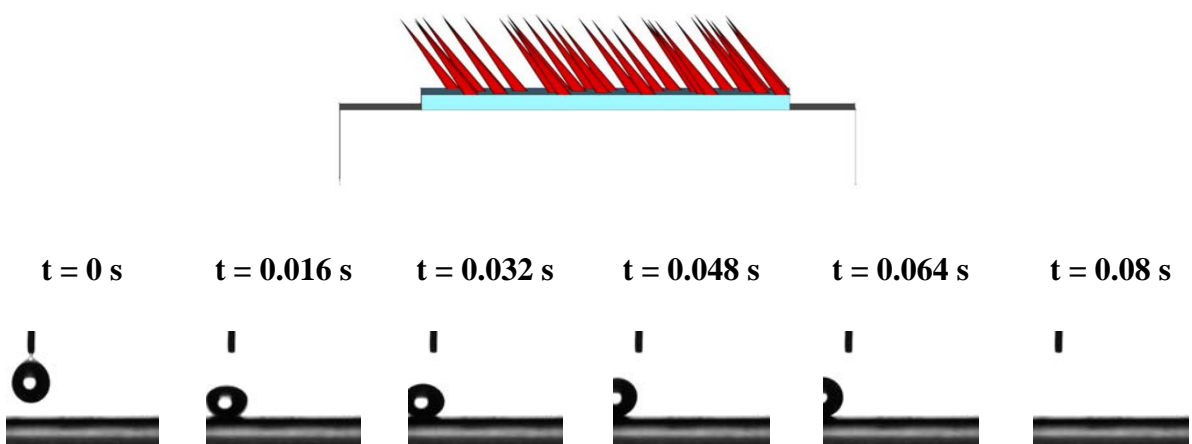
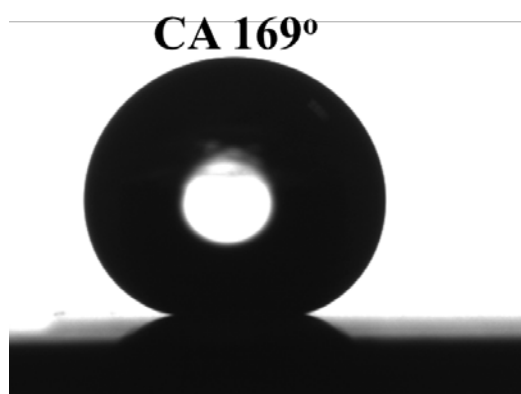


**Figure 4.22.** Selected snapshots of the impact and rebound of water drops on artificial surfaces of Si tilted spikes with an angle of irradiation of  $10^\circ$ .

As it can be noticed from Figure 4.22, the droplet prefers to move in the direction of the spikes, independently of the point of fall. So, it can be concluded, that surfaces with directional anisotropy were successfully fabricated. In order to optimize the system, the study was followed with the  $10^\circ$  tilted spikes.

#### 4.4.2.2. Wettability of surfaces with $20^\circ$ tilted spikes

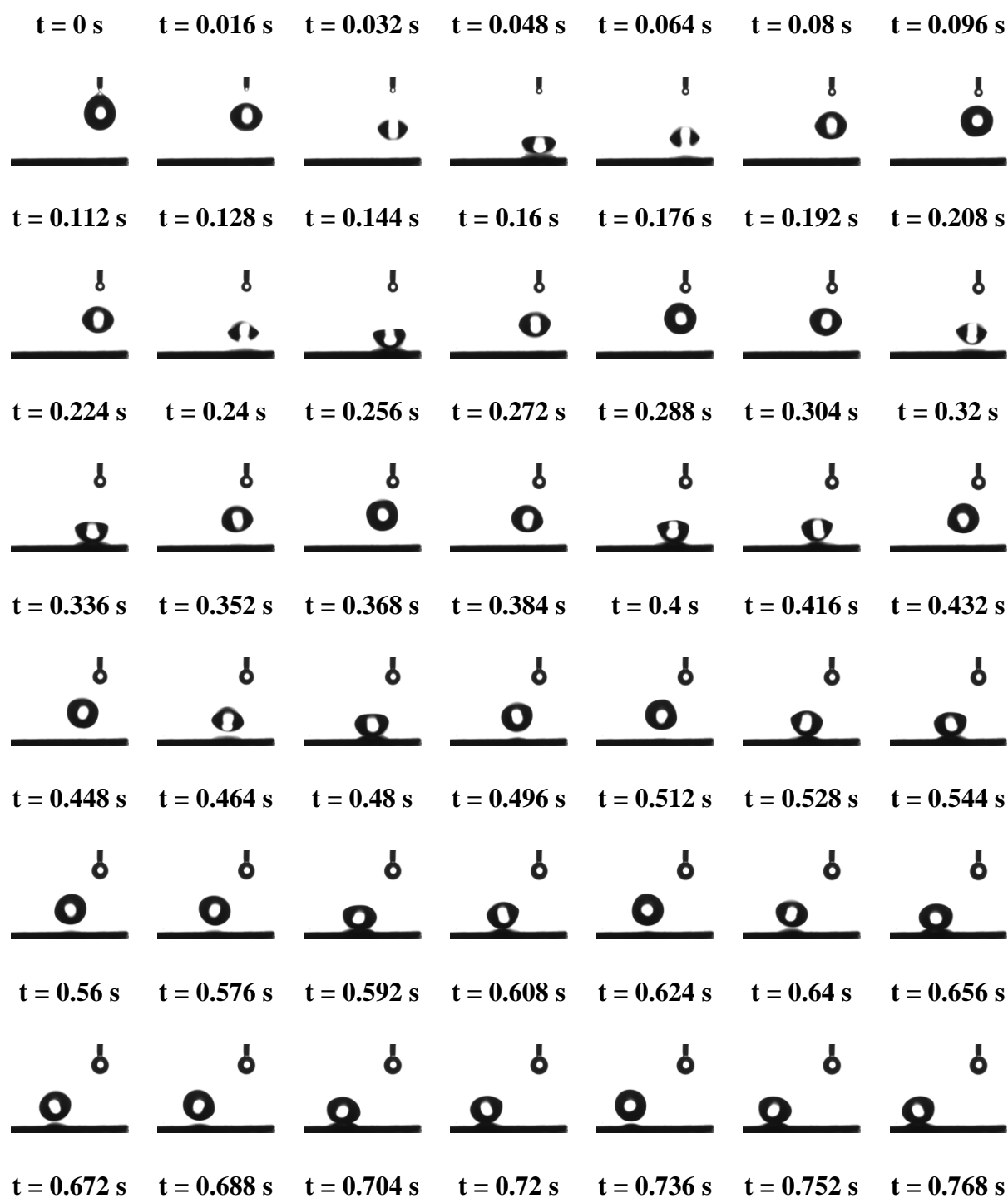
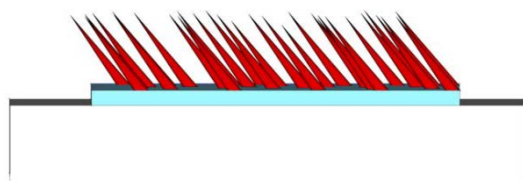
Figure 4.23 shows a representative water drop contact angle for  $20^\circ$  tilted spikes. Also in this case, the droplet could hardly stay on the surface during the experiment.



**Figure 4.23.** Representative water drop contact angle for  $20^\circ$  tilted spikes.

The contact angle for Si tilted spikes with an angle of irradiation of  $20^\circ$ , was found to be  $169 \pm 2^\circ$ . The surface was superhydrophobic with no hysteresis and the droplet could not equilibrate on the surface. Apparent contact angle measured not only from one side but from different directions including top view and no noticeable difference was observed.

Following the static contact angle measurements, bouncing droplet experiments were performed. For this purpose, a  $10 \mu\text{L}$  droplet fell on the surface from 4 mm height. In order to check if there is any directionality, droplets fell on different points of surface and by altering the orientation of the surface. Figure 4.24 shows snapshots of a droplet, bouncing on the surface with  $20^\circ$  tilted spikes, in the direction of the spikes.



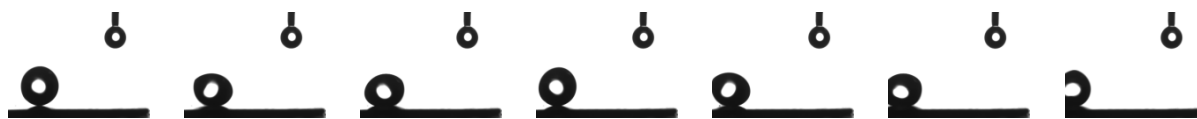


**Figure 4.24.** Selected snapshots of the impact and rebound of water drops on artificial surfaces of Si tilted spikes with an angle of irradiation of  $20^\circ$ .

According to Figure 4.24, the droplet hit the surface, first deformed and then retracted and bounced on the surface. In contrast to the  $10^\circ$  tilted spikes, the droplet could not sit on the surface and it runs the whole irradiated surface (10 cm) without stopping. The droplet stops only after attaching the flat silicon area. The velocity of the droplet motion was found to be 0.013 m/s and the restitution coefficient was 0.88.

Moreover, the droplet was running unidirectional, following the orientation of the spikes. The experiment was performed a couple of times and the result was always the same; anisotropic superhydrophobic surface with no adhesion and with unidirectional motion. In order to prove this, the experiment was repeated after changing the direction of the surface (Figure 4.25).

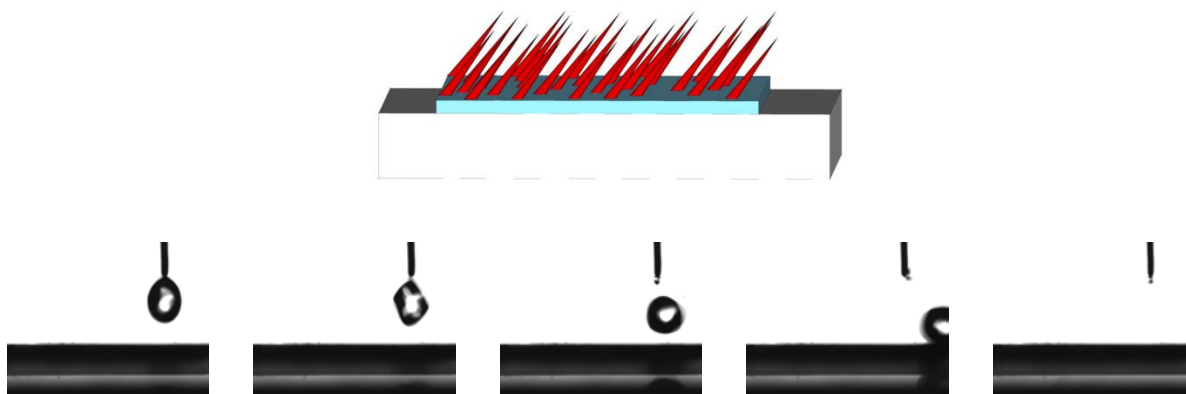


**Figure 4.25.** Selected snapshots of the impact and rebound of water drops on artificial surfaces of Si tilted spikes with an angle of irradiation of  $20^\circ$ .

According to the snapshots of Figure 4.25, by altering the direction of the spikes, the droplet motion is changing, which proves that the orientation of the droplet was not random.

#### 4.4.2.3. Wettability of surfaces with 30° tilted spikes.

Next, the wettability of the 30° tilted spikes was studied. Initially contact angle measurements were performed utilizing the sessile drop method (Figure 4.26).

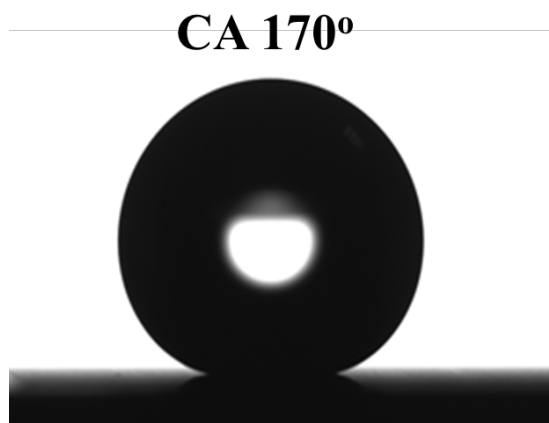


**Figure 4.26.** Representative water drop contact angle for 30° tilted spikes.

The contact angle value for the 30° tilted spikes is almost the same as in the previous cases of 10° and 20° tilted spikes. The roll-off behavior of the 30° tilted spikes was also investigated. Figure 4.27 shows snapshots of a droplet, bouncing on the surface with 30° tilted spikes, in the direction of the spikes.

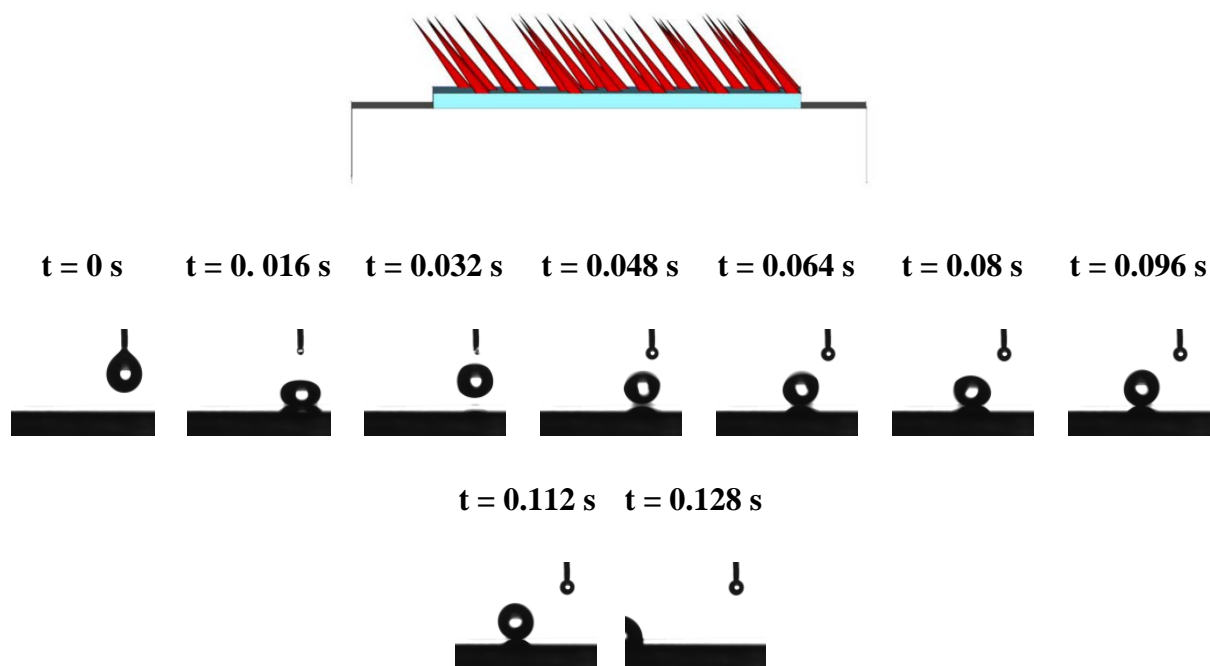


**Figure 4.27.** Selected snapshots of the impact and rebound of water drops on artificial surfaces of Si tilted spikes with an angle of irradiation of  $30^\circ$ .

Figure 4.27 shows that the droplet hit the surface, first deformed and then retracted and bounced on the surface. As happened with the  $20^\circ$  tilted spikes, the droplet could not sit on the surface and it run the whole irradiated surface without stopping. The velocity of the droplet motion was found to be 0.08 m/s, which is approximately six times larger than the value of the  $20^\circ$  tilted spikes and the restitution coefficient was 0.9.

Moreover, the droplet was running unidirectional, following the orientation of the spikes. The experiment was performed a couple of times and the result was always the same; anisotropic superhydrophobic surface with no adhesion and with unidirectional motion. The experiment was repeated with the droplet falling on the other side of the surface (Figure 4.28).

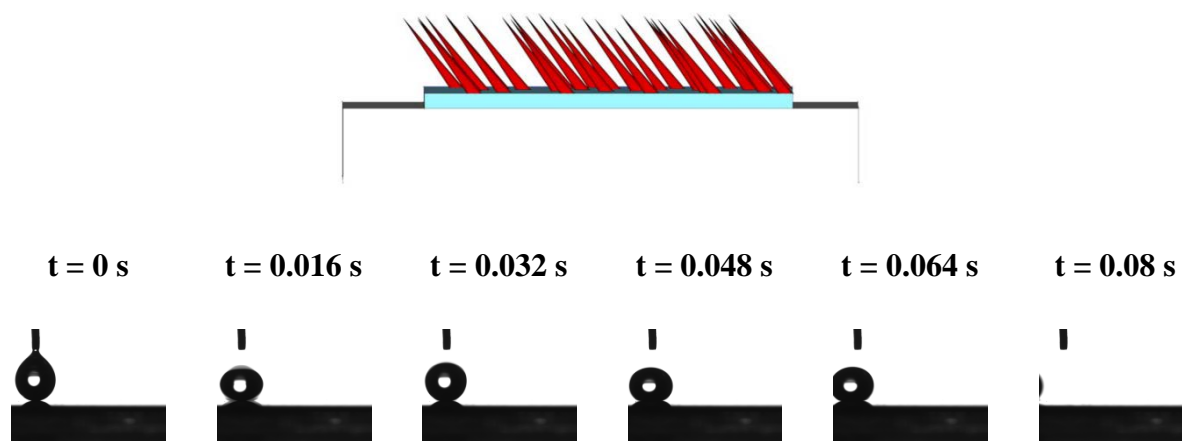


**Figure 4.28.** Selected snapshots of the impact and rebound of water drops on artificial surfaces of Si tilted spikes with an angle of irradiation of  $30^\circ$ .

As it can be noticed from Figures 4.27 and 4.28 the droplet prefers to move in the direction of the spikes, independently of the point of fall. So, it can be concluded, that surfaces with directional anisotropy were successfully fabricated.

#### 4.4.2.4. Wettability of surfaces with $45^\circ$ tilted spikes.

Figure 4.29 shows a representative contact angle measurement of  $45^\circ$  tilted spikes.

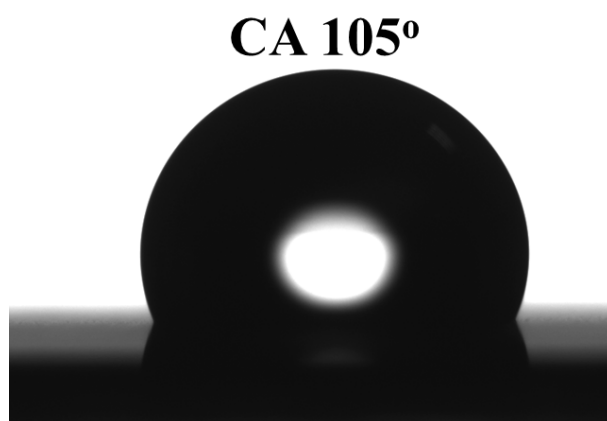


**Figure 4.29.** Representative water drop contact angle for  $45^\circ$  tilted spikes.

The results in the case of  $45^\circ$  tilted spikes are completely different. The surface is not superhydrophobic, exhibits high contact angle ( $105^\circ$ ) and high adhesion. The hysteresis was calculated approximately  $17 \pm 2^\circ$ . This was an expected result from the surface

characterization. Taking into account the SEM images, there are no hierarchically structures and their morphology resembles more ripples with tips than spikes. However, there was an anisotropic behavior observed, by measuring the sliding angle. When the droplet motion was in the direction of the spikes, the sliding angle was found to be  $39^\circ$ . On the contrary, when the droplet motion was opposite to the direction of the spikes, the sliding angle was about  $49^\circ$ . This can be explained by the anisotropy of the surface, which results in a preferential drop motion.

#### **4.5. Conclusions**

In summary, superhydrophobic surfaces were developed, non-adhesive, with directional droplet roll-off behavior. To the best of our knowledge, this is the first work, referring to tilted spikes, treated with fs-laser. In this work, Si substrates were treated with femto-second Laser in order to achieve the dual-scale roughness. However, the irradiation was not performed in a conventional way, but at a tilt angle. The substrate was tilted and as a result, the laser beam was not pointed perpendicular to the surface. This procedure led to the formation of tilted periodic spikes. Such surfaces after a silanization process exhibit anisotropic wettability, with a droplet motion on the direction of the spikes. It was observed that the velocity of the droplet motion was different, depending on the chosen tilt angle.

## B) Unidirectional wetting of surfaces with macro-, micro- and nano- structuring

### 4.6. Introduction

Anisotropic wettability has attracted much interest more recently. There are a lot of works in the literature to the directional wettability of groove-patterned surfaces.<sup>22,53,56,79</sup> Wu and co-workers showed that the wetting behavior on groove structures depends on the period and height of the pattern.<sup>56</sup> Micrometer-width grooves of five different dimensions were fabricated on PMMA substrates using hot embossing were developed by Yang *et al.*<sup>79</sup> Moreover, anisotropy has been achieved by imprinting hierarchical structures on groove-patterned surface, which allows the tuning of anisotropy without chemical treatment.<sup>53</sup> Furthermore, unidirectional control of anisotropic wetting was achieved through modification of PDMS microstructures.<sup>22</sup>

However, as mentioned in the previous section, there are few reports referring to single direction of liquid flow. Previously, non-adhesive superhydrophobic surfaces, with directional droplet roll-off behavior were described. In this work, a third level of macro-structuring will be introduced by patterning the inorganic surfaces using photolithography in order to enhance the anisotropic wetting behavior. Si substrates, patterned with grooves, will be irradiated with fs laser at a tilt angle as described before. These surfaces exhibit superhydrophilic directionality after thermal oxidation and superhydrophobic directional wettability after silanization. The effect of the depth and the diameter of the grooves on the final contact angle were investigated.

## 4.7. Experimental Part

### 4.7.1. Surface manufacturing with photolithography

The groove-patterned surfaces were developed by the Micro/Nano Electronics group of FORTH. Generally, the grooves were defined using positive photolithography (AZ5214). A Silicon (100) low resistivity n-type wafer was used to fabricate the groove patterned surfaces. To realize the hard mask for subsequent plasma etching of Silicon, 200nm of Aluminum was deposited by evaporation and lift-off in acetone. To transfer the pattern onto the Silicon surface, fluorine chemistry plasma etching (Vacutec Reactive Ion etching reactor) was used to reach a depth of 50 $\mu$ m. Subsequently, the aluminum hard mask was removed by wet etching in hydrofluoric acid 10%.

### 4.7.2. Surface manufacturing with fs laser

Si substrates, patterned with grooves, were utilized as substrates for the fabrication of Si spikes. Microstructuring of Si surfaces was performed by femtosecond (fs) laser (Yb:KGW) under a reactive gas ( $\text{SF}_6$ ) atmosphere at a pressure 500 Torr. The irradiation source was adjusted at a repetition rate of 1 kHz and pulse duration of 170 fs at a wavelength of 1026 nm. The fluence selected was 0.7 J/cm<sup>2</sup> and the y step distance was 16  $\mu$ m. The samples were kept in a chamber, mounted on a high precision X-Y translational stage at a tilt angle to the incident laser beam, as described in Figure 4.11. The samples were deposited with the grooves perpendicular to the laser beam scanning so that the tilted spikes would have the same orientation with the channels.

### 4.7.3. Silanization process of the surfaces

Samples treated with fs laser were cleaned in ultrasonic baths, as described in the section 4.2.2. Afterwards, the samples were placed in a flask containing 0.5 ml of dimethyldichlorosilane ( $(\text{CH}_3)_2\text{SiCl}_2$ , DMDCS) reagent and the hydrophobized surfaces were rinsed with toluene (two aliquots), ethanol (three aliquots), 1:1 ethanol/water (two aliquots), deionized water (two aliquots), ethanol (two aliquots), and deionized water (three aliquots). Finally the samples were dried in a clean oven at  $120^\circ\text{C}$  for 45 minutes.<sup>11</sup>

### 4.7.4. Thermal Oxide growth process on Silicon

A method to alter the wettability of the surface making it super-hydrophilic is to grow an oxide layer onto the silicon samples. For this reason, the samples were placed in a box furnace and heated at  $1000^\circ\text{C}$  for 60 min in air, resulting in a  $\sim 100\text{nm}$  thick oxide layer.

### 4.7.5. Wettability of the prepared samples

Wettability tests were performed using a surface tensiometer (OCA-40, Dataphysics) utilizing the sessile drop method.<sup>74</sup> Sessile contact angle titrations were repeated five times for each sample.

Furthermore, the roll-off angle of the sessile drop was measured. This was performed through a device unit, which allows the motor-driven and software controlled inclination of the instrument up to an angle of  $90^\circ$ . In cases that drop bouncing occurred, the velocity of the droplet motion was also calculated.

## 4.8. Results and Discussion

### 4.8.1. Surface characterization

Grooves were defined using positive photolithography (AZ5214). The pattern consisted of long stripes with different dimensions as described in the table below.

**Table 4.1.** Dimensions of the Si grooves-patterned surfaces.

Sample	Distance between the barriers ( $\mu\text{m}$ )	Width of barrier ( $\mu\text{m}$ )
Grooves A	1510	616 and 304 (two barriers)
Grooves B	231	171
Grooves C	124	76.7

From now on, the sample with 616  $\mu\text{m}$  and 304  $\mu\text{m}$  barriers separated by distance of 1.51  $\mu\text{m}$ , will be called “Grooves A”, the sample with 171  $\mu\text{m}$  separated by distances of 231  $\mu\text{m}$  “Grooves B” and the sample with 76.7  $\mu\text{m}$  separated by distances 124  $\mu\text{m}$  of “Grooves C”.

Figures 4.30-4.32 show the SEM image of “Grooves A, B, and C” respectively.

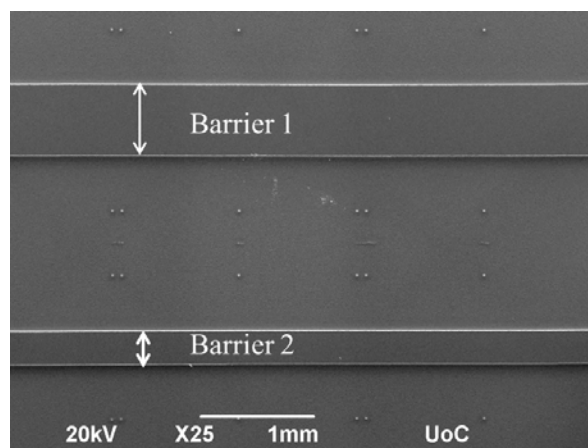


**Figure 4.30.** SEM image of Si substrate, patterned with “Grooves A”.

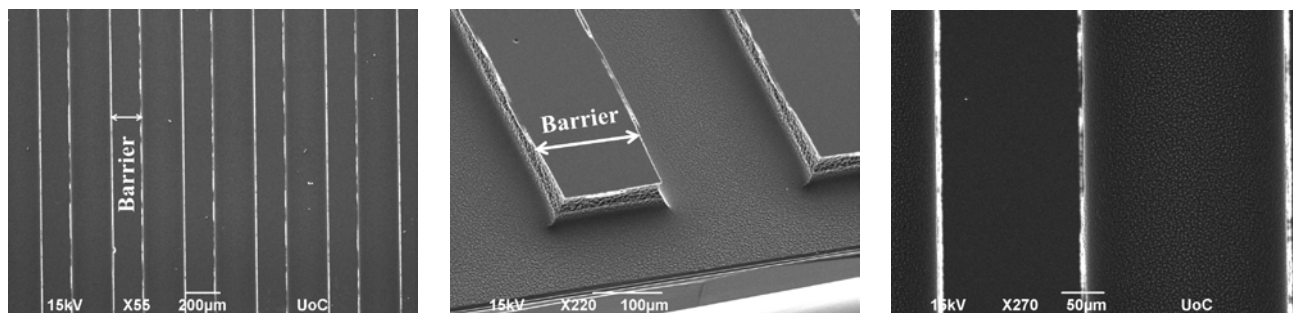


**Figure 4.31.** SEM image of Si substrate, patterned with “Grooves B”.

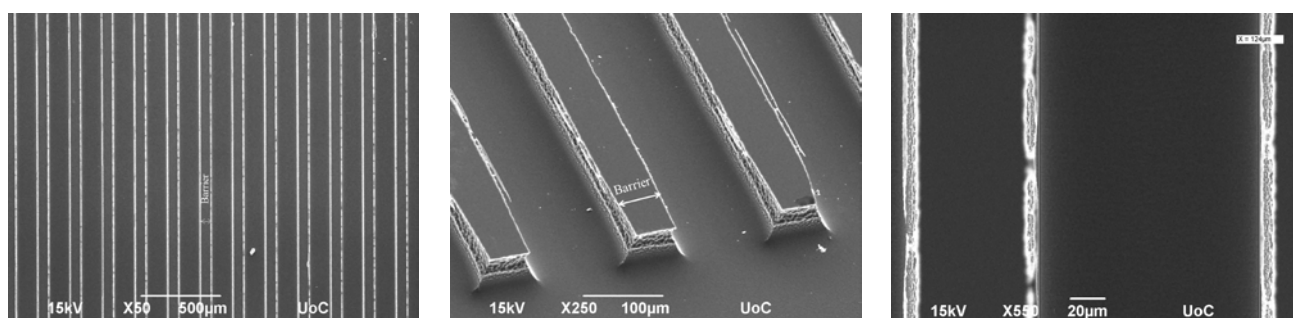


**Figure 4.32.** SEM image of Si substrate, patterned with “Grooves C”.

All the above surfaces, patterned with grooves, were irradiated with fs laser at  $30^\circ$  tilt angle as described in the experimental part (Figure 4.33). Taking into account the results of section A, the  $30^\circ$  tilted spikes exhibit the directional wettability with the highest velocity.

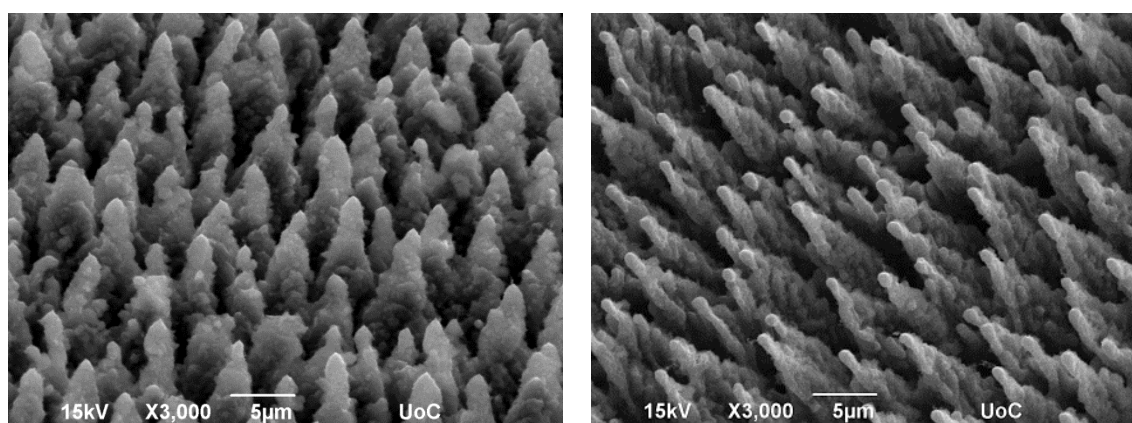


**Figure 4.33.** Top-view (left) and 45-degree-view (right) SEM characterization of Grooves A patterned with  $30^\circ$  tilted spikes.

### 4.8.2. Wettability of surfaces after thermal oxidation

Grooves A patterned with  $30^\circ$  tilted spikes were subjected to thermal oxidation, as described in the experimental part. Figure 4.34 shows snapshots of a  $3\ \mu\text{L}$  droplet, rolling on the surface with  $30^\circ$  tilted spikes, in the direction of the pattern.

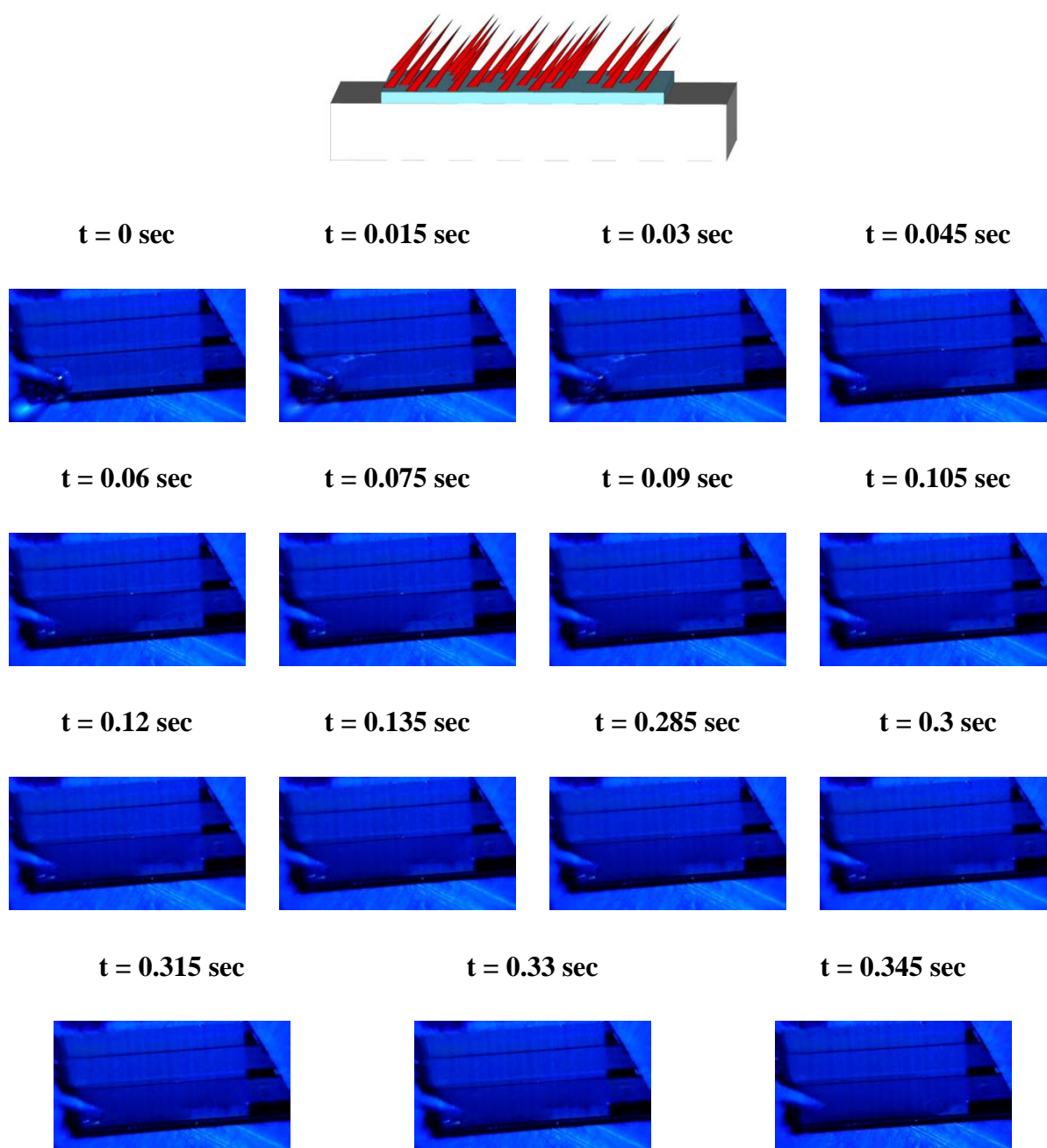


**Figure 4.34.** Selected snapshots of a  $3\ \mu\text{L}$  droplet, rolling on the surface with  $30^\circ$  tilted spikes, in the direction of the pattern.

Figure 4.34 shows the superhydrophilic behavior of the surface with directional spreading of the droplet between the two barriers and in the direction of the tilted spikes. The droplet runs along the channel of 10 mm in 0.345 sec, which means that it runs with a high velocity of approximately 0.29 m/s. The same procedure was repeated with conventional spikes on grooves, as a reference, and the spreading of the drop was directional along the channel, but half velocity.

### 4.8.3. Wettability of surfaces after silanization

Figure 4.35 shows a representative contact angle measurement of Grooves A patterned with 30° tilted spikes after silanization.



**Figure 4.35.** Representative contact angle measurement of Grooves A patterned with 30° tilted spikes after silanization.

The 10  $\mu\text{L}$  droplet “sits” between the two barriers with high contact angle of approximately 140°. Droplet with less volume could not be stabilized on the surface, because it was superhydrophobic without hysteresis. However, the 10  $\mu\text{L}$  did not start rolling off but it was stabilized between the two barriers.

In order to check if there is any anisotropic behavior, the sliding angle was measured in both directions, parallel and perpendicular to the grooves. This was performed through a device unit, which allows the motor-driven and software controlled inclination of the instrument up to an angle of 90°. Figure 4.36 shows selected snapshots from the sliding angle measurement,

with the droplet motion parallel to the channel of the Grooves A patterned with  $30^\circ$  tilted spikes.

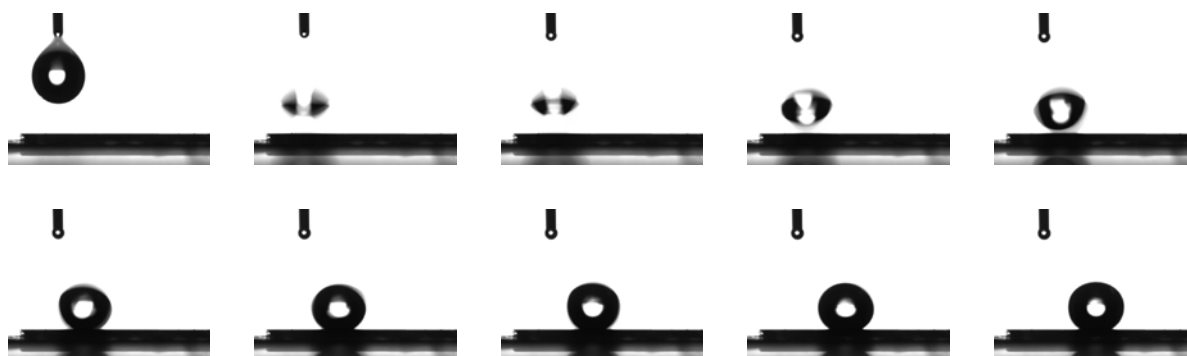


**Figure 4.36.** Selected snapshots from the sliding angle measurement, with the droplet motion parallel to the channel of the Grooves A patterned with  $30^\circ$  tilted spikes.

Figure 4.36 shows that the drop rolls off immediately at  $2^\circ$  inclination of the device in the direction of the channel and spikes. The opposite case is depicted in Figure 4.37, where the droplet motion is perpendicular to the grooves.

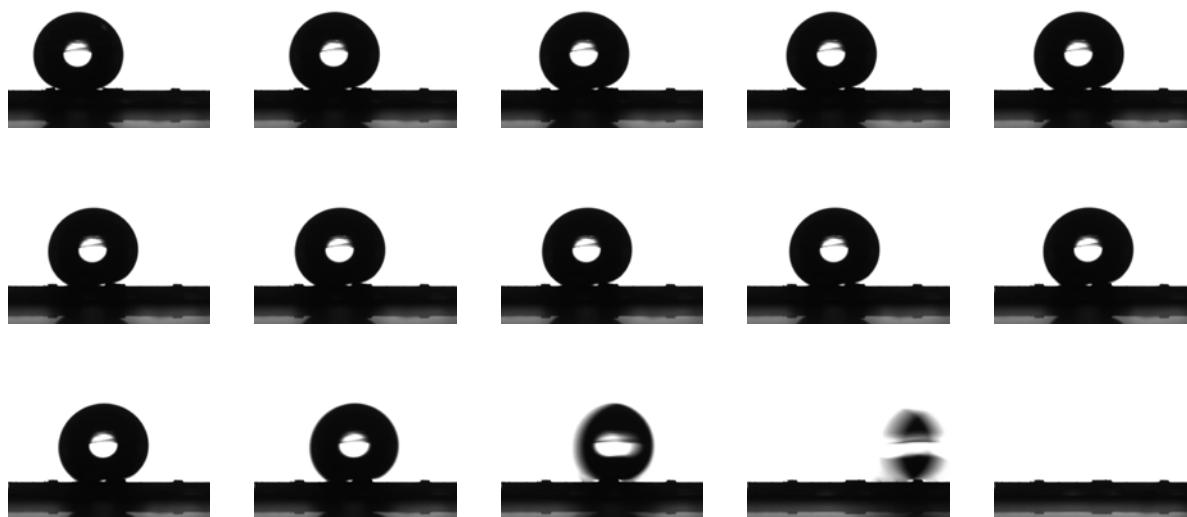


**Figure 4.37.** Selected snapshots from the sliding angle measurement, with the droplet motion perpendicular to the channel of the Grooves A patterned with  $30^\circ$  tilted spikes.

Comparing Figures 4.36 and 4.37, the behavior is completely different. In the latter case, the droplet could hardly “walk” perpendicular to the grooves and the sliding angle is about  $17^\circ$ .

Furthermore, it seems that the droplet “climbs” the barrier in order to move, without losing its shape. Initially, the droplet is being reformed, as it “tries to climb” the barrier, but after the whole droplet is above the barrier, then it gains its initial shape again. These results prove the anisotropic behavior of the surfaces and their directional superhydrophobic wetting along the pattern.

Following that, the wetting properties of Grooves B patterned with 30° tilted spikes were investigated. Figure 4.38 depict the water drop on the Grooves B patterned with 30° tilted spikes in three different magnifications.



**Figure 4.38.** Representative contact angle measurement of Grooves B patterned with 30° tilted spikes after silanization.

The surface is superhydrophobic ( $CA \sim 150^\circ$ ) with no hysteresis. The droplet is deformed due to the effect of gravity. However, this is unavoidable, as smaller droplets could not be stabilized on the surface. Moreover, it can be observed that the droplet sits on the surface with trapped air underneath, which supports the Cassie–Baxter model.

Next, the roll-off behavior of the droplet was studied. Figure 4.39 shows selected snapshots for the bouncing droplet on the Grooves B patterned with 30° tilted spikes after silanization.

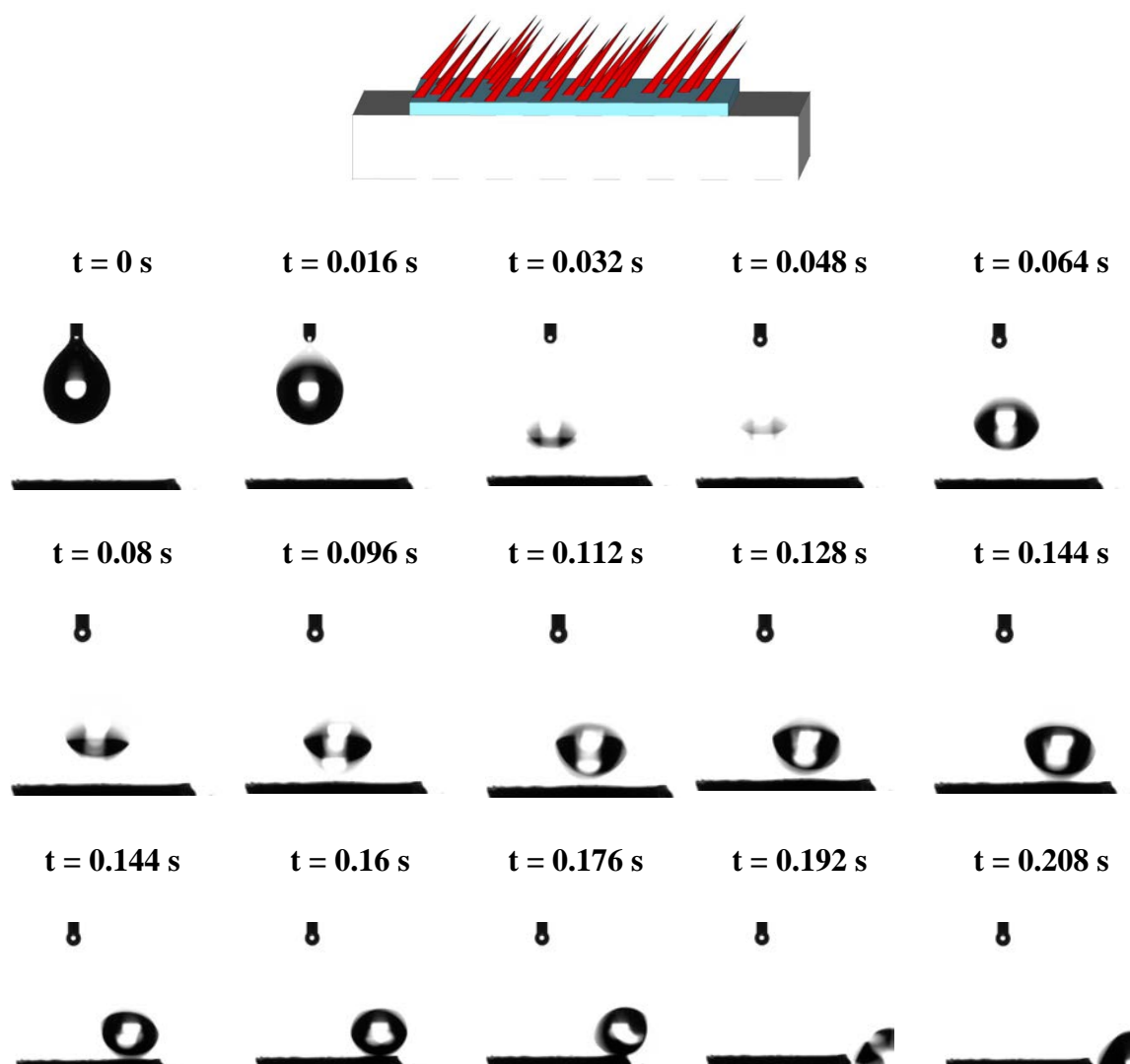


**Figure 4.39.** Selected snapshots of the impact and rebound of water drops on Grooves B patterned with  $30^\circ$  tilted spikes.

According to Figure 4.39, the droplet hits the surface, it first deforms and then retracts and bounces on the surface without stopping. The velocity of the droplet motion was found to be  $0.07\text{m/s}$ , which is very close to the velocity value without the grooves.

Moreover, the droplet ran unidirectional following the orientation of the spikes. The experiment was performed a couple of times and the result was always the same; anisotropic superhydrophobic surface with no adhesion and with unidirectional motion.

Finally, the behavior of the Grooves C patterned with 30° tilted spikes was investigated. Figure 4.40 depicts the water drop on the Grooves C patterned with 30° tilted spikes.



**Figure 4.40.** Representative contact angle measurement of Grooves C patterned with 30° tilted spikes after silanization.

The surface is superhydrophobic (CA~150°) with no adhesion. The droplet is deformed also in this case, due to the effect of gravity. Moreover, the droplet sits on the surface with trapped air underneath, which supports the Cassie–Baxter model.

Afterwards, the roll-off behavior of the droplet was studied. Figure 4.41 shows selected snapshots for the bouncing droplet on the Grooves C patterned with 30° tilted spikes after silanization.

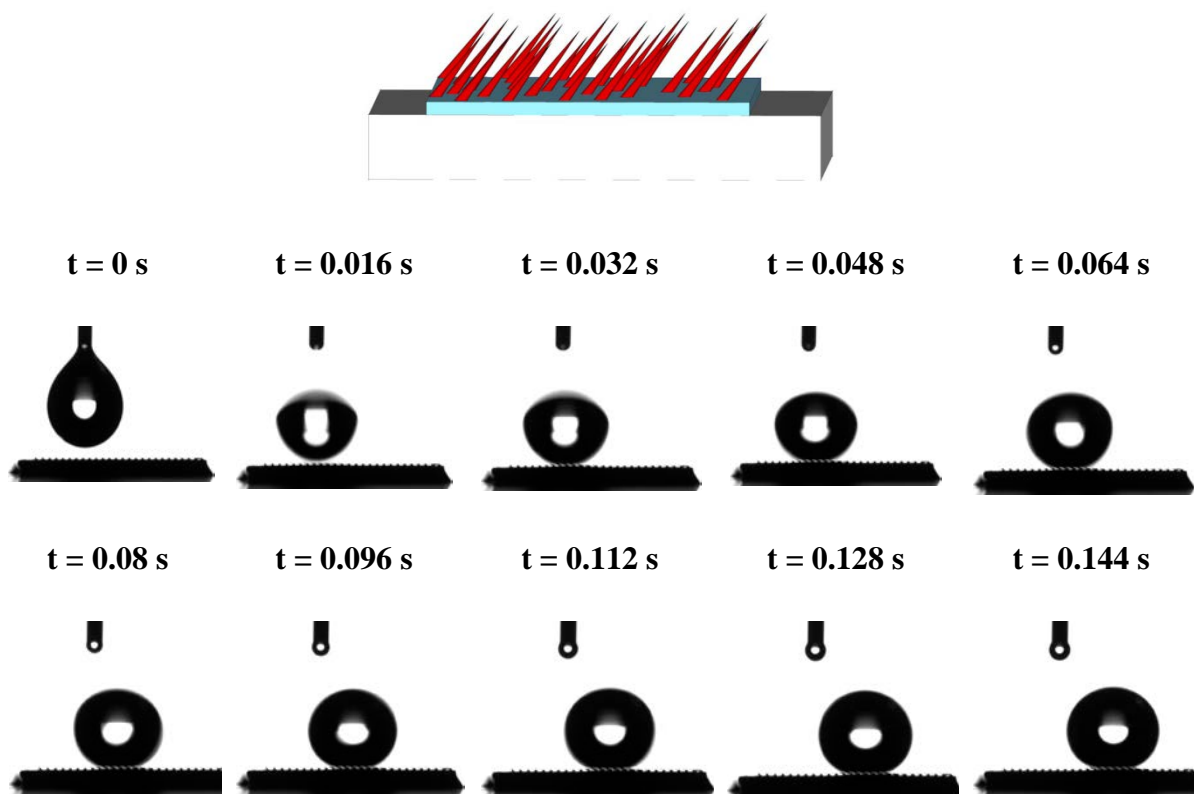


**Figure 4.41.** Selected snapshots of the impact and rebound of water drops on Grooves C patterned with 30° tilted spikes.

Figure 4.41 shows the droplet hitting the surface and starting bouncing on it. Finally, the droplet stopped on the surface, without running the whole irradiated surface and with high contact angle, which suggests the formation of solid-air-liquid interface. Moreover, the droplet ran unidirectional following the orientation of the spikes. The experiment was performed a few times and the result was always the same; anisotropic superhydrophobic surface with no adhesion and with unidirectional motion.

## 4.9. Conclusions

Anisotropic wettability has attracted much interest recently. In this work, a third level of macro-structuring was introduced by patterning the inorganic surfaces using photolithography in order to enhance the anisotropic wetting behavior. Si substrates, patterned with grooves, were irradiated with fs laser at a tilt angle. These surfaces exhibit superhydrophilic directionality after thermal oxidation, and superhydrophobic directional wettability, after silanization. The effect of the characteristics of the grooves on the final contact angle was investigated.

## C) Anisotropic surfaces with high adhesion and unidirectional properties

### 4.10. Introduction

Although superhydrophobic surfaces with high adhesion have been developed for microfluidic applications, there are still some technological difficulties. It still remains a challenge to directly manipulate liquids without any leaks.<sup>33</sup> Anisotropic patterns can eliminate the water losses by controlling the droplet motion.<sup>59</sup> Among the anisotropic structures, stripes have been widely studied, due to their simplicity.<sup>23</sup> Malvadkar *et al.* developed “pin-release” surfaces with anisotropic adhesive wetting properties.<sup>58</sup> Anisotropic wetting has been also achieved by submicrometer-scale grooved structures, developed on polymer films.<sup>52</sup> The anisotropic contact angle hysteresis has been investigated by Gleiche and his co-workers.<sup>80</sup>

In this work, superhydrophilic and superhydrophobic surfaces with high unidirectional hysteresis were developed. For this purpose, the irradiation of Si wafers was performed at a tilt angle. The substrate was tilted and as a result, the laser beam was not pointed

perpendicular to the surface. This procedure led to the formation of tilted periodic spikes. Such surfaces after a silanization process exhibit anisotropic wettability, with a droplet motion in the direction of the spikes. In order to achieve the high hysteresis, a laser beam with central wavelength of 800 nm was utilized and the different parameters of laser irradiation were investigated.

## 4.11. Experimental part

### 4.11.1. Surface manufacturing with fs laser

The experimental procedure for the femtosecond-laser microstructuring silicon involves several variable parameters, which have been discussed in the previous section (4.2.1). As this is the first work referring to tilted spikes, the fundamental investigation of the effect of different parameters was needed for both wavelengths.

The irradiation of n-type silicon wafers (Si(100), resistivity  $\rho = 2 - 8 \Omega \cdot \text{m}$ ) was performed with a regenerative amplified Ti:Sapphire laser (100 fs, central wavelength 800 nm, delivering 180 fs pulses at a repetition rate of 1 kHz) in 0.65 bar of SF<sub>6</sub>. Si substrates were irradiated with a fs laser at different tilt angles and the effect of fluence, step distance in the y-direction, repetition rate and the scanning speed were investigated. Furthermore the effect of HF treatment was studied.

### 4.11.2. Surface silanization

Samples, after irradiation were cleaned in ultrasonic baths of trichloroethylene, acetone and methanol followed by a 10% HF v/v aqueous treatment in order to remove the oxide grown on the surface.<sup>11</sup> Afterwards, the samples were placed in a flask containing 0.5 ml of DMDCS reagent. The vapor-phase reactions were carried out as described in section 4.2.2.

### 4.11.3. Surface wettability

Wettability tests were performed using a surface tensiometer (OCA-40, Dataphysics) utilizing the sessile drop method.<sup>74</sup> Sessile contact angle titrations were repeated five times for each sample.

Advancing and receding contact angles were determined by adding / removing volume to the drop dynamically. The maximum angle achieved, by increasing the solid/liquid interfacial area, is the advancing contact angle. The receding contact angle is the smallest possible angle, without decreasing its solid/liquid interfacial area, determined by removing volume from the drop dynamically.<sup>16</sup> The contact angle hysteresis was defined as the difference between the advancing and receding contact angle for a contact line moving to an opposite direction.<sup>75-77</sup>

## 4.12. Results and Discussion

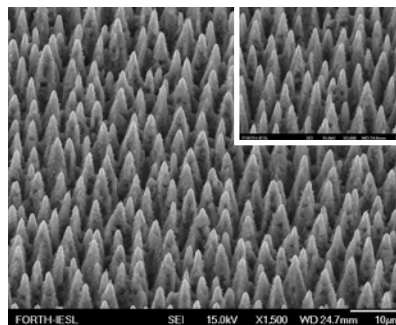
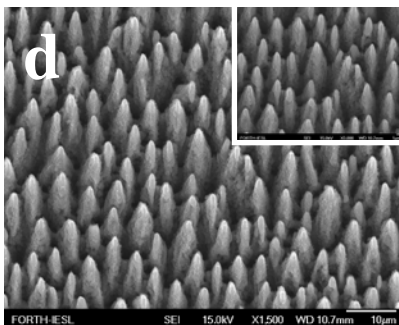
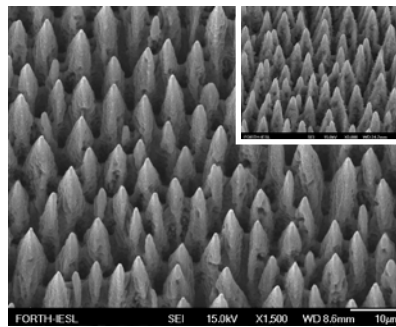
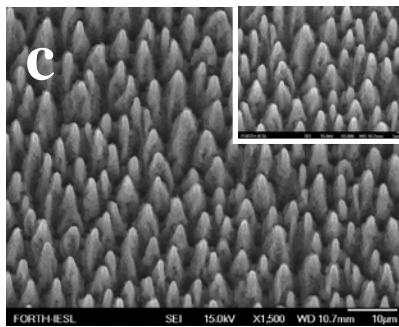
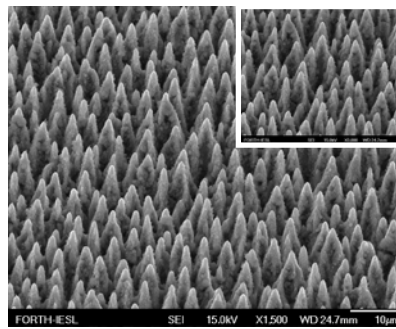
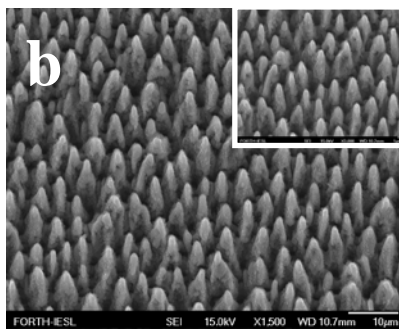
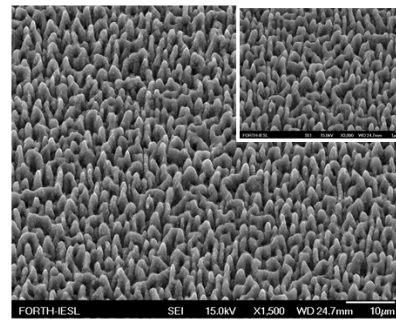
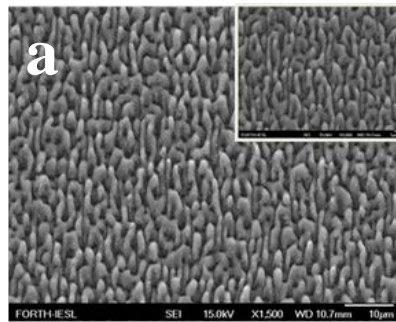
### 4.12.1. Surface characterization

#### 4.12.1.1. Effect of fluence

In this section the morphology of the spikes was examined at different laser fluencies. Samples were irradiated at a tilt angle  $30^\circ$  with fluencies varying from  $0.53$  to  $2.4 \text{ J} \cdot \text{cm}^{-2}$ . Figure 4.42 shows the top-view SEM images of the samples, taken parallel to the laser irradiation (left column) and perpendicular to the laser irradiation (right column).

SEM is taken parallel to the laser irradiation.

SEM is taken perpendicular to the laser irradiation.



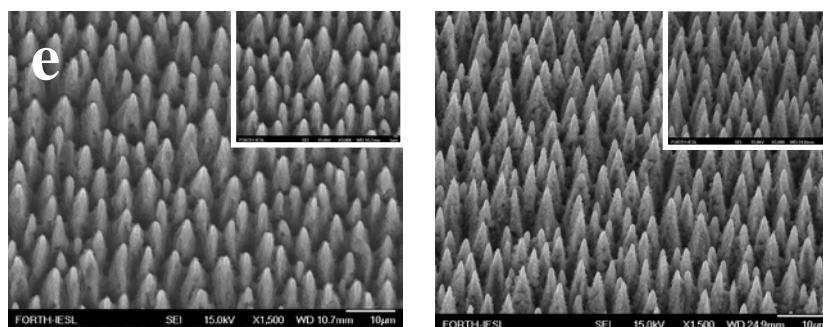


**Figure 4.42.** Top-view scanning electron micrographs comparing surface morphology for different fluencies: a)  $0.54 \text{ J} \cdot \text{cm}^{-2}$ , b)  $1.2 \text{ J} \cdot \text{cm}^{-2}$ , c)  $1.6 \text{ J} \cdot \text{cm}^{-2}$ , d)  $2.1 \text{ J} \cdot \text{cm}^{-2}$  and e)  $2.4 \text{ J} \cdot \text{cm}^{-2}$ . The insets show a greater magnification of the same areas.

Figure 4.42 shows that with increasing fluence (at constant shot number), the morphology goes from laser induced periodic surface structures to a coarsened surface to sharp microstructures. At a fluence of  $0.54 \text{ J} \cdot \text{cm}^{-2}$ , conical microstructures are developed. As the fluence is increased from  $0.54$  to  $1.2 \text{ J} \cdot \text{cm}^{-2}$ , an increase in the height and the density of the spikes is observed. For fluencies above  $1.2 \text{ J} \cdot \text{cm}^{-2}$ , the surface morphology looks very similar with a small increase in microstructure height and density. Comparing the images of the left and right columns, it can be concluded that the shape of spikes is asymmetric, as one side is more broadened.

Comparing the representative spikes of  $1026 \text{ nm}$  and  $800 \text{ nm}$  irradiation (Figures 4.12 and 4.42), it is obvious that the laser wavelength also affects the final morphology of the microstructures. The spikes are smaller, more dense and smoother for the  $800 \text{ nm}$  irradiation.

#### 4.12.1.2. Effect of y step distance

In this section the morphology of the spikes was examined at different step distances in the y-direction, by altering the step of irradiation at the y axis. Samples were irradiated at a tilted angle  $30^\circ$  and  $45^\circ$  with fluence  $2.1 \text{ J} \cdot \text{cm}^{-2}$ . Figure 4.43 and 4.44 depict the characterization of substrates, irradiated at a tilt angle  $30^\circ$  and  $45^\circ$  respectively, with scanning electron microscopy.

## Top-view SEM images. 45-degree-view SEM images.

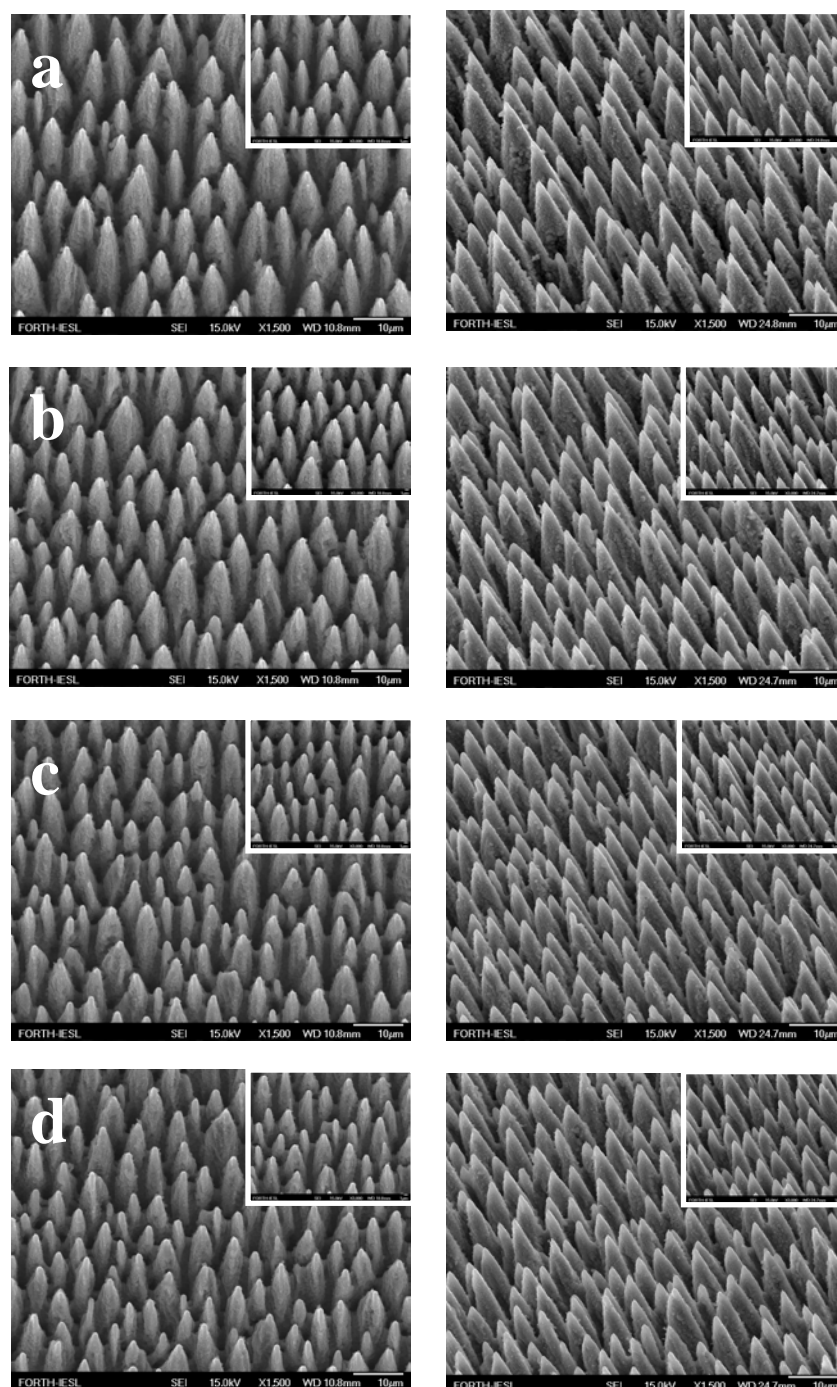


**Figure 4.43.** Top-view (left) and tilted-view (right) scanning electron micrographs, of samples irradiated at a tilt angle  $30^\circ$ , comparing the surface morphology by increasing the step distance in the y-direction: a)  $10\ \mu\text{m}$ , b)  $15\ \mu\text{m}$ , c)  $20\ \mu\text{m}$  and d)  $25\ \mu\text{m}$ .

Top-view SEM images. 45-degree-view SEM images.

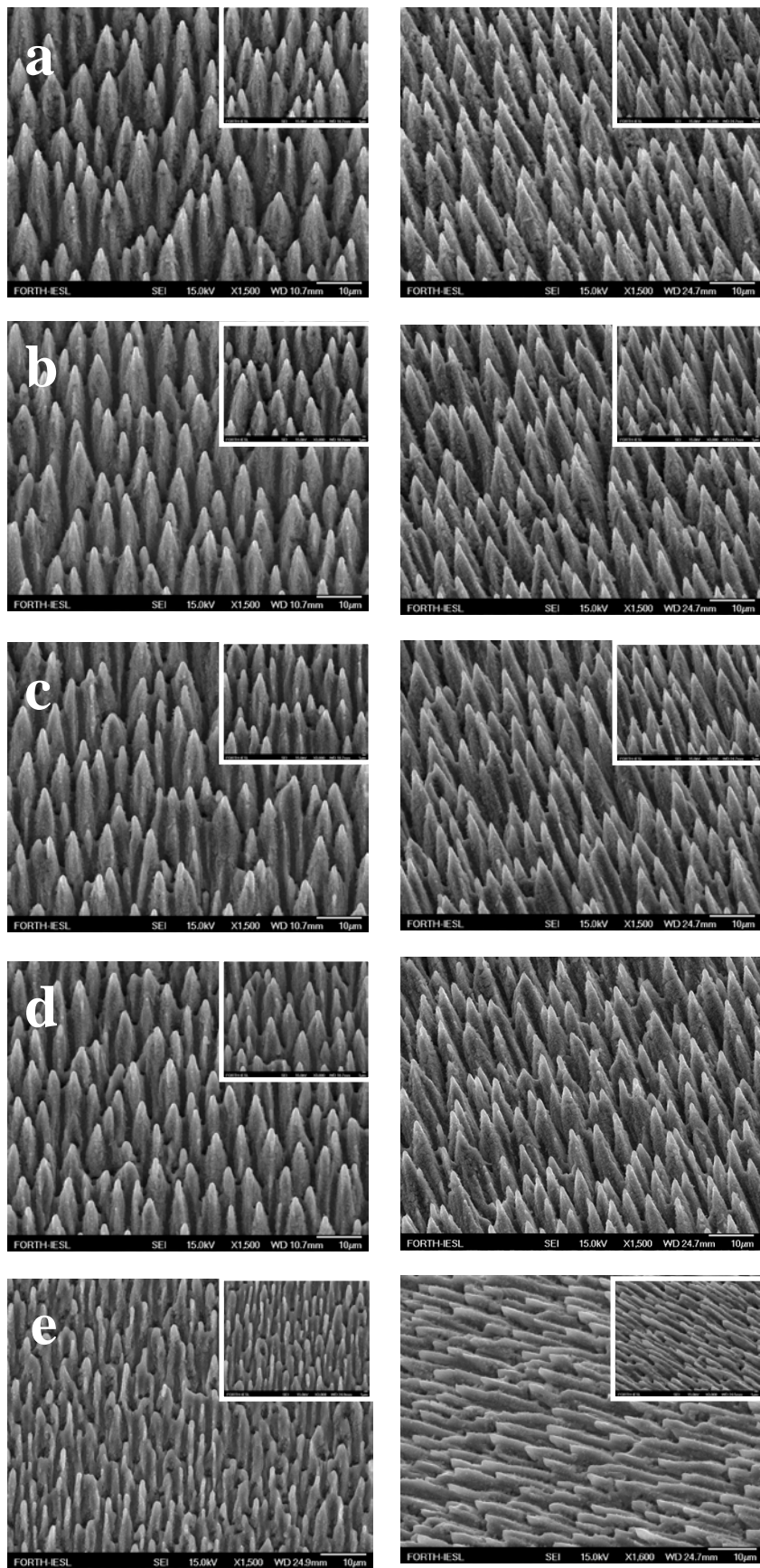


**Figure 4.44.** Top-view(left) and tilt-view (right) scanning electron micrographs, of samples irradiated at a tilt angle  $45^\circ$ , comparing the surface morphology by increasing the step distance in the y-direction: a)  $10\ \mu\text{m}$ , b)  $15\ \mu\text{m}$ , c)  $20\ \mu\text{m}$  d)  $25\ \mu\text{m}$  and e)  $30\ \mu\text{m}$ .

Figures 4.43 and 4.44, the y step distance affects the size and the density of the spikes. In all cases the spikes are ordered, uniform and they have conical shape. However, by increasing the y step distance, the density of the spikes is higher and the structures are shorter and thinner.

#### 4.12.1.3. Effect of HF

Samples, after irradiation were cleaned in ultrasonic baths of trichloroethylene, acetone and methanol followed by a 10 % HF v/v aqueous treatment in order to remove the oxide grown on the surface.

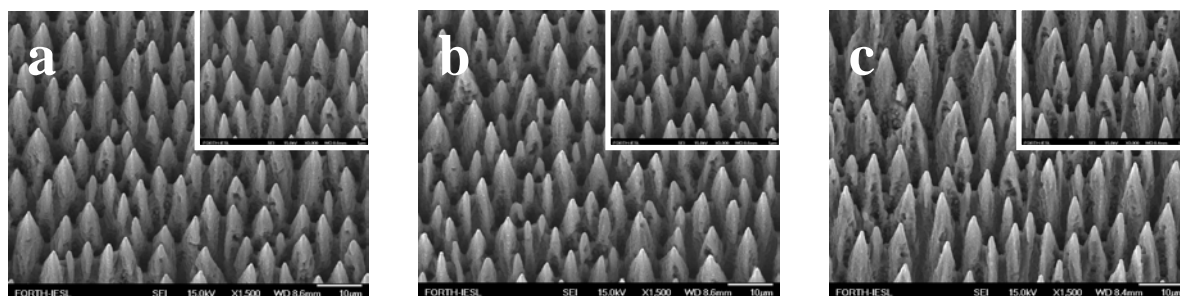


**Figure 4.45.** Top-view(left) scanning electron micrographs of samples irradiated at a tilt angle  $30^\circ$ , comparing the surface morphology after immersion of samples at HF 10 % v/v solution for: a) 0.5 h, b) 2 h and c) 4 h.

The exposure to HF solution does not affect the morphology of the spikes. The structures are stable and their shape and size did not change even after 4 h of immersing in 10% v/v HF aqueous.

## 4.12.2. Wettability of surfaces

### 4.12.2.1. Wettability after thermal oxidation

Samples were placed in a box furnace and heated at 1000°C for 60 min in air, resulting in a thick oxide layer. Figure 4.45 and 4.46 depict selected snapshots of a 10  $\mu\text{L}$  droplet, rolling on the surface with 30° tilted spikes, opposite to the direction and in the same direction of the pattern respectively.

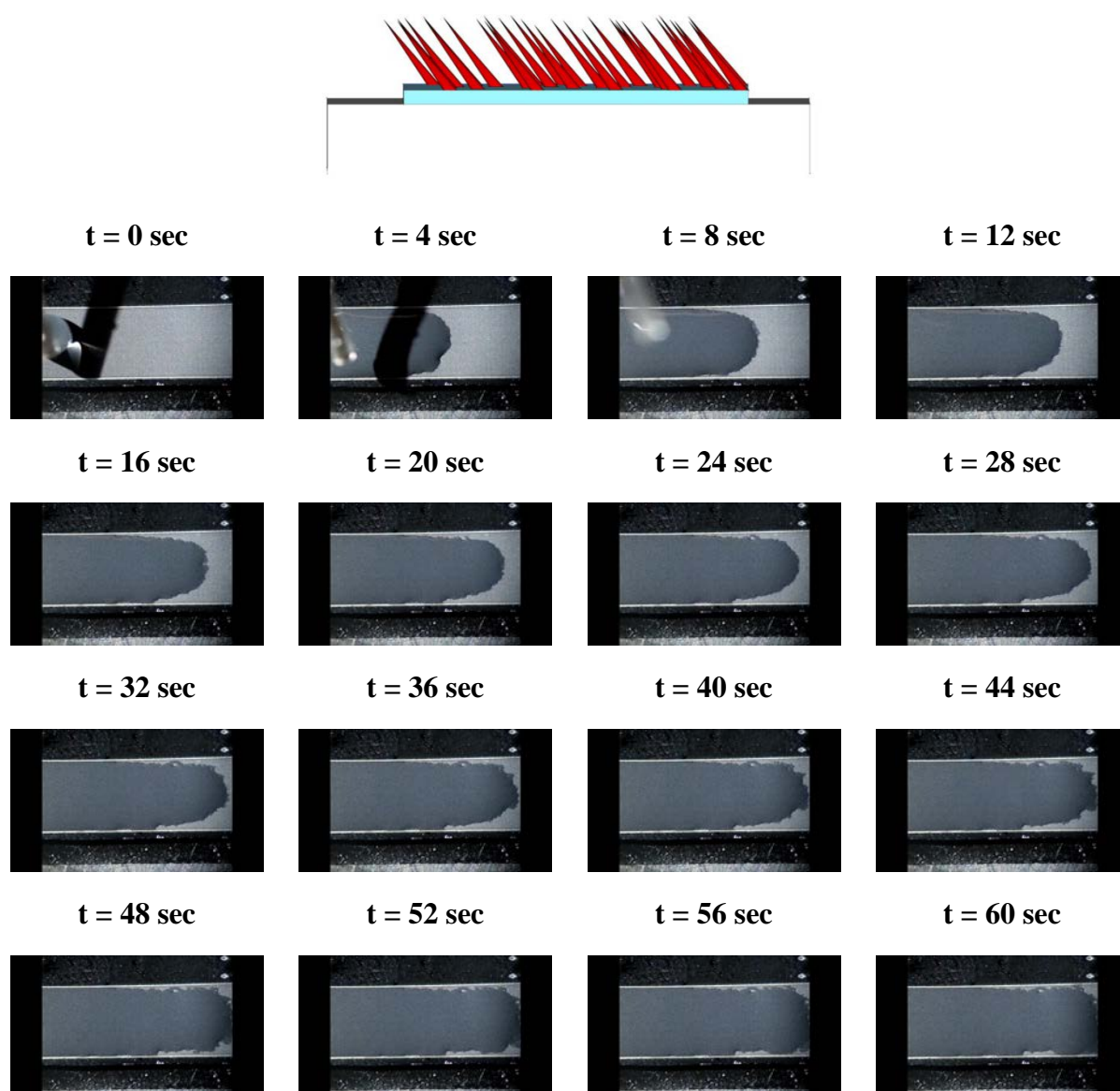


**Figure 4.46.** Selected snapshots of a 10  $\mu\text{L}$  droplet, spreading on the surface with 30° tilted spikes, opposite to the direction of the pattern.

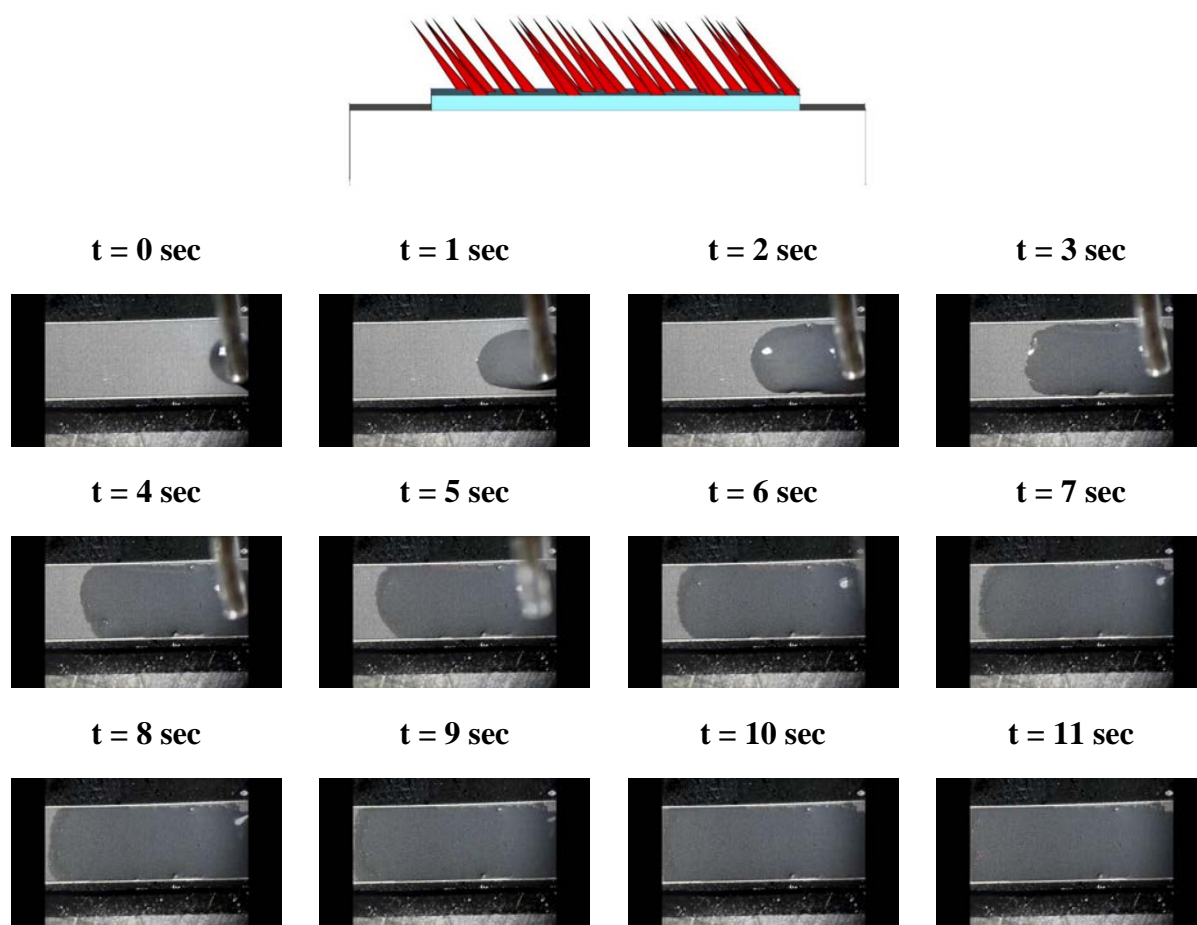


**Figure 4.47.** Selected snapshots of a 10  $\mu\text{L}$  droplet, spreading on the surface with  $30^\circ$  tilted spikes, in the direction of the pattern.

Comparing Figures 4.46 and 4.47, it can be concluded that there is a directionality of the droplet spreading, depending on the orientation of the spikes. In both cases the droplet spreads on the surface. However, when the droplet motion is in the opposite direction of the spikes, the spreading velocity is 2 mm/s, while in the direction of the tilt, the spreading velocity is 9 mm/s.

#### 4.12.2.2. Wettability after the silanization process

Figure 4.48 shows a representative contact angle measurement of Si substrate with  $30^\circ$  tilted spikes after silanization.

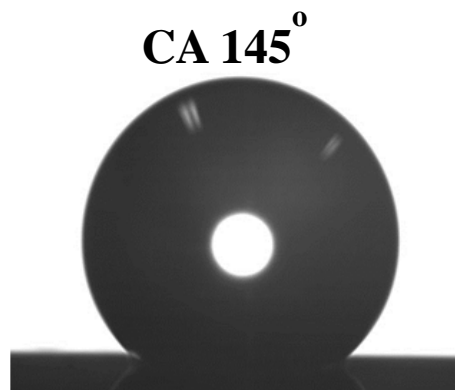
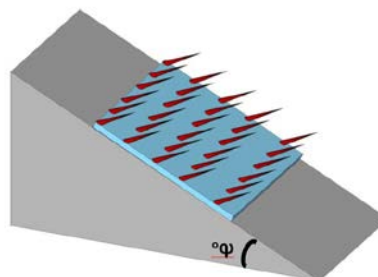
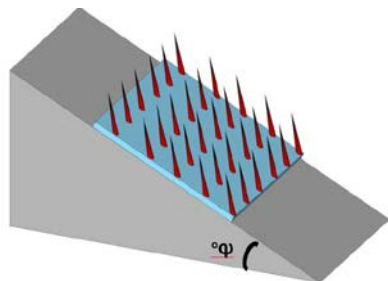


**Figure 4.48.** Representative contact angle of Si substrate irradiated at a tilted angle  $30^\circ$ .

In order to check if there is anisotropic hysteresis in the surfaces, the samples with the  $30^\circ$  tilted spikes was deposited in an inclined plate, with the angle varying from  $30^\circ$  to  $180^\circ$ . The sample was deposited in both directions of the spikes and the results were compared. Figures 4.49-451 show the representative water drops for the  $30^\circ$ ,  $45^\circ$ ,  $60^\circ$ ,  $90^\circ$  and  $180^\circ$  angle of inclination of the sample.

## Orientation of spikes

Angle  $\varphi^\circ$   
of  
inclined  
plate



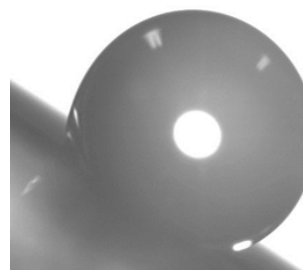
L 106°

R 120°

L 107°

R 118°

30°



L 102°

R 116°

L 119°

R 126°

45°



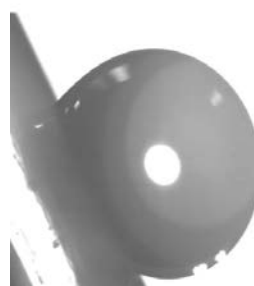
L 94°

R 119°

L 109°

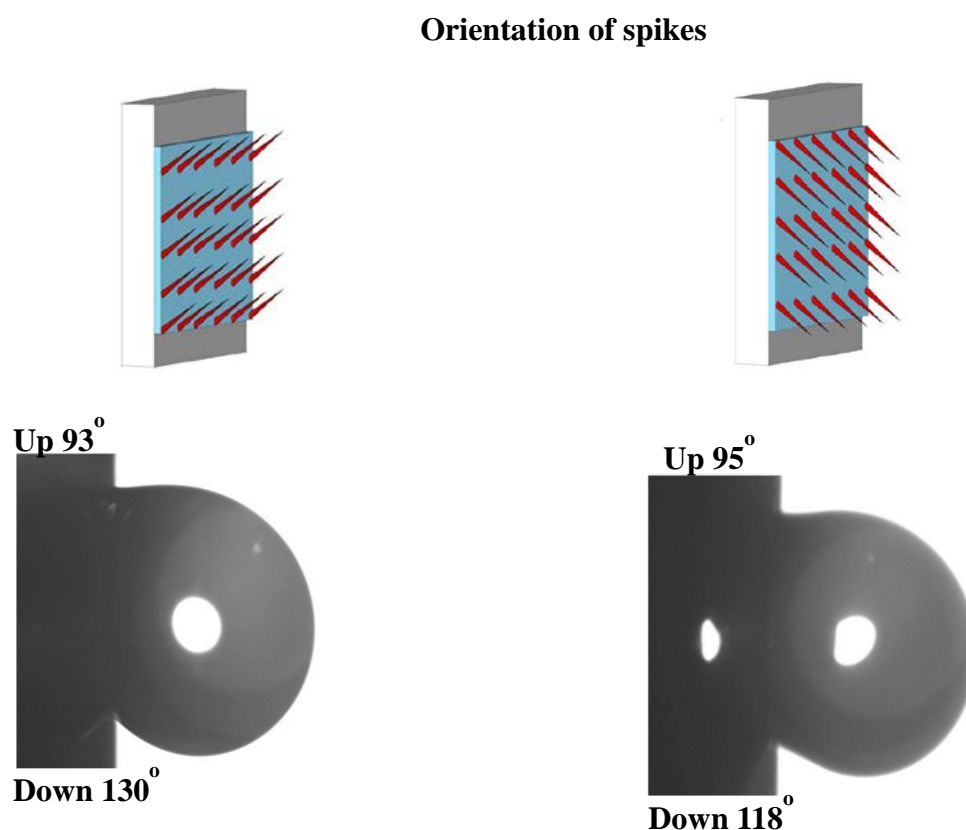
R 120°

60°



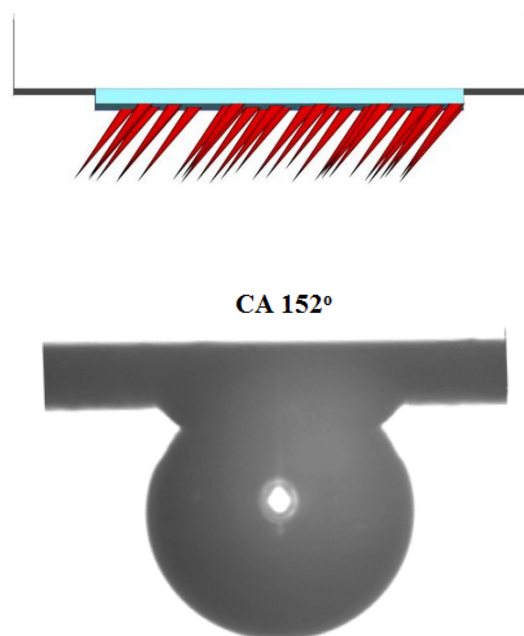
**Figure 4.49.** Representative water drops on the 30° tilted spikes, for the 30°, 45° and 60° angle of inclination of the sample plate.

Figure 4.49 shows that the droplets exhibit a lower difference between advancing and receding angle, in the direction coinciding with the tilted spikes, than in the direction against the tilted spikes. This behavior becomes more enhanced by increasing the angle of inclination of the plate.



**Figure 4.50.** Representative water drops of the  $30^\circ$  tilted spikes, for the  $90^\circ$  inclined plate.

Figure 4.50 confirms the fact that the droplets placed onto the microstructured surfaces exhibit a lower CAH in the direction of the spikes. When the spikes are positioned pointing up, the difference between the two angles is  $37^\circ$ . In the opposite scenario that the spikes are positioned pointing down, this difference is only  $23^\circ$ .

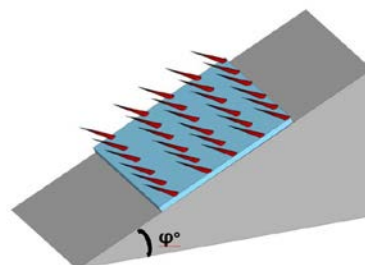
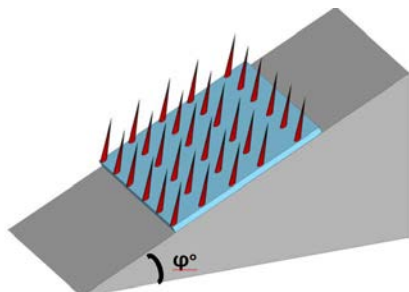


**Figure 4.51.** Representative water drops of the 30° tilted spikes, for the 180° inclined plate. The surface with 30° tilted spikes exhibit a superhydrophobic behavior with high adhesion, even when the tilted plate is inverted.

The anisotropic hysteresis in the surfaces, with the 45° tilted spikes was also examined. Figures 4.52-4.54 show the representative water drops for the 30°, 45°, 60°, 90° and 180° angle of inclination of the same plate.

## Orientation of spikes

Angle  $\varphi^\circ$   
of  
inclined  
plate



L 129°      R 103°



L 116°      R 92°

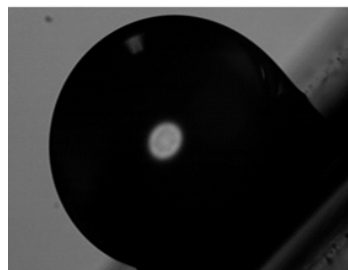


$30^\circ$

L 126°      R 88°

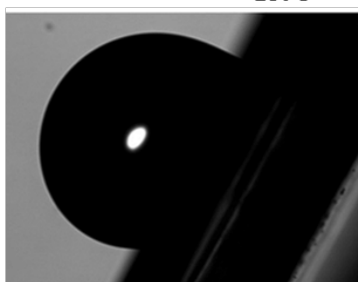


L 118°      R 91°

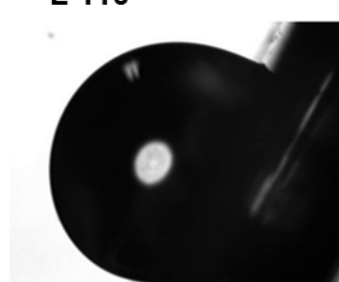


$45^\circ$

L 130°      R 93°



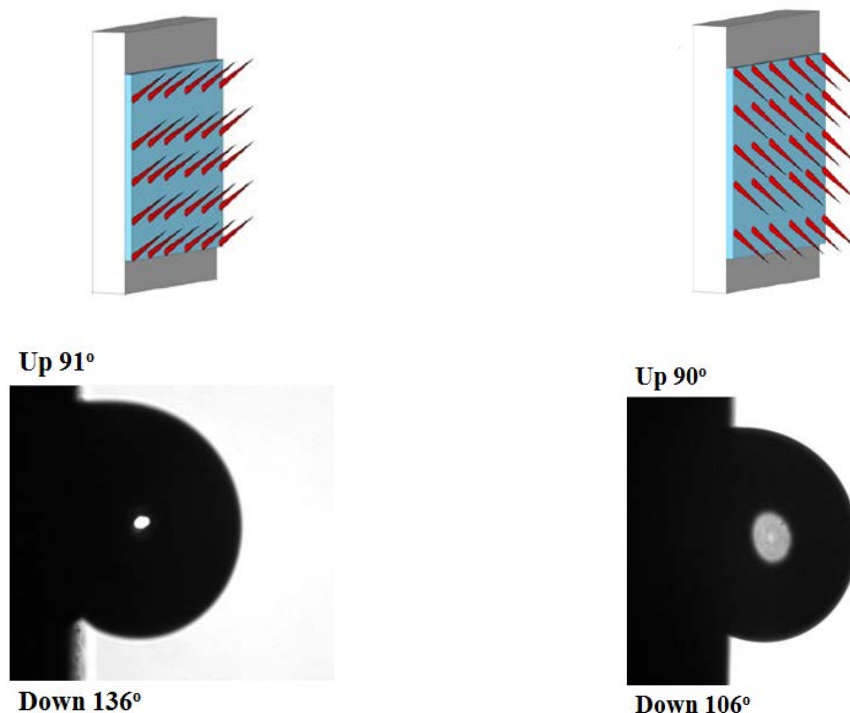
L 110°      R 80°



$60^\circ$

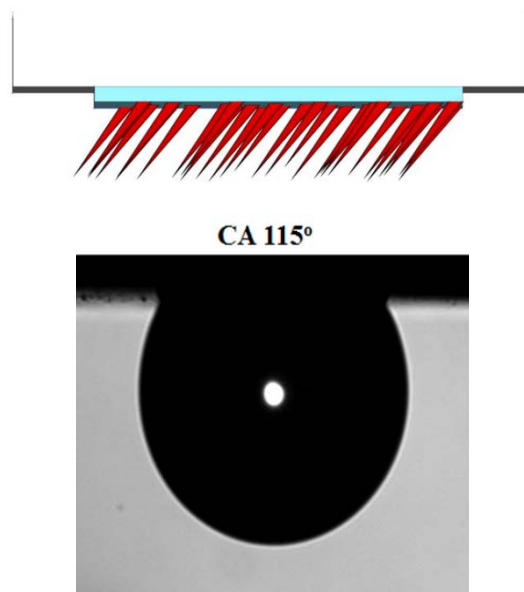
**Figure 4.52.** Representative water drops of the  $45^\circ$  tilted spikes, for the  $30^\circ$ ,  $45^\circ$  and  $60^\circ$  angle of inclination of the same plate.

Figure 4.52 shows that droplets exhibit a lower difference between advancing and receding angle, in the direction coinciding with the tilted spikes, than in the direction against the tilted spikes. This behavior is more enhanced by increasing the angle of inclination of the plate. This phenomenon seems to be enhanced in the case of  $45^\circ$  tilted spikes, comparing to the results of  $30^\circ$  tilted spikes.



**Figure 4.53.** Representative water drops of the  $45^\circ$  tilted spikes, for the  $90^\circ$  inclined plate.

Figure 4.53 confirms the fact that the droplets placed onto the microstructured surfaces exhibit a lower CAH in the direction of the spikes. When the spikes are positioned pointing up, the difference between the two angles is  $45^\circ$ . In the opposite scenario that the spikes are positioned pointing down, this difference is only  $16^\circ$ . Comparing to the  $30^\circ$  tilted spikes, the anisotropic behavior is more pronounced in the case of  $45^\circ$  tilted spikes, as the effect of the spikes orientation is enhanced.



**Figure 4.54.** Representative water drops of the 45° tilted spikes, for the 180° inclined plate.

The droplet remains “stuck” to the surface even when the sample is inverted. This proves the adhesion and the high hysteresis of the structures.

Afterwards, advancing and receding angle were measured for 30° and 45° tilted spikes.

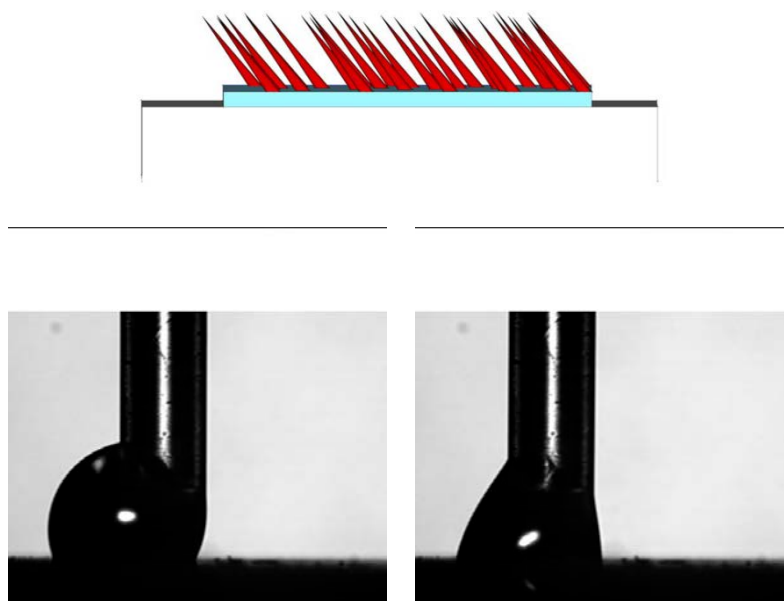


**Figure 4.55.** Advancing (left) and receding (right) contact angle measurement for the 30° tilted spikes.

According to Figure 4.55, as soon as the droplet touches the surface, it shows an obvious shift to the direction of the spikes. In the same way the droplet recedes, which proves the existence of controllable anisotropic behavior.

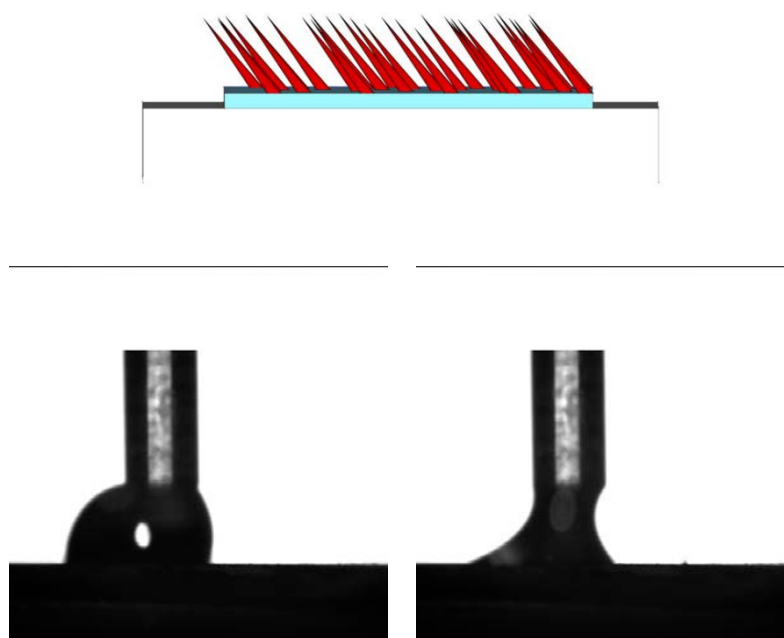


**Figure 4.56.** Advancing (left) and receding (right) contact angle measurement for  $45^\circ$  tilted spikes.

The  $45^\circ$  tilted spikes exhibit similar behavior with the  $30^\circ$  tilted spikes. There is a directional hysteresis on both samples.

### 4.13. Conclusions

Although, a vast number of anisotropic surfaces have been developed for microfluidic applications, there are still some technological difficulties. In this work, superhydrophilic and superhydrophobic surfaces with high unidirectional hysteresis were developed. This was achieved by the irradiation of Si wafers (central wavelength of 800 nm) at a tilt angle,  $30^\circ$  or  $45^\circ$ . Such surfaces after a silanization process exhibit anisotropic wettability, with a directional hysteresis. This phenomenon was enhanced in the case of  $45^\circ$  tilted spikes. Such

surfaces have many applications, such as in liquid transportation without loss and in the analysis of very small volumes of liquid samples.

#### 4.14. References

- (1) Schulte, A. J.; Droste, D. M.; Koch, K.; Barthlott, W. Hierarchically Structured Superhydrophobic Flowers with Low Hysteresis of the Wild Pansy (*Viola Tricolor*) - New Design Principles for Biomimetic Materials. *Beilstein J. Nanotechnol.* **2011**, *2* (1), 228–236.
- (2) Zorba, V.; Stratakis, E.; Barberoglou, M.; Spanakis, E.; Tzanetakos, P.; Anastasiadis, S. H.; Fotakis, C. Biomimetic Artificial Surfaces Quantitatively Reproduce the Water Repellency of a Lotus Leaf. *Adv. Mater.* **2008**, *20* (21), 4049–4054.
- (3) Anastasiadis, S. H. Development of Functional Polymer Surfaces with Controlled Wettability. *Langmuir* **2013**, *29* (30), 9277–9290.
- (4) Barthlott, W.; Neinhuis, C. Purity of the Sacred Lotus, or Escape from Contamination in Biological Surfaces. *Planta* **1997**, *202*, 1–8.
- (5) Neinhuis, C.; Barthlott, W. Characterization and Distribution of Water-Repellent, Self-Cleaning Plant Surfaces. *Ann. Bot.* **1997**, *79* (6), 667–677.
- (6) Callies, M.; Quéré, D. On Water Repellency. *Soft Matter* **2005**, *1* (1), 55.
- (7) Yong, J.; Chen, F.; Yang, Q.; Fang, Y.; Huo, J.; Hou, X. Femtosecond Laser Induced Hierarchical ZnO Superhydrophobic Surfaces with Switchable Wettability. *Chem. Commun.* **2015**, *51*, 9813–9816.
- (8) George, J. E. Fabrication of Superhydrophobic Surfaces from Femtosecond Laser Patterned Surfaces. *Proc. Indian Natl. Sci. Acad.* **2015**, *81* (2), 533–536.
- (9) Genzer, J.; Efimenko, K. Recent Developments in Superhydrophobic Surfaces and Their Relevance to Marine Fouling: A Review. *Biofouling* **2006**, *22* (5–6), 339–360.
- (10) Feng, X.; Jiang, L. Design and Creation of Superwetting/antiwetting Surfaces. *Adv. Mater.* **2006**, *18* (23), 3063–3078.
- (11) Barberoglou, M.; Zorba, V.; Stratakis, E.; Spanakis, E.; Tzanetakos, P.; Anastasiadis, S. H.; Fotakis, C. Bio-Inspired Water Repellent Surfaces Produced by Ultrafast Laser

- Structuring of Silicon. *Appl. Surf. Sci.* **2009**, 255 (10), 5425–5429.
- (12) Neinhuis, C. Characterization and Distribution of Water-Repellent, Self-Cleaning Plant Surfaces. *Ann. Bot.* **1997**, 79 (6), 667–677.
- (13) Balu, B.; Breedveld, V.; Hess, D. W. Fabrication Of “roll-Off” and “sticky” superhydrophobic Cellulose Surfaces-via Plasma Processing. *Langmuir* **2008**, 24 (9), 4785–4790.
- (14) Wang, B.-B.; Feng, J.-T.; Zhao, Y.-P.; Yu, T. X. Fabrication of Novel Superhydrophobic Surfaces and Water Droplet Bouncing Behavior — Part 1: Stable ZnO–PDMS Superhydrophobic Surface with Low Hysteresis Constructed Using ZnO Nanoparticles. *J. Adhes. Sci. Technol.* **2010**, 24 (15–16), 2693–2705.
- (15) Hao, C.; Li, J.; Liu, Y.; Zhou, X.; Liu, Y.; Liu, R.; Che, L.; Zhou, W.; Sun, D.; Li, L.; et al. Superhydrophobic-like Tunable Droplet Bouncing on Slippery Liquid Interfaces. *Nat. Commun.* **2015**, 6, 7986.
- (16) Quéré, D. Wetting and Roughness. *Annu. Rev. Mater. Res.* **2008**, 38 (1), 71–99.
- (17) Wang, S.; Liu, K.; Yao, X.; Jiang, L. Bioinspired Surfaces with Superwettability: New Insight on Theory, Design, and Applications. *Chem. Rev.* **2015**, 115 (16), 8230–8293.
- (18) Malvadkar, N. a; Hancock, M. J.; Sekeroglu, K.; Dressick, W. J.; Demirel, M. C. An Engineered Anisotropic Nanofilm with Unidirectional Wetting Properties. *Nat. Mater.* **2010**, 9 (12), 1023–1028.
- (19) Liu, M.; Zheng, Y.; Zhai, J. I. N.; Jiang, L. E. I. Bioinspired Super-Antiwetting Interfaces with Special Liquid - Solid Adhesion. **2010**, 43 (3).
- (20) Zheng, Y.; Gao, X.; Jiang, L. Directional Adhesion of Superhydrophobic Butterfly Wings. *Soft Matter* **2007**, 3 (2), 178.
- (21) Jokinen, V.; Leinikka, M.; Franssila, S. Microstructured Surfaces for Directional Wetting. *Adv. Mater.* **2009**, 21 (47), 4835–4838.
- (22) Tanaka, D.; Buenger, D.; Hildebrandt, H.; Moeller, M.; Groll, J. Unidirectional Control of Anisotropic Wetting through Surface Modification of PDMS Microstructures. *Langmuir* **2013**, 29 (40), 12331–12336.
- (23) Wang, S.; Wang, T.; Ge, P.; Xue, P.; Ye, S.; Chen, H.; Li, Z.; Zhang, J.; Yang, B. Controlling Flow Behavior of Water in Microfluidics with a Chemically Patterned

- Anisotropic Wetting Surface. *Langmuir* **2015**, *31* (13), 4032–4039.
- (24) Shastry, A.; Case, M. J.; Böhringer, K. F. Directing Droplets Using Microstructured Surfaces. *Langmuir* **2006**, *22* (14), 6161–6167.
- (25) Hanrock, M. J.; Sekeroglu, K.; Demirel, M. C. Bioinspired Directional Surfaces for Adhesion, Wetting and Transport. *Adv Funct Mater.* **2012**, *100* (2), 130–134.
- (26) Xia, D.; Johnson, L. M.; López, G. P. Anisotropic Wetting Surfaces with One-Dimensional and Directional Structures: Fabrication Approaches, Wetting Properties and Potential Applications. *Adv. Mater.* **2012**, *24* (10), 1287–1302.
- (27) Telford, A. M.; Hawkett, B. S.; Such, C.; Neto, C. Mimicking the Wettability of the Rose Petal Using Self-Assembly of Waterborne Polymer Particles. *Chem. Mater.* **2013**, *25* (17), 3472–3479.
- (28) Bhushan, B.; Her, E. K. Fabrication of Superhydrophobic Surfaces with High and Low Adhesion Inspired from Rose Petal. *Langmuir* **2010**, *26* (11), 8207–8217.
- (29) Bhushan, B.; Nosonovsky, M. The Rose Petal Effect and the Modes of Superhydrophobicity. *Philos. Trans. A. Math. Phys. Eng. Sci.* **2010**, *368*, 4713–4728.
- (30) Chang, F. M.; Hong, S. J.; Sheng, Y. J.; Tsao, H. K. High Contact Angle Hysteresis of Superhydrophobic Surfaces: Hydrophobic Defects. *Appl. Phys. Lett.* **2009**, *95* (6), 2009–2011.
- (31) Cho, W. K.; Choi, I. S. Fabrication of Hairy Polymeric Films Inspired by Geckos: Wetting and High Adhesion Properties. *Adv. Funct. Mater.* **2008**, *18* (7), 1089–1096.
- (32) Jin, M.; Feng, X.; Feng, L.; Sun, T.; Zhai, J.; Li, T.; Jiang, L. Superhydrophobic Aligned Polystyrene Nanotube Films with High Adhesive Force. *Adv. Mater.* **2005**, *17* (16), 1977–1981.
- (33) Hong, X.; Gao, X.; Jiang, L. Application of Superhydrophobic Surface with High Adhesive Force in No Lost Transport of Superparamagnetic Microdroplet. *J. Am. Chem. Soc.* **2007**, *129* (6), 1478–1479.
- (34) Lai, Y.; Gao, X.; Zhuang, H.; Huang, J.; Lin, C.; Jiang, L. Designing Superhydrophobic Porous Nanostructures with Tunable Water Adhesion. *Adv. Mater.* **2009**, *21* (37), 3799–3803.
- (35) Wang, S.; Jiang, L. Definition of Superhydrophobic States. *Adv. Mater.* **2007**, *19* (21),

- 3423–3424.
- (36) Geim, A. K.; Dubonos, S. V.; Grigorieva, I. V.; Novoselov, K. S.; Zhukov, A. A.; Shapoval, S. Y. Microfabricated Adhesive Mimicking Gecko Foot-Hair. *Nat. Mater.* **2003**, 2 (7), 461–463.
- (37) Lee, H.; Lee, B. P.; Messersmith, P. B. A Reversible Wet/dry Adhesive Inspired by Mussels and Geckos. *Nature* **2007**, 448 (7151), 338–341.
- (38) Chang, F. M.; Hong, S. J.; Sheng, Y. J.; Tsao, H. K. High Contact Angle Hysteresis of Superhydrophobic Surfaces: Hydrophobic Defects. *Appl. Phys. Lett.* **2009**, 95 (6), 2012–2015.
- (39) Hejazi, V.; Nosonovsky, M. Contact Angle Hysteresis in Multiphase Systems. *Colloid Polym. Sci.* **2013**, 291 (2), 329–338.
- (40) Extrand, C. W. Model for Contact Angles and Hysteresis on Rough and Ultraphobic Surfaces. *Langmuir* **2002**, 18 (21), 7991–7999.
- (41) Li, W.; Amirfazli, A. A Thermodynamic Approach for Determining the Contact Angle Hysteresis for Superhydrophobic Surfaces. *J. Colloid Interface Sci.* **2005**, 292 (1), 195–201.
- (42) Moradi, S.; Englezos, P.; Hatzikiriakos, S. G. Contact Angle Hysteresis of Non-Flattened-Top Micro / Nanostructures. **2014**, 3284 (3).
- (43) Reyssat, M.; Que, D. Contact Angle Hysteresis Generated by Strong Dilute Defects Contact Angle Hysteresis Generated by Strong Dilute Defects †. *Society* **2009**, 3906–3909.
- (44) Carre, A.; Mittal, K. L. *Superhydrophobic Surfaces - CRC Press Book*; CRC Press, 2009.
- (45) Kubiak, K. J.; Mathia, T. G. Anisotropic Wetting of Hydrophobic and Hydrophilic Surfaces - Modelling by Lattice Boltzmann Method. *Procedia Eng.* **2014**, 79 (1st ICM), 45–48.
- (46) Li, W.; Fang, G.; Li, Y.; Qiao, G. Anisotropic Wetting Behavior Arising from Superhydrophobic Surfaces: Parallel Grooved Structure. *J. Phys. Chem. B* **2008**, 112 (24), 7234–7243.
- (47) Neuhaus, S.; Spencer, N. D.; Padeste, C. Anisotropic Wetting of Microstructured

- Surfaces as a Function of Surface Chemistry. **2012**.
- (48) Honda, K.; Morita, M.; Masunaga, H.; Sasaki, S.; Takata, M.; Takahara, A. Room-Temperature Nanoimprint Lithography for Crystalline Poly(fluoroalkyl Acrylate) Thin Films. *Soft Matter* **2010**, *6* (5), 870–875.
- (49) Xia, D.; He, X.; Jiang, Y. B.; Lopez, G. P.; Brueck, S. R. J. Tailoring Anisotropic Wetting Properties on Submicrometer-Scale Periodic Grooved Surfaces. *Langmuir* **2010**, *26* (4), 2700–2706.
- (50) Yong, X.; Zhang, L. T. Nanoscale Wetting on Groove-Patterned Surfaces. *Langmuir* **2009**, *25* (9), 5045–5053.
- (51) Khare, K.; Zhou, J.; Yang, S. Tunable Open-Channel Microfluidics on Soft Poly(dimethylsiloxane) (PDMS) Substrates with Sinusoidal Grooves. *Langmuir* **2009**, *25* (21), 12794–12799.
- (52) Zhao, Y.; Lu, Q.; Li, M.; Li, X. Anisotropic Wetting Characteristics on Submicrometer-Scale Periodic Grooved Surface. *Langmuir* **2007**, *23* (11), 6212–6217.
- (53) Zhang, F.; Low, H. Y. Anisotropic Wettability on Imprinted Hierarchical Structures. *Langmuir* **2007**, *23* (14), 7793–7798.
- (54) Morita, M.; Koga, T.; Otsuka, H.; Takahara, A. Macroscopic-Wetting Anisotropy on the Line-Patterned Surface of Fluoroalkylsilane Monolayers. *Langmuir* **2005**, *21* (3), 911–918.
- (55) Yoshimitsu, Z.; Nakajima, A.; Watanabe, T.; Hashimoto, K. Effects of Surface Structure on the Hydrophobicity and Sliding Behavior of Water Droplets. *Langmuir* **2002**, *18* (15), 5818–5822.
- (56) Wu, D.; Chen, Q. D.; Yao, J.; Guan, Y. C.; Wang, J. N.; Niu, L. G.; Fang, H. H.; Sun, H. B. A Simple Strategy to Realize Biomimetic Surfaces with Controlled Anisotropic Wetting. *Appl. Phys. Lett.* **2010**, *96* (5), 10–13.
- (57) Chung, J. Y.; Youngblood, J. P.; Stafford, C. M. Anisotropic Wetting on Tunable Micro-Wrinkled Surfaces. *Soft Matter* **2007**, *3* (9), 1163.
- (58) Malvadkar, N. a; Hancock, M. J.; Sekeroglu, K.; Dressick, W. J.; Demirel, M. C. An Engineered Anisotropic Nanofilm with Unidirectional Wetting Properties. *Nat. Mater.* **2010**, *9* (12), 1023–1028.

- (59) Bliznyuk, O.; Jansen, H. P.; Kooij, E. S.; Zandvliet, H. J. W.; Poelsema, B. Smart Design of Stripe-Patterned Gradient Surfaces to Control Droplet Motion. *Langmuir* **2011**, *27* (17), 11238–11245.
- (60) Gregory D. Bixler. Bioinspired Surface for Low Drag, Self-Cleaning, and Antifouling: Shark Skin, Butterfly and Rice Leaf Effects. **2013**.
- (61) Mele, E.; Girardo, S.; Pisignano, D. Strelitzia Reginae Leaf as a Natural Template for Anisotropic Wetting and Superhydrophobicity. *Langmuir* **2012**, *28* (11), 5312–5317.
- (62) Bhushan, B. Bioinspired Structured Surfaces. *Langmuir* **2012**, *28* (3), 1698–1714.
- (63) Bixler, G. D.; Bhushan, B. Biofouling: Lessons from Nature. *Philos. Trans. R. Soc. A Math. Phys. Eng. Sci.* **2012**, *370* (1967), 2381–2417.
- (64) Liu, X.; Liang, Y.; Zhou, F.; Liu, W. Extreme Wettability and Tunable Adhesion: Biomimicking beyond Nature? *Soft Matter* **2012**, *8* (7), 2070.
- (65) Feng, L.; Zhang, Y.; Xi, J.; Zhu, Y.; Wang, N.; Xia, F.; Jiang, L. Petal Effect: A Superhydrophobic State with High Adhesive Force. *Langmuir* **2008**, *24* (8), 4114–4119.
- (66) Yang, S.; Ju, J.; Qiu, Y.; He, Y.; Wang, X.; Dou, S.; Liu, K.; Jiang, L. Peanut Leaf Inspired Multifunctional Surfaces. *Small* **2014**, *10* (2), 294–299.
- (67) Ramachandran, R.; Nosonovsky, M. Surface Micro/nanotopography, Wetting Properties and the Potential for Biomimetic Icephobicity of Skunk Cabbage *Symplocarpus Foetidus*. *Soft Matter* **2014**, *10* (39), 7797–7803.
- (68) Gao, H.; Wang, X.; Yao, H.; Gorb, S.; Arzt, E. Mechanics of Hierarchical Adhesion Structures of Geckos. *Mech. Mater.* **2005**, *37* (2–3 SPEC. ISS.), 275–285.
- (69) Autumn, K.; Sitti, M.; Liang, Y. a; Peattie, A. M.; Hansen, W. R.; Sponberg, S.; Kenny, T. W.; Fearing, R.; Israelachvili, J. N.; Full, R. J. Evidence for van Der Waals Adhesion in Gecko Setae. *Proc. Natl. Acad. Sci. U. S. A.* **2002**, *99* (19), 12252–12256.
- (70) Sher, M.-J. Intermediate Band Properties of Femtosecond-Laser Hyperdoped Silicon, 2013.
- (71) Crouch, C. H.; Carey, J. E.; Warrender, J. M.; Aziz, M. J.; MAzur, E.; Genin, F. Y. Comparison Of Structure And Properties Of Femtosecond And Nanosecond Laser-Structured Silicon. *Appl. Phys. Lett.* **2004**, *84* (11), 1850–1852.

- (72) Carey, J. E.; Crouch, C. H.; Mazur, E. Femtosecond-Laser-Assisted Microstructuring of Silicon Surfaces. *Opt. Photonics News* **2003**, *14* (2), 32–36.
- (73) Shen, M. Y.; Crouch, C. H.; Carey, J. E.; Mazur, E. Femtosecond Laser-Induced Formation of Submicrometer Spikes on Silicon in Water. *Appl. Phys. Lett.* **2004**, *85* (23), 5694–5696.
- (74) Anastasiadis, S. H.; Hatzikiriakos, S. G. The Work of Adhesion of Polymer/wall Interfaces and Its Association with the Onset of Wall Slip. *J. Rheol. (N. Y. N. Y.)* **1998**, *42* (4), 795.
- (75) Choi, W.; Tuteja, A.; Mabry, J. M.; Cohen, R. E.; McKinley, G. H. A Modified Cassie-Baxter Relationship to Explain Contact Angle Hysteresis and Anisotropy on Non-Wetting Textured Surfaces. *J. Colloid Interface Sci.* **2009**, *339* (1), 208–216.
- (76) Bracco, G.; Holst, B. *Surface Science Techniques*; 2013; Vol. 51.
- (77) Eral, H. B.; 'T Mannetje, D. J. C. M.; Oh, J. M. Contact Angle Hysteresis: A Review of Fundamentals and Applications. *Colloid Polym. Sci.* **2013**, *291* (2), 247–260.
- (78) Bhushan, B. *Biomimetics*. **2016**, 23–34.
- (79) Yang, J.; Rose, F. R. A. J.; Gadegaard, N.; Alexander, M. R. Effect of Sessile Drop Volume on the Wetting Anisotropy Observed on Grooved Surfaces. *Langmuir* **2009**, *25* (5), 2567–2571.
- (80) Gleiche, M.; Chi, L.; Gedig, E.; Fuchs, H. Anisotropic Contact-Angle Hysteresis of Chemically Nanostructured Surfaces. *Chemphyschem* **2001**, *2* (3), 187–191.

## Chapter 5

# 5. Covalent immobilization of metal nanoparticle containing microgels onto solid substrates

## 5.1. Introduction

Hydrogels are three-dimensional insoluble polymers, chemically or physically crosslinked, that are able to absorb large amounts of water.<sup>1-8</sup> Hydrogels in the form of colloidal gels with sizes between 100 nm and 1000 nm, are known as microgels.<sup>1-3,5,9-13</sup> The smart polymer microspheres have attracted great research interest due to their reversible changes in response to external stimuli such as temperature, pH, solvent quality, electric field, magnetic force, mechanical stress, ionic strength and light.<sup>3-5,8-10,13-17</sup> Accordingly, microgels can find numerous applications in energy, medicine, nanobiotechnology, light emitting devices, photovoltaics, detectors and biolabels,<sup>2,3</sup> in the fabrication of microlenses, in biosensors, in cosmetics<sup>18</sup> as well as in cell immobilization.<sup>3,7,11,14,17,19-22</sup> Their small size, extended circulating time, biocompatibility as well as their ability to incorporate drug molecules within the polymer network make them attractive for use in drug delivery.<sup>3-5,16,21</sup> Furthermore, such stimuli responsive microspheres can be utilized as thickeners, in waste removal<sup>3,16,23</sup> and for material reinforcement.<sup>24</sup>

pH-sensitive microgels have been frequently used in drug release formulations.<sup>3,6,23,25–28</sup> The elicitation behavior of the pH sensitive polyelectrolyte microgels arises from the difference between the pH in the stomach (<3) and the pH in the intestine.<sup>25,26</sup> Polycationic microgels, based on 2-(dimethylamino)ethylmethacrylate (DMAEMA), are used for drug release in the stomach,<sup>25</sup> while polyanionic microgels made of poly(acrylic acid) (PAA) or poly(methacrylic acid) (PMAA) can be used for the release of drugs in neutral environment.<sup>12,25,29,30</sup>

Moreover, pH-responsive microgels have gained attention in the field of catalysis, as they can be utilized as microreactors for the incorporation of nanoparticulate catalysts.<sup>6,7,12,23,31–35</sup>

Nowadays, the continuous requirement for high quality pharmaceutical products (such as vitamins), the necessity for a more “green” chemistry and “clean” technology processes and, at the same time, the need for a lower cost production, can come across only through a complete rethinking of the chemical production processes. Metal nanoparticles such as silver (Ag), platinum (Pt), copper (Cu), ruthenium (Ru), palladium (Pd) and gold (Au) have been extensively incorporated into microgels for use in catalysis.<sup>12,31,36</sup> Metallic particles are not stable in aqueous solutions as they have the tendency to aggregate. As a result, a stabilizing agent or a carrier system is necessary for their stabilization. Compared to other systems, microgels offer certain advantages such as higher interfacial area per unit mass of the hydrogel,<sup>37</sup> colloid stability, controllable growth of particles and desired functionality.<sup>5,31–35</sup>

However the hybrid nanoparticulate catalysts should also exhibit the suitability to flow chemistry. It is important to achieve the covalent immobilization of pH-responsive microgels under microfluidic flow conditions for their efficient implementation in mild industrial catalytic processes.<sup>38–40</sup> In the research community there are a lot of works referring to the immobilization of polymer networks onto surfaces, but none of them deal with the stability of the system under flow conditions.<sup>41–49</sup> In this work, the immobilization of the microgels was initially performed by conventional dip or drop casting as well as with the Pickering emulsion

and Vortical surface method.<sup>12</sup> However, these methods led to low homogeneity and multi-layer structures. For this purpose, microgels were immobilized onto glass substrates using the amine coupling chemistry.<sup>19</sup> The immobilized microgels were subjected to environmental changes (heating temperature, heating time, flow rate and pH) in order to examine their stability under microfluidic flow conditions for their efficient implementation in mild industrial catalytic processes. The surfaces after the immobilization of the microgel nanoparticles were studied by Scanning Electron Microscopy (SEM). Afterwards, the catalytic behavior of the synthesized metal containing microgels was studied through a model hydrogenation reaction.

### 5.1.1. Polymeric microgels

Microgels, first reported from Baker, as new “polymer molecules” with intramolecularly cross-linked structures,<sup>50</sup> can be defined as solvent-containing colloidal polymer networks that can swell or deswell in response to one or more external stimuli (pH, temperature, ionic strength, electric or magnetic field, light and/or chemical and biological stimuli).<sup>17,51</sup> Graham and his co-workers showed that the solvent solubility parameters are of great importance for the synthesis of microgels.<sup>52</sup> The polymer-like nature of the microgels enables them to control their shape, size and the suspension volume fraction.<sup>51</sup> Another advantage they exhibit, in comparison to other nanostructures, is their stability due to the crosslinking.<sup>53</sup> Furthermore, therapeutic agents can be introduced to the polymer network for targeted delivery.<sup>53</sup>

This work focuses on pH-responsive microgels, based on poly(acrylic) acid (PAA), poly(methacrylic acid) (PMAA) and poly(2-(diethylamino)ethylmethacrylate) (PDEAEMA).

### 5.1.2. Synthesis of the microgels

The microgels were synthesized utilizing with emulsion polymerization, by the group of Prof. M. Vamvakaki. Emulsion polymerization was first presented at 1942, during World War II, for producing synthetic rubbers from 1,3-butadiene and styrene.<sup>54-56</sup>

During the procedure, three types of particles are present: monomer droplets, inactive micelles in which polymerization is not occurring, and active micelles in which polymerization takes place. The latter act as meeting place for the organic monomer (oil-soluble) and the water-soluble initiator. Micelles are favored for the reaction, due to the high total surface area. During the process, the micelles are growing by the addition of monomers from the aqueous solution. The schematic presentation of the emulsion polymerization system is shown in Figure 5.1.<sup>54</sup>

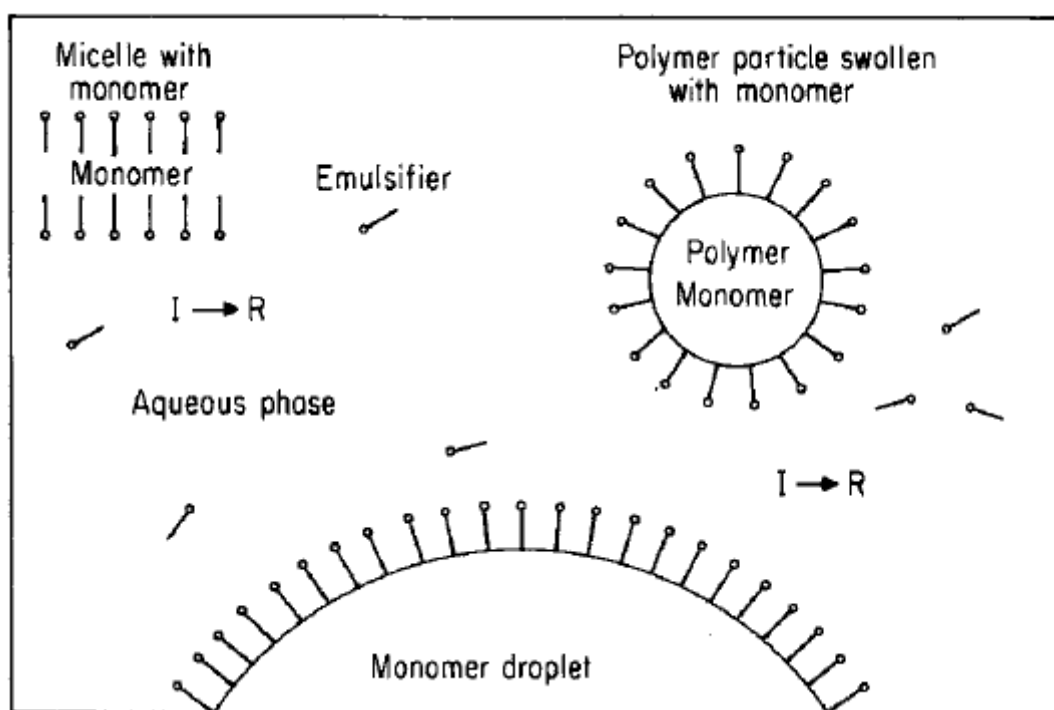


**Figure 5.1.** Schematic presentation of emulsion polymerization system.<sup>54</sup>

Comparing to bulk polymerization, emulsion polymerization has several advantages. Viscosity is not a significant parameter, as the polymer molecules are contained within the

micelles. The reaction temperature can be controlled by the continuous water phase, which is an excellent conductor of heat. Furthermore, high molecular weight polymers can be achieved without decreasing the polymerization rate. Moreover the final products, latexes, can be utilized in many cases directly, without further separations.<sup>54</sup> However the main drawback of the procedure is that the surfactants are difficult to be removed at the end of the process.

### 5.1.3. Synthesis of metal containing microgels

Microgel-metal nanoparticle hybrid materials can be prepared using two general strategies. The first route involves metal loading of the microgels using preformed inorganic particles, whereas in the second route, the nanoparticles are grown in situ within the microgels. The former method usually suffers from low particle loading and aggregation of the nanoparticles. Moreover, the polymer matrix exerts no control over the growth and size of the nanoparticles. To avoid such problems, the synthesis of metal nanoparticles in the presence of the polymeric stabilizer has been explored.<sup>57</sup>

### 5.1.4. Immobilization of microgels onto surfaces: Deposition techniques

The immobilization of microgels onto surfaces will be the necessary step for their efficient implementation in mild industrial catalytic processes. This can be achieved by the incorporation of functional groups within mainly the outer part of the carriers that can create the bonding of the carriers to the solid surfaces. Such groups can be, for example, carboxylic acid groups as a functional group of a comonomer incorporated during the synthesis of the ultrathin polymer layers.

Various means of attachment of the particles on the surfaces of interest have been attempted and the behavior has been investigated and optimized, either with physical adsorption or with covalent chemical bonding. Physical adsorption is a simple procedure for coating surfaces.

The adsorption of the molecules in this case, is a result of non-covalent interactions, like van der Waals forces, hydrogen bonding and hydrophobic interactions. Polymer adsorption is promoted when the exchange of solvent molecules in contact with the surface by segments of the polymer chain leads to a decrease in the total free energy of the system. In this case the enthalpic contribution of attractive polymer-surface contacts overcomes the loss of configurational entropy arising from confinement to the surface.<sup>58</sup> The main drawback of physical adsorption is that the molecules are not well anchored on the surfaces and they have the tendency to leach from the samples.<sup>59</sup> However, there are some cases in which this drawback may be turned into advantage. For example, the removal of immobilized enzymes from surfaces, when their activity has decayed, is highly attractive for the regeneration and the reuse of the surfaces.<sup>60</sup> On the other hand, covalent chemical bonding is ideal for stable and homogeneous immobilization of molecules on surfaces. Polymers, which have one or more reactive (binding) groups along the polymer chain, can react with binding sites on the surface, resulting in the development of covalent surface-polymer bonds.<sup>61</sup>

## 5.2. Experimental Part

### 5.2.1. Synthesis of metal containing microgels

#### Synthesis of PDEAEMA, PMAA and PAA based microgels

The pH sensitive microgels based on PDEAEMA, PMAA and PAA were synthesized by emulsion copolymerization of a functional monomer with a cross-linker in the presence of a stabilizer, as described previously.<sup>12,23,62,57,63</sup> DEAEEMA monomer and PEGMA stabilizer (10% wt. based on DEAEEMA) was employed for the synthesis of the amino based PDEAEMA microgels, while *t*-butyl-acrylate, *t*-BuA was used as the monomer and AOT as the stabilizer (8% wt based on *t*-BuA) for the synthesis of the P(*t*-BuA) microgels, which are

precursors to the PAA microgels. Next, the P(*t*-BuA) based microgels were hydrolyzed to convert the *t*-BuA segments into acrylic acid units via acid hydrolysis. In both cases, EGDMA was used as the cross-linker (1 % wt. based on the monomer). The PMAA microgels used in this work were prepared utilizing (*t*-butyl methacrylate (*t*-BuMA, Sigma-Aldrich)), following the same procedure, as described above.

### **Pd and Ru incorporation within the polymer microgels**

In a typical synthesis, the pH of a 0.5% wt. aqueous dispersion of PDEAEMA and PAA microgels was adjusted to 2.5 and pH 7, respectively. Next, the  $K_2PdCl_4$  and  $RuCl_3$  metal precursor solutions were added to the above dispersions for the synthesis of the Pd and Ru nanoparticles, respectively. After stirring at room temperature for 3 h, the excess metal precursor was removed by ultrafiltration. Subsequently, a ten-fold excess of  $NaBH_4$  aqueous solution was added under vigorous stirring for the reduction of the metal. The reduction of palladium ions took place under ambient conditions, while, for the formation of Ru nanoparticles, the reduction of  $Ru^{3+}$  occurred under a nitrogen atmosphere at 30°C. Finally, the microgel stabilized metal nanoparticles were extensively purified by ultrafiltration in pure water to remove the salts formed during reduction.<sup>12</sup>

#### **5.2.2. Characterization of the metal containing microgels**

The hydrodynamic size of the synthesized pH-sensitive microgel particles, before and after the metal nanoparticle formation, was studied by dynamic light scattering (DLS) using an ALV spectrophotometer and a Nd-YAG laser with  $\lambda = 532$  nm at 20°C. Moreover, the formation of the metal nanoparticles within the microgel particles was verified by transmission electron microscopy (TEM) using a JEOL JEM-2100 instrument at an electron accelerating voltage of 80 kV. Scanning electron micrographs were recorded using a field-

emission JEOL 7000 electron microscope operating at 15 kV. All the samples were sputter-coated with a 10 nm Au film to reduce charging. X-ray diffraction (XRD) patterns were collected on a PANalytical X'pert Pro MPD X-ray diffractometer using Cu K $\alpha$  radiation (45 kV, 40 mA) in Bragg–Brentano geometry. Thermogravimetric analysis was performed on a Perkin Elmer Pyris Diamond TG/DTA instrument under a nitrogen atmosphere. For a typical measurement, ~5 mg of a solid sample were placed in a platinum holder and were heated under constant nitrogen flow at a temperature ramp of 10°C/min.

### 5.2.3. Immobilization of microgels onto solid surfaces

Prior to microgel deposition onto the various substrates, the microgel dispersion was sonicated for a few minutes to increase the suspension homogeneity. Next, the polymer microgel particles were deposited onto the solid substrates utilizing several methods in order to investigate which one would give a uniform and dense particle layer onto the surface. At first, the conventional drop casting, dip coating, Pickering emulsion and Vortical surface methods were investigated. Finally the amine coupling method was utilized. The experimental details of each method are described below:

- **Drop casting**

In this method, a small amount of polymer solution was dropped onto the sample by pipette and left to dry in ambient conditions. Drop casting is a simple and quick process, low cost, with no waste of material or solution, for generating thin films of polymers. The main drawback of this method is that there are height variations in the resulted surfaces and uniform films are difficult to be achieved.<sup>64</sup>

- **Dip coating**

Dip coating is the most widely used method for industrial applications, due to the low cost and the high coating quality. According to the dip coating method, the substrate is slowly dipped into the vial containing the polymer solution, and withdrawn with a controlled low velocity, in order to obtain thin films. In case that thicker film is needed, it can be achieved by increasing the withdrawal speed. The dip coating process is depicted in Figure 5.2.<sup>65</sup>

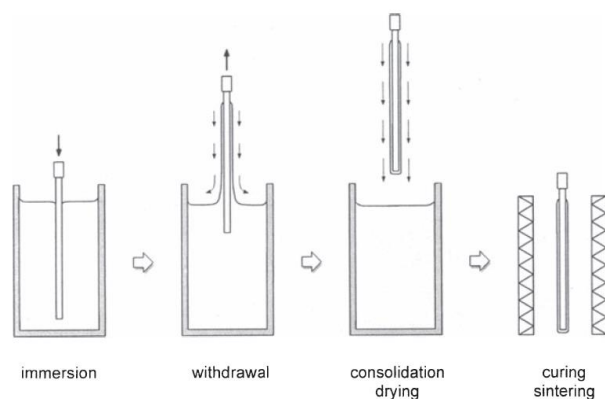


**Figure 5.2.** Schematic presentation of dip coating process.<sup>65</sup>

- **Pickering emulsion method**

This process is ideal for the fabrication of monolayer films through oil-water interfacial self-assembly. It has been proved that ethanol can act as an inducer and trap hydrophilic particles to a water-oil interface.<sup>44,66,67</sup> Due to the surface pressure of the oil-water interface, the particles are being compressed into a close-packed structure, which leads to monolayer films.<sup>68</sup> In this case, one liquid was the solvent of the suspension (water) and the second was hexane. The main advantage of the Pickering emulsion method is the three-phase system that allows the interactions between the nanoparticles, with repulsive or attractive forces.<sup>69</sup> The schematic presentation of pickering emulsion process, is depicted in Figure 5.3.

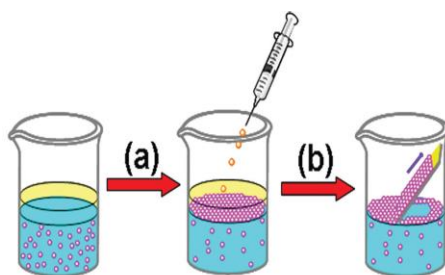


**Figure 5.3.** Pickering Emulsion method followed for “trapping” the microgel particles at an interface.<sup>68</sup>

- **Vortical surface method**

In this process the particles are spread onto the air-liquid interface, through a spreading agent. Ordered close-packed monolayer film of particles can be obtained on a vertical water surface by the water flow. By dipping the surface vertically on the solution on a steady speed, the particles are transferred onto the double sides of the substrate. Figure 5.4 describes in detail the Vortical surface method.<sup>49</sup>

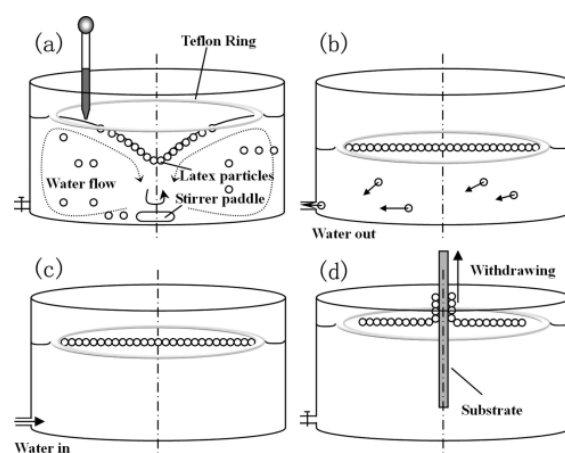


**Figure 5.4.** Vortical surface method followed for “trapping” the microgel particles at an interface.<sup>49</sup>

According to Figure 5.4 a, a beaker filled with the microgel suspension, was deposited in a magnetic stirrer in order to produce a vortex and a hollow Teflon ring was allowed on the water surface. Ethanol was used also in this case as an inducer. Water under the latex film was piped out from a penstock setting at the bottom of the beaker, and the ring sank down with the water level (Figure 5.4 b). The rotation makes the water move away from the center, working as a centrifugal pump. The water flow trapped the microgels to the center of the beaker. Clear water was injected into the beaker, while the Teflon ring maintained the film structure unchanged by moving up and down, during the water replacing process (Figure 5.4 c). For an appropriate speed (120 rpm), the particles are being compressed into close-packed structures on the water surface. Finally vertical withdrawal of the glass substrate from the beaker takes place and a microgel film layer is formed on the double surface sides of the glass substrate (Figure 5.4 d).<sup>49</sup>

- **Covalently attachment method-amine coupling**

Initially, all glass substrates were cleaned with aqueous solution of Hellmanex (10% v/v) for 3h in order to increase the hydroxyl group content. After Hellmanex treatment, the substrates

were extensively rinsed with deionized water and ethanol and were dried with a nitrogen flow. This protocol resulted in sufficiently clean and hydrophilic surfaces for the absorption of APTES.<sup>70</sup> Silanization with silane compounds was used as a process for the modification of glass surfaces.<sup>19</sup> Silane coupling agents have the ability to form a durable bond between organic and inorganic materials. 3-Aminopropyl-triethoxysilane (APTES, Sigma-Aldrich) was utilized as a surface modification agent.<sup>71,72</sup> The glass substrates were placed in a well closed vial and degassed with nitrogen. Subsequently, a degassed solution of 0.14 ml APTES in 10 ml dry ethanol were transferred to the vial containing the glass substrates. The glass substrates were kept in the above solution for 24 h under a nitrogen atmosphere at room temperature before being washed extensively with ethanol and dried under nitrogen gas flow.

Next the silanized glass slides were transferred in a vial and were degassed with nitrogen. A degassed aqueous dispersion of an appropriate amount of microgels and N-(3-Dimethylaminopropyl)-N'-ethylcarbodiimide/N-hydroxysuccinimide (EDC/NHS) was added.<sup>73</sup> The molar ratio of microgel suspension:EDC:NHS was 1:1:2. The pH of the solution was adjusted between 3 and 4 and the substrates were kept in the above solution under a nitrogen atmosphere for 24 h. Finally, the substrates were extensively washed with water and ethanol and dried under a nitrogen flow. The procedure is depicted in Figure 5.5.

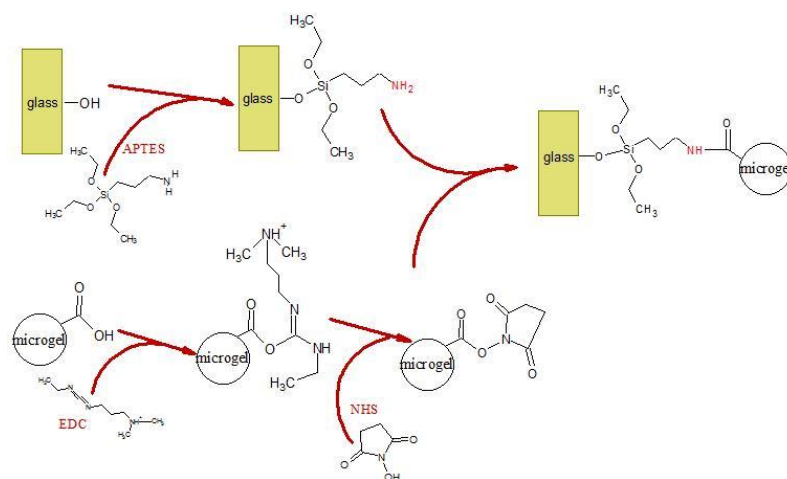


**Figure 5.5.** Schematic presentation of the immobilization procedure.

The effects of different deposition parameters, such as the concentration of the suspension and substrate orientation were tested. The durability of the microgel particles deposited onto the surfaces against hydration and shear forces was tested utilizing repeated immersion of the surfaces into water undergoing mechanically-generated hydrodynamic flow. The characterization of the surfaces was performed using FE-SEM.

#### 5.2.4. Stability tests

In order to verify the stability of the microgel layers on the substrates, the samples were subjected to stability tests either by changing the environmental conditions (pH, temperature) or by the flow of pure water on the substrate. It is important to achieve the covalent immobilization for their efficient implementation in industrial catalytic processes such as the Pd-catalyzed reduction of nitro compounds or the Pd-catalyzed Suzuki-Miyaura reactions.<sup>38–40</sup> The temperature range examined was 40–80 °C.<sup>38–40</sup> In addition, the anchored microgels were tested for their stability, by immersing them in different pH solutions.

The samples were also subjected to water flow through rinsing with de-ionized water (flow rate of  $2.1 \cdot 10^{-5} \text{ m}^3/\text{s}$ ). The velocity of the water flow was calculated at 1.07 m/s and the

Reynolds number  $Re=10.7$ . The schematic presentation of this procedure is depicted in Figure 5.6. The water flowed through a pipe (diameter 0.5 cm). The plate was tilted to  $30^\circ$ . The sample was fixed 10 cm below the hole of the pipe.

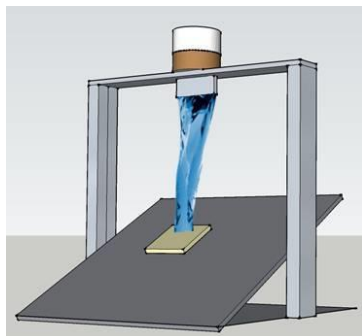


**Figure 5.6.** Schematic presentation of the water flow stability test.

The surfaces were characterized, before and after the applied stimuli, using SEM (Zeiss Supra 35VP).

#### **5.2.5. Surface analysis with Image J and Matlab code**

In order to quantitatively determine the density and distribution of the microgels, before and after the stability tests, the ImageJ software was used. The results were crosschecked with a Matlab software code.

The Matlab code used is presented in the Table 5.1.

**Table 5.1.** Matlab code for the analysis of the FE-SEM images.

---

```
function s = calcSurfaceAlt(path, thresLow, thresHigh)

% inputs:

% path: directory location (as string) of all *.tif files

% thresLow, thresHigh: optional inputs for contrast enhancement. Defaults are 100 and
150

% s: surface area statistics

% Notes:

% 1) Truncate bottom info by keeping only 700 pixels of height. Seems correct for
current

% images

% 2) min value varies (66-85) but using 100 is good for contrast enhancement purposes
and

% max value varies (199-248) but saturating using an upper threshold of 150 makes for

% better contrast enhancement. The resulting default range is only 50 compared to
original

% range of about 160. Stretching out the final range of 50 to the full 255 creates

% over-saturation between background and spheres and results in clean bimodal histogram

% making easier the identification of appropriate threshold.

% 3) Image resolution (scale at 200nm or 1um) may affect the threshold setting for

% separation. At low res (1um of 5th image) a threshold of 130 is picking up background

% whereas in higher res (20nm of images 1-4) a threshold of 130 is missing some spheres

% and a lower setting may be preferable. Suggestion would be to put images in separate

% folders according to resolution and run analysis with different thresholds instead of

% overcomplicating code with manual input for every image.

% 4) This version varies the threshold for 0 to 255 and keeps all the statistics in order

% to see how the area changes and possibly identify trends to help choose a better
```

---

```
% threshold

maxVal = 255;

if isempty(thresLow)

    thresLow = 10; %default value 100

end

if isempty(thresHigh)

    thresHigh = 1500; % default value 150

end

thresSurf = 0:5:255;

numThres = length(thresSurf);

files = dir([path '*.*tif']);

numFiles = length(files);

s = zeros(numFiles,numThres);

for ii = 1:numFiles

    fname = [path '/' files(ii).name];

    img = imread(fname,'tif');

    img(701:end,:) = [];

    areaTot = numel(img);

%   disp([min(img(:)) max(img(:))]);

    img = (img - thresLow)*(maxVal/(thresHigh-thresLow));

%   medfilt2(img,[5 5]); % uncomment this for median filtering

    for jj = 1:numThres

        imgSphere = img > thresSurf(jj);

        areaSphere = sum(imgSphere(:));

        s(ii, jj) = areaSphere/areaTot;

    end

end
```

```
end  
  
% uncomment below to see images  
  
figure(3*(ii-1)+1), imshow(img); % saturated image  
  
figure(3*(ii-1)+2), imshow(imgSphere); % binary image with white for spheres  
  
figure(3*(ii-1)+3), hist(double(img(:)),20); % histogram of saturated image  
  
end  
  
figure, plot(thresSurf, s.);  
  
end
```

### 5.2.6. Hydrogenation reaction with metal containing microgels as catalysts

Catalytic metal nanoparticles (NPs) possess extremely high surface-to-volume ratio in comparison to bulk metals and represent highly active and selective catalysts for a variety of organic reactions. However, the presence of a suitable stabilizing support to prevent the metal NPs from aggregating and, thus, avoid the reduction of their surface area, is essential.<sup>35</sup> Polymeric stabilizers can control the NP characteristics and properties by manipulating the polymer molecular structure, size and composition.<sup>74</sup> Their use allow the combination of certain advantages of both homogeneous (high activity and selectivity) and traditional heterogeneous (easy recovery from the reaction mixture and a possibility of catalyst regeneration) catalysis. The PDEAEMA, PAA and PMAA particles, due to their amine and carboxylic acid functional groups, are ideal hosts for the incorporation of a large variety of metal nanoparticulate catalysts such as palladium (Pd) and gold (Au).

The catalytic behavior of the synthesized metal containing microgels was studied through a model hydrogenation reaction<sup>75</sup> (Figure 5.7).

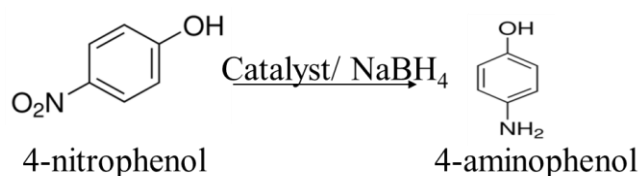


**Figure 5.7.** Model hydrogenation reaction.

For this purpose, 12 mg of the microgel suspension, (PDEA/Au (1.5 % w/w in Au) or PMMA/Pd (1.5 % w/w in Pd)) were added to 5 mL aqueous solution of 4-nitrophenol (4-NP) (5mM). Subsequently, the above solution was mixed with 2.5 mL fresh NaBH<sub>4</sub> solution (0.1 M). The excess of NaBH<sub>4</sub> is used to protect the as-prepared 4-AP from aerial oxidation compared with 4-NP and catalyst.<sup>34,76</sup> The reaction was carried out at ambient conditions with continuous stirring.<sup>76</sup>

Parts of the mixture were taken out at different time intervals and after filtration, their catalytic activity was calculated with UV–vis absorption spectra.<sup>76</sup> The results were crosschecked with the NIST (National Institute of Standards and Technology) Chemistry WebBook. The calibration curve was constructed from known concentrations of 4-NP with NaBH<sub>4</sub>. In order to optimize the system, the reaction was performed at various pH values. The hydrogenation reaction was also performed, without the addition of the microgels, as a control experiment.

## 5.3. Results and Discussion

### 5.3.1. Characterization of metal containing microgels

The swelling behavior of the synthesized pH-sensitive microgels based on PDEAEMA and PAA was investigated by DLS. The hydrodynamic radius of the microgels was measured at two different pH values, when the particles are neutral and when the ionizable groups were fully charged. The shape and the morphology of the microgel particles were studied by FE-

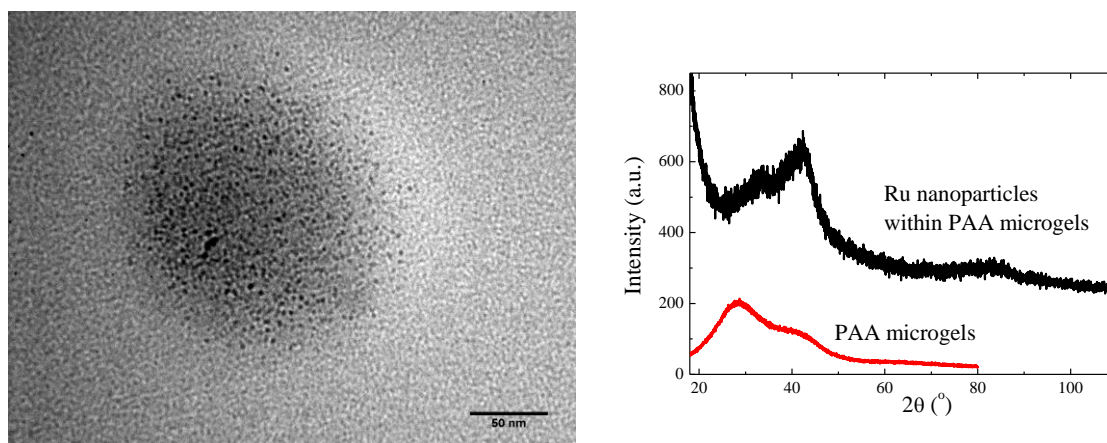
SEM. The characterization data for the PDEAEMA and PAA microgels as well as PMAA microgels are presented in Table 5.2.

**Table 5.2.** Characterization data for the synthesized pH-responsive microgels.

Functional microgel	$R_h$ at low pH (DLS) (nm)	$R_h$ at high pH (DLS) (nm)	Diameter (SEM) (nm)
PDEAEMA	278	180	210
PMAA	86	155	82
PAA	113	180	60

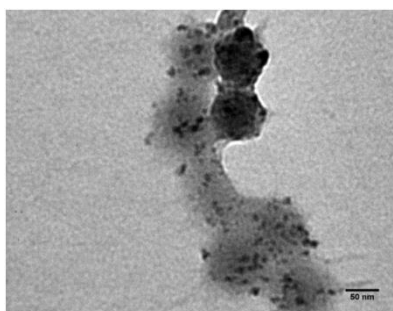
Moreover, TEM images (as in Figure 5.8 a) verified the formation of fairly monodispersed Pd nanoparticles with an average diameter of  $3.3 \pm 1.8$  nm embedded within the PDEAEMA microgels. The Pd loading of the PDEAEMA microgels was estimated by TGA to be ~13 wt %.

Figure 5.8 b shows the XRD patterns of the Ru-containing PAA microgel particles and their precursor PAA microgels. The appearance of the peak at  $2\theta = 44^\circ$  is characteristic of Ru nanocrystals confirming the successful formation of the Ru nanoparticles within the PAA microgels.



**Figure 5.8.** (a) TEM image of a PDEAEMA microgel containing Pd nanoparticles. The scale bar denotes 50nm. (b) XRD patterns of PAA microgels containing Ru nanoparticles and the precursor PAA microgels.

The hydrodynamic radius of the synthesized PMAA microgel particles, before and after the Pd nanoparticle formation, was found to be 160 nm and 164 nm at pH 3.5, respectively. The Pd content of the microgels was found 32 wt% by thermogravimetric analysis (TGA). Moreover, TEM analysis of the Pd nanoparticles containing PMAA microgels showed the presence of spherical metal nanoparticles with an average diameter of  $3.3 \pm 1.8$  nm (Figure 5.9).



**Figure 5.9.** TEM image of the PMAA microgels containing Pd nanoparticles. The scale bar denotes 50 nm.

### 5.3.2. Immobilization of microgels onto solid surfaces

- **Drop casting**

The microgel suspension was diluted to concentrations 0.01% wt. and 0.001% wt. in order to eliminate the formation of aggregates. Furthermore, to ensure that large agglomerates would not be present on the surfaces, suspensions were filtered with 1.2  $\mu\text{m}$  pore size syringe filters. Initially, the samples were prepared from suspension at pH below the pKa value of the polymer (PMAA). At these conditions, the hydrophobic character of the microgel particles dominate, so it was anticipated that particles would easily “escape” from the suspension and get anchored on the substrate surface. That was achieved but lead also to aggregate and multilayer formation.

Figure 5.10 depicts FE-SEM images of PMAA microgels (0.01% wt.) immobilized onto glass substrate with the drop casting method.

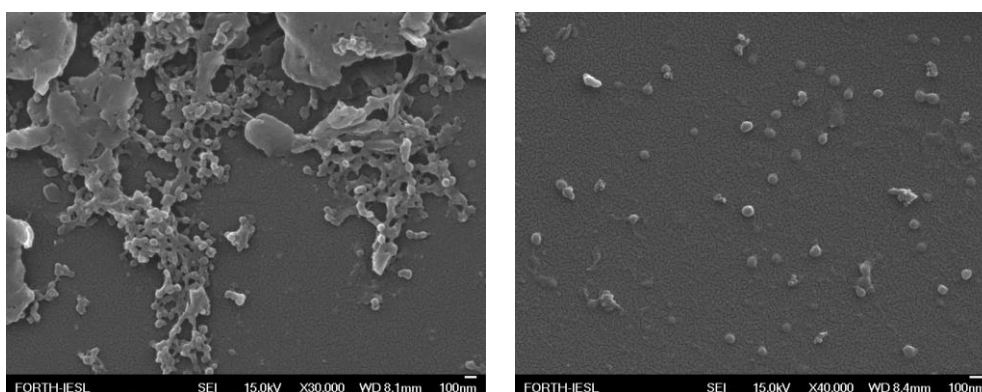


**Figure 5.10.** FE-SEM images of PMAA microgels (0.01% wt) on glass substrate using drop casting method.

Figure 5.10 revealed a non-uniform dispersion of the particles throughout the surface area. Regions containing aggregates that formed networks were observed together with individual particles. Reduction of the suspension concentration leads to a reduction of the aggregate formation together with an increase of the inter-particle distance for the individual particles.

Figure 5.11 presents FE-SEM images of PMAA microgels (0.001% wt.) immobilized onto glass substrate with the drop casting method. Both images have been taken from the same sample.

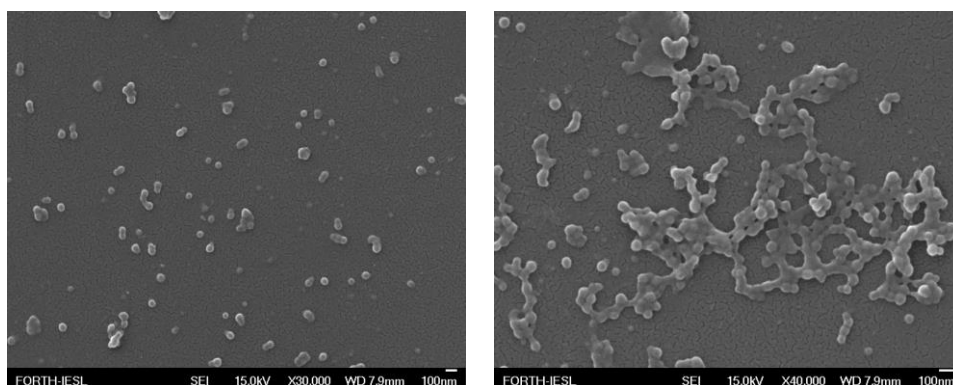


**Figure 5.11.** PMAA microgels (0.001% wt) on glass substrate using drop casting method.

According to Figure 5.11, dilution prevented the formation of large moieties but did not stop the formation of “network like” aggregates. The dendritic structures of aggregates that dominates at high concentrations (0.01% wt) seem to be replaced by less complicated structures (at concentration 0.001% wt), where the remaining dendritic aggregates coexist with larger numbers of individual microgel particles. At the same time regions containing mostly individual particles are increasingly evident although the number of polymeric microgels per unit area is significantly reduced.

Experiments are also performed using PMAA microgel suspension at pH above the  $pK_a$  value of the polymer. In this case, the PMAA chains are hydrophilic since monomers are negatively charged. As a result formation of aggregates was suppressed and individual microgel particles were dispersed on the substrate. The effect of pH value is shown in Figure 5.12.

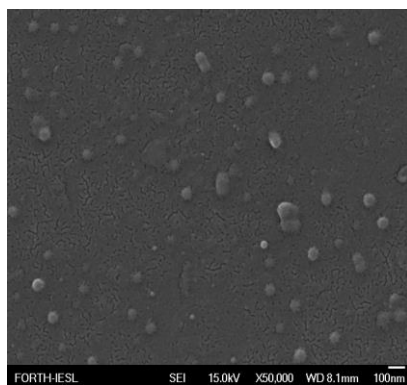


**Figure 5.12.** PMAA microgels anchored on glass substrate with drop casting method, prepared from suspensions with pH higher than the  $pK_a$  of PMAA at  $c=0.001\%$  wt.

At high pH, few microgels were attached individually onto the surface. Dendritic aggregates do not exist in this case.

In order to test the endurance and sustainability of the polymeric particles placed on the surface substrates were dipped in pure water for various periods of time (Figure 5.13).

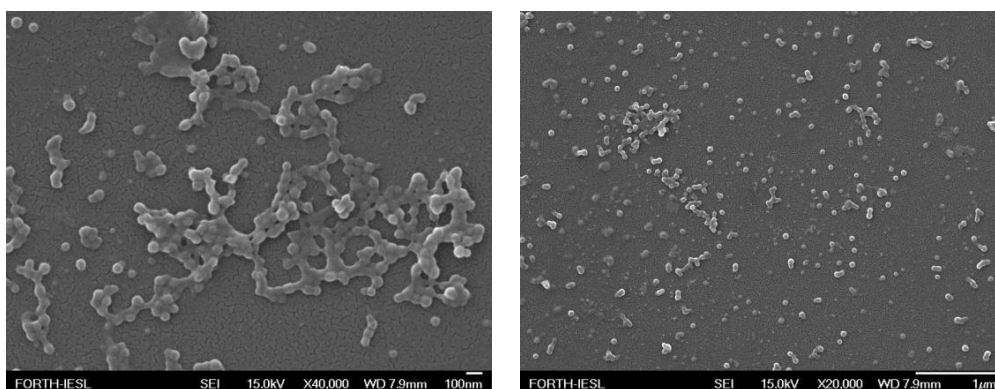


**Figure 5.13.** PMAA microgels (0.001% wt) on glass substrates before (left) and after (right) extra immersion in pure water for a period of two hours.

It is evident from the above FE-SEM images (Figure 5.13) that immersion of the substrates in pure water results in reducing the aggregates formed and enhancing the number of individual particles dispersed onto the surface. This could be explained if one assumes that the microgel particles are more loosely attached to one another than to the substrate surface. The presence

of pure water increases their mobility and favors their migration to other areas of the substrate or away from it (suspend in water).

- **Dip coating**

In dip coating, the substrate is submerged in the suspension vertically for about 1 minute and then slowly withdrawn, and left in ambient conditions to dry. Figure 5.14 presents FE-SEM images of PMAA microgels (0.01% wt) anchored on glass substrate, with the dip coating method.

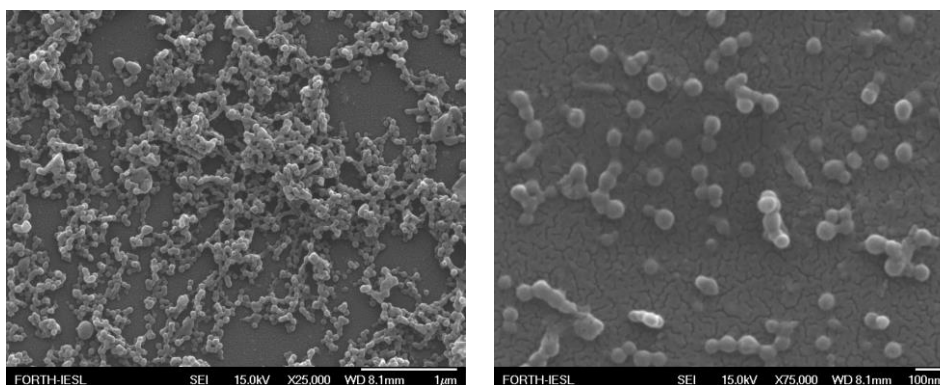


**Figure 5.14.** PMAA microgels (0.01% wt) on glass substrate using dip coating method.

The results are similar to the drop casting method. On the same substrate, aggregates co-exist with individual microgel particles. However, comparing the Figures 5.11 and 5.14, it seems that with dip coating, more microgels are being attached to the surface, either as aggregates or as individual particles.

The endurance and sustainability of the polymeric particles placed on surface were also tested in this case by dipping the substrates in pure water for various periods of time (Figure 5.15).

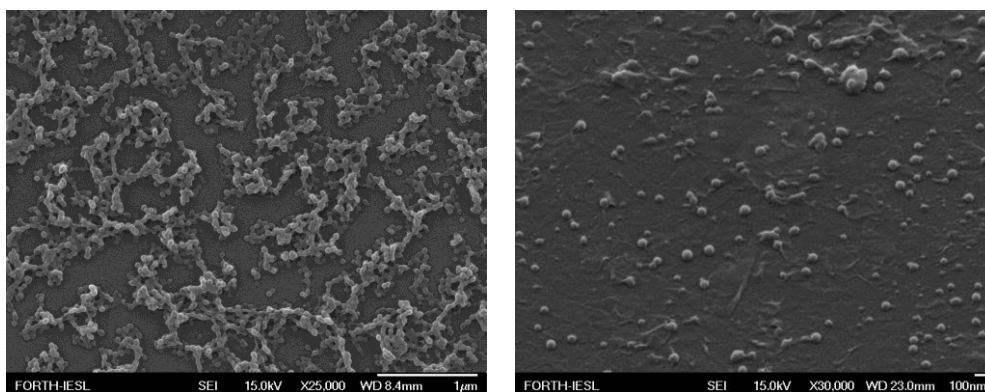


**Figure 5.15.** PMAA microgels (0.01% wt) on glass substrates before (left) and after (right) extra immersion in pure water for a period of two hours.

Figure 5.15 shows that few of the microgels remained after the immersion of the sample in the water. Both methods, drop casting and dip coating led to low homogeneity and multi-layer structures.

- **Pickering emulsion method**

The PAA microgels were deposited onto solid surfaces from their aqueous suspensions at microgel concentration 0.3% wt. The pH of the suspension was kept above the pKa value of PAA in order to enhance the hydrophilicity of the particles and have the microgels in a negatively charged state. It was observed that dipping or drop casting from “as prepared” suspensions lead to low homogeneity and revealed the tendency of the microgels to form dendritic aggregates on the surfaces. In order to form ultra-thin films and increase homogeneity, the Pickering emulsion method was utilized.<sup>68</sup> In this process, microgels are being segregated-compressed at a hexane-water interface using ethanol as an inducer. Reduction of the suspension concentration led to a reduced number of microgels on the surface and, thus, to an increase of the inter-particle distances. This is illustrated in Figure 5.16, which shows PAA microgel particles deposited on glass substrates from their aqueous suspensions at concentrations 0.34% wt. and 0.035% wt.

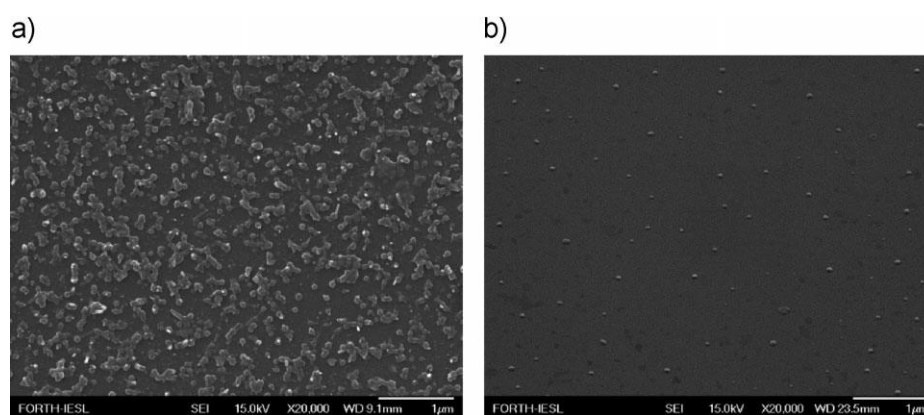


**Figure 5.16.** PAA microgels deposited onto glass substrates utilizing the Pickering emulsion method. The suspension concentrations were (a) 0.35% wt. and (b) 0.035% wt.

Additional factors that should be taken into account in order to obtain a thin homogeneous film are the amount of ethanol and its injection rate. The addition of ethanol to the suspension gradually decreases the surface charge, very likely because of competitive adsorption of ethanol molecules.<sup>68</sup> Increasing the amount of ethanol added to the PAA suspension from 5% wt. to 50% wt., led to significant increase of the number of particles per unit area and a respective decrease of the inter-particle distances; further addition of ethanol led to the formation of aggregates (Figure 5.17).

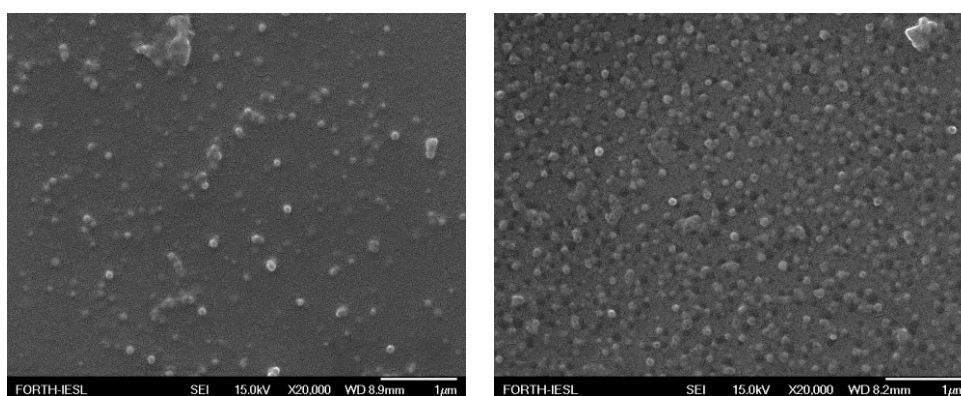


**Figure 5.17.** PAA deposited onto glass substrates utilizing the Pickering emulsion method with the addition of 5% wt. (left) and 50% wt. (right) of ethanol.

The type of substrate dipping affected the dispersion of the PAA microgels as well. Horizontal dipping proved to be more promising as it led to a better dispersion of the particles onto the surface and reduced inter-particle distances, as illustrated in Figure 5.18.

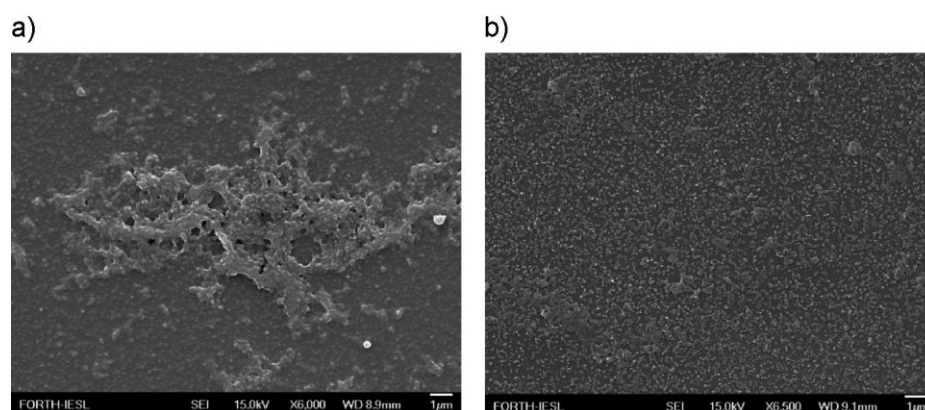


**Figure 5.18.** PAA deposited onto glass substrates utilizing the Pickering emulsion method and (a) vertical and (b) horizontal dipping.

The dispersion of the PAA microgels onto the surfaces was compared with that of hydrophilic hard silica particles (Figure 5.19) of comparable size and suspension concentration; in both cases the Pickering emulsion method was utilized with horizontal dipping. Such comparison illustrates the soft character of the PAA microgels, which are seen (Figures 5.17, 5.18) as “laying down” onto the glass surface as opposed to the silica particles which are “sitting onto” the surface (Figure 5.19) due to their hard sphere behavior. This “laying down” may also explain the limited mobility of the PAA microgels on the surface and, thus, their larger inter-particle distances and the lack of a well-defined layer.

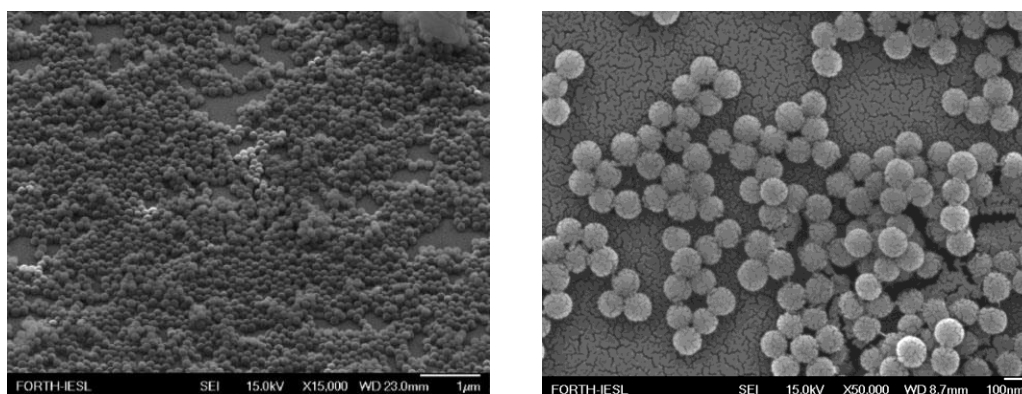


**Figure 5.19.** Silica particles deposited onto glass substrate from an aqueous suspension at 0.35% wt. using the Pickering emulsion method.

The deposition of the metal nanoparticles containing microgels onto surfaces was also investigated. Figure 5.20 shows PDEAEMA microgels with Pd-nanoparticles onto a glass substrate prepared from a suspension in water (0.3% wt.), similar to that used for the deposition of the neat microgels.

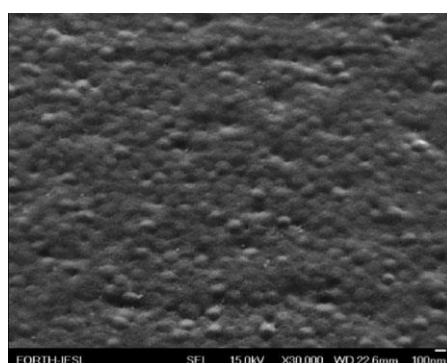


**Figure 5.20.** FE-SEM image of Pd-containing PDEAEMA microgels on a glass substrate.

The metal-loaded microgels form a close-packed structure. Moreover, FE-SEM images revealed that the metal nanoparticle loaded microgels seem to shrink when compared with those before metal nanoparticle formation, which could be attributed to ion re-organization inside the microgels due to the existence of the metal nanoparticles. The dispersion of the polymer microgels onto the surfaces was tested for stability and endurance. Figure 5.21 shows

typical FE-SEM images of PDEAEMA microgels loaded with Pd metal nanoparticles following rinsing with pure water or immersion in pure water for an extended period of time.

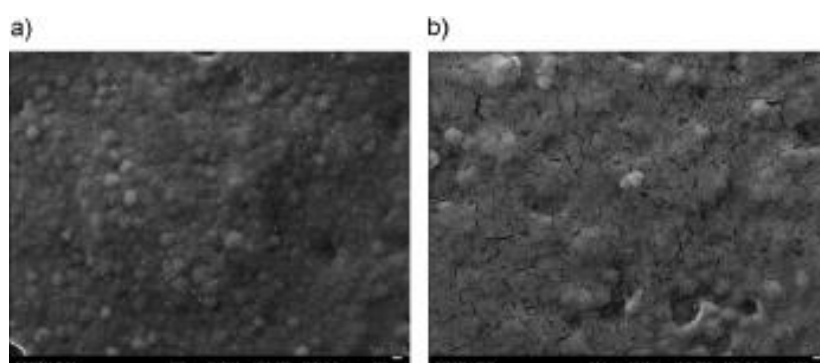


**Figure 5.21.** Pd-containing PDEAEMA microgels on a glass substrate following rinsing with water (a) and after immersion in water for 24h (b).

It is evident from Figure 5.21, that the microgels remain attached onto the substrate even after 24h immersion in water. The interparticle distance is similar to that before rinsing with water, which illustrates that the microgels are not only well anchored onto the substrate but also have the tendency to be “glued” with their neighbors.

Following the study of PDEAEMA/Pd coated surfaces, PAA microgels containing Ru nanoparticles were immobilized onto glass substrates. Suspensions in water were prepared at concentration (0.3% wt) similar to the suspension used for the non-loaded microgel suspensions.

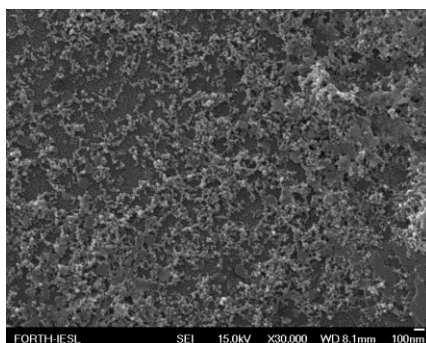


**Figure 5.22.** PAA-Ru microgels dispersed on glass (left) using the Pickering emulsion method.

Images taken in FE-SEM (Figure 5.22), show that the polymeric carriers formed dendritic aggregates similar with the one formed by the polymeric PMAA microgel particles. The size of the observed particles was significantly reduced compared with the polymeric particles in the absence of the metal nanoparticles. For the metal-containing microgels the size was around 20 nm, whereas for the pure polymeric microgel particles the size was about 60 nm. This could be attributed to charge re-organization inside the microgel because of the presence of metal nanoparticles that caused the shrinkage of the particles. Note that the microgel particles are electrostatically stabilized in the present case. The addition of Ru nanoparticles could cause the “neutralization” of the stabilizer and therefore permit the formation of aggregates with dendritic shape.

The polymeric microgel particles loaded with Ru nanoparticles were tested for stability and endurance when immersed in pure water for extended periods of time, varying from 1 hour to 24 hours. The substrate used was glass, which was left to dry in air at room temperature and then examined with FE-SEM. Figure 5.23 shows images of PAA microgels loaded with Ru nanoparticles as prepared ( $c=0.3\%$  wt) and after they are left immersed in water.

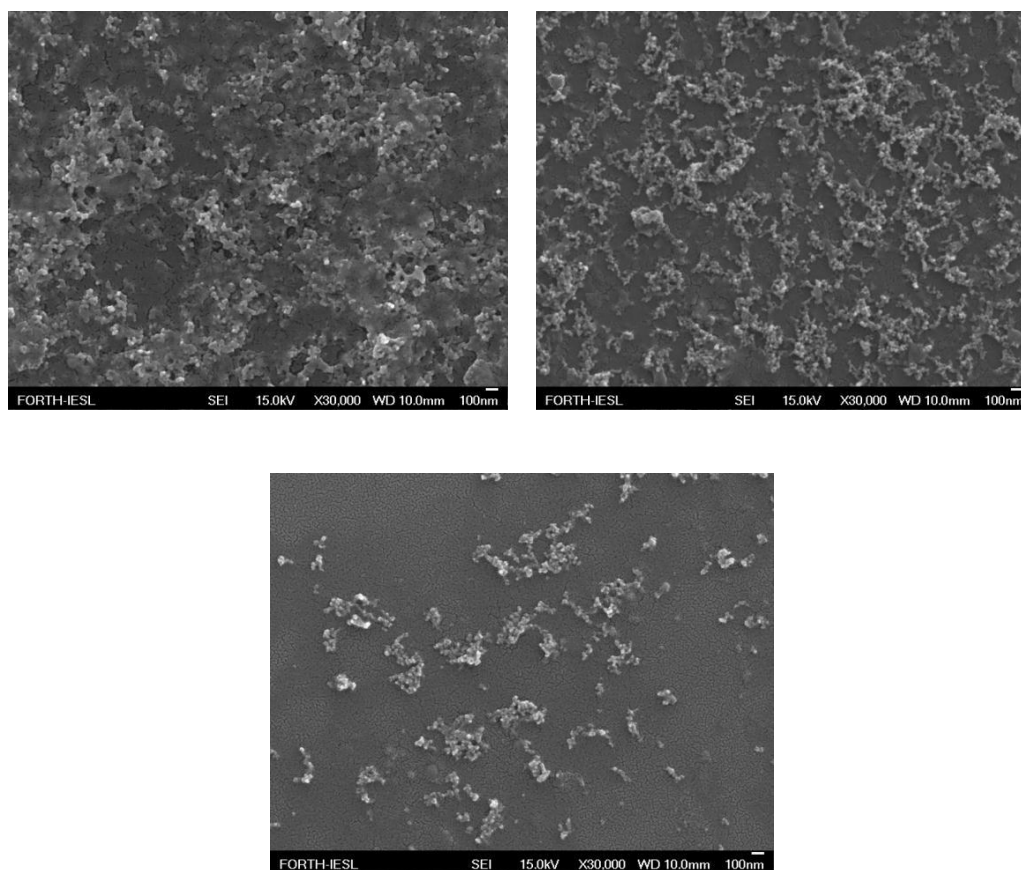


**Figure 5.23.** PAA-Ru microgel polymeric particles immersed in water for various time intervals; As prepared (upper left), 1 hr (upper right), and 24 hrs (lower).

One can see that after immersion for 1 hour in pure water the dispersion pattern seems to remain unaffected. The particles still form the dendritically shaped aggregates and there is no significant difference as the number of particles per unit area is concerned. When moving to 24 hours of immersion in water it is obvious that a number of particles have been removed from the substrate as a result of the mobility that was induced to the particles from the solvent present. It seems that it is preferable energetically for some particles to leave the substrate and be re-suspended in water.

- **Vortical surface method**

During dipping of the surface, inevitably, it passes through the layer of hexane which could cause some alteration to the dispersion of the microgel particles. In order to clarify this, a second method for trapping the particles to an interface was utilized, using vortex as the driving force. FE-SEM images, taken from samples prepared using the vortical surface method, are shown in Figure 5.24.

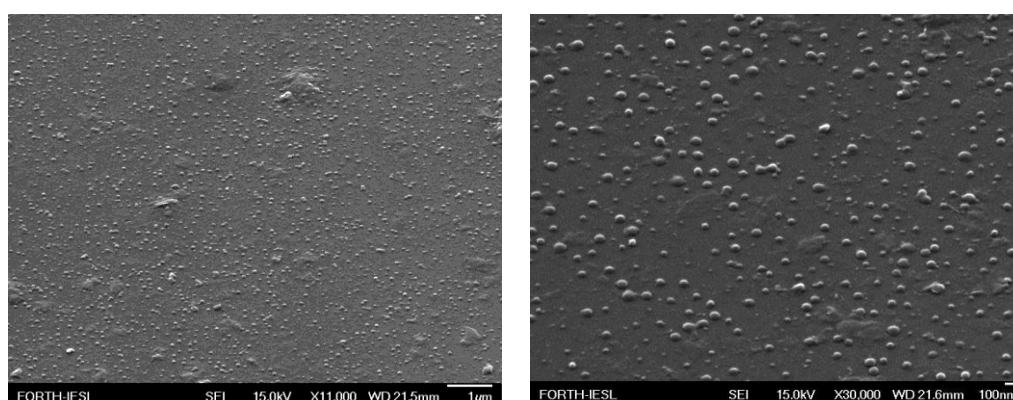


**Figure 5.24.** PAA microgel particles on a glass surface ( $c=0.35\%$  wt) using the vortical surface method.

As one can see comparing Figures 5.18 and 5.24 the results are similar if not better for the case of Pickering emulsion, meaning that possible presence of tiny amount of hexane does not cause any negative effect at the distribution of the microgel particles on the solid surface.

The same procedure was repeated for the Ru-containing PAA microgels. The results are shown in Figure 5.25.

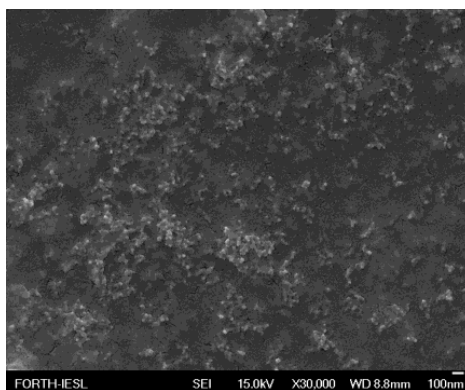


**Figure 5.25.** PAA-Ru microgels dispersed on glass substrate, using the vortical surface method.

Comparing the Figures 5.23 and 5.25, one cannot observe any significant difference. Images taken with FE-SEM (Figure 5.25), show that the polymeric carriers formed dendritic aggregates similar with the one formed by the Pickering emulsion method.

- **Amine coupling method**

PMAA microgels, with and without the Pd metal nanoparticles, were covalently immobilized onto glass substrates from their aqueous dispersions at a concentration of 0.07 wt%, according to the procedure described in the experimental part. The distribution of the microgels on the substrates was studied by Field-Emission Scanning Electron Microscopy (FE-SEM).

The SEM images shown in Figure 5.26 confirm that, both the PMAA and Pd nanoparticle containing PMAA microgels were immobilized onto the glass surfaces and the grafted microgel layer covers the substrate uniformly and homogeneously. Furthermore, when comparing the images for the microgels with and without the metal nanoparticles, one can conclude that there is no significant difference in the microgel packing density due to the presence of the Pd nanoparticles within the microgels.

In order to verify the stability of the microgel layers on the substrates, the samples were subjected to stability tests either by changing the environmental conditions or by the flow of

pure water on the substrate. First, the samples were rinsed with de-ionized water in a flow rate of  $2.1 \cdot 10^{-5} \text{ m}^3/\text{s}$ . Figure 5.27 shows FE-SEM images of Pd / PMAA samples after rinsing with 2 L and 10 L of water.

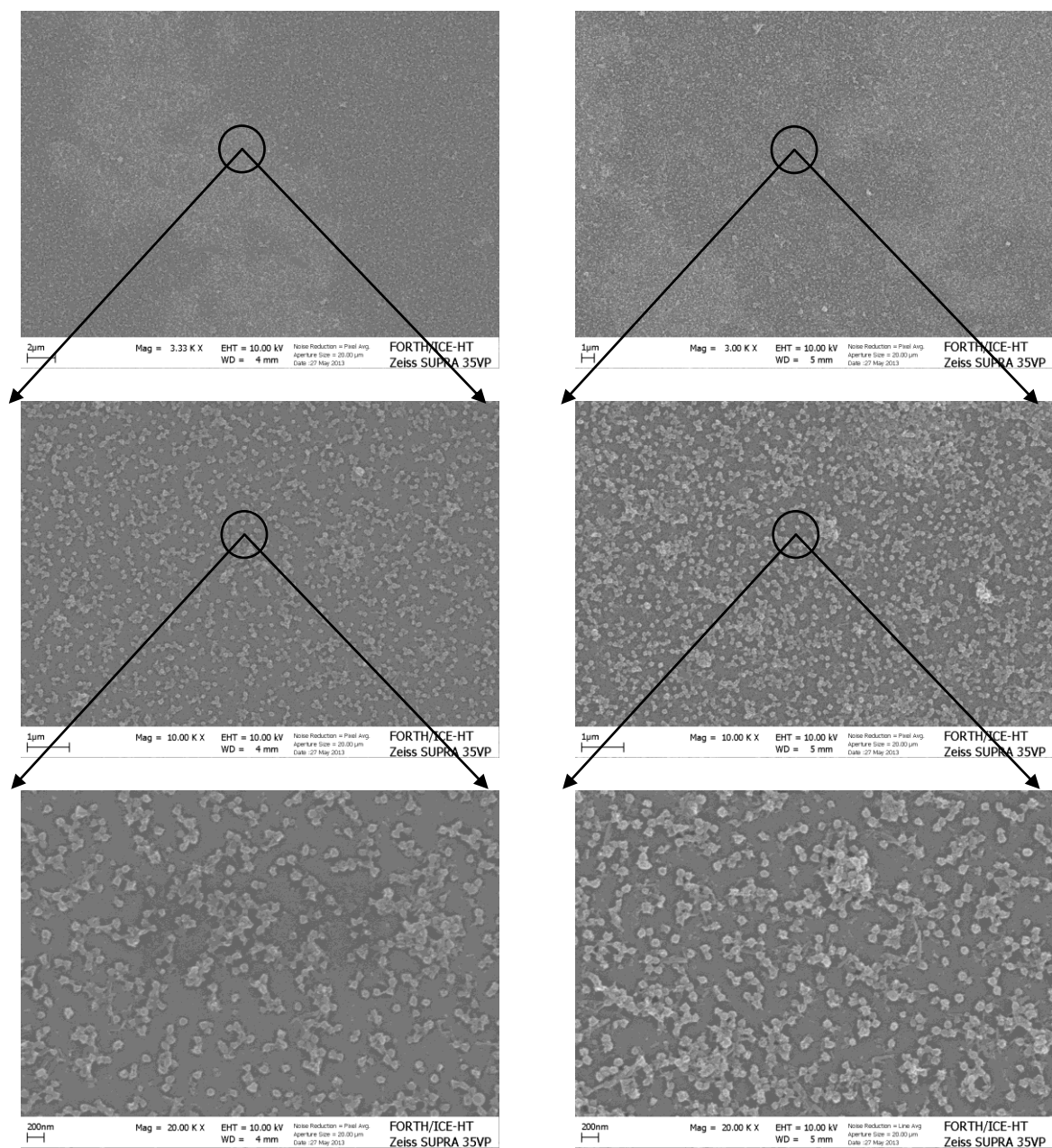


**Figure 5.26.** FE-SEM images of PMAA microgels (left column) and Pd containing PMAA microgels (right column) covalently bound onto glass substrates at three different magnifications (3.33 KX, 10.00 KX and 20.00 KX).

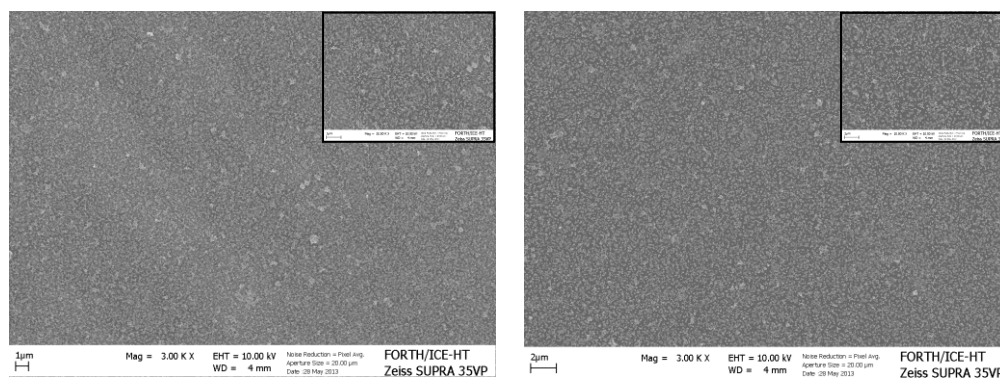


**Figure 5.27.** FE-SEM images of the Pd nanoparticle containing PMAA sample rinsed with 2 L of water (left) and 10 L of water (right). The insets are higher magnification images.

By comparing Figures 5.26 and 5.27, it can be justified that the surface concentration of anchored microgels did not decrease upon rinsing with water and thus the microgels were not detached from the substrate surface.

Next, the samples were immersed in pH 8 aqueous solutions for 24 h to investigate the effect of the solution pH on the anchoring of the microgels. In parallel, different samples were subjected to temperature tests. For this reason, substrates with chemically bound microgels were heated at 40°C and 80°C for 4 to 24 h and the stability of the anchored microgels was studied with FE-SEM. Figures 5.28 to 5.31 show FE-SEM images of the samples after immersing at high pH and high temperature aqueous solutions.

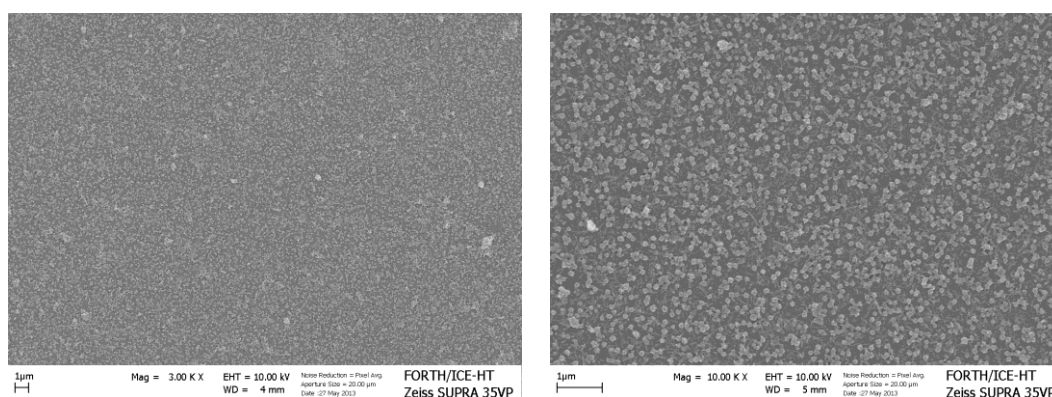


**Figure 5.28.** FE-SEM images of Pd nanoparticle containing PMAA microgels anchored on glass substrates after heating at 40°C for 4 h (left) and heating at 40°C for 4 h and rinsing with 2 L of de-ionized water (right).

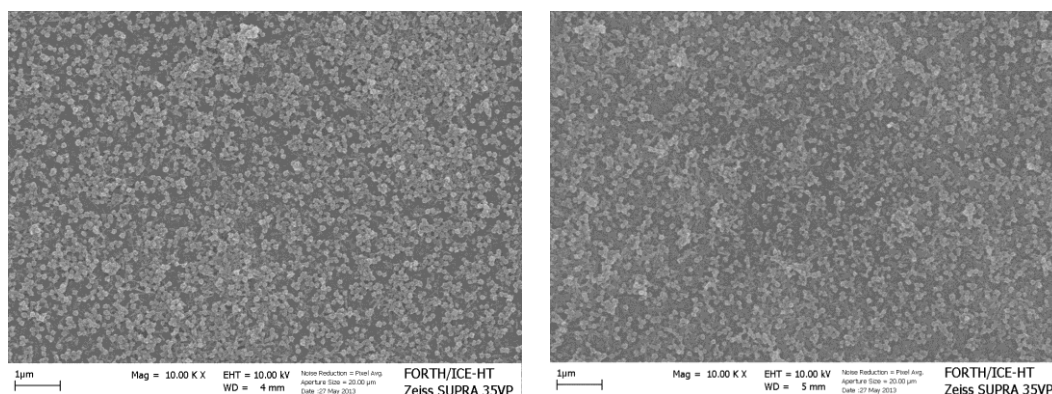


**Figure 5.29.** FE-SEM images of Pd nanoparticle containing PMAA microgels anchored on glass substrates after heating at 40°C for 24 h (left) and heating at 40°C for 24 h and rinsing with 2 L of de-ionized water (right).

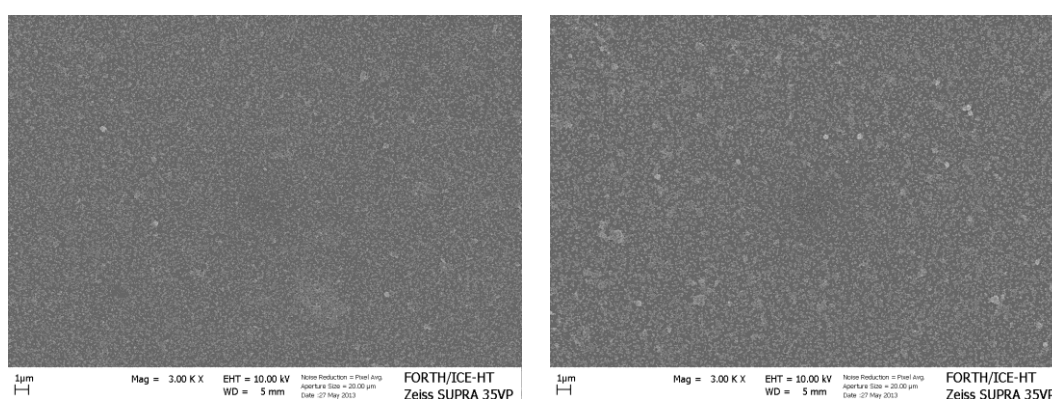


**Figure 5.30.** FE-SEM images of Pd nanoparticle containing PMAA microgels anchored on glass substrates after heating at 80°C for 24 h and heating at 80°C for 24 h and rinsing with 2 L of de-ionized water.

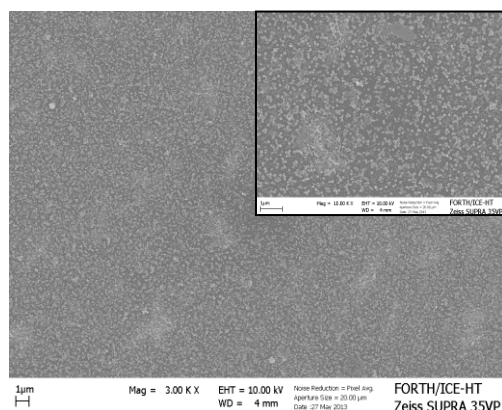


**Figure 5.31.** FE-SEM images of Pd nanoparticle containing PMAA microgels anchored on glass substrates after immersion in high pH water for 24 h. The insets show FE-SEM images from the same samples at higher magnification.

From Figures 5.26 and 5.28 to 5.31, it can be concluded that the anchoring of the microgels is not affected by the solution conditions and the microgel particles remain attached onto the substrate and maintained their original shape and size. This suggests that the covalently bound microgels are strongly anchored on the substrate and retain their characteristics at different pH and temperature values. The measurements were repeated in triplicates to assess the reproducibility of the results.

Figure 5.32 shows the image of a substrate after the combination of all the tests.

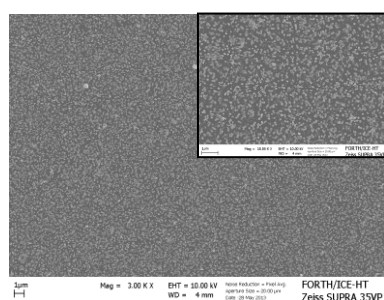


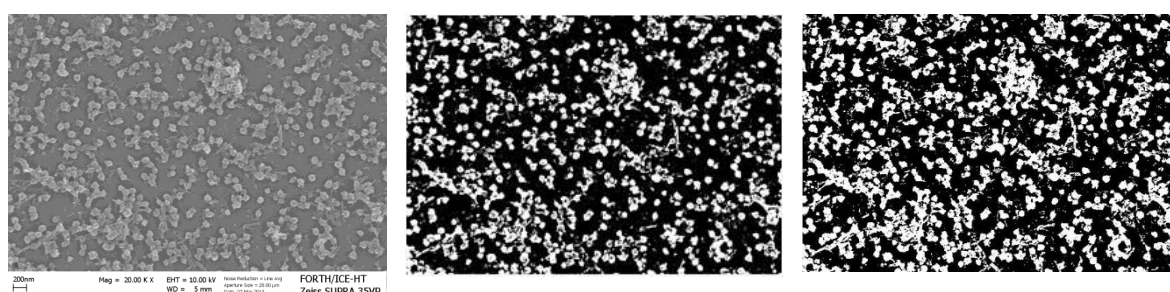
**Figure 5.32.** FE-SEM image of a sample after immersion in pH, heated at 80°C and rinsing

with water flow. Inset is the sample at higher magnification.

Even after combining the effect of solution pH and temperature and rinsing with 2 L water the area occupied by the particles is similar to that of the as-prepared sample, verifying the strong attachment of the microgels on the substrates.

### 5.3.3. Determination of microgels density, before and after the stability tests with Image J and Matlab code

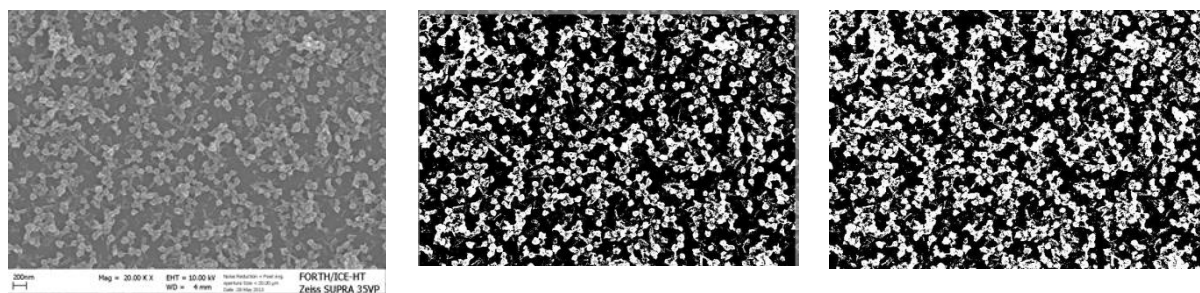
In order to verify the stability of the microgel layers on the surface substrates, the FE-SEM images were analyzed with ImageJ and the density of the particles before and after the rinsing with water was quantified. For this purpose, the images were converted to binary images using ImageJ, by selecting the same threshold in all cases. Before the segmentation, pixel values of the images were converted into micrometers unit using the scale factor. All the calculations were repeated with a Matlab code to test the reliability of the results. The segmentation of the FE-SEM image of the Pd nanoparticle containing PMAA sample (as prepared), is depicted in Figure 5.33.



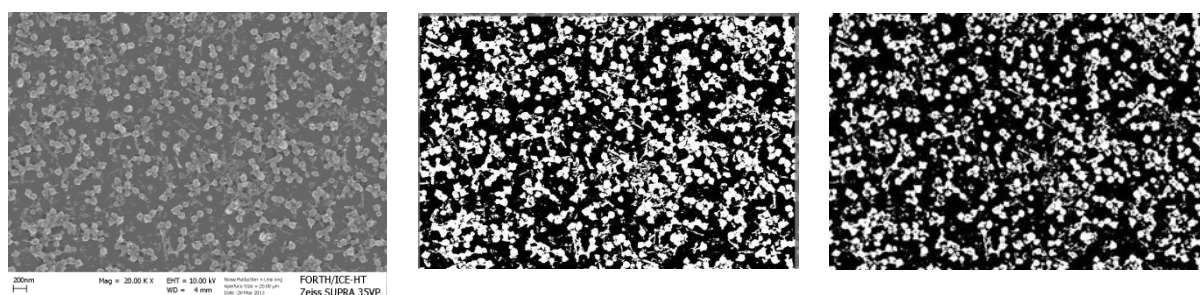
**Figure 5.33.** FE-SEM images of the Pd containing PMAA microgels anchored on a glass substrate: (left) original FE-SEM image, (center) after transformation to the binary image

with ImageJ and (right) after transformation using a Matlab code.

Figure 5.34 and 5.35 depict the FE-SEM images of the Pd containing PMAA microgels anchored on a glass substrate after rinsing with 2 L and 10 L of water respectively.

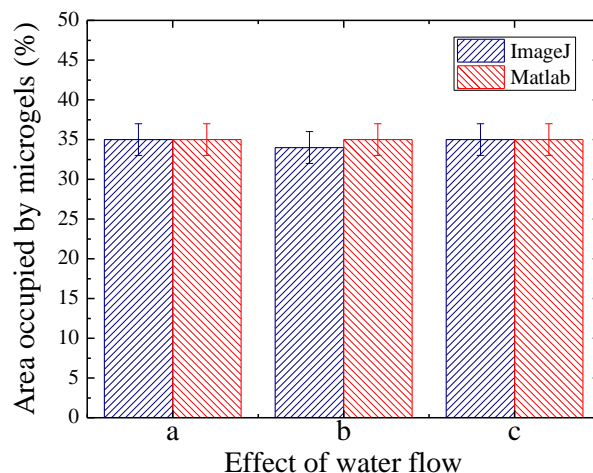


**Figure 5.34.** FE-SEM images of the Pd containing PMAA microgels anchored on a glass substrate after rinsing with 2 L of water: (left) original FE-SEM image, (center) after transformation to the binary image with ImageJ and (right) after transformation using a Matlab code.



**Figure 5.35.** FE-SEM images of the Pd containing PMAA microgels anchored on a glass substrate after rinsing with 10 L of water at 20.00K X magnification: (left) original image, (center) after transformation to the binary image with ImageJ, (right) after transformation using a Matlab code.

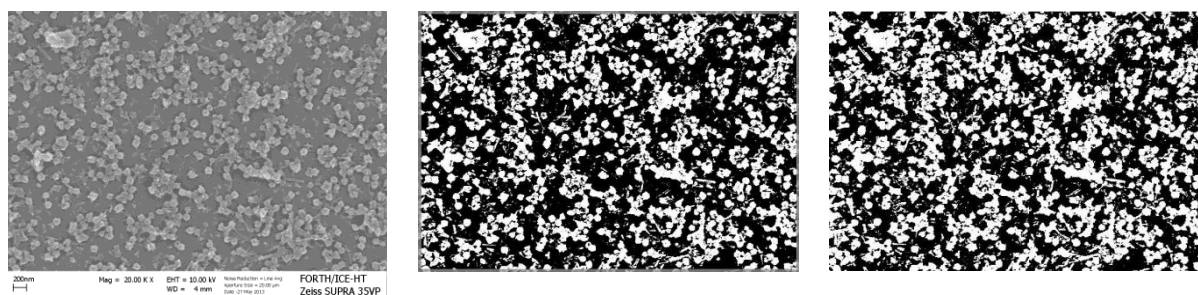
The microgels in the binary 8-bit grayscale images appear as white on a black background with specific intensity values 0 and 255, respectively. Thus, by calculating the white/black area ratio, the fractional area occupied by the microgel particles can be determined (Figure 5.36), which corresponds to the surfaces concentration of the microgel particles.



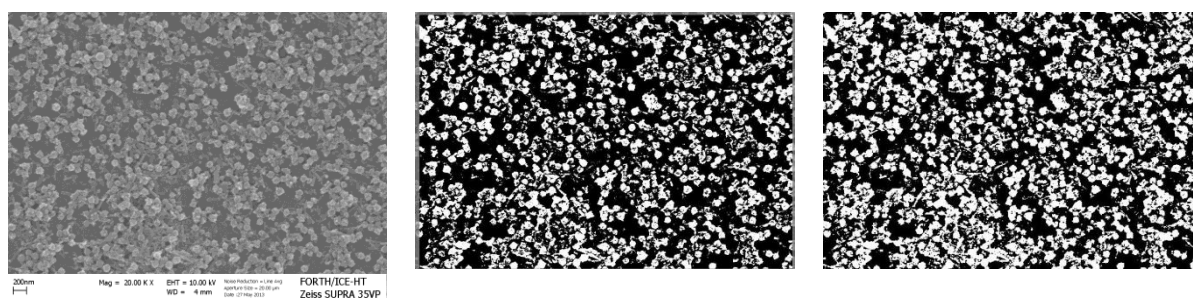
**Figure 5.36.** Histogram of the area occupied by the microgels: for the a) as prepared sample, (b) after rinsing with 2 L of water and (c) after rinsing with 10 L of water. The images were analyzed with ImageJ and a Matlab code.

Figure 5.36 shows that the area occupied by the microgels before the stability test is approximately  $35 \pm 2\%$  using both methods, ImageJ and Matlab. The number density of the particles was calculated to be  $\sim 220$  microgels/ $\mu\text{m}^2$ . Moreover, the surface density of microgels after rinsing with water is approximately unchanged, which confirms that the particles are stably anchored on the substrate and they remained attached despite the shear from the water flow.

Similar samples were immersed in pH 8 aqueous solutions for 4 to 24 h to investigate the effect of the solution pH on the anchoring of the microgels. In parallel, different samples were subjected to temperature tests. For this reason, substrates with chemically bound microgels were heated at  $40^\circ\text{C}$  and  $80^\circ\text{C}$  for 4 to 24 h and the stability of the anchored microgels was studied with FE-SEM. Figures 5.37 and 5.38 show the images, before and after the surface analysis, for the anchored microgels heated at  $40^\circ\text{C}$  for 24 h, after rinsing with water.



**Figure 5.37.** FE-SEM images of the Pd containing PMAA microgels anchored on a glass substrate after heating at 40°C for 24 h at 20.00K X magnification: (left) original image, (center) after transformation to the binary image with ImageJ, (right) after transformation using a Matlab code.



**Figure 5.38.** FE-SEM images of the Pd containing PMAA microgels anchored on a glass substrate after heating at 40°C for 24 h and rinsing with 2 L of water at 20.00K X magnification: (left) original image, (center) after transformation to the binary image with ImageJ, (right) after transformation using a Matlab code.

The surface analysis of the Figures 5.37 and 5.38, are summarized in the histogram of the Figure 5.39.

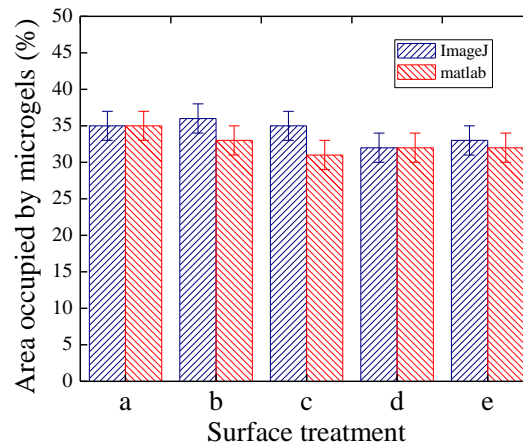


**Figure 5.39.** Histogram of the area occupied by the Pd nanoparticle containing microgels for a) the as prepared sample, b) after heating to 40°C for 4 h, c) after heating to 40°C for 4 h and rinsing, d) after heating to 40°C for 24 h and e) after heating to 40°C for 24 h and rinsing.

According to the surface analysis with both methods, the microgels remained attached despite the heating at 40°C and the extra rinsing with water in each case. The minimum surface ratio calculated, was find to be  $31\pm 2\%$ , with the as-prepared sample to have  $35\pm 2\%$ . The difference between the two values is not significant, as the error bars are overlapping.

As a next step, the samples were heated at 80°C for 4 h, before and after rinsing with water. The results are depicted in Figures 5.40 and 5.41 respectively.

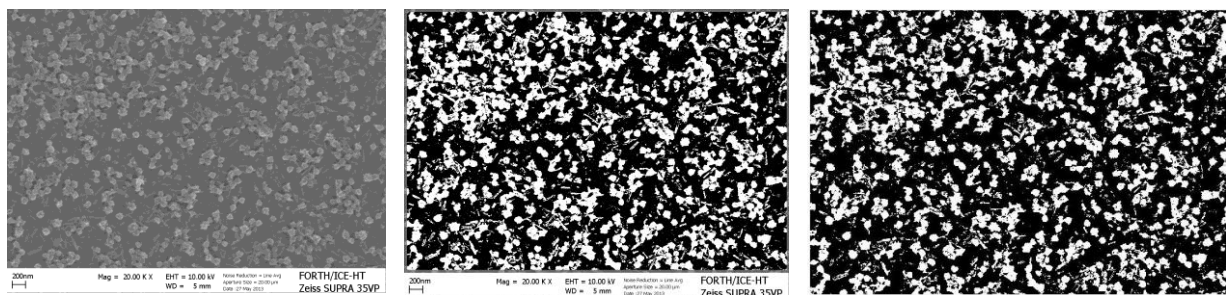


**Figure 5.40.** FE-SEM images of the Pd containing PMAA microgels anchored on a glass substrate after heating at 80°C for 4 h at 20.00K X magnification: (left) original image, (center) after transformation to the binary image with ImageJ, (right) after transformation using a Matlab code.

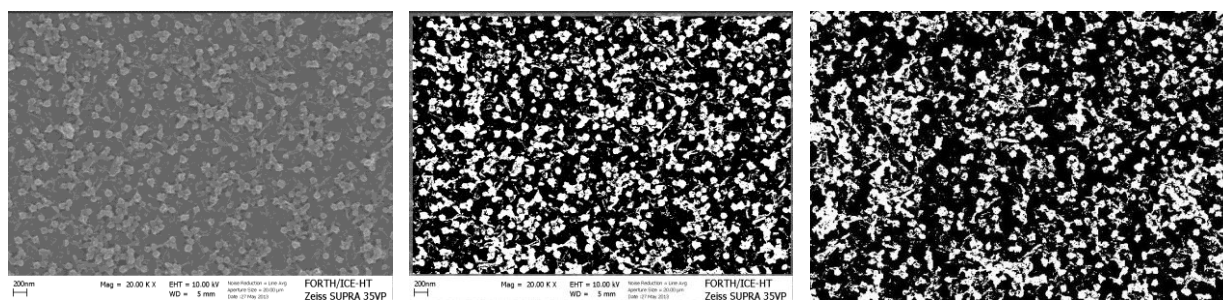


**Figure 5.41.** FE-SEM images of the Pd containing PMAA microgels anchored on a glass substrate after heating at 80°C for 4 h and rinsing with 2 L of water at 20.00K X magnification: (left) original image, (center) after transformation to the binary image with ImageJ, (right) after transformation using a Matlab code.

Afterwards, the samples were heated at 80°C for 24 h and the results are depicted in Figures 5.42 and 5.43.

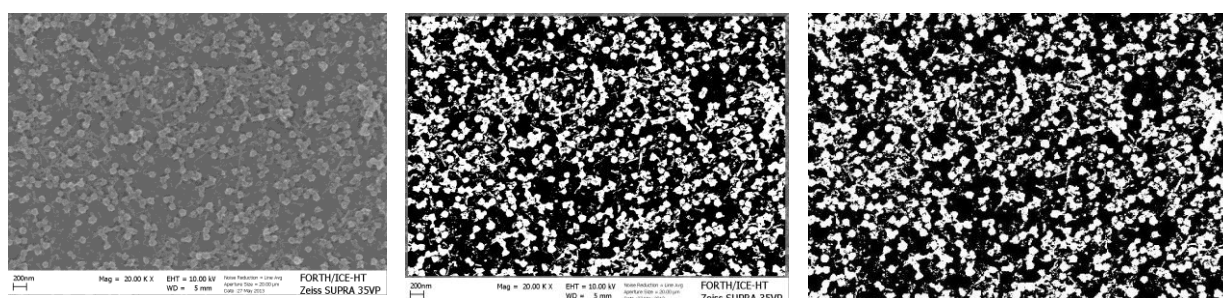


**Figure 5.42.** FE-SEM images of the Pd containing PMAA microgels anchored on a glass substrate after heating at 80°C for 24 h at 20.00K X magnification: (left) original image, (center) after transformation to the binary image with ImageJ, (right) after transformation using a Matlab code.

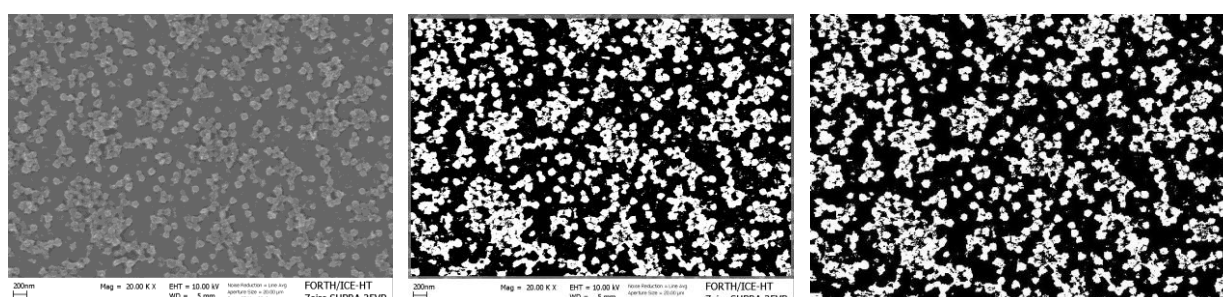


**Figure 5.43.** FE-SEM images of the Pd containing PMAA microgels anchored on a glass

substrate after heating at 80°C for 24 h and rinsing with 2 L of water at 20.00K X magnification: (left) original image, (center) after transformation to the binary image with ImageJ, (right) after transformation using a Matlab code.

The surface analysis of the Figures 5.40 to 5.43, are summarized in the histogram of the Figure 5.44.

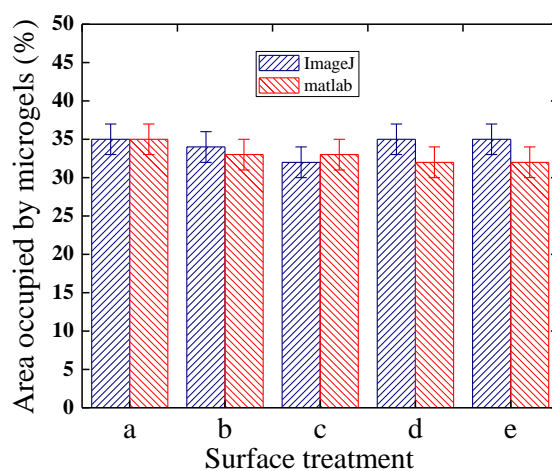


**Figure 5.44.** Histogram of the area occupied by the Pd nanoparticle containing microgels for a) the as prepared sample, b) after heating to 80°C for 4 h, c) after heating to 80°C for 4 h and rinsing, d) after heating to 80°C for 24 h and e) after heating to 80°C for 24 h and rinsing.

Figure 5.44 proves the covalent attachment of Pd/PDEAEMA microgels, as they survived the temperature stability tests. They remained well anchored on the surface even after heating at 80°C for 24 h and rinsing with de-ionized water, which confirms the effectiveness of the amine coupling method.

After the heating tests, the samples were subjected to pH stability tests. The surface analysis of the samples after immersion in high and low pH solutions for 24 h, is depicted in the Figure 5.45.

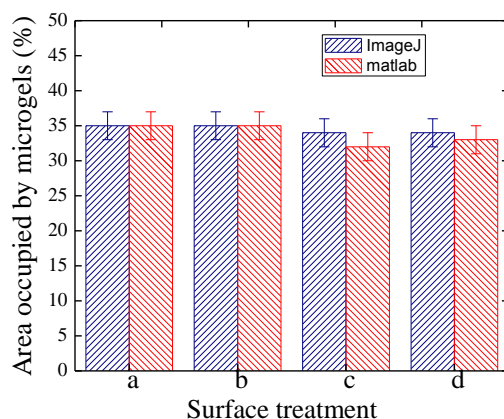


**Figure 5.45.** Histogram of the area occupied by the Pd nanoparticle containing microgels after a) immersion at low pH for 24 h, b) immersion at low pH for 24 h and rinsing, c) immersion at high pH for 24 h, and d) immersion at high pH for 24 h and rinsing.

Figure 5.45 shows that the pH does not affect the anchoring of the microgels. Next, the samples were subjected to combined stability tests (pH and temperature, pH and rinsing with water, temperature and rinsing with water, and pH, temperature and water rinsing). Figure 5.46 depicts the results for these combined stability tests.

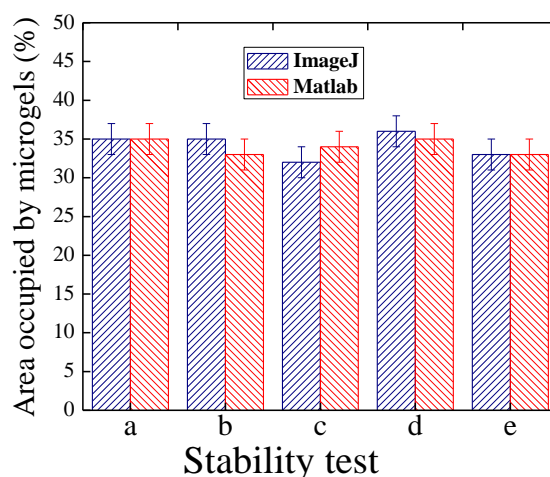


**Figure 5.46.** Histogram of the area occupied by the microgels for a) the as prepared sample b) after immersion in pH 8 and heating at 80°C, c) after immersion in pH 8 and rinsing with 2 L water, d) after heating at and rinsing with water and e) after immersion in pH 8, heating at 80°C and rinsing with 2 L water.

Figure 5.46 is the strongest evidence, supporting the efficiency of the amine coupling method in the anchoring of the functionalized microgels. Even after the application of combined stability tests (pH, temperature, water flow), the area occupied by the microgels, is approximately the same. So, this method, can be successfully applied for the development of micro-reactors, utilized for the performance of reactions under flow conditions.

#### 5.3.4. Catalytic activity of metal containing microgels on a model hydrogenation reaction

The catalytic activity of PDEA/Au and PMAA/Pd nanoparticles was investigated by a model hydrogenation reaction of reducing 4-nitrophenol (4-NP) into 4-aminophenol (4-AP) in the presence of Sodium borohydride ( $\text{NaBH}_4$ ). The excess of  $\text{NaBH}_4$  is used to protect the as-prepared 4-AP from aerial oxidation compared with 4-NP and catalyst.<sup>34,76</sup> The reaction was carried out under ambient temperature and pressure conditions with continuous stirring. At the end of the reaction centrifugation of the samples was performed in order to precipitate the

microgels. Ultraviolet-visible spectroscopy (UV-Vis) was utilized to determine the decreasing concentration of 4-NP. The experimental details of the reaction, are described in the experimental part.

Initially standard aqueous solutions of 4-NP and 4-AP were measured with UV-Vis absorption spectrum. (Figure 5.47)

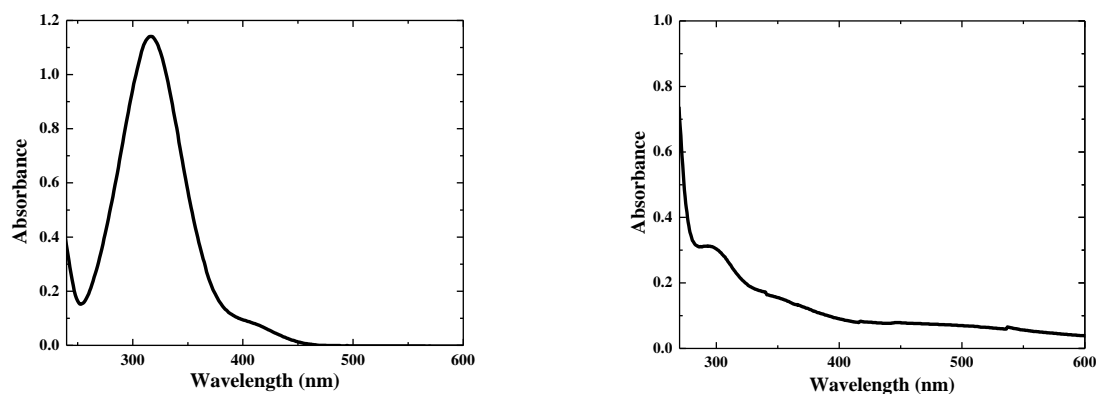


**Figure 5.47.** UV-Vis absorption spectrum for 4-NP in the absence of  $\text{NaBH}_4$  (left) and for 4-AP (right).

According to Figure 5.47, 4-NP shows a distinct spectral profile with an absorption maximum at 340 nm, while 4-AP at 300 nm. Following that, the calibration curve was constructed from known concentrations of 4-NP with  $\text{NaBH}_4$ . Comparing Figures 5.47 and 5.48, it is observed that with the addition of  $\text{NaBH}_4$ , there is a new peak of 4-NP at 400 nm, which is attributed to the absorption of 4-nitrophenolate anion.<sup>76</sup> The yellow-green color of the solution of 4-NP and  $\text{NaBH}_4$ , remains unaltered with time in the absence of the microgels. In other words, the reduction of 4-NP did not occur without the nanocatalysts.

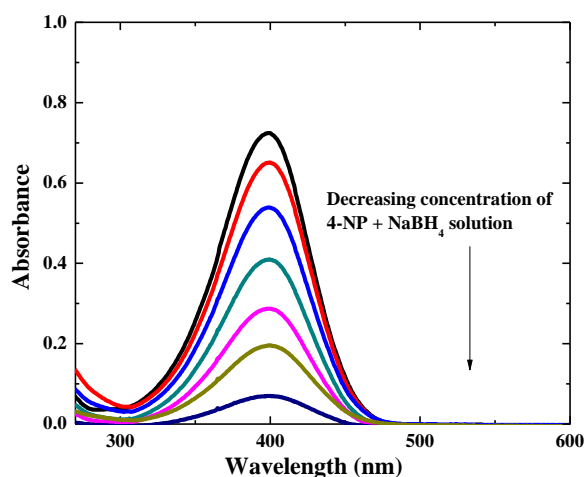


**Figure 5.48.** Calibration curve of a standard aqueous solution of 4-NP+NaBH<sub>4</sub>.

The reaction was performed at various pH values. However at high pH values of aqueous solutions the PDEA-Au nanocatalysts were not well dispersed and the reaction could not be performed. On the other hand, at low pH values, the peak of 4-NP was moved at a wavelength around 300nm (Figure 5.49). Comparing the Figures 5.47 and 5.49, the low pH make it difficult for the product 4-AP to be distinguished accurately.

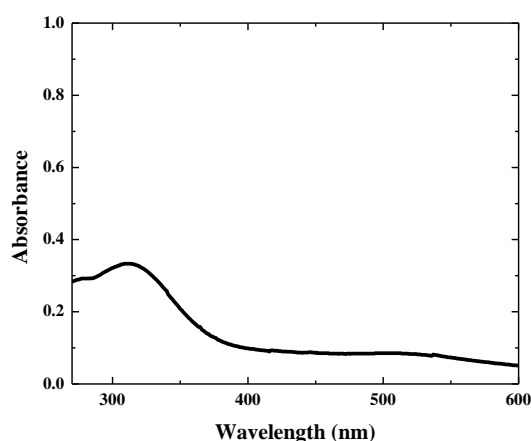


**Figure 5.49.** spectrum of hydrogenation reaction of PDEAEMA-Au in low pH after 10 min reaction.

In order to overcome this, PDEA-Au microgels were charged via an ion-exchange reaction with iodomethane ( $\text{CH}_3\text{I}$ ) which made them well dispersed at high pH aqueous solutions. The nanocatalysts (22mg PDEA-Au, 0.0065 mmol) were initially dissolved in 1 mL of tetrahydrofuran (THF) and the solution was mixed with 0.1mmol of  $\text{CH}_3\text{I}$ . Following that, the hydrogenation reaction was carried out as above. Figure 5.50 shows that the PDEA-Au microgels are convenient catalysts for the reaction as the concentration of the 4-NP was reduced 78% at the first 20 min.

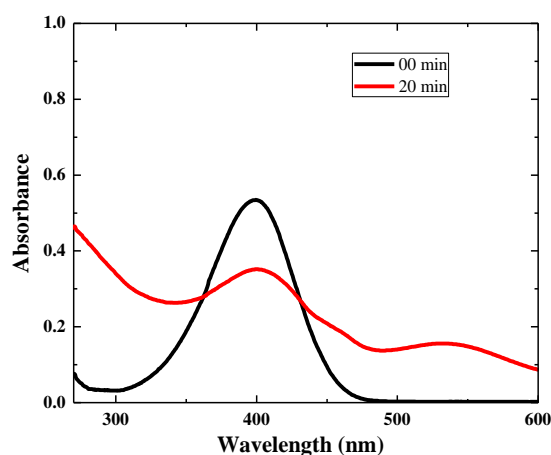


**Figure 5.50.** Hydrogenation reaction of PDEA-Au nanocatalysts after the ion-exchange reaction.

The hydrogenation of 4-NP was carried out also under basic conditions with PMAA/Pd with the same procedure as with PDEA-Au nanocatalysts (Figure 5.51).

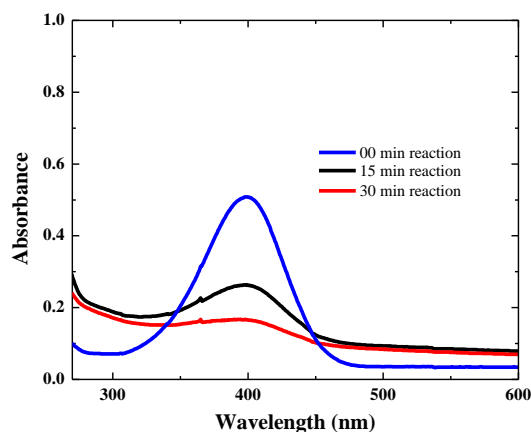


**Figure 5.51.** Hydrogenation reaction using PMAA-Pd nanocatalysts under basic conditions.

The PMAA-Pd microgels proved to be effective nanocatalysts for the hydrogenation of 4-NP as in 30 min there was only 6% of the 4-NP (Figure 5.51).

After these encouraging results, the direct synthesis of quaternized microgels was performed, and the metal containing nanoparticles, were tested for their catalytic activity. The conditions of the reaction were the same as previous. However, in this case 120 mg of PDEAEMA/Au (75% quaternized, 1.5 % in Au), were added to the aqueous solution of 4-NP+NaBH<sub>4</sub> (Figure 5.52).

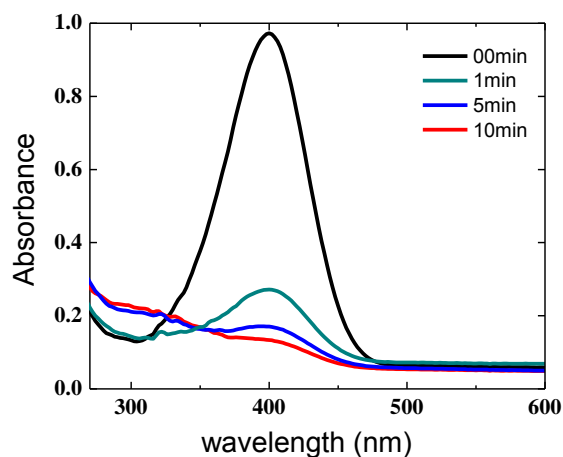


**Figure 5.52.** Hydrogenation reaction using 120 mg of PDEAEMA/Au nanocatalysts (75% quaternized, 1.5 % in Au).

According to the above results, approximately the 70% of 4-NP was reduced into 4-AP at only 1 min. This proves the efficiency and the high activity of the nanocatalysts, making them ideal for the performance of catalytic reactions. In order to study the kinetic of the reaction, the same procedure was repeated with 90 mg of PDEAEMA/Au nanocatalysts (75% quaternized, 1.5 % in Au) (Figure 5.53).

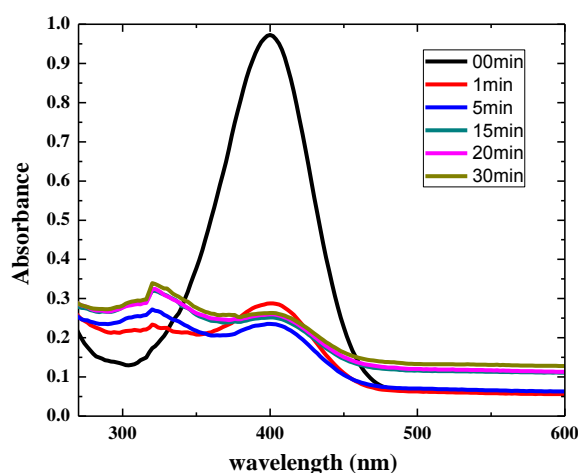


**Figure 5.53.** Hydrogenation reaction using 90 mg of PDEAEMA/Au nanocatalysts (75% quaternized, 1.5 % in Au).

Comparing of Figures 5.52 and 5.53 shows that there are not specific differences in the rate of the reaction. In both cases, 70 % of 4-NP is being reduced to 4-AP. The reduction of 4-NP by  $\text{NaBH}_4$  occurs very rapidly in the presence of the PDEAEMA/Au microgels, which could be visualized with the discoloration of the characteristic yellow- green color of 4-nitrophenolate ion.

Afterwards, the reaction was performed by utilized even smaller quantity of the microgels. In this case, 60 mg of PDEAEMA/Au nanocatalysts (75% quaternized, 1.5 % in Au), were added to the aqueous solution of 4-NP+ $\text{NaBH}_4$  (Figure 5.54).

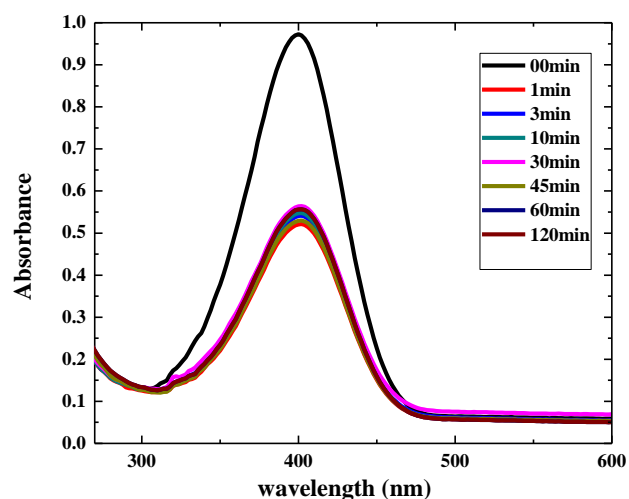


**Figure 5.54.** Hydrogenation reaction using 60 mg of PDEAEMA/Au nanocatalysts (75% quaternized, 1.5 % in Au).

Comparing the Figure 5.54 with the previous results, there is a noticeable decrease in the reaction rate, as at the first minute, only 45 % of 4-NP has been reduced. It is interesting that, by increasing the reaction time, we do not observe a continuation of reduction of 4-NP. Even after 2 h of reaction, the % of the reduced 4-NP, is the same as in the first minute. This happens because the amount of the catalysts is inadequate for the reduction of the 4-NP and the reaction cannot be performed without the presence of the catalysts.

So, the main outcome of these experiments, referring to the catalytic activity of the microgels, is that the reduction reaction of 4-NP happens instantaneously, in the presence of the metal containing microgels.

#### 5.4. Conclusions

In this work, PDEAEMA, PAA and PMAA microgels, with and without metal nanoparticles, were successfully synthesized and immobilized onto glass substrates. Initially, the attachment of the microgels onto surfaces was performed by dip or drop casting method. However, these methods led to low homogeneity and multi-layer structures. In order to form uniform films, Pickering emulsion method and Vortical surface method, were utilized. The drawback of the above procedures was that few of the microgels remained attached after a water flow test. However the hybrid nanoparticulate catalysts should also combine the suitability to flow chemistry. It is important to achieve the covalent immobilization of pH-responsive microgels under microfluidic flow conditions for their efficient implementation in mild industrial catalytic processes. For this purpose, the amine coupling method was utilized. The immobilized microgels were subjected to environmental changes (heating temperature, heating time, flow rate and pH) in order to examine their stability under microfluidic flow conditions.

The metal containing microgels were uniformly and homogeneously distributed on the substrates and the area occupied by the microgels was found to be  $35\pm 2\%$  for both samples. The microgels proved to be strongly attached onto the substrates and survived all the stability tests (even the combination of water rinsing, pH, and temperature increase) with almost no microgel removal from the substrates.

The catalytic behavior of the synthesized metal containing microgels was studied through a model hydrogenation reaction. According to the results, the reduction reaction did not occur

without catalysts. Furthermore, the catalytic reaction, in the presence of the appropriate amount of catalysts, occurs directly, with a very high rate. It needs less than one minute for the reduction to be completed.

These results are particularly attractive for the strong and irreversible binding of catalytically relevant nanoparticles on microfluidic wall channels to be employed in mild industrial catalytic processes under flow.

## 5.5. References

- (1) Abrol, S.; Caulfield, M. J.; Qiao, G. G.; Solomon, D. H. Studies on Microgels. 5. Synthesis of Microgels via Living Free Radical Polymerisation. *Polymer (Guildf)*. **2001**, *42* (14), 5987–5991.
- (2) Baig, M. W.; Siddiq, M. Quantum Mechanics of In Situ Synthesis of Metal Nanoparticles within Anionic Microgels. *J. Theor. Chem.* **2013**, 1–5.
- (3) Das, M. Stimulus-Responsive Microgels: Design, Properties and Applications. *Stimulus-Responsive Microgels: Design, Properties and Applications* Mallika Das Department of Chemistry. **2008**.
- (4) De Geest, B. G.; Urbanski, J. P.; Thorsen, T.; Demeester, J.; De Smedt, S. C. Synthesis of Monodisperse Biodegradable Microgels in Microfluidic Devices. *Langmuir* **2005**, *21* (23), 10275–10279.
- (5) Li, Y. Smart Microgels for Controlled Uptake and Release, Wageningen University, 2011.
- (6) Vinogradov, S. V. Colloidal Microgels in Drug Delivery Applications. *Curr Pharm Des.* **2006**, *12* (36), 4703–4712.
- (7) Nayak, S. Design, Synthesis and Characterization of Multiresponsive Microgels, Georgia Institute of Technology, 2005.
- (8) Sahiner, N.; Godbey, W. T.; McPherson, G. L.; John, V. T. Microgel, Nanogel and Hydrogel-Hydrogel Semi-IPN Composites for Biomedical Applications: Synthesis and Characterization. *Colloid Polym. Sci.* **2006**, *284* (10), 1121–1129.
- (9) Gawlitza, K. P-NIPAM Microgels as Stimuli Responsive Matrix for Embedding Functional Inorganic and Organic Particles, Berlin, 2012.
- (10) Hanel, C.; Likos, C.; Blaak, R. Effective Interactions between Multilayered Ionic Microgels. *Materials (Basel)*. **2014**, *7* (12), 7689–7705.
- (11) Hendrickson, G. R. Harnessing Microgel Softness for Biointerfacing, Georgia Institute of Technology, 2013.
- (12) Kaliva, M.; Frysali, M. A.; Flouraki, C.; Papoutsakis, L.; Vamvakaki, M.; Anastasiadis, S. H. Metallic Nanocatalysts Embedded within pH-Responsive Polymeric Microgels and Deposition onto Solid Substrates. *Macromol. Symp.* **2013**, *331–332* (1), 17–25.
- (13) Parasuraman, D. Poly(N-Isopropylacrylamide) Based Microgels and Their Assemblies for Organic Molecule Removal from Water, University of Alberta, 2012.
- (14) Cai, J.; Guo, J.; Ji, M.; Yang, W.; Wang, C.; Fu, S. Preparation and Characterization of Multiresponsive Polymer Composite Microspheres with Core-Shell Structure. *Colloid Polym. Sci.* **2007**, *285* (14), 1607–1615.
- (15) Geisel, K.; Isa, L.; Richtering, W. The Compressibility of Ph-Sensitive Microgels at the

- Oil-Water Interface: Higher Charge Leads to Less Repulsion. *Angew. Chemie - Int. Ed.* **2014**, *53* (19), 4905–4909.
- (16) Haider, I.; Siddiq, M.; Shah, S. M.; ur Rehman, S. Synthesis and Characterization of Multi-Responsive Poly (NIPAM-Co-AAc) Microgels. *IOP Conf. Ser. Mater. Sci. Eng.* **2014**, *60*, 12046.
- (17) Klinger, D.; Landfester, K. Stimuli-Responsive Microgels for the Loading and Release of Functional Compounds: Fundamental Concepts and Applications. *Polym. (United Kingdom)* **2012**, *53* (23), 5209–5231.
- (18) Hou, L.; Wu, P. Microgels with Linear Thermosensitivity in a Wide Temperature Range. *Macromolecules* **2016**, *49* (16), 6095–6100.
- (19) Argentiere, S.; Blasi, L.; Ciccarella, G.; Cazzato, A.; Barbarella, G.; Cingolani, R.; Gigli, G. Smart Surfaces for pH Controlled Cell Staining. *Soft Matter* **2009**, *5* (21), 4101.
- (20) Nayak, S.; Andrew Lyon, L. Soft Nanotechnology with Soft Nanoparticles. *Angew. Chemie - Int. Ed.* **2005**, *44* (47), 7686–7708.
- (21) Hashmi, S. M.; Dufresne, E. R. Mechanical Properties of Individual Microgel Particles through the Deswelling Transition. *Soft Matter* **2009**, *5* (19), 3682.
- (22) Kobayashi, H.; Winkler, R. G. Structure of Microgels with Debye-Hückel Interactions. *Polymers (Basel)*. **2014**, *6* (5), 1602–1617.
- (23) Christodoulakis, K. E.; Vamvakaki, M. pH-Responsive Microgel Particles Comprising Solely Basic or Acidic Residues. *Macromol. Symp.* **2010**, *291–292* (1), 106–114.
- (24) Karg, M.; Hellweg, T. New “smart” poly(NIPAM) Microgels and Nanoparticle Microgel Hybrids: Properties and Advances in Characterisation. *Curr. Opin. Colloid Interface Sci.* **2009**, *14* (6), 438–450.
- (25) Balamuralidhara, V.; Pramodkumar, T. M.; Srujana, N.; Venkatesh, M. P.; Vishal, N.; Gupta, K. L.; Krishna, K. L.; Gangadharappa, H. V. pH Sensitive Drug Delivery Systems: A Review. *Am. J. Drug Discov. Dev.* **2011**, *1* (1), 24–48.
- (26) Byssel, H. Interaction Between Microgels and Oppositely Charged Peptides, Uppsala Universitet, 2009.
- (27) Oh, J. K.; Drumright, R.; Siegwart, D. J.; Matyjaszewski, K. The Development of Microgels/nanogels for Drug Delivery Applications. *Prog. Polym. Sci.* **2008**, *33* (4), 448–477.
- (28) Pérez-Alvarez, L.; Sáez-Martínez, V.; Hernaez, E.; Herrero, M.; Katime, I. Specific pH-Responsive Folate-Conjugate Microgels Designed for Antitumor Therapy. *Macromol. Chem. Phys.* **2009**, *210* (6), 467–477.
- (29) Khare, A. R.; Peppas, N. A. Release Behavior of Bioactive Agents from pH-Sensitive Hydrogels. *Journal of biomaterials science. Polymer edition.* 1994, pp 275–289.
- (30) Brannon-Peppas, L.; Peppas, N. A. Dynamic and Equilibrium Swelling Behaviour of pH-Sensitive Hydrogels Containing 2-Hydroxyethyl methacrylate1. *The Biomaterials: Silver Jubilee Compendium.* 2006, pp 51–60.
- (31) Farooqi, Z. H.; Khan, S. R.; Begum, R.; Kanwal, F.; Sharif, A.; Ahmed, E.; Majeed, S.; Ijaz, K.; Ijaz, A. Effect of Acrylic Acid Feed Contents of Microgels on Catalytic Activity of Silver Nanoparticles Fabricated Hybrid Microgels. *Turkish J. Chem.* **2015**, *39*, 96–107.
- (32) Lu, Y.; Proch, S.; Schrunner, M.; Drechsler, M.; Kempe, R.; Ballauff, M. Thermosensitive Core-Shell Microgel as a “nanoreactor” for Catalytic Active Metal Nanoparticles. *J. Mater. Chem.* **2009**, *19* (23), 3955.
- (33) Lu, Y.; Mei, Y.; Drechsler, M.; Ballauff, M. Thermosensitive Core-Shell Particles as Carriers for Ag Nanoparticles: Modulating the Catalytic Activity by a Phase Transition in Networks. *Angew. Chemie - Int. Ed.* **2006**, *45* (5), 813–816.

- (34) Mei, Y.; Lu, Y.; Polzer, F.; Ballauff, M.; Drechsler, M. Catalytic Activity of Palladium Nanoparticles Encapsulated in Spherical Poly Electrolyte Brushes and Core-Shell Microgels. *Chem. Mater.* **2007**, *19* (5), 1062–1069.
- (35) Zhang, J. T.; Wei, G.; Keller, T. F.; Gallagher, H.; Stötzl, C.; Müller, F. a.; Gottschaldt, M.; Schubert, U. S.; Jandt, K. D. Responsive Hybrid Polymeric/metallic Nanoparticles for Catalytic Applications. *Macromol. Mater. Eng.* **2010**, *295* (11), 1049–1057.
- (36) Khan, S.; Farooqi, Z.; Ajmal, M. Synthesis, Characterization, and Silver Nanoparticles Fabrication in N-Isopropylacrylamide Based Polymer Microgels for Rapid Degradation of P-Nitrophenol. *J. Dispers. Sci. Technol.* **2012**, No. December 2014, 37–41.
- (37) Ma, L.; Liu, M.; Liu, H.; Chen, J.; Cui, D. In Vitro Cytotoxicity and Drug Release Properties of pH- and Temperature-Sensitive Core-Shell Hydrogel Microspheres. *Int. J. Pharm.* **2010**, *385* (1–2), 86–91.
- (38) Denc, I.; Ott, D.; Kralisch, D.; Noe, T.; Meuldijk, J.; Croon, M. De; Hessel, V.; Laribi, Y.; Perrichon, P. Eco-E Ffi Ciency Analysis for Intensi Fi Ed Production of an Active Pharmaceutical Ingredient : A Case Study. **2014**.
- (39) Mark, L. Catalytic Transfer Hydrogenation of Aromatic Nitro Compounds in the Presence of Nickel Thiolato-Complexes. **1988**, *223*, 221–223.
- (40) Altman, R. a.; Buchwald, S. L. Pd-Catalyzed Suzuki-Miyaura Reactions of Aryl Halides Using Bulky Biarylmonophosphine Ligands. *Nat. Protoc.* **2007**, *2* (12), 3115–3121.
- (41) Schmidt, S.; Motschmann, H.; Hellweg, T.; von Klitzing, R. Thermoresponsive Surfaces by Spin-Coating of PNIPAM-Co-PAA Microgels: A Combined AFM and Ellipsometry Study. *Polymer (Guildf)*. **2008**, *49* (3), 749–756.
- (42) Seeber, M.; Zdyrko, B.; Burtovvy, R.; Andruk, T.; Tsai, C.-C.; Owens, J. R.; Kornev, K. G.; Luzinov, I. Surface Grafting of Thermoresponsive Microgel Nanoparticles. *Soft Matter* **2011**, *7* (21), 9962.
- (43) Zhang, T.; Qian, J.; Tuo, X.; Yuan, J.; Wang, X. Fabricating Ordered Porous Monolayers from Colloidal Monolayer and Multilayer. *Colloids Surfaces A Physicochem. Eng. Asp.* **2009**, *335* (1–3), 202–206.
- (44) Li, Y. J.; Huang, W. J.; Sun, S. G. A Universal Approach for the Self-Assembly of Hydrophilic Nanoparticles into Ordered Monolayer Films at a Toluene/water Interface. *Angew. Chemie - Int. Ed.* **2006**, *45* (16), 2537–2539.
- (45) Park, Y. K.; Yoo, S. H.; Park, S. Assembly of Highly Ordered Nanoparticle Monolayers at a Water/ Hexane Interface. *Langmuir* **2007**, *23* (21), 10505–10510.
- (46) Seo, Y. S.; Yoon, K.; Rafailovich, M. Highly Ordered Monolayer Formation of Silica Beads Assisted by Ultra-Sound and Microscopic Barrier at Air/water Interface. *J. Ind. Eng. Chem.* **2010**, *16* (6), 879–883.
- (47) Hall, D. B.; Underhill, P.; Torkelson, J. M. Spin Coating of Thin and Ultrathin Polymer Films. *Polym. Eng. Sci.* **1998**, *38* (12), 2039–2045.
- (48) Jiang, P.; Prasad, T.; McFarland, M. J.; Colvin, V. L. Two-Dimensional Nonclose-Packed Colloidal Crystals Formed by Spincoating. *Appl. Phys. Lett.* **2006**, *89* (1), 1–3.
- (49) Pan, F.; Zhang, J.; Cai, C.; Wang, T. Rapid Fabrication of Large-Area Colloidal Crystal Monolayers by a Vortical Surface Method. *Langmuir* **2006**, *22* (17), 7101–7104.
- (50) Baker, W. O. Microgel, a New Macromolecule. Relation to Sol and Gel as Structural Elements of Synthetic Rubber. *Rubber Chem. Technol.* **1949**, *41* (3), 511–520.
- (51) Lyon, L. A.; Fernandez-Nieves, A. The Polymer/Colloid Duality of Microgel Suspensions. *Annu. Rev. Phys. Chem.* **2012**, *63* (1), 25–43.
- (52) Graham, N. B.; Cameron, A. Nanogels and Microgels: The New Polymeric\materials Playground. *Pure Appl. Chem* **1998**, *70* (6), 1271–1275.

- (53) Fisher, O. Z. Novel pH-Responsive Microgels and Nanogels as Intelligent Polymer Therapeutics, 2008.
- (54) Odian G. *Principles of Polymerization, Chapter 4: Emulsion Polymerization*; 2004; Vol. 4th Ed.
- (55) Lovell, Peter A. - 1997 - Emulsion Polymerization and Emulsion Polymers.pdf.
- (56) Harkins, W. D. A General Theory of the Mechanism of Emulsion Polymerization 1. *J. Am. Chem. Soc.* **1947**, 69 (6), 1428–1444.
- (57) Palioura, D.; Armes, S. P.; Anastasiadis, S. H.; Vamvakaki, M. Metal Nanocrystals Incorporated within pH-Responsive Microgel Particles. *Langmuir*. 2007, pp 5761–5768.
- (58) Kontturi, K. *Modification of Surfaces with Adsorption of Amphiphilic Polymers*; 2013.
- (59) Kong, F.; Hu, Y. F. Biomolecule Immobilization Techniques for Bioactive Paper Fabrication. *Anal. Bioanal. Chem.* **2012**, 403 (1), 7–13.
- (60) Mohamad, N. R.; Marzuki, N. H. C.; Buang, N. A.; Huyop, F.; Wahab, R. A. An Overview of Technologies for Immobilization of Enzymes and Surface Analysis Techniques for Immobilized Enzymes. *Biotechnol. Biotechnol. Equip.* **2015**, 29 (2), 205–220.
- (61) Erban, R.; Chapman, S. J. On Chemisorption of Polymers to Solid Surfaces. *J. Stat. Phys.* **2007**, 127 (6), 1255–1277.
- (62) Christodoulakis, K. E.; Vamvakaki, M. Amphoteric Core–Shell Microgels: Contraphilic Two-Compartment Colloidal Particles. *Langmuir* **2009**, 26 (2), 639–647.
- (63) Pavlopoulou, E.; Portale, G.; Christodoulakis, K. E.; Vamvakaki, M.; Bras, W.; Anastasiadis, S. H. Following the Synthesis of Metal Nanoparticles within pH-Responsive Microgel Particles by SAXS. *Macromolecules*. 2010, pp 9828–9836.
- (64) Hashim, U.; Farehanim, M. A.; Azizah, N.; Norhafiezah, S.; Fatin, M. F.; Ruslinda, A. R.; Ayub, R. M. Comparison of Drop Casting vs. Spray Pyrolysis MWCNTs Technique for Surface Modification Based Interdigitated Electrode. *Proc. - 2015 2nd Int. Conf. Biomed. Eng. ICoBE 2015* **2015**, No. March, 30–31.
- (65) Puetz, J.; Aegerter, M. a. Dip Coating Technique. *Sol-Gel Technol. Glas. Prod. Users* **2004**, 37–48.
- (66) Reincke, F.; Hickey, S. G.; Kegel, W. K.; Vanmaekelbergh, D. Spontaneous Assembly of a Monolayer of Charged Gold Nanocrystals at the Water/Oil Interface. *Angew. Chemie - Int. Ed.* **2004**, 43 (4), 458–462.
- (67) Xu, L.; Han, G.; Hu, J.; He, Y.; Pan, J.; Li, Y.; Xiang, J. Hydrophobic Coating- and Surface Active Solvent-Mediated Self-Assembly of Charged Gold and Silver Nanoparticles at Water-Air and Water-Oil Interfaces. *Phys. Chem. Chem. Phys.* **2009**, 11 (30), 6490–6497.
- (68) Chen, H.; Hu, L.; Fang, X.; Wu, L. General Fabrication of Monolayer SnO<sub>2</sub> Nanonets for High-Performance Ultraviolet Photodetectors. *Adv. Funct. Mater.* **2012**, 22 (6), 1229–1235.
- (69) Dai, L. L.; Sharma, R.; Wu, C. Self-Assembled Structure of Nanoparticles at a Liquid-Liquid Interface. *Langmuir* **2005**, 21 (7), 2641–2643.
- (70) Morigaki, K.; Baumgart, T.; Jonas, U.; Offenhäusser, A.; Knoll, W. Photopolymerization of Diacetylene Lipid Bilayers and Its Application to the Construction of Micropatterned Biomimetic Membranes. *Langmuir* **2002**, 18 (10), 4082–4089.
- (71) Arslan, G.; Özmen, M.; Gündüz, B.; Zhang, X.; Ersöz, M. Surface Modification of Glass Beads with an Aminosilane Monolayer. *Turkish J. Chem.* **2006**, 30 (2), 203–210.
- (72) Howarter, J. a.; Youngblood, J. P. Optimization of Silica Silanization by 3-Aminopropyltriethoxysilane. *Langmuir* **2006**, 22 (26), 11142–11147.

- (73) Fischer, M. J. Amine Coupling through EDC/NHS: A Practical Approach. *Methods Mol Biol.* **2010**, *627*, 55–73.
- (74) Astruc, D.; Bönnemann, H.; Nagabhushana, K. S.; Richards, R. M.; Bronstein, L. M.; Matveeva, G.; Sulman, E. M.; Chandler, B. D.; Gilbertson, J. D.; Vallribera, A.; et al. *Nanoparticles and Catalysis Vol. 1*; 2008.
- (75) Das, S. K.; Parandhaman, T.; Pentela, N.; Islam, a K. M. M.; Mandal, A. B.; Mukherjee, M. Understanding the Biosynthesis and Catalytic Activity of Pd, Pt, and Ag Nanoparticles in Hydrogenation and Suzuki Coupling Reactions at the Nano – Bio Interface. *J. Phys. Chem. C* **2014**, *118*, 24623–24632.
- (76) Mu, B.; Zhang, W.; Wang, A. Facile Fabrication of Superparamagnetic Coaxial Gold/halloysite nanotubes/Fe<sub>3</sub>O<sub>4</sub> Nanocomposites with Excellent Catalytic Property for 4-Nitrophenol Reduction. *J. Mater. Sci.* **2014**, *49* (20), 7181–7191.

## Chapter 6

### 6.1 Concluding remarks

In this thesis, novel multifunctional surfaces which would be able to alter their wetting behavior even all the way from superhydrophilic to superhydrophobic in response to changes in single or multiple external stimuli, were successfully developed.

In **Chapter 2**, a multi-functional surface with a ZnO coating deposited onto a hierarchically roughened surface has been fabricated with a two-step process. First, silicon (Si) wafers are irradiated with femtosecond (fs) laser pulses in order to produce Si surfaces with dual scale roughness (Si spikes). Then, the rough Si samples are coated with a ZnO film prepared by a simple sol-gel process. The wettability and the photocatalytic activity of the surfaces have been investigated. High photocatalytic activity is achieved with a ~90% decolorization of a model dye in ~60 min. The systems exhibit a reversible wettability behavior from superhydrophilic (upon UV irradiation) to superhydrophobic (upon heating). The stability of the behavior is investigated extensively and the system proves to be quite stable. To the best of our knowledge, this is the first work on the development of surfaces with both high photocatalytic activity and reversible wettability behavior from superhydrophobic to superhydrophilic. The combination of photocatalysis with reversible wettability with a single coating makes the system appropriate for a variety of applications, such as self-cleaning surfaces, air purification, marine coatings or fog-proofing.

Moreover, ZnO nanowires with high photocatalytic behavior were developed as well. In order to achieve this, initially ZnO nanowires were grown on ZnO pre-coated glass substrates via

aqueous solution growth. The samples were subsequently coated with polymers with the spin coating method. Polymethylmethacrylate (PMMA) and poly(2-vinylpyridine) (P2VP) were utilized for this purpose. The influence of the parameters of the spin coating process were studied. Samples were characterized with Scanning Electron Microscopy and were tested for their photocatalytic behavior with Fourier Transform Infrared spectroscopy (FTIR). Stearic acid was utilized as a test organic pollutant. Samples were also tested for their wettability. All samples exhibited photocatalytic activity, with the behavior depending on the thickness of the polymer film. The highest photocatalytic degradation of the model dye achieved was found to be ~85%, for the thinnest polymer film. This was attributed to the fact that the very thin polymer film did not reduce the high surface-to-volume ratio of the ZnO nanowires.

The contact angle of ZnO nanowires covered with P2VP was higher compared to the bare ZnO nanostructures. This behavior was enhanced by increasing the concentration of the polymer in the toluene solution, thus, by increasing the thickness of the polymer film. The contact angle value was modified from 63° to 137° by changing the coating conditions.

P2VP coated ZnO nanowires were also tested for their pH responsiveness and the samples maintained their reversible behavior for 3 cycles (switching from 72° at pH 2 to 109° at pH 12). That happened because the ZnO nanorods are being removed with the repetitive immersion in acidic conditions.

In **Chapter 3**, parahydrophobic polymer surfaces were developed. The procedure involves the preparation of hierarchical roughened micro/nano-structured surfaces utilizing fs laser irradiation of silicon substrates and their functionalization using end-anchored poly(2-vinyl pyridine), P2VP, or poly(N-isopropyl acrylamide), PNIPAm, chains utilizing the “grafting to” method. The effect of the molecular weight of the polymers on the surface wettability results was investigated and the results found to be reproducible in all cases. The same method was

applied successfully for both carboxy- and hydroxy-terminated polymers. Furthermore, multi-responsive surfaces were developed utilizing a mixture of end-functional P2VP/PNIPAm chains “grafted to” the hierarchical surfaces. “Sticky” highly hydrophobic surfaces were achieved, with reversible and controllable wetting characteristics, imitating plant leaves with “parahydrophobic” behavior. These surfaces can be successfully applied in industry as switchable valves, biosensors, tunable microlenses and for selective liquid separation.

These, P2VP- and PNIPAm-coated surfaces were also applied for cell seeding. To our knowledge, cellular response on P2VP surfaces has not been reported in the literature. P2VP appears to favor cell attachment and proliferation within 7 days of culture. Together with the topographical features induced with the laser treatment, directionality of the attached cells has been also achieved. Cells were initially attached onto the PNIPAM-coated surfaces, as well. However, due to the fixation process, which was used to prepare the samples for SEM imaging, where glutaraldehyde at a low temperature (9°C) was used, the cell layer that was formed apparently detached from the surface since the temperature was far below the polymer transition temperature (32°C). This explains why there were very few cells observed with the SEM. Thus, the PNIPAM-coated Si surfaces are not representative and conclusive for the cell seeding.

In **Chapter 4**, non-adhesive superhydrophobic surfaces were developed with directional droplet roll-off behavior. To the best of our knowledge, this is the first work referring to tilted spikes treated with fs-laser. In this work, Si substrates were treated with femto-second laser in order to achieve the dual-scale roughness. However, the irradiation was not performed in a conventional way but at a tilt angle. The substrate was tilted and, as a result, the laser beam was not pointed perpendicular to the surface. This procedure led to the formation of tilted periodic spikes. Such surfaces after a silanization process exhibit anisotropic wettability, with a droplet

motion on the direction of the spikes. It was observed that the velocity of the droplet motion depended on the chosen tilt angle.

In parallel, a third level of macro-structuring was introduced by patterning the inorganic surfaces using photolithography in order to enhance the anisotropic wetting behavior. Si substrates, patterned with grooves, were irradiated with fs laser at a tilt angle. These surfaces exhibit superhydrophilic directionality after thermal oxidation and superhydrophobic directional wettability after silanization. The effect of the characteristics of the grooves on the final contact angle was investigated.

Furthermore, superhydrophilic and superhydrophobic surfaces with high unidirectional hysteresis were developed. This was achieved by the irradiation of Si wafers utilizing a fs-laser beam with central wavelength of 800 nm at a tilt angle, 30° or 45°. Such surfaces after a silanization process exhibit anisotropic wettability with a directional hysteresis. This phenomenon was enhanced in the case of 45° tilted spikes. Such surfaces can be applied in liquid transportation without loss and in the analysis of very small volumes of liquid samples.

In **Chapter 5**, poly(2-(diethylamino)ethylmethacrylate), PDEAEMA, poly(acrylic) acid, PAA, and poly(methacrylic acid), PMAA, microgels, with and without metal nanoparticles, were successfully synthesized and immobilized onto glass substrates. Initially, the attachment of the microgels onto surfaces was performed by the dip coating or drop casting method. These methods led to low homogeneity and multi-layer structures. In order to form uniform films, the pickering emulsion method and the vortical surface method were utilized. The drawback of the above procedures was that few of the microgels remained attached after a water flow test. However the hybrid nanoparticulate catalysts should also combine the suitability to flow chemistry. It is important to achieve the covalent immobilization of pH-responsive microgels under microfluidic flow conditions for their efficient implementation in mild industrial

catalytic processes. For this purpose, an amine coupling method was utilized: the glass substrates were first functionalized with amine groups using 3-aminopropyl-triethoxysilane followed by the covalent binding of the PMAA or PAA microgels via their carboxyl moieties forming an amide bond. The immobilized microgels were subjected to environmental changes (heating temperature, heating time, flow rate and pH) in order to examine their stability under microfluidic flow conditions. The metal containing microgels were uniformly and homogeneously distributed on the substrates and the area occupied by the microgels was found to be  $35\pm 2\%$  for both samples under the specific microgel dispersion concentration used. The microgels proved to be strongly attached onto the substrates and survived all the stability tests (even the combination of water rinsing, pH, and temperature increase) with almost no microgel removal from the substrates. The catalytic behavior of the synthesized metal containing microgels was studied through a model hydrogenation reaction. According to the results, the reduction reaction did not occur without catalysts. Furthermore, the catalytic reaction, in the presence of the appropriate amount of catalysts, occurs readily, with a very high rate. It needs less than one minute for the reduction to be completed. These results are particularly attractive for the strong and irreversible binding of catalytically relevant nanoparticles on microfluidic wall channels to be employed in mild industrial catalytic processes under flow.

## 6.2 Future work

Some of the projects mentioned in the previous chapters can be benefited by carrying out more experiments. Some of those experiments are mentioned in this subsection.

In **Chapter 2**, multi-functional surfaces were developed with a ZnO coating deposited onto a hierarchical roughened surface. The resulted surfaces exhibited both high photocatalytic activity and reversible wettability. One can imagine adding one more property to the surface, by grafting a responsive polymer on the ZnO film, either to enhance a property of ZnO or to

add a new one. Furthermore, ZnO is also known for its oleophobicity. So, the same surfaces can be tested for their oleophobic behavior. Such surfaces can be applied for long-term anti-fogging, self-cleaning, anti-fouling and oil and water separation.

Polymer brush-functionalized ZnO nanowires with high photocatalytic behavior were also developed. P2VP-coated ZnO nanowires were tested for their pH responsiveness and the samples did not maintain their reversible behavior. In order to develop nanowires with both high photocatalytic activity and reversible wettability, TiO<sub>2</sub> can be used instead of ZnO. TiO<sub>2</sub> is also photocatalytically active and exhibits reversible wettability; however, it is stable under acidic or alkaline pH conditions.

In **Chapter 3**, parahydrophobic polymer surfaces with reversible wettability were developed and applied for cell seeding. According to the preliminary study, P2VP appears to favor cell attachment and proliferation. On PNIPAm-coated surfaces, cells were initially attached onto the substrate. However, due to the fixation process, the cell layer detached from the surface. In order to study the pH- and/or thermo- responsive behavior of cells, live-cell imaging experiments should be performed. The design of temperature-responsive polymer surfaces for the controllable cell attachment-detachment has provided an enormous potential to fabricate clinically applicable regenerative medicine. Depending on the application, the surfaces should promote cell adhesion (e.g., in an implant) or promote cell detachment (e.g., in cell sheet engineering). So, responsive surfaces with controllable cell attachment can be applied for the development of smart systems for tissue engineering.

Furthermore, multi-responsive surfaces were developed utilizing a mixed P2VP/PNIPAm polymer brush. However, X-ray photoelectron spectroscopy (XPS) should be done in order to quantitatively verify the real composition of the mixed P2VP/PNIPAm brush.

In **Chapter 4**, non-adhesive superhydrophobic surfaces were developed, with directional droplet roll-off behavior. In parallel, superhydrophilic and superhydrophobic surfaces with

high unidirectional hysteresis were fabricated. This work will be benefited by a model providing reasonable predictions of the observed wetting behavior and the key design parameters required to enhance the anisotropic adhesion. Ongoing work includes optimizing the droplet transport mechanism and grafting responsive polymers.

In **Chapter 5**, PDEAEMA, PAA and PMAA microgels, with and without metal nanoparticles, were successfully synthesized and immobilized onto glass substrates. The catalytic behavior of the synthesized metal containing microgels was also studied. Ongoing work includes the study of the kinetics of the reaction. The next step in this project will be to investigate the catalytic behavior of the immobilized microgels.